IMAGE-GUIDED ROBOTICS FOR

AUTONOMOUS VENIPUNCTURE

by

ALVIN I. CHEN

A dissertation submitted to the

Graduate School –New Brunswick

Rutgers, the State University of New Jersey

and

The Graduate School of Biomedical Sciences

In partial fulfillment of the requirements

For the degree of

Doctor of Philosophy

Graduate Program in Biomedical Engineering

Written under the direction of

Dr. Martin L. Yarmush

And approved by

_____

_____

_____

_____

_____

New Brunswick, New Jersey

October 2016

ABSTRACT OF THE DISSERTATION

Image-Guided Robotics for Autonomous Venipuncture

By ALVIN I. CHEN

Dissertation Director: Martin L. Yarmush

Performed over 1.5 billion times each year, venipuncture is the most ubiquitous clinical intervention and leading cause of medical injury in the United States. This dissertation describes the development of a medical device aimed at minimizing venipuncture-related adverse events by drawing blood and placing peripheral vascular catheters in an automated manner. The device may be particularly suited to challenging populations, including pediatric, geriatric, chronically-ill, and obese patients, for whom the rates of success depend heavily on practitioner skill. The device combines 3D near-infrared and ultrasound imaging, computer vision software, and a miniaturized dexterous robot that inserts the needle based on real-time image guidance. Methods to robustly segment, localize, and track the pose of the vessels are presented, and robotic prototypes capable of autonomously aligning and servoing the needle under real-time image guidance are introduced. In imaging studies on human volunteers spanning a broad range of demographic characteristics, the device was able to detect a majority of forearm veins that remained invisible to clinical visual assessment. In cannulation studies on *in vitro* and *in vivo* models, the device demonstrated significant improvements in first-stick accuracy and completion time compared to unassisted and image-guided manual venipuncture techniques. The results of these studies may be used to inform future clinical trials evaluating device feasibility in normal and difficult patient groups. Once translated, the device may be targeted to high-volume laboratory testing facilities and hospitals, and the underlying technologies may be extended to other diagnostic and interventional procedures, including automated point-of-care blood analysis, in-clinic and at-home hemodialysis venipuncture, peripherally-inserted central catheter placement, and emergency or military use.

ACKNOWLEDGEMENTS

TABLE OF CONTENTS

LIST OF FIGURES

Chapter 2

Chapter 3

Chapter 4

Chapter 5

Supplementary

LIST OF TABLES

Supplementary

LIST OF ABBREVIATIONS

2D .... *two-dimensional*

3D .... *three-dimensional*

ACF .... *antecubital fossa*

ANCOVA .... *analysis of covariance*

ANOVA .... *analysis of variance*

BMF .... *blood-mimicking fluid*

BSA .... *bovine serum albumin*

CVC .... *central venous catheter*

DH .... *Denavit-Hartenberg*

DOF .... *degrees of freedom*

DOG .... *difference of Gaussians*

FE .... *finite element*

F-LSD .... *Fisher's least significant difference*

FOV .... *field of view*

FPGA .... *field-programmable gate array*

FPS .... *frames per second*

GMP .... *good manufacturing practices*

GUI .... *graphical user interface*

GVF .... *gradient vector flow*

IL-20 .... *Intralipid-20%*

Chapter 1 – Introduction

1.1. Clinical challenges of peripheral venous access

The cannulation of veins and arteries is a central aspect of medical care and is necessary for collecting blood samples, delivering fluids, and monitoring patient health. For 90% of patients admitted to hospital, ambulatory, and emergency care settings, venipuncture represents a first step in the medical intervention[1]. Outside the hospital, venipuncture enables a majority of the diagnostic services provided by primary care clinics and laboratory testing facilities[2]. Carried out 1.4 billion times each year in total, venipuncture is the most commonly performed invasive medical routine in the United States (U.S.)[3].

Today, venipuncture procedures are conducted almost exclusively by trained clinical personnel. In this approach, the operator visually locates or palpates for a suitable vein and then introduces a cannula aiming to reach the center of the vein. In standard practice, practitioners use their knowledge of surface and vessel anatomy, as well as anatomical landmarks, to identify vessels before cannulation. Oftentimes, however, it is difficult to find a suitable cannulation site, particularly in patients with small veins, dark skin, or a high body weight. When a vein is identified, it may also be difficult to estimate its depth or to accurately place the cannula if the vein moves. For these reasons, successful venipuncture depends heavily on the patient's physiological characteristics and the operator's experience and skill[4,5].

Depending on the cannulation site, manual techniques for peripheral vascular access have an overall success rate of 70 to 95%[3,6]. The success rate can decrease below 50% in difficult populations, including pediatric, geriatric, and chronically-ill patients[7–10]. On average, difficult patients require three needle stick attempts per vessel, and the incidence of complications increases six-fold when more than three attempts are made by the same operator. Venipuncture injuries due

to multiple failed attempts significantly increase the likelihood of bruising, internal bleeding, acute pain, accidental puncture of nerves or arteries, and delays in medical treatment[11]. The inaccurate placement of a peripheral catheter increases the chance of extravasation and tissue damage, and repeated failures may necessitate a switch to riskier and more costly interventions such as central venous access[3,12]. Repeated failures have also been associated with an increased likelihood of accidental contact with contaminated sharps, which exposes the practitioner to the risk of blood-borne diseases, including Hepatitis B, Hepatitis C, and HIV[13–15]. As a consequence of these challenges, venipuncture remains the number one cause of patient and practitioner complications in the U.S., and difficulties are estimated to cost the U.S. healthcare system $5B each year[16] (see Appendix for a summary of venipuncture-related costs).

1.2.   Medical complications associated with peripheral venous access

The most common complications or adverse events seen during peripheral venous access are described below and listed approximately in order of their frequency of occurrence[11,17–19].

Pain: Needle pain is usually reported by patients as the worst aspect of a healthcare encounter and may induce stress symptoms, anxiety, and onset of needle phobia[20–22]. Avoidance of healthcare visits, e.g., for immunization or regular blood work, has been strongly associated with the fear of needle pain. Pain is exacerbated when repeated needle insertion attempts are needed, for example, in difficult populations or when complications such as hematoma and nerve puncture occur.

Failure to access the vessel: Incorrect needle positioning, incorrect angle of penetration, inadequate skin traction, and vessel collapse can all result in a failed attempt at accessing the vessel. In this case, repeated insertions are needed, either at the same site or, if the vessel is compromised, at a different site. If it is believed that the selected vein should be accessible, the standard practice is to withdraw the venous access device to just beneath the skin and reattempt the insertion.

Stoppage of blood flow into the flashback chamber: The most common way to confirm that the needle has been successfully inserted into the vessel is by confirming flashback of the blood in the flashback chamber at the base of the needle. If blood does not flow into the flashback chamber upon insertion, or stops flowing during collection, the position of the needle must then be adjusted (often blindly), or the needle must be withdrawn and inserted at a different site. Possible reasons for a stoppage of blood flow or a lack of flashback include vessel collapse or constriction, accidental penetration of the posterior wall of the vessel, slippage of the needle from within the vessel during collection, placement of the needle against a venous valve, and difficulties advancing the catheter.

Hematoma: Hematomas are one of the most frequent occurrences following peripheral venous access and are typically formed when blood leaks out of the vessel and into the surrounding tissues[11]. Hematomas are caused by an injury to the wall of the vessel during puncture and can be seen under the skin as a large bruise. The bruise can cause discomfort and pain and can complicate further cannulations at that location. Hematomas are particularly common in children and elderly patients. In children, small vessels can easily rupture if the needle tip punctures the posterior wall. In elderly patients, vessels become brittle due to hardening of the elastin and collagen fibers in the vessel wall, and this likewise increases the chance of vessel rupture.

Unintended arterial puncture: It can sometimes be difficult to distinguish arteries from veins. To avoid accidental arterial punctures, practitioners are normally taught to palpate the vein carefully to ensure that there is no detectable pulse before attempting to insert the needle. However, particularly in young children and obese patients, it may be difficult to detect palpation, and arteries may be easily mistaken as veins. Accidental arterial puncture can sometimes be recognized by observing pulsation of blood into the flashback chamber. However, if an accidental arterial puncture is not recognized, the delivery of intravenous fluids into the arterial circulation can lead to serious complications.

Peripheral nerve damage: Accidental puncture of superficial nerves is rare but possible when the nerves are located near a vessel[23–25]. Nerve injuries most often occur when the needle is not accurately inserted into the vessel, or when the vessel rolls away from the needle and causes the needle to puncture an adjacent nerve. Nerves in the antecubital fossa (ACF) classically lie on a plane just beneath the veins, making them vulnerable to injury. The median nerve is particularly susceptible to accidental puncture, as it is located just posterior to the basilic vein in the ACF and can lead to acute pain, numbness, and (in rare cases) temporary paralysis of the region around the cannulation site.

Phlebitis: Superficial phlebitis, i.e., inflammation of the superficial veins, can be caused by the accidental puncture of the posterior vessel wall or rupture of the lateral walls during needle or catheter insertion[26]. Particularly when delivering medications, mechanical movements of the needle or catheter can lead to irritation of the vessel lining. If undetected, serious medical complications can result. The risk of phlebitis has been associated with demographic factors related to difficult venous access and is particularly high in patients in which the veins are difficult to see or secure.

Extravasation: Though more closely associated with the placement of the catheter than the actual insertion of the needle, extravasation may sometimes occur following procedures in which the needle tip ruptures the posterior vessel wall, causing leakage of medication out of the vessel lumen and into the surrounding tissues[27]. Depending on the medication, amount of exposure, and location, extravasation can potentially cause serious injury and permanent harm, for example, by inducing severe inflammation or tissue necrosis.

Central venous access following failed peripheral access: Though peripheral access is generally safer, easier to obtain, and less painful than central venous access, central venous access is oftentimes required if a suitable peripheral vessel is not available or after multiple failed peripheral access attempts[9,28]. The risk of serious complications, including mechanical injury,

accidental puncture of the central arteries, bleeding, thrombosis, embolism, and infection, are all dramatically increased in central venous access compared to peripheral venous access procedures.

Blood-borne disease transmission due to contact with used sharps: Aside from complications to the patient, venipuncture procedures also represent the leading cause of blood-borne disease transmission among US healthcare workers. In 2009, 64% of working nurses reported injuries from contaminated needles; 66,000 were infected with Hepatitis B, 16,000 with Hepatitis C, and 1000 with HIV[14,29]. Annually, accidental contaminated sharps injuries among U.S. healthcare personnel lead to hospital costs of approximately $100K to treat the injuries, $160K for excess needles, and $200K as a result of lowered productivity[14]. Large service providers for diagnostic laboratory blood testing, including Quest Diagnostics and LabCorp, have reported annual losses of approximately $160M due to contaminated sharps injuries to phlebotomists[30,31]. The likelihood of contact with a used needle increases dramatically with repeated insertion attempts, largely as a result of stress and anxiety. Thus, a significant proportion of sharps-related worker injuries occur when performing venous access in neonatal and pediatric patients, elderly patients, and other difficult groups.

Summary: Ideally, new technologies should demonstrate a clear ability to minimize the likelihood of adverse events. Recent studies have shown that the majority of these adverse events occur as a direct result of inaccurate cannula insertion. Thus new technologies and approaches that improve cannulation accuracy would likely reduce the rate of venipuncture-related complications, particularly in difficult patients.

1.3. Adjunct imaging technologies

The challenges associated with venipuncture have led to the adoption of imaging technologies most commonly utilizing near-infrared (NIR) light or ultrasound (US) signals to visualize otherwise invisible subcutaneous vessels. NIR imaging devices typically operate in the wavelength range of 760 to 1000 nm, as the decreased absorption and scattering of light through skin tissue at these

wavelengths can allow vessels up to 3 mm beneath the skin to be observed[32]. These devices can, in some cases, provide a noticeable increase in vessel contrast compared to standard visualization and can potentially allow hands-free visualization of the vascular map. Nevertheless, existing NIR systems are limited to providing a two-dimensional (2D) representation of the vasculature and offer no information regarding the depth of the vessel within the tissue. The maximum spatial resolution of current NIR devices further limits their effectiveness. In particular, the scattering of light in the tissue leads to a significant decorrelation of the spatial information, and this prevents the needle tip from being visualized once it is in the skin. Possibly as a result of these drawbacks, the evidence from recent clinical studies suggest that NIR imaging devices do not improve cannulation success rates and that such devices may in fact lead to worse outcomes compared to standard practices[33,34].

The use of US imaging has also shown potential for improving cannulation success and reducing complications[35]. US modalities suited to imaging vascular structures and surrounding anatomy include 2D imaging, Doppler color flow, and spectral Doppler. The main advantage of US over optical approaches is the capacity for imaging tissues residing far beneath the penetration limits of light. To effectively utilize US, however, the operator must be able to interpret 2D images of vessel lumens and differentiate these from surrounding structures. The technique also requires the necessary hand-eye coordination to manipulate the probe and needle simultaneously according to the live image display. The supplemental use of color Doppler to confirm the presence and direction of blood flow requires an understanding of the mechanisms of Doppler image generation. This skill set must then be paired with the manual dexterity to perform the three-dimensional (3D) task of placing a needle or catheter into a vessel target based on 2D images. For these reasons, the utility US-guided vessel cannulation tends to vary greatly from one operator to another[33,36,37].

In the end, successful vessel access depends most directly on how accurately the one can advance the needle, particularly in the presence of hidden vessels, patient movement, and tissue deformation. While imaging devices can help to identify vessels that would otherwise be hard to

find, they may also inhibit other modes of sensory feedback that are important for needle insertion, including the operator's tactile response. Imaging devices may furthermore entail a departure by the operator from standard practices and established habits, and this may negatively affect performance. Overall, research findings have been mixed regarding the efficacy of imaging devices, with several studies observing no significant differences in first-stick success rates, number of attempts, or procedure times compared to standard techniques[33–38]. The absence of clinical improvement suggests that the accurate insertion of the cannula, and not the initial localization of the vein, may be the primary cause of difficulties during venipuncture.

1.4.   Medical robotic technologies

One alternative approach to manual venipuncture that has received recent attention is to leverage the potential benefits of robotics[39,40] in performing the cannulation. In principle, a robotic system would be able to servo the needle in real-time[41,42], and its performance would not be dependent on human factors such as operator training and experience. Robotic systems could utilize imaging modalities such as NIR or US to provide exact information about the 3D position of a target vessel and translate this information into movement commands based on the robot's kinematic configuration. By handling the cannula insertion task, such systems could significantly reduce the learning curve for lesser trained personnel and allow them to work with patients who might otherwise prove challenging. Robotic technologies could also enable routine procedures to be carried out in a supervised autonomous manner. If made sufficiently affordable, robotic technologies may find use outside of the central hospital in settings such as the diagnostic testing lab, physician's office, or nursing home. In environments of extreme stress such as the ambulance, the trauma center, or the combat zone, a robotic device may outperform trained personnel and could allow medical attention to be fully devoted to other urgent aspects of patient care.

Over the past few decades, robotic systems have slowly entered the realm of modern medicine[43,44], where their primary role has been to assist medical practitioners in a wide range of surgical interventions, including prostatectomy[45,46], orthopedic and neurosurgery[47], endoscopy[48,49], brachytherapy[50]. Such systems are used to precisely manipulate medical instruments within the operating workspace of the procedure, and some have demonstrated the ability to carry out complex soft-tissue suturing procedures in an autonomous fashion with comparable performance to trained surgeons[51]. Recently, a number of robotic systems have achieved regulatory approval for central and peripheral intravascular or endovascular surgical procedures[52,53], and some research groups are working on developing robotic systems to perform central vascular catheterization[54–56]. Nevertheless, while surgical robots have the potential to improve treatment times and postoperative outcomes, their size, cost, and complexity make them incompatible for use outside the operating room. Thus, despite significant advances in the fields of robotics and computer-aided medical intervention, there is no clinically or commercially available technology that successfully utilizes a robotic methodology for the purpose of peripheral venous access.

1.5. Hypothesis and research objectives

The goal of my dissertation research is to develop a portable medical device that performs peripheral venous access procedures in an automated manner and with improved accuracy and speed compared to manual cannulation techniques. **The central hypothesis is that the use of NIR and US vessel imaging, in combination with robotically-guided cannulation, can significantly reduce the number of needle placement attempts in normal and difficult patient populations.** The rationale for this work is that such a device would have the potential to (1) provide healthcare professionals the ability to draw blood and start intravenous lines with unparalleled accuracy and speed, (2) minimize the effects of patient and practitioner variability on cannulation success, and (3) remove the practitioner from contact with exposed sharps, thus eliminating the risk of blood-

borne transfection. In this way, the likelihood of adverse events associated with difficult venipuncture could be substantially reduced.

The device employs NIR and US imaging techniques to visualize subcutaneous vessels, an image analysis framework to extract relevant position information, and a miniaturized dexterous robot that performs the cannulation. The device operates by mapping the 3D spatial coordinates of a selected vessel and guiding the needle into its center under real-time image feedback. In the chapters that follow, I present methods to robustly segment, localize, and track the pose of superficial vessels in real-time using image guidance, and I describe how these functions are integrated within the robotic system to enable device autonomy. I then demonstrate, through human clinical imaging studies, *in vitro* cannulation studies, and *in vivo* experiments, the ability of the device to visually identify and cannulate superficial veins with higher rates of success than unassisted and image-guided manual techniques. The device, once translated, may be conducive to use in high-volume facilities, such as diagnostic labs and hospitals, and may impact a range of other arenas, including pediatric, geriatric, emergency, and military use. The device may also serve as a platform to merge automated venipuncture with on-device diagnostic blood analysis, which would allow critical patient information to be provided at the point-of-care. Finally, the technology may be adapted for other peripheral vascular interventions as well as for applications outside of the clinical domain.

1.6. Outline of the dissertation

Chapter 2 describes our approach to 3D vessel imaging and localization. I discuss the design of the imaging systems[57] and their validation in human clinical studies[58]. I also describe the computer vision and image analysis techniques that the system implements in order to extract 3D spatial position information in real-time from the acquired images. In the NIR images, these include methods for enhancement, segmentation, feature extraction, registration, stereo reconstruction, and

tracking of the detected vessels and the forearm surface. In the US images, these include segmentation and tracking of the vessel and needle. Several of the more computationally expensive steps are optimized using code developed for parallel graphics processing. I evaluate the reliability and speed of each image analysis step using image and video datasets acquired from our human studies. I then suggest possible ways to further improve our imaging and image analysis approach.

Chapter 3 presents the design of the robotic system. I describe three prototype generations that were sequentially developed as part of my thesis work[58-61]. The most recent system comprises 9 degrees of freedom (DOF) to allow itself to align with a target vessel in a large workspace of possible orientations. The kinematic and motion control systems are described, as is the force-sensitive needle insertion mechanism, which may in turn be used for blood sample collection or for peripheral catheter placement. The accuracy and precision of the robot are evaluated through a series of positioning experiments and robotic guidance studies. Methods to improve the speed, adaptability, and overall intelligence of the robot are examined with particular focus on advancements in probabilistic learning and dynamic control. Ongoing work to further miniaturize the system is also discussed.

Chapter 4 presents the results of *in vitro* and *in vivo* studies carried out to evaluate the performance of the device in comparison to manual cannulation techniques. Needle insertion parameters and tissue material properties hypothesized to affect device performance are first investigated using customizable, multilayered tissue-mimicking phantoms that simulate the mechanical, optical, and acoustic characteristics of human skin and vessels over a broad demographic range[62]. In a series of simulated *in vitro* blood draw and intravenous infusion experiments, measures of accuracy and completion time are compared to results obtained by unassisted, NIR-guided, and US-guided manual cannulation[63]. *In vivo* experiments are then carried out using an animal model for neonatal and pediatric venipuncture[64]. Venous and arterial cannulations are performed in the tail of anesthetized rats, and the success rates of needle insertion

and blood collection using the device are again compared with outcomes from unassisted, NIR-guided, and US-guided manual cannulation trials. I then describe the design of a low-cost, handheld, and highly miniaturized prototype device developed specifically to perform rodent tail vessel cannulations and discuss the potential advantages of the device for preclinical applications.

Finally, Chapter 5 summarizes the results and main conclusions of the dissertation and discusses ongoing work in preparation for planned human feasibility studies, subsequent clinical trials, and commercial translation. I also discuss a number of factors, including device safety, usability, cost, and clinical acceptance, that I believe will ultimately determine the impact of image-guided robotic technologies for venipuncture. I then suggest several ways in which this technology may be extended beyond venipuncture, including work being done to couple the device with microfluidics-based assays for rapid point-of-care blood testing[65,66]. Finally, I discuss the possibility of extending to clinical interventions beyond routine venipuncture, including image-guided peripherally-inserted central catheter (PICC) placement, central venous catheter (CVC) placement, hemodialysis catheter placement, peripheral endovascular interventions, and surgical operations on other peripheral tissues.

Chapter 2 – Bimodal 3D near-infrared and ultrasound imaging of peripheral vessels

Parts of Chapter 2 were adapted from the publications listed below. All excerpts represent the original work of Alvin Chen, whose specific contributions as first author of the publications included: designing and conducting the described experimental studies; generating the presented data and corresponding figures; writing, editing, and revising the original text; and addressing reviewers' comments as corresponding author of the original manuscript submissions.

A. Chen, M. Balter, T. Maguire, M. Yarmush. 3D near-infrared and ultrasound imaging of peripheral blood vessels for real-time localization and guidance. *Medical Image Computing and Computer Assisted Interventions* 9902, 130–137 (2016).

A. Chen, K. Nikitczuk, J. Nikitczuk, T. Maguire, M. Yarmush. Portable robot for autonomous venipuncture using 3D near-infrared image guidance. *Technology* 1(1), 72–80 (2013).

2.1. Overview

Two imaging approaches that have shown promise in facilitating vascular access, particularly in difficult patient populations, are US and NIR imaging. In Chapter 2, a bimodal vessel imaging is introduced for mapping and localizing subcutaneous vessels in three dimensions based on the combined use of NIR stereo vision, US, and image analysis (**Figure 2-1**)[57]. In this approach, 3D maps of subcutaneous vessels are generated in real-time over a broad field-of-view (FOV) using NIR illumination in the wavelength range between 700 and 1000 nm. Local position information about the vessel target and the needle is then captured through US. The imaging approach also incorporates techniques from the field of computer vision to extract 3D position pose information from the images; in later chapters, this information is provided as an input to the robotic system. In the NIR modality, the computer vision techniques consist of algorithms for automated skin surface and vessel segmentation, stereo correspondence, and motion tracking. In the US modality, the techniques involve segmenting the target vessel, determining blood flow, and tracking needle as it advances through the tissue. Several of the more computationally expensive steps are optimized using code developed for parallel graphics processing. During the procedure, the clinician may

choose a vessel as the cannulation target, either based on standard visualization and palpation or by selecting from the device's graphical user interface (GUI) ; this step is left to the clinician's decision-making. A prototype imaging device integrating these functions is developed and evaluated on normal and difficult patient groups in comparison to manual visualization by clinical experts. The results provide evidence of the system's clinical potential – both as a standalone imaging tool and as a means for autonomous, image-guided robotic cannulation. In addition to describing the imaging and image analysis approach, the optical and acoustic properties of human skin and vessels that affect NIR and US imaging quality is reviewed, and recent advancements and current limitations of both techniques, as applied to needle guidance, are summarized. Finally, some of the limitations of the current system are discussed, and methods to improve the imaging approach and the associated computer vision techniques are proposed.
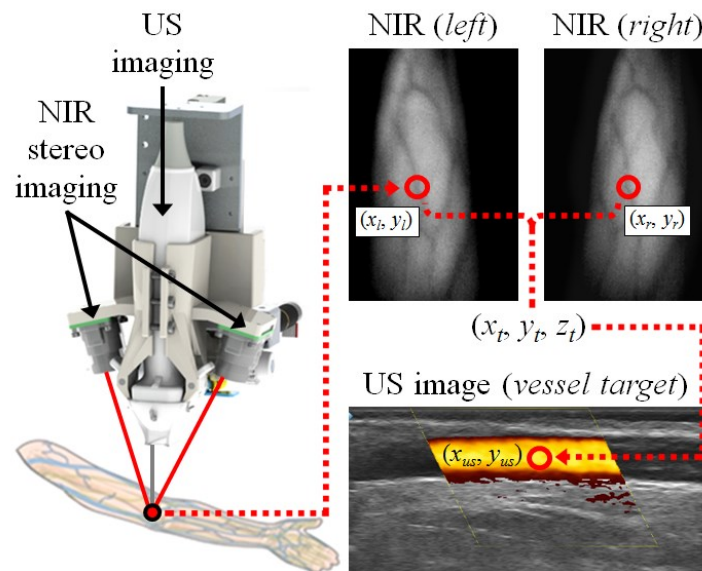
Figure 2-1. Bimodal NIR+US vessel imaging. The two imaging modalities are combined to determine the 3D position (x_i, y_i, z_i) of a selected vessel target and to guide the needle to the target. With the use of computer vision approaches, the full 6-DOF vessel pose (x_i, y_i, z_i, α_i, β_i, γ_i) may also be estimated.

2.2. Background and previous work

2.2.1. *Nomenclature*

λ = wavelength (nm) $\qquad$ f = frequency (MHz)

μ = extinction coefficient (cm^{-1}) $\qquad$ α = acoustic attenuation (dB cm^{-1})

μ_a = absorption coefficient (cm^{-1}) $\qquad$ β = acoustic backscatter (sr^{-1} cm^{-1})

μ_s = scattering coefficient (cm^{-1}) $\qquad$ Z = acoustic impedance ($10^6 \cdot$ kg m^{-2} s^{-1})

$\mu_s{}'$ = reduced scattering coefficient (cm^{-1}) $\qquad$ c = velocity of sound (m s^{-1})

φ = percent volume fraction (%) $\qquad$ ρ = mass density (kg m^{-3})

2.2.2. *Optical properties of human skin and vessel tissues*

The extinction (attenuation) of light by a biological tissue can be determined from the optical properties of each tissue component (**Table 2-1**). In the skin and blood vessels, the main tissue components are (1) melanin pigment in the epidermis, (2) keratin, collagen and elastin fibers in the epidermis and dermis, (3) lipid in the hypodermis, (4) hemoglobin in blood, and (5) water, which often makes up the bulk tissue volume[67,68]. Thus for a tissue, extinction can be approximated by:

$$\mu(\lambda) = \varphi_{\text{melanin}} \ \mu_{\text{melanin}}(\lambda) \ + \ \varphi_{\text{fibers}} \ \mu_{\text{fibers}}(\lambda) \ + \ \varphi_{\text{lipid}} \ \mu_{\text{lipid}}(\lambda)$$

$$+ \ \varphi_{\text{hemoglobin}} \ \mu_{\text{hemoglobin}}(\lambda) \ + \ \varphi_{\text{water}} \ \mu_{\text{water}}(\lambda)$$

where φ is the relative volume of each tissue component expressed as a percentage. The extinction coefficient at any wavelength is, in turn, defined as the sum of the absorption and scattering coefficients, i.e., $\mu(\lambda) = \mu_a(\lambda) + \mu_s(\lambda)$. Compared to light in the visible spectrum (VIS), NIR light travels further into the tissue before being absorbed or scattered[69]. This increased penetration is conducive to imaging subsurface tissues such as blood vessels. An overview of the parameters relevant to the optical design of the phantoms is summarized in this section. The reader is referred to surveys by other researchers[68] for a comprehensive review of tissue optical properties.

Table 2-1. Relative composition of human tissues.

Tissue Layer	Volume Percentages (φ) of Tissue Components				
	Melanin	*Fibers*	*Lipid*	*Hemoglobin*	*Water*
Epidermis	1–10% (I,II) 11–20% (III,IV) 21–45% (V,VI)	40%	0%	<1%	15–60% (fluctuates based on hydration)
Dermis	0%	50%	0%	<1%	50%
Hypodermis	0%	0%	80%	<1%	20%
Vessel wall	0%	25%	0%	<1%	75%
Whole blood	0%	0%	0%	2%	98%

Optical absorption: The optical absorption (μ_α) of the main tissue components in the skin and vessels have been well-characterized in the literature[68,70]. Of the three skin layers, absorption is strongest in the epidermis due to the presence of melanin, which provides the pigmentation seen in the skin[69]; as such, the volume fraction of melanin in the epidermis defines each person's skin tone. The absorption profile of melanin is inversely dependent on wavelength, and at higher wavelengths the variability in epidermis pigmentation between different skin types is dramatically reduced.

Absorption in the dermis and vessel walls is relatively minor (<1 cm^{-1}), as both tissues mainly consist of weak absorbers such as collagen, elastin, and water[32,71–73]. Absorption in the hypodermis is significant at the lipid absorption peaks and minor elsewhere[74]. Absorption in venous and arterial blood is strong, particularly near wavelengths corresponding to local maxima in the absorption spectrums of deoxyhemoglobin and oxyhemoglobin, respectively[75]. **Table 2-2** provides the values of μ_α for the five peripheral tissues at three deoxyhemoglobin absorption peaks, namely 556, 758, and 914 nm, based on literature findings.

Optical scattering: The reduced scattering coefficient μ_s' of most biological tissues can be approximated by power law expressions,

$$\mu_s' = \mu_{s_1}'(\lambda/500)^{-n_s}$$

where μ_{s_1}' is the reduced scattering coefficient at 1 nm and n_s is the power law constant describing the dependence on wavelength. μ_s' can be further expressed as a lumped parameter that incorporates the anisotropy factor g (the average cosine of the scattering angle):

$$\mu_s' = \mu_s(1 - g).$$

μ_s' is not as well characterized for the constituent materials compared to μ_α. However the scattering characteristics of the whole tissue layers have been studied extensively[32,68–74], and the power law constants (μ_{s_1}' and n_s) for the skin, vessel wall, and whole blood are listed in **Table 2-2**. Nearly all of the internal scattering in the skin occurs in the dermis and hypodermis layers, which are 1 to 2 orders of magnitude thicker than the epidermis. Collagen and elastin fibers contribute the greatest scattering effect in the dermis, while in the hypodermis the main scatterers are the lipid droplets[32,68]. Scatter in the vessel wall is similar to that of the dermis, and the scattering properties of whole blood are similar to those of water.

Table 2-2. Summary of optical properties of human skin and vessel tissues.

Tissue Layer	Absorption (μ_a)			Scatter (μ_s')					Ref(s)
	556 nm	758 nm	914 nm	556 nm	758 nm	914 nm	μ_{s_1}	n_s	
Epidermis	24.2	8.64	4.66	60.7	42.4	34.1	*68.7*	*1.16*	68–70,76
	71.9	25.6	13.8						
	152.9	54.5	29.3						
Dermis	3.39	0.34	0.21	39.6	25.5	19.5	*46.0*	*1.42*	32,68–70
Hypodermis	0.94	0.13	0.72	17.1	13.9	12.3	*18.4*	*0.67*	32,68–70,74
Vessel wall	12.0	0.51	0.31	36.1	23.1	17.6	*42.1*	*1.45*	71–73
Whole blood	294.5	8.43	4.2	20.5	16.7	14.8	*22.0*	*0.66*	71–73

2.2.3. *Acoustic properties of human skin and vessel tissues*

A tissue's acoustic behavior is determined by the mass density c of the tissue, the velocity of sound v in the tissue, the tissue's acoustic impedance Z (which is a function of c and v), and

its acoustic attenuation α[77]. An acoustic impedance mismatch at a material interface is analogous to an optical index mismatch; in both cases, strong reflections of the incident wave occur at the interface. Acoustic attenuation, meanwhile, is a measure of the energy loss of sound propagation in the tissue and, like optical scatter, can be approximated using power law expressions,

$$\alpha(f) = \alpha_1 f^n \quad (\text{dB cm}^{-1})$$

where f is the frequency of sound, α_1 is the attenuation at 1 MHz, and n is the power constant. As with optical attenuation, $\alpha(f)$ can be further separated into acoustic absorption and backscatter components. However these are not well-characterized in the literature and were not be taken into consideration when designing the phantoms.

Table 2-3 provides some measurements of tissue layer acoustic properties reported in two studies[78,79]. The general agreement between different studies is strong. Fibrous tissues such as the epidermis, dermis, and vessel walls have higher mass densities and thus higher Z compared to water. In contrast, the density of adipose tissue is significantly lower than that of water and thus Z is low. The low density of adipose, on the other hand, allows it to be a strong thermal insulator by readily converting incident energy (acoustic waves) into heat. As a result, the hypodermis is a very strong acoustic attenuator. The upper skin layers and vessel wall exhibit acoustic attenuation characteristics as well, but because these layers are much thinner than the hypodermis the overall effect is diminished.

Finally, blood, which comprises >95% water by volume, is a relatively weak attenuator. Blood echogenicity, that is, the weak signal caused by backscatter from the red blood cells flowing past the US transducer, is a critical parameter in Doppler-based imaging techniques. In designing phantoms for Doppler imaging, consideration must be given not only to the amplitude of the backscatter signal but also to the size of the individual scatterers, the velocity of the fluid flow, and the pattern of the flow, i.e., continuous or pulsatile movement.

Table 2-3. Acoustic properties of human skin and vessel tissues.

Tissue Layer	v (m s^{-1})	c (g cm^{-3})	Z ($10^6 \cdot$ kg m^{-2} s^{-1})	α_1 (dB cm^{-1} MHz^{-1})	n	Ref(s)
Epidermis	1540	1.151	1.99	0.44	1.55	[78]
Dermis	1580	1.151	1.8	0.26	1.55	[78]
Hypodermis	1440	0.928	1.38	0.60	1.00	[79]
Vessel wall	1575	1.065	1.68	0.95	1.09	[79]
Whole blood	1584	1.055	1.66	0.15	1.21	[79]
Water	1480	1.000	1.48	0.002	2.00	[79]

2.2.4.   Limitations of current methods of US-guided venous access

Compared to light waves, US waves can penetrate more deeply into human tissue, allowing tissue structures that are beneath the penetration limits of light to be identified. US also has the potential to exceed the spatial resolution of standard optical imaging approaches, depending on the frequency of the US system. US modalities suited to imaging vascular structures and surrounding anatomy include 2D imaging, Doppler color flow, and spectral Doppler. To image small, peripheral vessels, linear array US transducers capable of transmitting and receiving acoustic signals at relatively high frequencies (>12 MHz) are preferred. The size and cost of US imaging devices have been dramatically reduced in recent years, and portable, handheld, battery-powered, and wireless systems are now becoming available[80–82].

Nevertheless, for the purpose of needle guidance, ultrasonography requires a fairly long learning curve[35]. To effectively utilize US, the operator must be able to interpret 2D images of vascular lumens and differentiate these from surrounding structures. The technique also requires the necessary hand-eye coordination to manipulate the probe and needle simultaneously according to the live image display. The supplemental use of color Doppler to confirm the presence and direction of blood flow requires an understanding of the mechanisms of Doppler image generation. This skill set must then be paired with the manual dexterity to perform the 3D task of placing a

needle or catheter into a vessel target based on 2D images. Specifically, in order to visualize the needle in the image, the transducer is most commonly held in the longitudinal orientation with the imaging plane parallel with the vessel. The operator must then align the needle so that it is parallel with the imaging plane (and thus the vessel), and maintain the needle in the plane as it is advanced into the vessel. Lateral deviations of 1 or 2 mm will cause the needle to disappear from the image. Similarly, if the vessel deforms or rolls laterally away from the image plane, it too can become invisible. Patient movement will likewise cause significant image artifacts and make it difficult to maintain the visibility of needle and the target vessel. Alternatively, if the operator orients the transducer in the transverse view, with the imaging plane perpendicular to the vessel axis, these challenges may be avoided. However, in the transverse view, it is impossible to visualize the entire length of the needle; instead, the only the reflection of single cross-section of the needle can be observed, specifically at its point of intersection with the transverse US plane. It is very difficult to visualize the needle as it punctures the vessel, and thus the operator is left to infer the needle position based on the motion of the vessel and whether flashback was observed in the needle hub.

US-guided cannulations are also made more difficult by the fact that the transducer must remain in contact with the patient's skin at all times, since any air pockets that form in the acoustic coupling gel will significantly degrade the image quality. Thus in many cases, a second operator is needed to hold the transducer while the first performs the cannulation. The need for US gel further increases the time needed to complete the procedure. Together, these challenges limit the effectiveness of US-guided peripheral cannulation to all but the most experienced operators. Meanwhile, even for clinicians with substantial training, the potential benefits of utilizing US may simply not be worth the added complexity, particularly in real-world scenarios where patients may be anxious or scared, fidgeting (or, in the case of children, moving and crying), or otherwise uncooperative. For all of these reasons, the outcomes of peripheral venous or arterial cannulations guided solely by US tend to vary greatly from one operator to another.

2.2.5.   Limitations of current methods of NIR-guided venous access

The second imaging method that has received early adoption involves the projection of light onto the skin[83–87]. Optical imaging devices most commonly utilize light in the NIR wavelength range (typically 700 – 1000 nm). Compared to visible light, NIR waves penetrate more deeply into scattering tissues and may resolve vessels that lie up to 3 mm below the skin[32,68]. Hemoglobin in the vessels absorb the light, leaving an image of the underlying vascular pattern that is invisible to human eyesight but which may be captured by a camera sensitive to NIR light. Once captured by the camera, the images are then processed and displayed back onto the patient's skin in real time as a hologram. With this approach, NIR technologies can, in some cases, provide a noticeable increase in vessel contrast compared to standard visualization and can potentially allow hands-free visualization of the vascular map. Unlike US transducers, NIR devices do not need to make contact with the patient's skin and are therefore less cumbersome to use. Furthermore, because the images are acquired in a top-down manner and provide a "bird's-eye" view of the vasculature, difficulties related to the vessel or the needle escaping the FOV of the device are entirely avoided. More recent devices that integrate the imaging components into augmented-reality eyewear technology have the potential to further improve the usability of the NIR approach[88].

Nonetheless, the NIR imaging approach has its own limitations. First, the spatial resolution of the NIR image is much lower than the resolution of a standard clinical US image acquired at a relatively high acoustic frequency. Since the camera must resolve the image over a sufficiently wide FOV to capture all of the suitable cannulation sites, the magnification of the lens must be low. A camera with a large pixel array sensor could provide increased spatial resolutions, but the sensitivity (quantum efficiency) of the sensor would be compromised since the individual CMOS or CCD elements would need to be smaller. The spatial resolution of the NIR images is also hampered by the scattering of light in the superficial layers of the skin. These scattering effects inhibit the visualization of structural details and limit the maximum possible imaging depth.

Vessels beyond 3 mm in depth, for example, remain invisible under NIR illumination. The vessel wall is a particularly strongly scattering tissue and, as a result, the position of the needle tip within the vessel lumen is nearly impossible to visualize. Unfortunately, the majority of adverse events result from small, millimeter-scale, vessel motions and needle positioning errors that occur both before and after the needle is inside the vessel. Existing NIR imaging devices lack the resolution needed to guide the adjustment of the needle when such issues arise.

Another major limitation of the NIR approach is that the projected top-down 2D images provide no information about the depth of the vessel and thus cannot inform the operator about whether the needle tip has punctured through the posterior vessel wall. This is significant because many of the adverse events that occur during cannulation, including poor sample collection, hematoma, and extravasation, occur most commonly due to posterior wall puncture. Finally, with current NIR imaging systems, it may be difficult to differentiate arteries from veins, particularly in obese patients or children where the pulsatile arterial flow is more difficult to discern via palpation. As a result of these limitations, clinicians often use NIR imaging devices preoperatively to approximate the location of a suitable vein. The cannulation itself is performed without NIR guidance.

2.2.6. *Clinical studies report negative outcomes for NIR and US guidance*

In recent years, a number of randomized trials have been conducted to evaluate the clinical value of US and NIR imaging for peripheral venous access. In five independent systematic meta-analytic reviews conducted since 2013 on the use of US guidance for peripheral catheterization in patients with difficult venous access[36–38,89], a consensus was reached that the clinical efficacy of US guided peripheral intravenous cannulation is not supported by the current literature, few outcomes reached statistical significance, and larger well-controlled trials are needed. It was also found that outcomes were sometimes worsened by the use of US guidance. Finally, in the studies where improvements were observed using US-guidance, the authors found that the practitioners were

much more well-trained than what would normally be expected. The authors concluded that US-guidance improved cannulation success rates only when operated by trained clinicians, for example anesthesiologists and cardiologists, and not when operated by nurse practitioners and phlebotomists. In general, significant improvements in first-stick success rates, number of attempts, or procedure times have not been observed in the current literature.

Similar meta-analytic studies have also been conducted to evaluate the effectiveness of NIR imaging on venipuncture success rates. Heinrichs *et. al.* provided a comprehensive review of randomized control trials and found no differences in first-attempt success using NIR devices in children[34]. The also observed that clinicians often used the NIR imaging devices solely to approximate the location of a suitable vein; the actual cannulation was then attempted without NIR guidance. The authors concluded that, while it is possible that NIR devices are efficacious in other patient populations, the evidence did not support a benefit in pediatrics. Curtis *et. al.* compared the use of US and NIR vascular imaging to unassisted peripheral venous catheterization in 418 children at a pediatric emergency department[33]. They did not find a significant improvement in first-attempt success rates using either imaging technology. In children 3 years and younger, the use of NIR imaging led to significantly worse success rates (-20.1%, $p = 0.026$).

In addition to these broader studies, clinical trials have also been carried out to evaluate particular models of existing commercial NIR imaging devices. For example, De Graaf *et. al.* evaluated the use of three NIR imaging systems (the VeinViewer Flex system, the AccuVein AV300 system, and the VascuLuminator Vision system) in 1913 children in the age range of 0–18 years who were scheduled for elective surgery[90]. The authors observed that suitable cannulation targets were identified with greater frequency among the patient population using either the VeinViewer (307/322 (95.3%)) or the AccuVein (239/254 (94.1%)) devices compared to using the VascuLuminator (229/257 (89.1%)) system ($p = 0.03$) system. However, the first-stick success rates observed with these devices was not significantly different than the success rates obtained by

standard methods of unassisted venipuncture (73.1% without NIR guidance, 75.3% with NIR guidance, $p = 0.93$). Aulagnier *et. al.* compared the use of the AccuVein AV300 system to unassisted intravenous catheter insertion in 266 adults[91]. Neither completion time nor the secondary outcomes (failure and pain) were significantly reduced using the AccuVein, and a qualitative assessment of the device by the clinical operators showed that the feedback was more often negative than positive. Cuper *et. al.* conducted studies in 491 children in the age range of 0–18 years who were in need of intravenous cannulation at a tertiary pediatric referral hospital[92]. They found no differences in first-attempt success (-1%, $p = 0.69$) or completion time (+19 sec, $p = 0.26$) with or without the use of NIR imaging.

2.3.   Rationale and approach

We aimed to develop an imaging system to improve peripheral vessel visualization that could overcome the major limitations of current imaging techniques by providing (1) depth-resolved 3D maps of the subcutaneous vasculature to a depth of at least 3 mm over the approximate FOV of an adult forearm, (2) high-resolution visualization of a local vessel target and its flow characteristics, and (3) visualization of the needle as it is advanced through the tissue and of the needle tip when it is inside the vessel lumen. Ideally the cost of the system would be comparable to or less than that of existing NIR and US imaging devices, and the system would be amenable for use both as a standalone imaging tool and as a means for image-guided, robotic cannulation.

The system we developed uses a combination NIR stereo imaging and US imaging to map the 3D structure of peripheral vessels. Bimodal imaging devices have been previously used for tracking biopsy needles within tissues[93]. In these devices, the stereo cameras are used to estimate the pose of the needle, and the pose information is projected onto the 3D US image plane and the 2D views of each camera. Guidance cues are provided to the user in the form of alignment markers displayed on-screen, and the user is tasked with aligning the visible needle with the alignment markers

simultaneously, as doing so would ensure the proper insertion trajectory. Illumination of the needle

is provided the ambient visible light. In contrast, our approach utilizes NIR illumination, rather than

ambient light, in order to increase the visibility of subcutaneous vessels. **Figure 2-2** illustrates the

design of the bimodal imaging system, highlighting the NIR stereo cameras and the US transducer.

Here, the system is mounted on a flexible articulated arm that the operator can adjust to scan the

patient. The flexible arm also allows the system to be positioned above a suitable vessel target that

the clinician selects for cannulation.
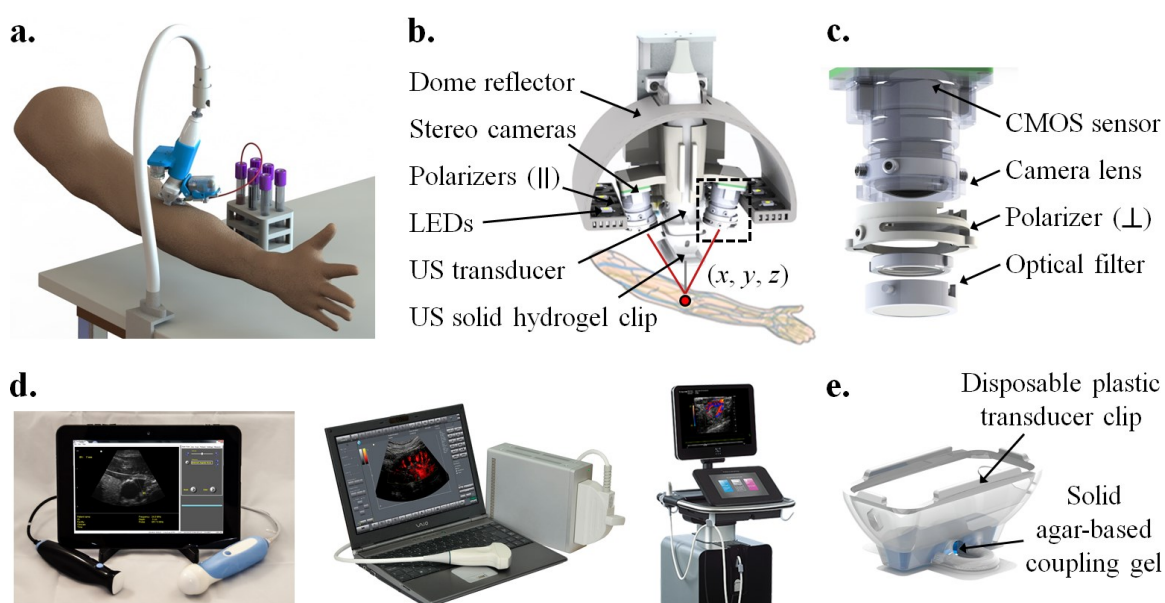
Figure 2-2. Design of handheld imaging device. Imaging system coupled with a 3-DOF needle insertion mechanism for semi-automated cannula insertion. The system is mounted on a flexible articulated arm that the operator can adjust to scan the patient. The arm also allows the system to be positioned above a selected vessel target. **(b)** Hardware components including the pair of NIR-sensitive CMOS cameras, LED arrays, dome reflector, and optical elements. LEDs with center wavelengths around 690 and 830 nm were used to maximize absorption from deoxyhemoglobin and oxyhemoglobin in blood while minimizing absorption due to water, fat, and melanin. Red dotted lines show the light path of the inverted NIR LEDs. Black dotted rectangle shows one of the NIR camera subsystems. Also shown is the 18 MHz linear array US transducer and the US hydrogel clip. **(c)** Main optical components of the NIR camera subsystem. Each camera acquires 752x480 pixel images at 15 FPS. **(d)** US transducers used with imaging system. *Left:* 12 MHz single-element scanning sector probe; *Center:* 18 MHz linear array transducer; *Right:* 40 MHz high-frequency linear array transducer. **(e)** Disposable US transducer clip containing solid coupling hydrogel.

The device operates by first using NIR imaging to generate a 3D map of the vessels over the FOV of an adult forearm. Once an appropriate cannulation site has been identified, the device is then lowered onto the patient's arm until the US transducer makes contact with the skin. The US imaging modality is then used to provide a high magnification longitudinal view of the selected vein, confirm blood flow, and finally track the needle as it pierces the tissue. Both the NIR and US images are processed and analyzed in real-time. The 3D positions of the cannulation site and the needle tip are both tracked from one frame of the image sequence to the next, and cues are provided to the operator as the needle is inserted until the needle tip position converges with the vessel target position, that is, until the vessel is punctured.

Figure 2-2 (a) also shows a simple 3-DOF motorized needle insertion mechanism that may be coupled with the imaging system to perform the cannulation in a semi-automated manner. In contrast to the fully autonomous robotic systems presented in later chapters, the majority of the alignment task must still be performed by the operator if the imaging system is used in a standalone manner. Coupling the imaging system with the motorized insertion mechanism simplifies the cannulation task for the operator by eliminating the need to simultaneously align the needle and the US probe with the vessel target.

2.4. Methods

2.4.1. 3D NIR stereo imaging approach

The signal-to-noise ratio (SNR) in peripheral vein imaging depends on the extent of hemoglobin absorption relative to melanin absorption and tissue scatter. In comparison to VIS light, for which the penetration depth is less than 1 mm, light in the NIR spectrum is relatively resilient to melanin absorption and tissue scatter (**Figure 2-3**) and thus can penetrate up to 3 mm through skin[32]. The device takes advantage of the increased penetration to improve the contrast of subcutaneous veins relative to background tissue.

The general optical scheme of the NIR device for imaging venous structures consists of an illumination source, a diffuser, polarizers, an NIR filter, a CMOS camera, a video processor, and a monitor, as shown in **Figure 2-2 (b, c)**. Six arrays of surface-mount light-emitting diodes (LEDs) were designed and used as the illumination source. Each array contains 32 surface mount LEDs. 12 of the LEDs in each array have a center wavelength of 690 nm (SMC690, Marubeni America Corp., CA, U.S.), half-width of 20 nm, and viewing half angle of ±55°. The radiant intensity of each LED at operating current was measured using a digital photometer (Tektronix J-6512) to be 2.0 mW/sr, giving a total radiant intensity at 690 nm of 12 x 2.0 mW/sr = 24.0 mW/sr. The remaining 20 LEDs have a center wavelength of 830 nm (SMC830, Marubeni America Corp., CA, U.S.), half-width of 35 nm, and viewing half angle of ±55°. The radiant intensity of each LED at operating current is 5.0 mW/sr, giving a total radiant intensity at 880 nm of 20 x 5.0 mW/sr = 100.0 mW/sr. The increased radiant intensity 880 nm compared to 690 nm compensates for the decreased quantum efficiency of the cameras at higher NIR wavelengths.
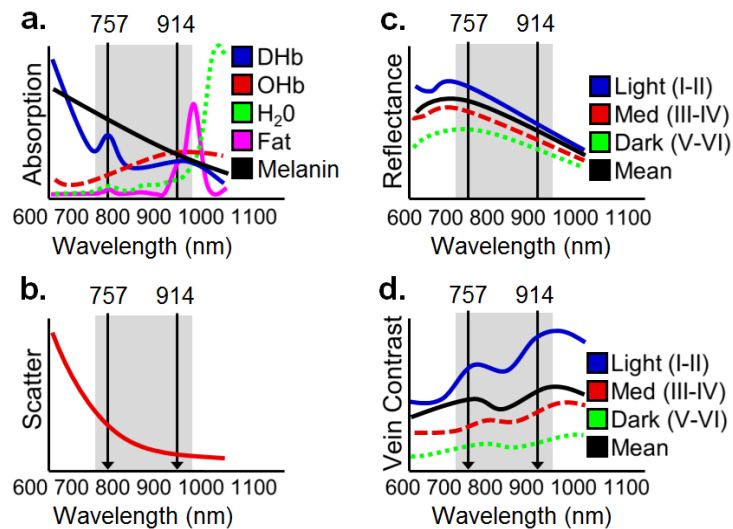
Figure 2-3. Optical properties of human skin in the NIR wavelength range. **(a)** Absorption coefficients (μ_a), **(b)** scattering coefficients (μ_s'), **(c)** reflectance, and **(d)** vessel contrast of human skin between 600 and 1100 nm. Vessel contrast was measured in three subjects with different skin tones. Vessel contrast was defined as the vessel-to-background intensity ratio, $I_C = |I_V - I_B| / (I_V + I_B)$.

Two miniature monochrome CMOS cameras (VRmMS-12, VRMagic UAB, DEU) are used as the detectors. The cameras form a 3D depth sensor based on the use of stereo vision. The 3D information is used to compute the depth and pose of the arm and vessels, and this information is then used to direct the robot. Each camera acquires 752x480 images at 15 FPS. Each camera measures 28x19x5mm and are controlled by a single multi-sensor camera board to allow synchronous capture. The controller board includes a field-programmable gate array (FPGA) with 256 MB RAM that can perform basic low-level image processing. The small size of the cameras allows them to fit well within the robotic system, as will be discussed in later chapters. The CMOS sensors in each camera (Aptina MT9V024) exhibit a large pixel size (6 μm x 6 μm) and increased sensitivity to NIR light (57% quantum efficiency at 690 nm, 34% efficiency at 830 nm, 15% efficiency at 940 nm, etc.). Each camera is mounted with a miniature camera lens with an FOV of 120º (Marshall Electronics V-4402.1-2.5-HR 1/3" 2.1mm f/2.5 Lens).

To block unwanted ambient light, we used 15 mm diameter dual-band bandpass filters with center wavelengths of 688nm and 828 nm and bandwidths of 13 nm and 12 nm, respectively (BrightLine FF01-688/828, Semrock, Rochester, NY, U.S.). Two layers of ground-glass and holographic diffusers (Edmund Optics, NJ, U.S.) were used with the LED array to improve the uniformity of intensity across the skin. To minimize spectral reflections from the skin surface, 12.5 mm diameter NIR linear polarizing filters with wavelength range of 750 to 850 nm (Edmund Optics, NJ, U.S.) were placed in front of each camera. A rectangular dielectric polarizing film with the same wavelength range was placed in front of the six LED arrays in a perpendicular orientation relative to the polarizers in front of the cameras. The polarized waves propagating to the arm surface and backscattering within the first few path lengths retain their polarization and are filtered upon reaching cameras. In contrast, waves propagating past the first few path lengths lose their initial polarity and are received by the cameras. Cross-polarization gating in this manner has been shown to reduce surface reflections by approximately 7-8% of the total tissue scatter[94].

2.4.2.   *B-mode and Doppler US imaging approach*

Different US transducers may be interchanged within the imaging system depending on the requirements on center frequency, bandwidth, spatial resolution, and imaging depth. We have used three different transducers (**Figure 2-2 (e)**). The first is a single-element sector probe (SeeMore NF-MV-12 Vascular Probe, Interson Corp., U.S.). The electronic elements are simplified to a single PCB board embedded in the probe, which can in turn be connected directly via a USB connection to a host computer. The center frequency is 6 MHz, but the transducer can also be pulsed at 12 or 24 MHz. To produce the 2D (x, z) image, the single piezoelectric crystal is mechanically scanned along an arc with a DC brushed motor. The depth range is 0 to 25 mm, and the focus is 10 mm. Each sector line generates a 2048x1 vector, and 128 vertical scan lines are generated with each pass of the mechanically scanned crystal. The resulting 2048x128 array of backscattered intensity data is then interpolated using a lookup table to form the final 600x600 B-mode image. In total, 12 B-mode images are acquired per second. The main limitation of using the single-element transducer was that Doppler images cannot be generated, as doing so would require an impractically high mechanical scanning speed. Furthermore, even though 128 scanlines were generated per image, the spatial resolution was limited to approximately 150 μm per pixel. Finally, processing techniques such as compound imaging are not feasible using the scanning sector probe.

The second transducer that we used is an 18 MHz linear array transducer with 256 piezoelectric elements at 100 μm pitch (L18-10L30H-4, Telemed UAB, LTU). The depth range is 2 to 30 mm, the depth focus is 8 mm, and the lateral imaging window is 30 mm. 794x580 images are generated at 30 FPS, and the system is capable of compound, color Doppler, and spectral Doppler imaging with gain control of 50 dB. The beamformer measures 54 x 220 x 158 mm in volume and is connected to the transducer by a ZIF-260 pin connector interface. The beamformer is connected to the host computer via USB.

The third transducer is a 40 MHz linear array transducer with 256 piezoelectric elements at 100 μm pitch (MS 550S, Fujifilm VisualSonics Inc., U.S.). The depth range is 1 to 13 mm, the depth focus is 4 mm, and the lateral imaging window is 20 mm. Like the L18-10L30H-4, the system is capable of compound, color Doppler, and spectral Doppler imaging. The radiofrequency data can also be saved for further processing. The transducer is connected to a VisualSonics Vevo 2100 system, and is most commonly used for imaging small superficial structures in animals.

To avoid the need to apply liquid acoustic gel on the skin, we developed a solid agar-based hydrogel contained within a plastic clip that can be easily attached to the US transducer head before the procedure **Figure 2-2 (f)**. After the procedure, the clip can be detached and discarded. The clip is 3D-printed in ABS plastic, and would for commercial use be distributed in a sterilized package. The coupling hydrogel is synthesized from 0.5% sterile-filtered agar powder (Sigma Aldrich, U.S.). One of the challenges of developing the solid gel is was controlling its mechanical rigidity. Ideally, the gel must be rigid enough to remain within the plastic clip (a commercial liquid gel would flow out of the clip onto the skin). However, the gel must also demonstrate sufficient mechanical compliance to deform when the clip is placed in contact with the skin surface. Compliance is important to minimize the presence of air pockets between the skin and the gel surface. An overly rigid gel would also compress the vessel before the needle can be inserted. The 0.5% agar gel exhibited elastic behaviors with a Young's modulus of 5 kPa. Reducing the agar concentration below 0.5% significantly worsened the mechanical integrity of the gel. In future studies we will investigate alternative materials, including non-Newtonian (shear-thickening) polymers and hydrogels such as polydimethylsiloxane (PDMS) and guar gum, respectively.

2.4.3. *Computer vision and image analysis approach*

The sequence of image analysis routines (**Figure 2-5**) are executed continuously on a laptop computer (MSI-WS60, Micro-Star International Co., Ltd) equipped with a CUDA-enabled GPU

(Quadro K2100m, NVIDIA Corp.). Real-time implementations of the algorithms were developed in C++. Where possible, code from open libraries such as OpenCV and PCL or frameworks such as OpenCL were utilized. In the following section, I provide a short summary of each of the image analysis steps. Details of the algorithmic methods are provided in Section 2.7.
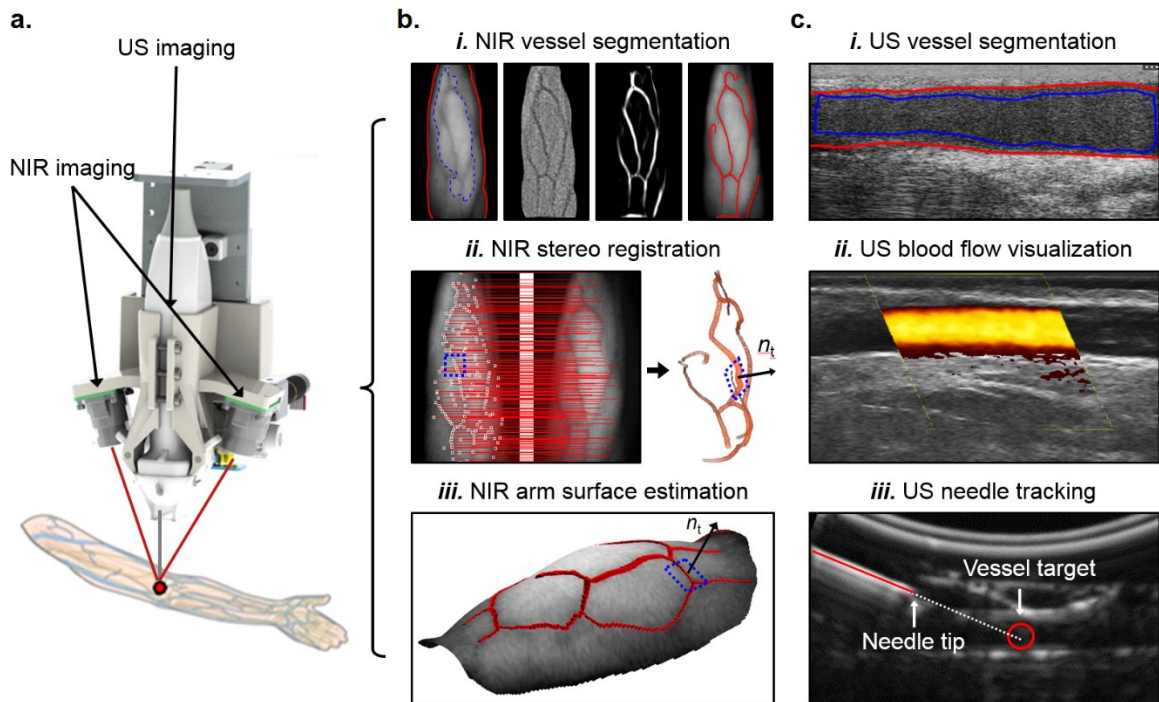
Figure 2-4. Computer vision methods for NIR and US image analysis. **(a)** The two imaging modalities are combined to provide 3D position information for needle guidance. **(b)** NIR image analysis approach. (*i*) Segmentation of forearm and blood vessels. Arm surface is segmented using an active contours approach. Vessels are segmented by enhancing curvilinear ridge-like structures using a second-order match filtering procedure. (*ii*) Feature point registration between left and right stereo images to obtain a 3D map of the vasculature. Feature points (white squares) are the local maxima of the gray-weighted distance transform of the segmented images. Registration is constrained to the epipolar lines of the stereo rig (red stripes). The normal vector n_t and tangent plane (blue square) about the vessel target are computed from the 3D map. (*iii*) 3D arm surface estimation based on real time dense stereo correspondence. **(c)** US image analysis approach. (*i*) The target vessel is segmented using active contours (red outline). The contour is initialized by finding a region in the vessel using threshold and morphological operations (blue outline). (*ii*) Blood flow may be confirmed using Doppler imaging or speckle motion tracking. (*iii*) The needle is tracked during the cannulation using a Hough line detector and a probabilistic state estimation filter.
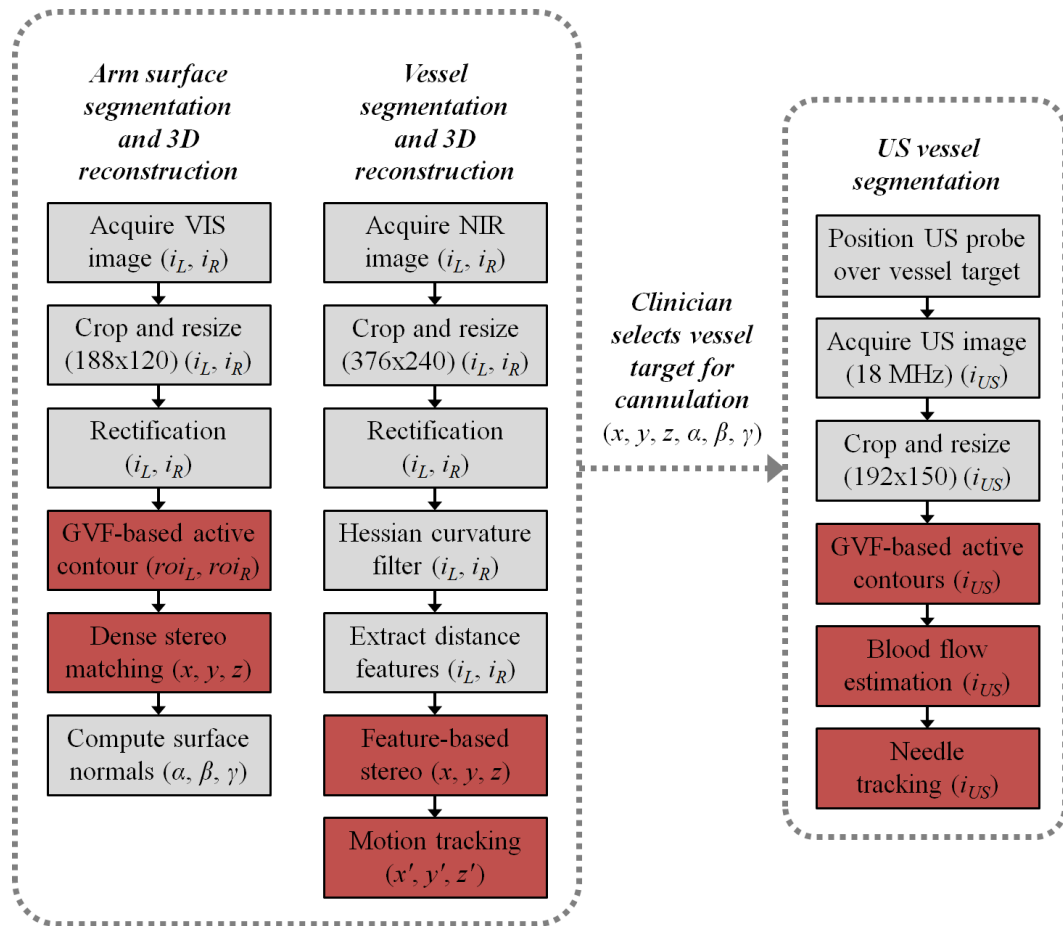
Figure 2-5. Summary of NIR and US image analysis routines. Visible-light images acquired under 690 nm illumination are used to extract the arm surface. NIR images acquired under 830 nm illumination are used to segment the blood vessels and estimate their 3D position below the skin. Once the cannulation target is selected and the US probe is lowered, the target vessel is then segmented from the US image scans. Gray boxes indicate routines performed on a CPU processor. Red boxes indicate GPU-enabled computations.

Stereo camera calibration: Camera calibration software was adapted from an open-source toolkit[95] and rewritten in LabVIEW. A planar grid with circular control points was machined to the base of the system. During the calibration, the grid is imaged by the stereo camera pair at different viewing heights to form a nonplanar cubic calibration rig. The intrinsic and extrinsic parameters of the stereo setup are then extracted using the method of Heikkilä[96], allowing the camera coordinates to be registered to the robot frame. The resulting reprojection error is approximately ±0.1 mm in

our setup, which translates to an (x, y, z) image reconstruction error of approximately 1 mm, given the image resolution of the cameras.

Ultrasound image calibration: To register the US system to the robot frame, the curvilinear coordinate system of the US transducer must be converted to the rectangular coordinate system of the image displayed on-screen. In this process of scan conversion, the raw B-mode scan lines extracted from the curved US transducer are spatially interpolated based on the known geometry of the transducer, sampling frequency, and line density[97]. Small spatial errors in the scan conversion are then minimized using an N-shaped fiducial-based calibration method[98], which allows the pixel coordinates of the US image to be mapped back to the robot coordinates.

Arm segmentation based on active contours with gradient vector flow (GVF) energy formulation: As an initial step to extract the arm surface, a segmentation approach based on active contours is employed to obtain the 2D region of interest (ROI) of the arm from video images captured under illumination by the 690 nm LEDs. Left and right images are first rescaled to 188x120 pixels (factor of 0.25) to reduce the computation time, since only an approximation of the ROI is needed. Active contours segmentation is then performed to identify the boundaries of the arm in each image (**Figure 2-6 (a)**). In the first image frame, the contour is initialized by threshold and morphological operations. In all subsequent frames, the contours are initialized based on the segmentation result from the previous frame. A fundamental aspect of active contour segmentation is the formulation of the external force that pushes the contour into regions of high negative gradient (intensity edges). Here we used an external force based on the GVF field, which has been shown to reduce the sensitivity of the final contour to initialization and enable the contour to move into concavities[99,100]. To increase the speed of the optimization step, we applied an OpenCL implementation of GVF designed for parallel processing on a GPU[101].
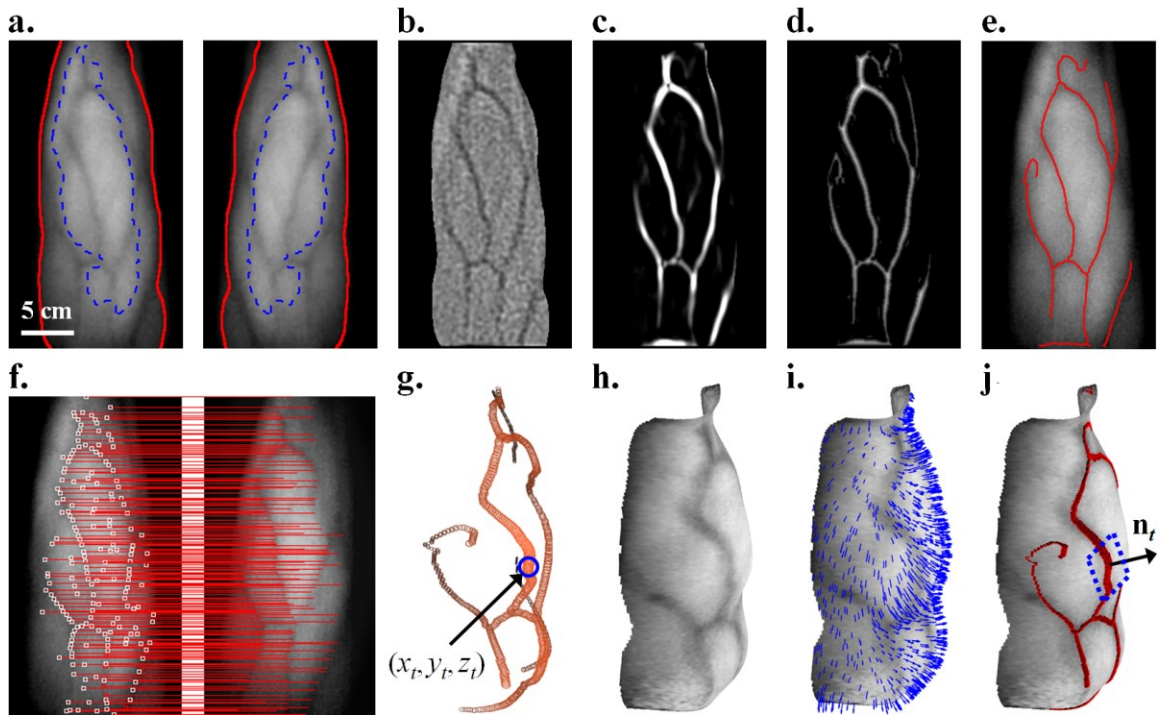
Figure 2-6. Segmentation and 3D reconstruction of peripheral forearm vessels from NIR images in one adult subject. **(a)** Regions-of-interest segmented from left and right NIR stereo images using an active contours approach (red outlines). Initial contours, determined by basic thresholding and morphological processing (blue dotted lines), are iteratively expanded using an energy minimization and contour evolution formulation based on the GVF external force. **(b)** Line enhancement based on the DOG filter (left image shown). **(c)** Vessel enhancement based on Hessian curvilinear filter. **(d)** Gray-weighted distance transform image. **(e)** Result of segmentation and skeleton pruning (red lines). A cannulation target (blue circle) is selected by the clinician. **(f)** Non-rigid registration of feature points along vessel centerlines in left and right stereo images. The local maxima of the distance images from **(g)** are used as the feature points (white squares). Registration is constrained along the epipolar lines of the stereo image pairs (red horizontal lines). **(h)** 3D point cloud of the arm surface based on dense stereo correspondence. **(i)** Surface normal (blue arrows) computed for each point in the 3D point cloud. **(j)** 3D reconstruction of vessels (red). Diameters were determined from the local maxima of the distance images from (d). The blue circle again indicates the selected cannulation target. (l) Tangent plane (dotted blue square) and normal vector n_t about the cannulation target.

Vessel segmentation based on local curvature: The overall segmentation approach was to model the vessels as curvilinear line- or tube-like structures. After first rescaling to 376x240 pixels (factor of 0.5), line structures inside the 2D arm ROI are enhanced by computing the scale-dependent difference of Gaussians (DOG) image (**Figure 2-6 (b)**). A second-order filtering method[102] is then introduced in which tubular structures are enhanced based on eigendecomposition

of the second partial derivatives (Hessian matrix) of the image (**Figure 2-6 (c)**). Segmentation is performed by modeling the resulting image as a mixture of two histogram distributions representing vessels and background. The gray-weighted distance transform of the binary segmentation image is shown in **Figure 2-6 (d)** and the final skeleton in **Figure 2-6 (e)**.

Vessel and arm surface 3D reconstruction: The 3D positions $(x_i,\ y_i,\ z_i)$ along each vessel are computed by extracting feature points i and performing point registration between the left and right stereo images. We use the local intensity maxima of the distance map of the vessel segmentation images as feature points **Figure 2-6 (d)**. The points lie along the vessel centerlines, and the intensity of each point represents the vessel diameter about (i). Non-rigid point registration[103] is constrained to occur only along the epipolar lines between the stereo cameras **Figure 2-6 (f)**. The resulting 3D vessel geometry is shown in **Figure 2-6 (g)**.

The 3D arm surface is needs to be estimated when the full 6-DOF pose information ($x_i,\ y_i,\ z_i,\ \alpha_i,\ \beta_i,\ \gamma_i$) about each feature point i can be utilized, for example to align the US transducer with the target vessel. For this, we use a CUDA-optimized Bayesian network algorithm[104] for real-time dense stereo correspondence. **Figure 2-6 (h)** shows the resulting 3D point cloud of the arm. The surface normal vectors n_t about each 3D vessel point (**Figure 2-6 (i)**), along with the tangent plane with respect to the arm surface, define the pose of the vessels (**Figure 2-6 (j)**).

Vessel motion tracking: Pairwise vessel feature points $\left(x_i^{left},\ y_i^{left}\right)$ and $\left(x_i^{right},\ y_i^{right}\right)$ are tracked between frames via optical flow estimation based on a pyramidal implementation of the differential method proposed by Lucase-Kanade[105]. We applied the OpenCV implementation of the algorithm, which is optimized for CUDA processing. Pairs of feature points are discarded if either point deviates beyond a minimum tolerance from the epipolar line between the points (that is, $y_i^{left} \neq y_i^{right}$). Furthermore, to ensure that the vessel target does not drift from the vessel centerline over time, new feature points are extracted from the segmented vessel images at every

tenth frame, and non-rigid point registration is performed as described previously. The updated vessel target is then set to the nearest feature point.

Vessel segmentation from US images: To isolate the target vessel in the US image after the transducer is lowered over the skin, we again apply the active contours segmentation model using the GVF external force (**Figure 2-7**). Here, US images are rescaled to 192x150 pixels before processing. As was done in the NIR arm segmentation step, the contour is initialized in the first US frame using threshold and morphological operations. The US system may also be used to confirm blood flow by displaying Color Doppler images for visualization.

Initial contour: 5 ms
GVF snake: 17 ms

Initial contour: 6 ms
GVF snake: 24 ms

Initial contour: 6 ms
GVF snake: 22 ms
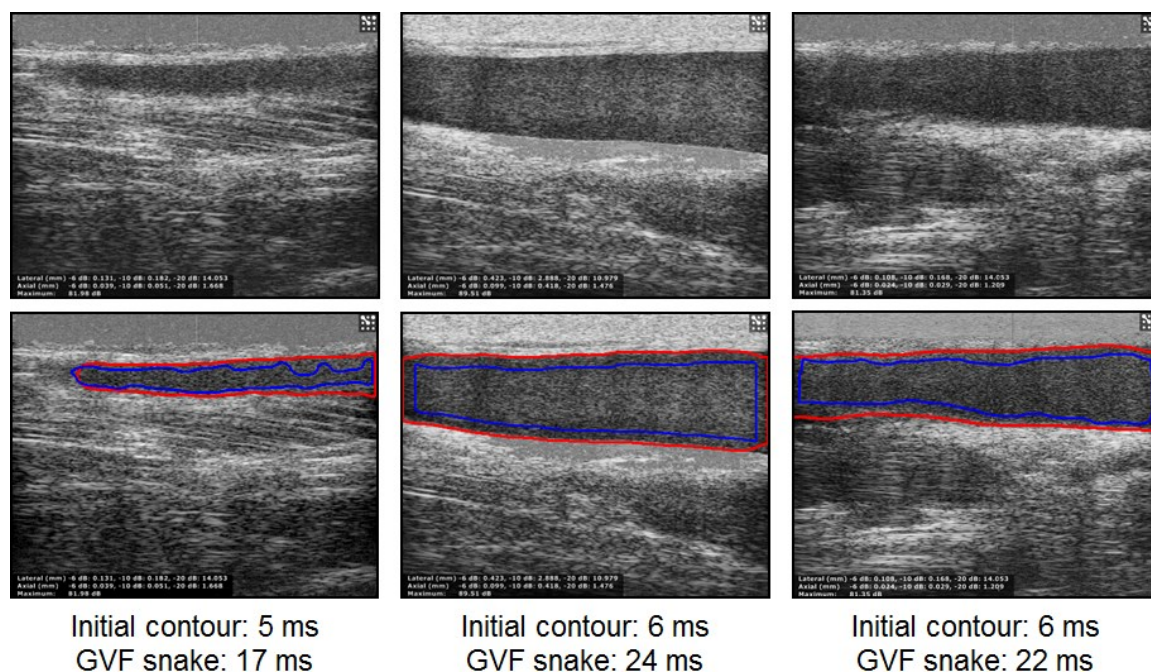
Figure 2-7. Active contours segmentation of vessel lumens in longitudinal US images. Results are shown for 3 adult subjects (columns). Top row: B-mode images acquired with an 18 MHz transducer. *Bottom row:* Segmentation results. Initial contours (blue outlines) were determined by basic image processing and can be seen to lie fairly close to the vessel boundaries. Final active contours (red outlines) were propagated using the GVF energy model. Processing times for the initial and final contours are also shown.
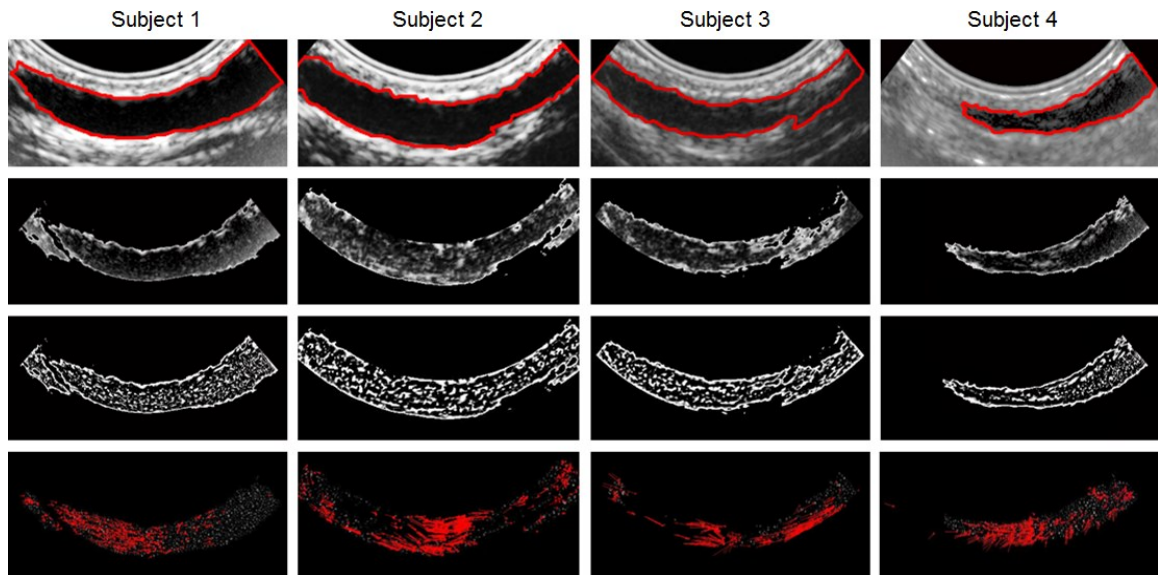
Figure 2-8. Blood flow velocities estimated from longitudinal B-mode US images of four patients (columns) based on speckle motion tracking. Images were acquired at 30 FPS using a 12 MHz single-element scanning sector probe. Rows show main processing steps (*row 1:* active contour segmentation result; *rows 2:* speckle enhancement based on DOG; *row 3:* speckle enhancement based on scale-dependent Hessian filter; *row 4:* Speckle motion vectors computed using Lucas Kanade optical flow. The average per-frame processing time is 22.5 ± 9.1 ms.

Blood flow estimation from US images: Blood flow velocities were estimated from 12 MHz B-mode US images based on speckle tracking (**Figure 2-8**). To first detect the weak echoes from red blood cells, we enhance the speckle contrast using DOG and a scale-dependent Hessian-based filter. Speckle motion vectors are computed using optical flow-based tracking. The average per-frame processing time is 22.5 ± 9.1 ms. Spurious vectors are removed by identifying outliers in the motion probability distribution, and the resulting flow profiles are compared to Doppler US measurements (**Figure 2-9**).

Needle segmentation and tracking from US images: Needle segmentation was performed by combining a log-Gabor wavelet filter to enhance line-like structures within a predefined ROI and a line detector based on the probabilistic Hough transform[106] (**Figure 2-10**). The needle tip location was then determined with subpixel resolution using a Shi-Tomasi feature extractor. Once integrated

with the robotic system, real-time speeds were achieved by reducing the ROI search space using probabilistic priors as determined from the kinematic output of the robot.

The general approach described above may be adapted to using a wide range of line enhancement and detection techniques and feature extractors to localize the needle tip. To compare the accuracy and computation time of different feature extraction approaches, we implemented a range of needle segmentation and tracking algorithms (

Table 2-4). Our goal was to identify an approach that would result in minimal error while maintaining a processing rate of 15 frames per second (FPS). In total, we compared two methods for image enhancement (the directional log-Gabor filter and the Hessian line filter), three methods of line detection (the Hough transform, probabilistic Hough transform, and random sample consensus (RANSAC) algorithm), three methods of needle tip extraction (a rotationally invariant template matcher, the Harris corner detector, and the Shi-Tomasi corner detector), and three methods of motion tracking based on optical flow (a pyramidal implementation of the Lucas-Kanade algorithm[105], the Horn-Schunck method[107], and a variational approach proposed by Brox *et. al.*[108]). Shown in blue in **Figure 2-10** is the approach described above, which has been implemented in the NIR+US imaging system. **Figure 2-11** shows the results of the needle detection approach obtained in real-time during robotically-guided cannulations in a gelatin phantom.
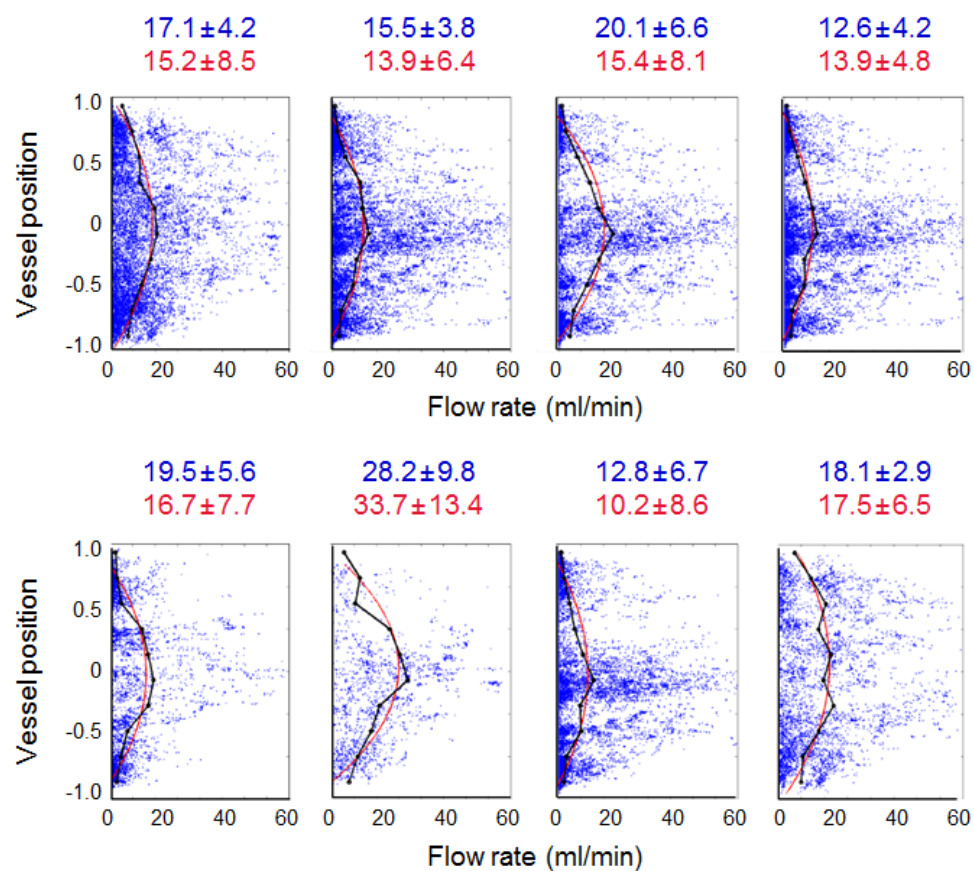
Figure 2-9. Blood flow velocity profiles in superficial forearm veins of eight adult subjects. US images were acquired at 12 MHz. Black lines show the mean velocities based on axial position in vessel. Red lines show parabolic second-order best-fit estimation of parabolic (laminar) flow. Also shown are quantitative estimates of the venous blood flow velocities. *Red:* flow velocities estimated using speckle tracking approach. *Blue:* flow velocities estimated using Doppler ultrasound.
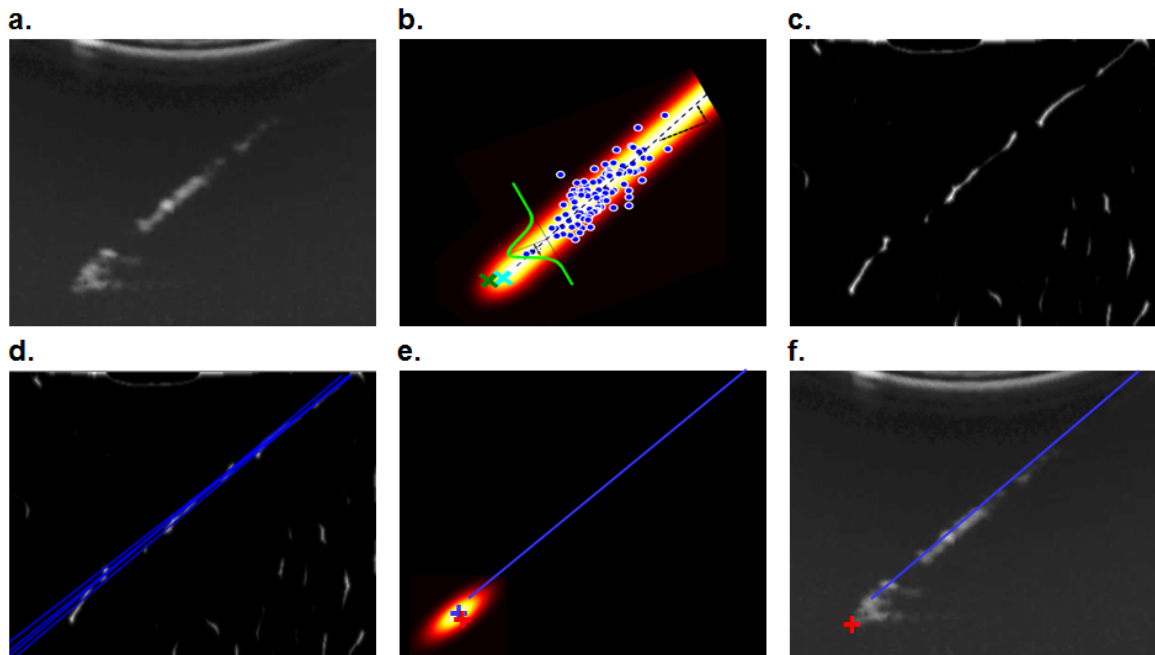
Figure 2-10. Needle segmentation based on log-Gabor wavelets, probabilistic Hough transform, local-invariant feature detection, and kinematic prior estimation. **(a)** Longitudinal B-mode US image of needle in a gelatin-based phantom. Image was acquired using a 12 MHz single-element scanning sector transducer. Disconnected segments of the needle can be seen. **(b)** Gaussian probabilistic prior distribution of the expected needle position and orientation based on the known kinematic state of the robotic system (or the estimated state of freehand needle insertion). **(c)** Result of the log-Gabor wavelet filter. **(d)** Result of the probabilistic Hough transform. Candidate lines are weighted based on the prior probability to determine the MAP estimation of the needle orientation. **(e)** Probability distribution of the needle tip position based on the robot kinematic state (in freehand insertions, this may be estimated from the result of the Hough transform). **(f)** Final result of needle segmentation and needle tip position estimation.

Table 2-4. Comparison of methods for needle segmentation, needle tip extraction, and motion tracking. Shown in blue is the approach that has been implemented in the NIR+US imaging system.

Method	Software implemen-tation	Mean error distance vs. kinematic ground-truth	Std. dev. of error distances	Mean computation time (ms)	Std. dev. of computation time (ms)
NEEDLE SHAFT SEGMENTATION					
Manual Detection	*Manual*	*0.65°*	*0.17°*	*n/a*	*n/a*
Hough transform Matlab implementation	Matlab	1.22°	0.70°	2231.4 ms	388.6 ms
Hough transform w/ Hessian line filter	OpenCV (CUDA)	1.02°	0.71°	163.9 ms	27.2 ms
Hough transform w/ log-Gabor filter	OpenCV (CUDA)	1.03°	0.66°	170.2 ms	30.1 ms
Probabilistic Hough w/ Hessian line filter	OpenCV (CUDA)	0.97°	0.57°	27.7 ms	8.6 ms
Probabilistic Hough w/ log-Gabor filter	OpenCV (CUDA)	0.89°	0.46°	32.7 ms	9.3 ms
RANSAC w/ Hessian line filter	LabVIEW	1.05°	0.54°	92.5 ms	28.5 ms
RANSAC w/ log-Gabor filter	LabVIEW	0.80°	0.31°	95.9 ms	21.1 ms
NEEDLE TIP EXTRACTION					
Manual Detection	*Manual*	*0.52 mm*	*0.25 mm*	*n/a*	*n/a*
Rotationally invariant template matching via norm cross-correlation of the gradient image	LabVIEW	11.72 mm	3.57 mm	7.7 ms	3.1 ms
Harris corner detector	OpenCV (CUDA)	1.207 mm	0.53 mm	6.2 ms	0.8 ms
Shi-Tomasi corner detector	OpenCV (CUDA)	0.93 mm	0.51 mm	5.4 ms	1.1 ms
NEEDLE MOTION TRACKING					
Pyramidal Lucas Kanade optical flow	OpenCV (CUDA)	0.28 mm	0.12 mm	2.3 ms	0.5 ms
Horn Schunck dense variational optical flow	OpenCV (CUDA)	0.25 mm	0.10 mm	35.1 ms	9.0 ms
Brox dense variational optical flow	OpenCV (CUDA)	0.48 mm	0.17 mm	161.3 ms	34.6 ms
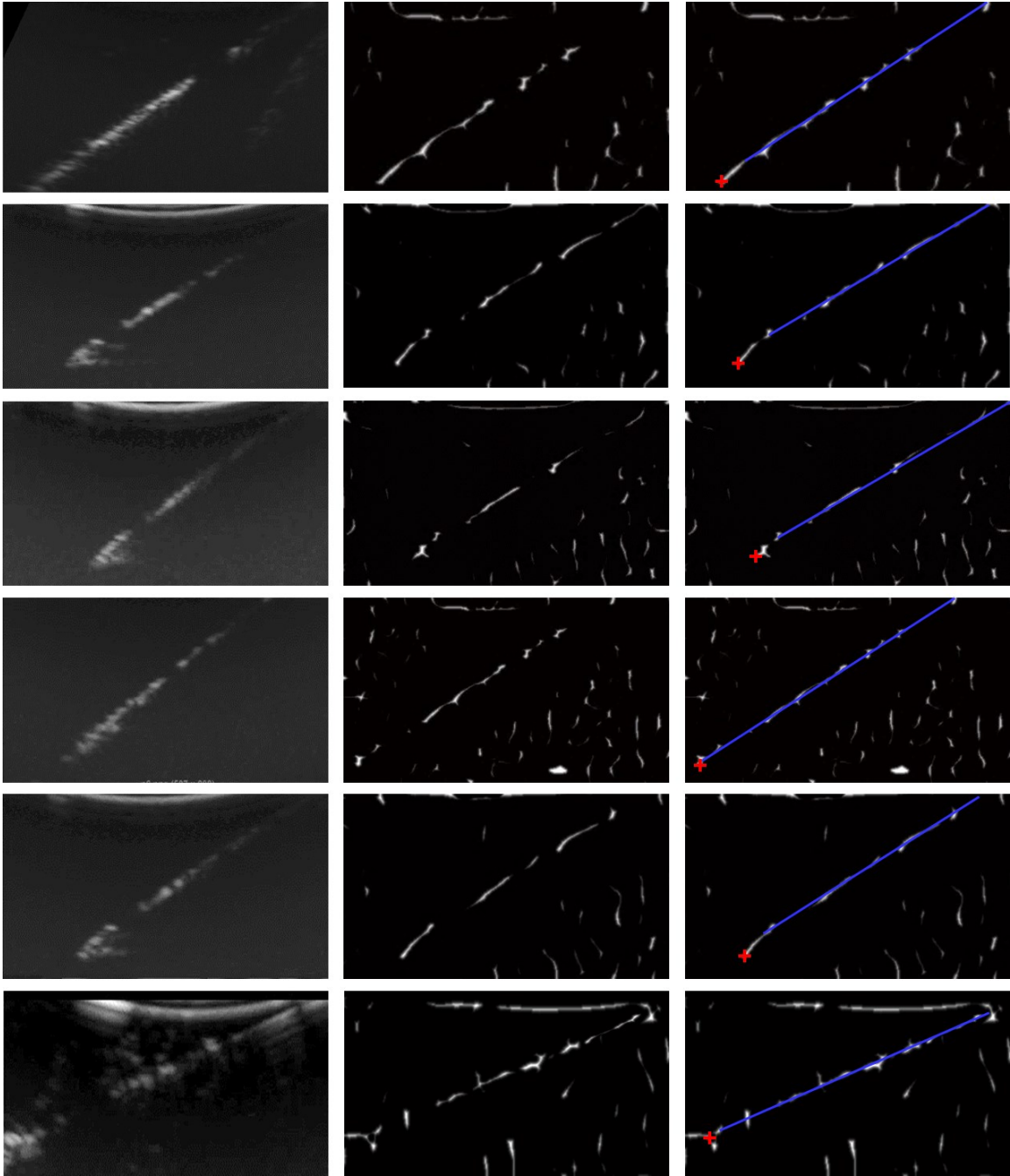
Figure 2-11. Segmentation results of straight needle in a gelatin phantom. *Left column:* longitudinal B-mode US images were acquired at 12 MHz. *Middle column:* line-like structures were enhanced using a log-Gabor wavelet filter. *Right column:* Needle segments detected using a OpenCV implementation of the probabilistic Hough transform and Shi-Tomasi feature extractor optimized for CUDA.

Vessel structure recognition and labeling based on graph matching: Determining a suitable cannulation site can often be challenging and requires a thorough understanding of vessel anatomy. To support the clinician in his or her decision-making process, we introduced an image recognition approach to suggest suitable vessels for cannulation. The overall goal is to introduce a software capable of learning each patient's vessel structure, using the structure information to label candidate vessels, and displaying the information to the clinician in a way that is easily interpreted by the clinician. For each image, the three major forearm veins, i.e., median cubital, cephalic, and basilic veins, are labeled and displayed in a color-coded fashion based on their ranked order of preference. Besides decreasing the reliance of the device on clinical expertise, the software may allow workers with less training, such as nurse assistants and technicians, to oversee the procedure. The software also represents a step toward full device autonomy.

We have implemented three vessel selection methods as initial steps toward achieving this goal. The first method quantifies the suitability of each segmented vessel based solely on image features. Given a vessel v with skeleton S, we defined the suitability (Ψp) of a 3D point p for puncture by observing the visual cues used by clinicians in their decision process. Ψp is given as:

$$\Psi_p = \left(\omega_1 \frac{L}{\max\limits_{v} L} + \omega_2 \frac{A_p}{\max\limits_{v} A_p} + \omega_3 \frac{C}{\max\limits_{v} C} + \omega_4 \frac{1 - I_p}{I_v} + \omega_5 \frac{1 - 2D}{L} + \omega_6 H \right) \Big/ \sum \omega_i$$

where L is the skeleton length of v; A_p is the vein cross sectional area about p; C the contrast; I_p the intensity at p; I_v the mean intensity of v; D the distance between p and the skeleton midpoint, and ω_i, $i = 1\dots6$ the weights for each term, each set to 1 in our studies. H is the output of the Hessian vessel enhancement step shown in **Figure 2-6** (d).

The second method assumes that the structure of the major vessels in the forearm are largely conserved, and that graphs of an individual's vessel structure may be matched to template maps of vessel anatomy, e.g., medical textbook diagrams. We employ a "path similarity" graph matching

algorithm recently developed by Latecki *et. al.*[109]. Here, path dissimilarity matrices are computed and matching costs are computed for each node of the patient and template skeleton graphs **Figure 2-12 (a)**. Structure representation then becomes a bipartite assignment problem, which can be performed using combinatorial optimization methods such as the Hungarian algorithm[110]. The major advantage of this approach, which computes the geodesic path distances between the endpoints on the graph rather than analyzing the graph itself, is its stability when the vessels are discontinuous. In such images, though the distances between branches remain similar, the graph itself becomes fragmented, causing standard matching approaches to produce unreliable results.

The third method also models the structure of the graphs, though rather than matching based on path distances, the "shape context" of individual points lying on the vessel are used as the feature descriptor **Figure 2-12 (b)**. The notion of shape contexts was first described by Belongie *et. al.*[111]. They provide an efficient representation of the magnitude and angular distance of each skeleton point to each other. Shape context histograms are generated and matched based on simple cost functions such as the sum of squared differences (SSD). The bipartite assignment of nodes on the patient graph to the template graph can again be performed with the Hungarian algorithm.

The effectiveness of this feature-based approach is evaluated in a study of 101 adult patients, as described in Chapter 2.5.2. Some of the limitations of using only image features are discussed. Preliminary results of the path similarity and shape context approaches are shown in **Figure 2-12 (c)**. In future work, we will evaluate the accuracy of the graph-based approaches in comparison to annotated results provided by a clinical expert. The dataset generated from the completed 101-patient study will be used for these studies. The goal will be to show that the reliability of vessel labeling can be improved using graphs when the segmented vessels are highly discontinuous.
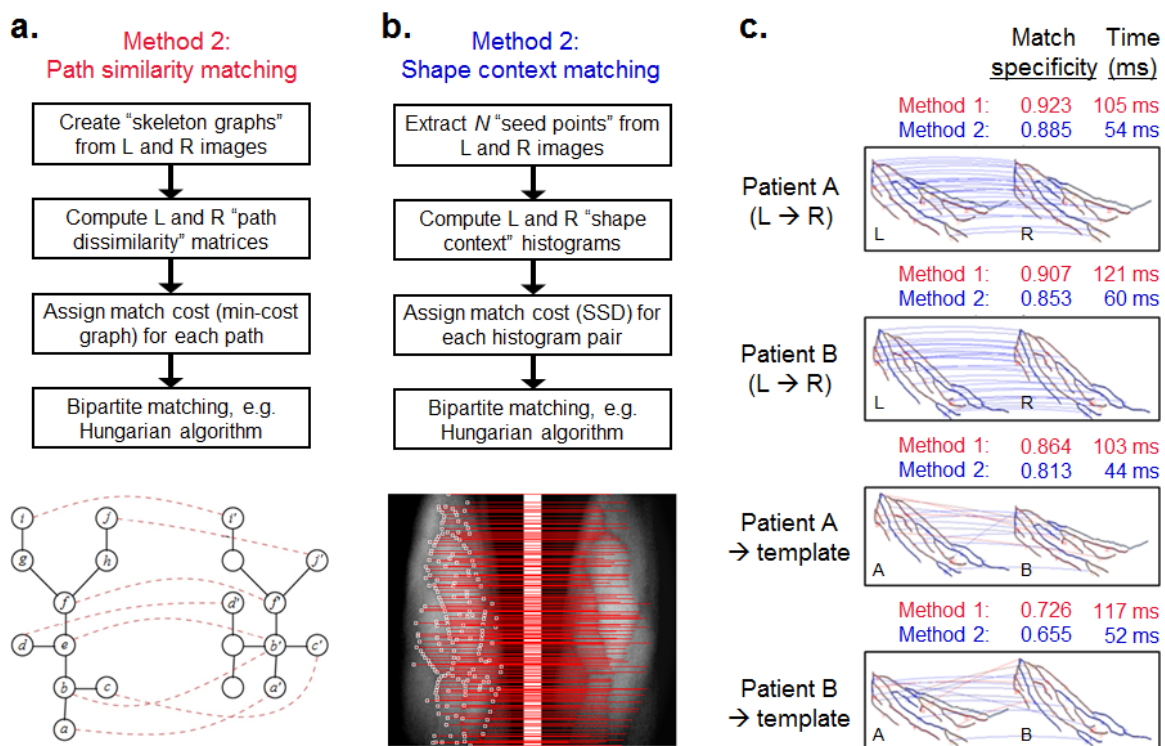
Figure 2-12. Algorithms for vessel recognition based on graph matching. **(a)** Structure recognition based on path similarity graph matching. **(b)** Structure recognition based on shape context histogram matching. **(c)** Results of 4 patients demonstrating matching of vessel skeleton graphs using the two methods. Match specificity is defined as the percentage of vessel branches (graph edges) with correct correspondence/labeling.

Bayesian integration of segmentation, structure, depth, and motion: The Bayesian framework provides a way to merge different information sources by representing them as prior probability densities that influence the posterior estimation of a hidden state, i.e., the true vessel position and pose. We use a Bayesian model for coupling the stereo, segmentation, structure, and motion information that I described in the previous sections of Chapter 2.4. The approach involves introducing the labeling information provided by the arm and vessel segmentation steps, the motion vectors resulting from optical flow, and the graph representation of vessel structure, as additional constraints in the computation of the 2D disparity function f during stereo correspondence. Specifically, these constraints are passed around as conditional messages between neighboring

nodes of a Markov random field (MRF) to propagate information inferred about the global disparity

(a process known as loopy belief propagation (LBP), as described in Chapter 2.7.3).

A similar approach may be implemented to maximize the information use from the processed

US images. Here, the labeling information provided by the vessel segmentation step may be merged

with the speckle motion vector maps generated from blood flow estimation. For active contour

segmentation, information derived from the image about the boundary of the object is used as the

data term that directs energy minimization and contour evolution. Others have shown that region

statistics (and in our case motion vectors) may be incorporated without substantial modification of

the energy model[112]. It may also be possible to integrate needle tip information if a model of tissue

deformation due to needle stresses can be developed; however, this has not yet been explored.

At present, we have developed Matlab software prototypes for both the NIR and US image

analysis components. Further work in this area will involve leveraging CUDA optimization to

ensure real-time performance. Once the algorithms are real-time capable, they may then be

incorporated into the system software to improve the robustness of the vessel localization steps in

the presence of image artifacts, motion noise, ambiguity, and uncertainty.
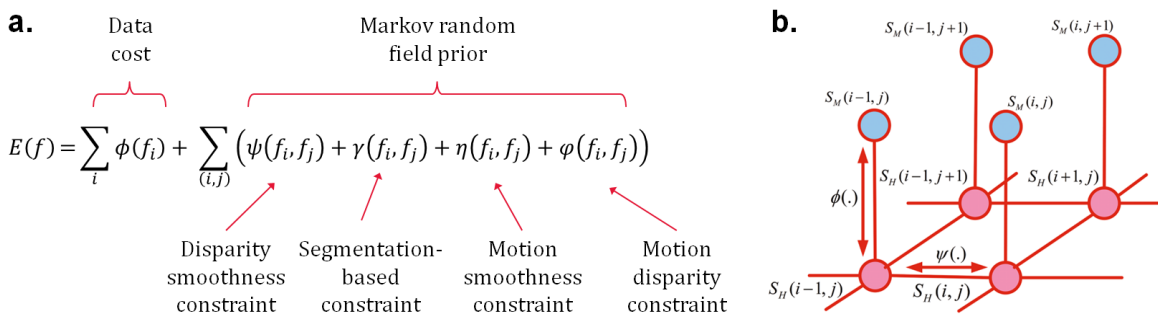
Figure 2-13. Bayesian integration of segmentation, structure, depth, and motion. **(a)** Energy model updated in belief propagation during stereo correspondence. **(b)** Diagram showing how messages are passed from neighboring nodes of the MRF to propagate information inferred about the global disparity.

Active stereo from structured illumination: Currently, the imaging system relies on robust stereo correspondence to provide accurate 3D estimations the arm and vessels. Unfortunately, stereo correspondence remains one of the most active fields of computer vision research, largely because current methods have not achieved satisfactory results in many real-world environments. In our system, inaccurate stereo estimation leads to inaccurate positioning of the US probe. One alternative approach is to make use of structured illumination to minimize ambiguities in the correspondence step. Figure 2-14 shows a schematic of a structured illumination setup that we have begun to develop. In this approach, a pattern projector is implemented in conjunction with a stereoscopic detector. Our system uses a laser diode emitting a lower wavelength of NIR light (here, 760 nm) through a diffraction grating that produces a pattern on the arm surface (a digital projector may also be used in place of the laser diffraction configuration). Meanwhile, a higher wavelength of NIR light (here, 940 nm) is emitted via LEDs to detect the vessels in the traditional manner. The laser diode and LEDs are pulsed at 50 FPS to generate disparity maps in rapid succession. In future studies, we will compare the accuracy of the passive and active methods. We will also investigate methods to merge passive and active stereo information to further improve the disparity estimate.
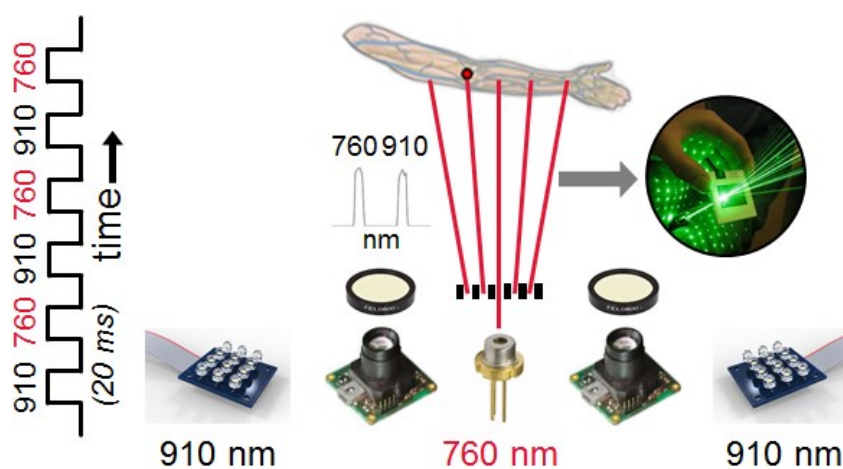
Figure 2-14. Active stereo correspondence from structured illumination. A pattern is generated based on laser diffraction and projected on the arm. The pattern provides markers to aid in the disparity estimation.

2.4.4. Combining bimodal NIR+US imaging and motorized needle insertion

Finally, we investigated whether it is feasible to couple the NIR+US imaging system and image analysis framework with a motorized needle insertion mechanism to perform cannulations in a semi-automated manner (**Figure 2-15**). The main advantage of this approach is the potential ability to precisely update the position and orientation of the needle in real-time based on image feedback. We developed a 3-DOF mechanized robotic manipulator (**Figure 2-2**) capable of insertion standard Butterfly needles or intravenous catheters at angles between 15° and 30°. A more detailed description of the manipulator design will be given in Chapter 3.6, where the manipulator is coupled with a 6-DOF base positioning system, resulting in a fully-autonomous 9-DOF robot capable of aligning, servoing, and inserting the needle with target vessels in the human forearm, hand, and wrist. In contrast, the experiments described in this section utilize only the 3-DOF manipulator. The system is operated in a handheld manner; the clinician manually scans the patients arm using the NIR+US imaging system and, once a suitable vessel is located, reorients the imaging device so that the needle is aligned with the selected vessel. Alignment markers are provided on the graphical display to assist the operator in orienting the device. When correct alignment is indicated on the GUI, the operator may then issue a command via the GUI or by pressing a button to direct the device to insert the needle. Compared to manual needle insertion, the semi-automated device may reduce the need for complex hand-eye coordination by the operator, who would otherwise need to insert the needle and manipulate the NIR+US imaging system simultaneously. Furthermore, by mounting the system on a passive flex-arm, it may be possible to perform the cannulation in a hands-free manner. The semi-automated system is also less costly than a fully autonomous device. Nevertheless, compared to a fully automated device, increased human intervention is needed, and it is likely that manual errors would not be fully eliminated. The advantages and limitations of the semi-automated approach are discussed later in Chapter 3.
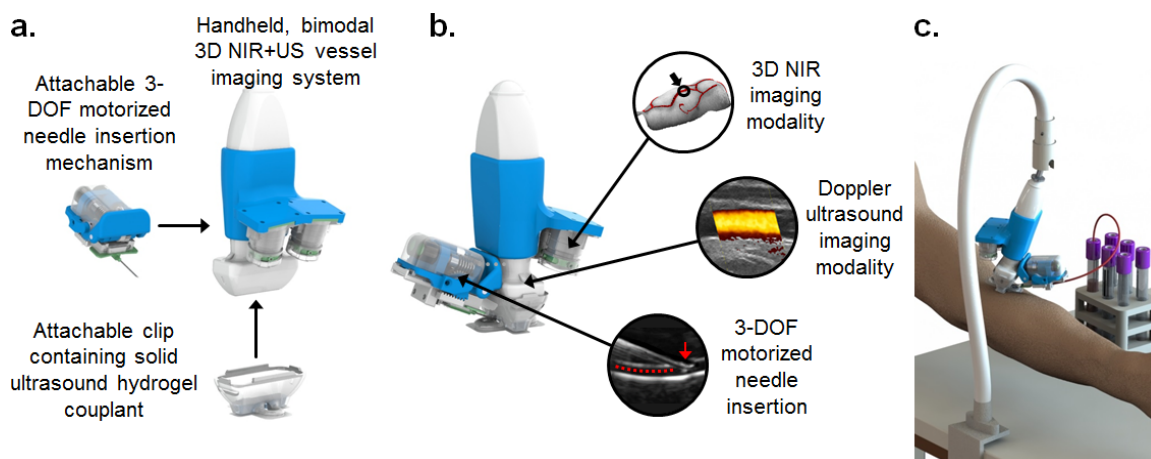
Figure 2-15. Combining bimodal NIR+US imaging and motorized needle insertion. **(a)** The coupled system includes the handheld imaging system, an attachable 3-DOF needle insertion mechanism, and an attachable clip containing a solid US coupling hydrogel. **(b)** Schematic of main system functions. The US transducer may be oriented for transverse imaging (as shown in the device render) or for longitudinal imaging (as shown in the inset figures). **(c)** The system may be mounted on a flexible articulated arm that the operator can adjust to scan the patient. The arm also allows the system to be positioned above a selected vessel target. Using the flexible arm allows the cannulation procedure to be performed in a hands-free manner.

2.5. Results

2.5.1. *Optimization of NIR vessel imaging in human subjects*

Previous studies have compared the visibility of peripheral veins under NIR and VIS light. Various designs of NIR imaging systems for vein detection have also been developed, some of which have achieved commercial adoption. However, to our knowledge, there has yet to be described a systematic evaluation of the parameters that may affect peripheral forearm vein imaging. We applied orthogonal experimental design[113,114] to compare the imaging proficiency of the device under NIR and VIS conditions across 24 patients (**Table 2-5**)[58]. For each patient, the left and right forearm and ACF were scanned under VIS and NIR light, and the NIR images were segmented. Five device parameters, i.e., wavelength, the angle-of-incidence of the light source to the arm, the distance of the light source from the arm, power per LED, and the orientation of the cross-polarizers, and three demographic parameters, i.e., age, body mass index (BMI), and

Fitzpatrick skin type (FST), were assessed. Imaging performance was defined as the length of segmented veins divided by the length of the forearm. All five parameters were found to affect performance significantly, and the optimal imaging conditions determined from the results.

Statistical approach: Taguchi design of experiments was applied to optimize device imaging parameters. An experimental array comprising the control variables was tested against an array comprising the noise variables, with the result providing a model of imaging robustness with respect to patient variability. Imaging performance was defined as the total path length of the detected veins, normalized by the length of the patient's forearm from wrist to elbow, and is here represented by φ. In turn, φ was used to derive the robustness measure, namely the Taguchi nominal SNR, by the equation $SNR = \log(\varphi^2/\sigma^2)$, where σ is the standard deviation of the distribution of φ across the sample. Fractional factorial (orthogonal) arrays were used to reduce the number of runs; a 5-variable 4-level L16 orthogonal design was used for the control array, and a 3-variable 2-level L4 design was used for the noise array. Six patients (replicates) were selected per run. The order of the experimental runs was randomized to eliminate the potential for study bias.

Main effects of the device parameters were evaluated across the sample population, and the set of device imaging conditions that maximized the SNR was identified **(Figure 2-16)**. One-way analysis of variance (ANOVA) was performed to determine whether varying the control conditions changed the path lengths of the detected veins. Post-hoc analysis using Fisher's least significant difference (F-LSD) was conducted following the ANOVA to identify the specific experimental levels between which the performance difference was significant. Significant differences, defined as two-tailed p-values < 0.05, were observed for all five device parameters.

Control array: device settings	Units	1	2	3	4
Wavelength	nm	*470*	*760*	*880*	*940*
LED distance to arm	cm	*6*	*12*	*18*	*24*
LED angle of incidence	degrees	*0*	*45*	*90*	*135*
Polarizer orientation	degrees	*0*	*30*	*60*	*90*
LED diode power	mW	*50*	*100*	*150*	*200*

Noise array: demographics	Units	1	2
Age	years	*<18*	*18+*
Body mass index (BMI)	unitless	*<22*	*22+*
Fitzpatrick skin type (FST)	unitless	*I-III*	*IV-VI*

Noise Array (L4)	1	2	3	4
Age	−	−	+	+
BMI	−	+	−	+
FST	−	+	+	−

Control Array (L16)	Wave length	LED distance to arm	LED angle of incidence	Polarizer orient-ation	LED diode power
1	−	−	−	−	−
2	−	o	o	o	o
3	−	+	+	+	+
4	−	+ +	+ +	+ +	+ +
5	o	−	o	+	+ +
6	o	o	−	+ +	+
7	o	+	+ +	−	o
8	o	+ +	+	o	−
9	+	−	+	+ +	o
10	+	o	+ +	+	−
11	+	+	−	o	+ +
12	+	+ +	o	−	+
13	+ +	−	+ +	o	+
14	+ +	o	+	−	+ +
15	+ +	+	o	+ +	−
16	+ +	+ +	−	+	o

5 device parameters (16 runs)
3 demographic parameters (4 runs)
6 replicates
384 total trials

Table 2-5. Fractional factorial experimental design to identify NIR imaging parameters in 24 patient sample. Taguchi orthogonal arrays were used to reduce the experimental size. Device parameters were evaluated using a 5-variable 4-level L16 orthogonal array. Demographic parameters were evaluated using a 3-variable 2-level L4 array. Six patients were selected per run for a total of 24 patients. Imaging performance φ was defined as the total path length of the detected veins, normalized by the length of the patient's forearm from wrist to elbow. The outcome score was defined by the Taguchi *SNR*, defined as $\boldsymbol{SNR = \log(\varphi^2/\sigma^2)}$, where σ is the standard deviation in the set. In total, 384 trials were carried out to assess imaging performance.
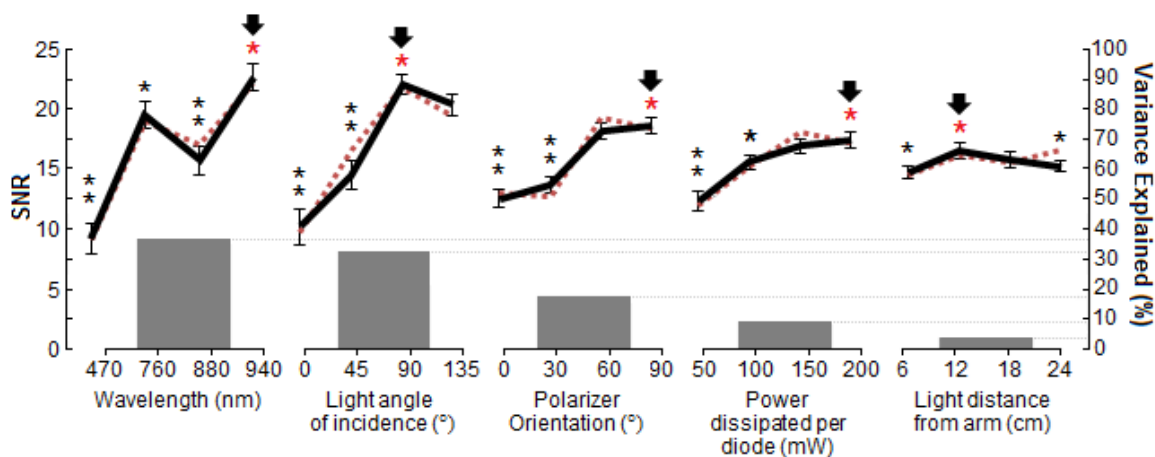
Figure 2-16. Main effects plot showing the Taguchi SNR and explained variance (%) for five imaging parameters. Error bars show the standard deviation for each level. Bar plot shows the variance contributed by each parameter. Device parameters maximizing SNR are indicated by the black arrows. Parameters contributing statistically significant changes to imaging performance are indicated by red stars (*) above the arrows. Significant differences between levels within each demographic condition are indicated by black stars: two-tailed p-value < 0.05 (*), 0.01 (**).

2.5.2. *Comparison of NIR imaging and segmentation to expert visualization*

In the clinic, the focus of venipuncture is on the major veins of the ACF and forearm. For most blood draws, the phlebotomist will try to access the median cubital vein in the ACF by default. For intravenous infusions, the cephalic and basilic veins in the forearm are most commonly used. Thus in order to demonstrate clinical proof-of-concept for the imaging system, we compared the effectiveness of the device in detecting these three major veins to the effectiveness of the standard landmark technique performed by an experienced clinician[58]. 101 patients spanning a broad range of demographics were recruited (**Figure 2-17**). The left and right forearm and ACF of each patient was imaged by the device using VIS and NIR light and then analyzed manually by the phlebotomist. The path length of detected veins was quantified and normalized by forearm length following a series of segmentation routines (**Figure 2-18**), as described above. In the device's case, path length was calculated directly from the image with a pixel to cm conversion. In the clinician's case, markers were drawn at 1 cm increments along the patient's arm over detected veins, and the number

of markers was counted. Age, sex, BMI, and FST, were documented for each patient and correlated to device performance.

Across the study population, the path length of detected veins per patient was observed to correlate inversely with two demographic factors, BMI and FST, to significant effect (**Figure 2-19 (a)**). Neither age nor sex correlated significantly with path length, though in the case of age, a contributing factor may have been the lack of volunteers less than 10 years old. For all demographic groups, mean path length per patient was observed to be significantly greater with the device using NIR imaging compared to the phlebotomist. Furthermore, for all groups, the regression coefficients[115] representing physiological influence on path length were significantly reduced in the device trials compared to the control trials, indicating that the imaging performance of the device is less affected by demographic variability.
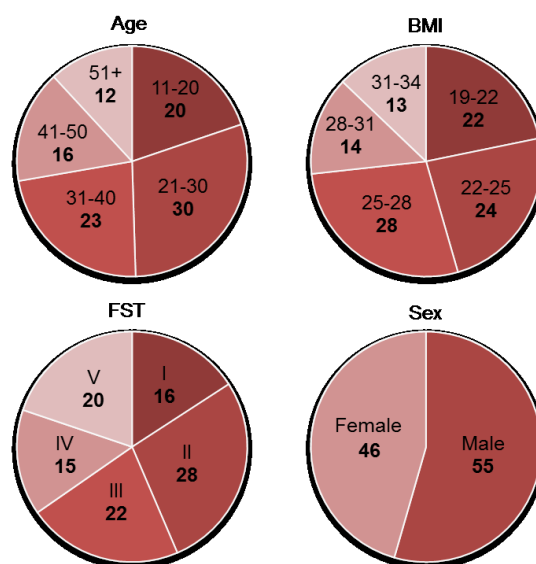
Figure 2-17. Demographic distribution of 101 patients recruited for human imaging study. Patients were recruited at Rutgers University following IRB-approved protocols.
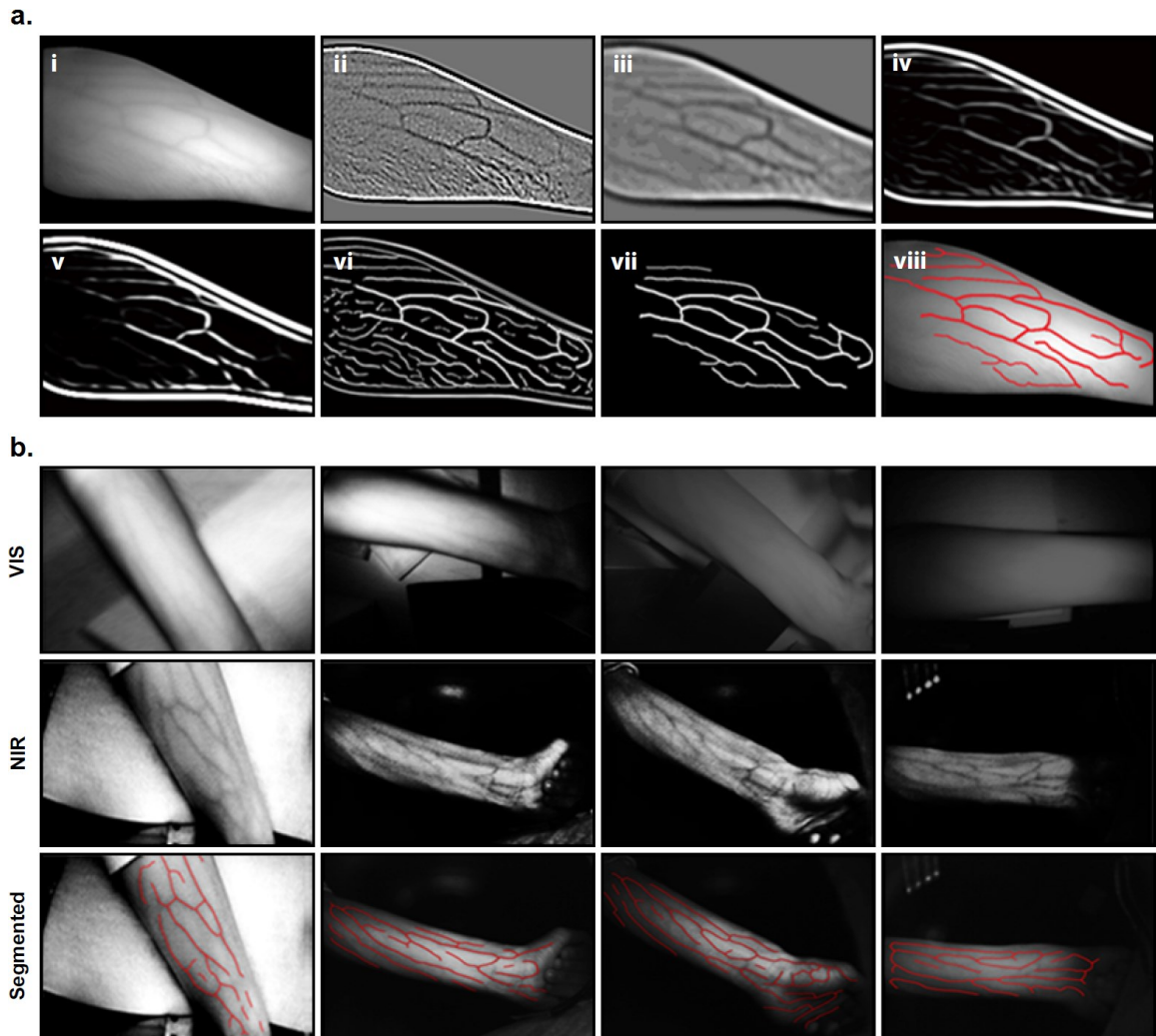
Figure 2-18. Vessel segmentation based on local second-order curvatures. **(a)** Veins extracted from NIR images based on vessel geometry. (i) NIR image; (ii) Edge enhancement based on the DOG filter; (iii) Gaussian smoothing; (iv) Ridge enhancement based on second-order directionality of the eigenvectors in the Hessian matrix; (v) anisotropic curvilinear matched filter based on log-Gabor wavelets; (vi) local intensity normalization; (vii) segmentation based on the distance transform; (viii) skeletonization based on fast iterative thinning. **(b)** Forearm images of four patients from different demographic groups. *Top row:* VIS image; *center row:* NIR image; *bottom row:* vein segmentation of NIR images. *From left to right:* light skin and low BMI (19.1); light skin and normal BMI (23.4); dark skin and moderately high BMI (26.8); dark skin and very high BMI (35.0).
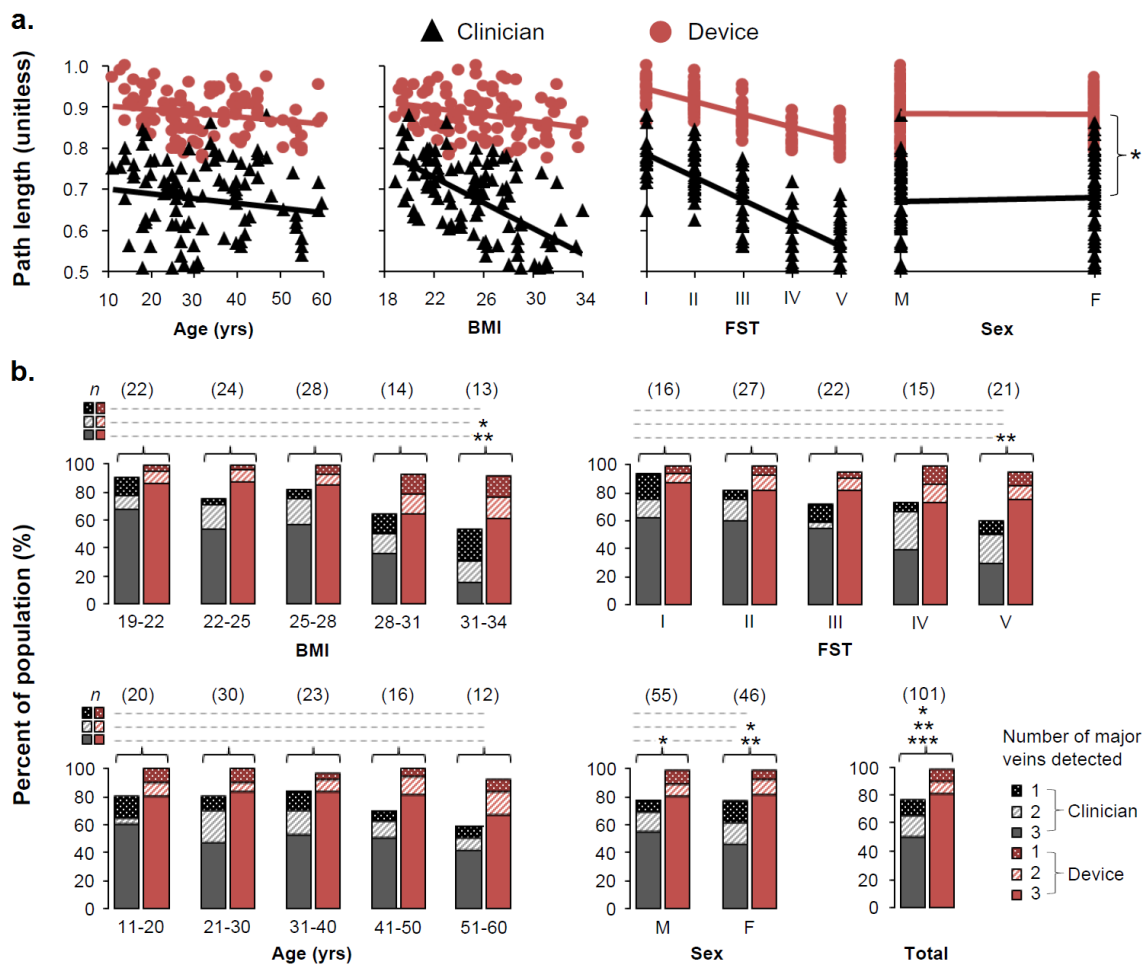
Figure 2-19. Device demonstrates improved vein visualization compared to clinician across 101 patients. **(a)** Effects of three demographic groups (age, sex, body mass index (BMI), and Fitzpatrick skin type (FST)) on the total path length of detected veins, normalized by the forearm length from wrist to elbow. Path lengths were quantified during the imaging routine by the device under NIR light and by the clinician using standard visual and tactile techniques. Multiple regression of the device and clinical control data was performed independently using least-squares fit. Significant effects were observed for BMI and FST, but not for age and sex. ANCOVA was conducted within each demographic grouping to determine whether the intercepts and slopes of the regression models were significantly different between the device and clinical controls. Significant differences (p-values < 0.05, indicated by asterisks (*)) between intercepts and slopes were observed in all cases. **(b)** Comparison of vein detection by the device and by the clinician. Results are categorized by into demographic groupings of age, BMI, FST, and sex. Numbers of samples per group are shown in parentheses. Statistical significance between the percent outcomes of the device and control trials was assessed using a one-sample t-test applied to percentages. Asterisks indicate statistical significance between outcomes, defined as having two-tailed p-values less than 0.10 (*), 0.05 (**), or 0.01 (***). The device was observed to detect at least one, two, or three of the major peripheral forearm veins in a significantly greater percentage of the sample population compared to the clinical control.
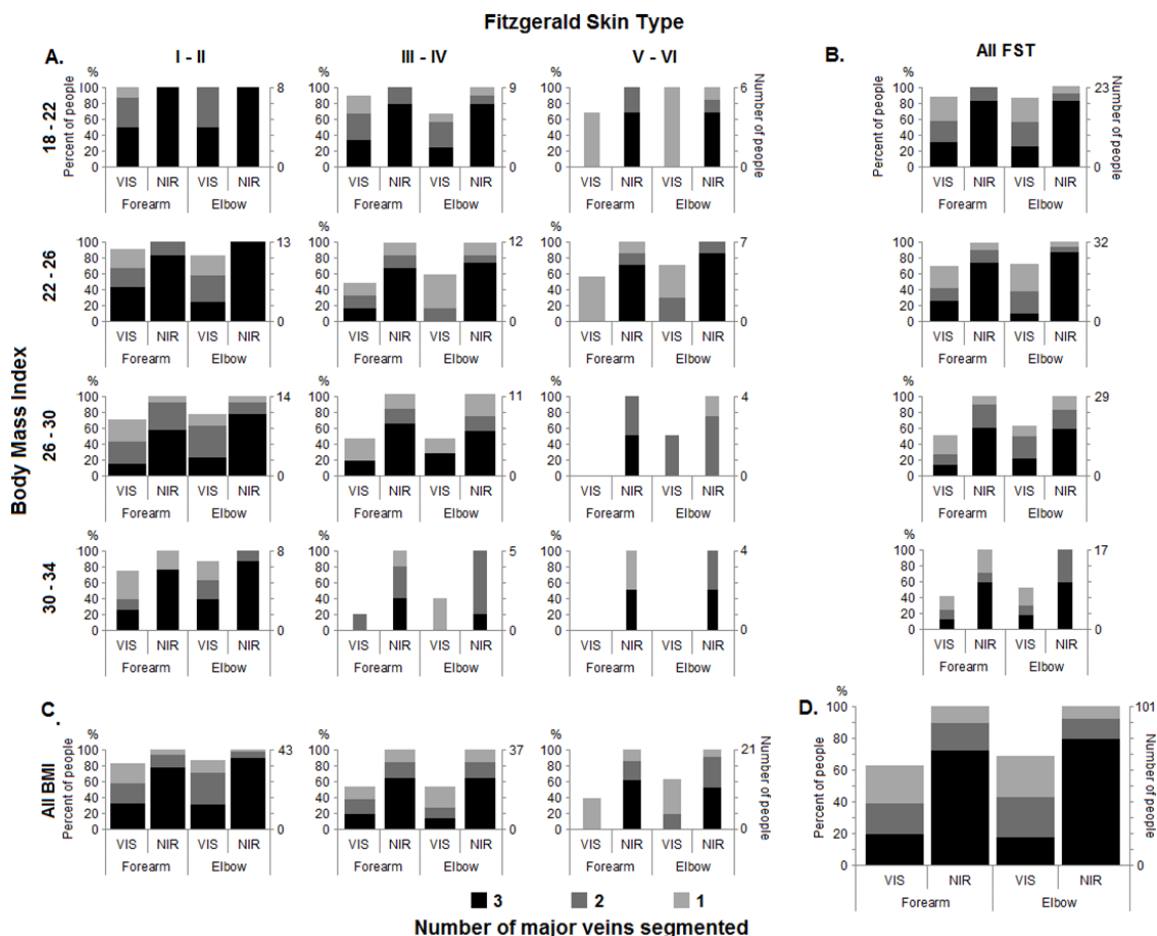
Figure 2-20. VIS and NIR vessel visualization in relation to BMI and skin type. The capacity to segment the three major veins in the forearm and ACF is shown in relation to the two demographic factors, BMI and FST, having previously demonstrated significant effects on visibility. A comparison of segmentation in VIS and NIR conditions is also presented. The number of people per demographic grouping is represented numerically on the right axes and visually by the width of the bars. **(a)** Segmentation results segregated by BMI (vertical, 4 groups) and FST (horizontal, 3 groups). BMI and FST are observed to inhibit vein segmentation to a greater extent under VIS light than multispectral NIR light. **(b**) Results in relation to BMI alone. **(c)** Results in relation to FST alone. **(d)** Results across the full population sample of 101 volunteers. Across all demographic groupings, the device was observed to detect at least one, at least two, or all three of the major peripheral forearm veins in a significantly greater percentage of the sample population using NIR light compared to VIS light. Statistical significance between the percent outcomes of the NIR and VIS imaging trials was assessed using a one-sample t-test applied to percentages45. Asterisks indicate significance between outcomes, defined as having two-tailed p-values less than 0.05 (*) or 0.01 (**).

We additionally determined the percentage of patients for which the major peripheral veins of the forearm and ACF were detected. The device was observed to detect at least one, two, or three of the major veins in a significantly greater percentage of the population compared to the

phlebotomist (**Figure 2-19 (b)**). In 76 of 101 patients, the phlebotomist detected at least one of three major veins was detected by the phlebotomist. Meanwhile the device detected at least one major vein in 99 of 101 patients, representing an improvement of 30.3% over the manual approach. All three major veins were detected by the phlebotomist in 51 of 101 patients, while the device detected all three veins in 81 patients (58.8% improvement). Differences between phlebotomist and device outcomes were the most pronounced in more difficult patients, such as those presenting with dark skin or high BMI, indicating that the phlebotomist was affected by these conditions to a greater extent compared to the device. **Figure 2-20** compares vein segmentation and detection by the device under VIS and NIR imaging conditions, in relation to BMI and FST. A significant improvement in vein detection was observed using NIR imaging compared to VIS imaging.

Finally, we evaluated the device's ability to autonomously select suitable locations for cannulation based on graph matching (see Chapter 2.4.3). In 89 of 101 patients, the algorithmically chosen cannulation site was confirmed by the phlebotomist as suitable for venipuncture. The most frequently chosen vein was the median cubital vein in the ACF (segmented in 92 patients and selected for cannulation in 70), followed by the cephalic vein (segmented in 75 patients and selected for cannulation in 17) and the basilic vein (segmented in 61 patients and selected in 8). Most of the discrepancies resulted from the clinician preferring certain vessels despite them being slightly smaller or less visible, indicating that anatomical knowledge was a key part of the decision process.

Summary of statistical approach: To assess the effects of demographic variability on the normalized path lengths of detected veins **(Figure 2-19 (a))**, multiple regression was applied using least-squares fit. The main effects for the four demographic parameters (age, sex, BMI, and skin type) were evaluated for the device and control sets independently. Significant effects, defined as effects having a two-tailed p-value < 0.05, were observed for BMI and FST in both the device and control trials. No significant effects were observed for age or sex. The overall coefficient of determination (R^2) was quantified to determine the proportion in the variability of path lengths

explained by demographic variability. After adjusting to take into account sample sizes and the statistical dimensionality of each factor, R^2 was found to 69.2%, indicating that the majority of variability can be explained by demographic differences, with the minority being therefore attributed to experimental variability. Correlation between demographic parameters was assessed by quantifying variation inflation factors. Multicollinearity, defined as a variation inflation factor > 10 for any case, was not observed. One-way analysis of covariance (ANCOVA) was conducted within each demographic group to determine whether the intercepts and slopes of the regression models were significantly different between the device and clinical controls. Significant effects (two-tailed p-values < 0.05) were observed in all cases, indicating that the differences in the magnitudes and slopes of the response between groups were not due to chance.

To compare the population percentage for which veins were successfully detected by the device and by the clinician (**Figure 2-19 (b)**), one-sample t-tests of percents were applied within-level for each demographic parameter, as well as to the overall population. Similarly, one-sample t-tests of percents were used to compare device imaging with NIR or VIS light. Because sample sizes within each level were small compared to the overall sample population, statistical significance between the outcomes of the device and control trials was defined based on two-tailed p-values at several different significance levels (p < 0.10 (*), 0.05 (**), 0.01 (***)). A significant difference was observed between the clinician and the device in the percentage of the total population for whom at least one, two, or all three of the major forearm veins were detected. Within the patient groups, significant differences were most readily observed in patients with more difficult demographic profiles. Differences were not observed within all groupings, most likely due to small sample size.

2.5.3. *Comparison of NIR+US imaging and segmentation to expert annotation*

The speed and accuracy of each image analysis step were investigated on 9 adult subjects (**Figure 2-21**). Representative NIR segmentation, 3D reconstruction, and US segmentation results

are shown, and the average computational processing times for each step are listed. Unsurprisingly, the stereo matching routines were the most demanding (80 and 125 ms). The remaining steps each required less than 50 ms. The overall frame rate was found to be at 10.8 FPS by executing independent steps in parallel and carrying out demanding computations over multiple frames. Shown also are the root mean squared errors (RMSE) for the arm segmentation, NIR vessel segmentation, vessel tracking, and US vessel segmentation steps over 30 s relative to manual segmentation and tracking by a clinical expert. Errors are expressed as a % of the average per-frame segmentation area or motion displacement. The greatest error (9.6%) was observed in the NIR vessel segmentation step, largely due to the removal of small disconnected segments during post-processing. However, removal of these segments is not expected to affect insertion accuracy, as clinicians preferentially target long, continuous vessels when performing venipuncture.

Average RMSE's for the NIR arm segmentation and US vessel segmentation steps were 4.5% and 4.9%, respectively. The errors were mostly due to inaccuracies in the initialization of the active contours. While the GVF algorithm is relatively more stable to initialization, the accuracy was nevertheless affected in a small number of cases. Currently we are investigating more robust approaches to initialize the GVF contour, including implementing region growing techniques or utilizing the US speckle statistics or Doppler image information.

The NIR vessel motion tracking step resulted in an average RMSE of 3.3%. The largest tracking error occurred on Subject 4 due to a rapid arm motion that caused the vessel target to be lost. In such circumstances, the vessel target must be re-selected. As an alternative to Lucas Kanade optical flow tracking, dense optical flow algorithms based on variational methods[108,116], level sets[117], and motion segmentation[118,119] could potentially be implemented to enforce spatial smoothness constraints on the optical flow fields. It may also be possible to adapt the non-rigid point registration approach used here for stereo registration to perform motion tracking. However, the increased robustness of these alternative techniques will need to be weighed against their added

computational costs. NIR stereo reconstruction errors were not assessed in these studies, since such errors are more readily evaluated in conjunction with robotic cannulation. A focus of future studies will be to assess the 3D accuracy of the vessel maps by comparing reconstruction errors in human subjects to previous results by our group on patterned tracking targets.

a.

b.

c.

Image analysis step	Processing time (ms)
NIR image rectification	**11.5 ± 2.7** (each frame)
NIR arm segmentation	**46.2 ± 16.5** (per 2 frames)
NIR arm stereo matching	**80.1 ± 20.2** (per 2 frames)
NIR vessel segmentation	**49.1 ± 6.6** (per 5 frames)
NIR vessel stereo matching	**125.3 ± 33.9** (per 5 frames)
NIR vessel motion tracking	**10.6 ± 1.8** (each frame)
US vessel segmentation	**42.2 ± 17.4** (per 2 frames)

d.

Image analysis step	1	2	3	4	5	6	7	8	9	Avg.	S.D.
NIR arm segmentation	4.5%	4.1%	2.9%	6.3%	8.5%	4.2%	3.7%	1.6%	5.1%	**4.5%**	*1.9%*
NIR vessel segmentation	10.1%	11.2%	8.4%	9.2%	8.5%	8.7%	10.5%	11.8%	8.0%	**9.6%**	*1.3%*
NIR vessel motion tracking	1.6%	3.7%	1.6%	9.9%	2.4%	2.2%	3.8%	2.6%	1.5%	**3.3%**	*2.5%*
US vessel segmentation	5.9%	5.4%	4.7%	4.3%	4.5%	3.1%	7.6%	6.2%	2.2%	**4.9%**	*1.5%*

Figure 2-21. Bimodal NIR+US imaging assessment on 9 healthy adult subjects. **(a)** Representative NIR segmentation and 3D reconstruction results. **(b)** Representative US segmentation results, with initialization shown in blue and final contours in red. **(c)** Average per-frame processing times. **(d)** Root mean squared errors relative to manual segmentation and tracking.

2.5.4. *Evaluation of NIR+US guided manual and semi-automated cannulation*

Finally, we investigated whether it is feasible to couple the NIR+US imaging system with a motorized needle insertion mechanism. **Figure 2-22** presents the experimental design and results of cannulation studies performed on tissue-mimicking phantoms simulating a range of human physiological properties. These phantoms are simplified variations on the fully customizable

multilayered phantoms that will be described in Chapter 4.2. Here, we evaluated the effects of vessel diameter, tissue elasticity, and skin tone on the first-stick accuracy and completion time of unassisted manual cannulation, NIR+US guided manual cannulation, and NIR+US guided robotic cannulation. Cannulations were performed on phantoms containing vessels with diameters of 0.8, 1.6, and 2.4 mm, tissue elasticities of 5, 15, and 50 kPa, and skin pigmentation matching that of light, medium, and dark toned patients. For each condition, 12 trials were conducted, and all manual trials were carried out by an expert clinician. Cannulation success was defined as the collection of at least 1 mL of fluid having blood-like viscosity that was perfused through the vessels.

The use of NIR+US guidance was observed to increase first-stick accuracy compared to unassisted cannulation, most notably in difficult conditions, i.e., small vessels, low elasticity, and dark skin tone. However, completion time was also seen to increase. Meanwhile, robotic cannulation increased accuracy and decreased completion time compared to manual techniques. These findings suggest a potential for improvement in venipuncture accuracy using image-guidance and for increased efficiency using robotic insertion. Additional measures of success, including the distance of the needle tip from the vessel center, the extent of random needle motion within the tissue, and the average blood volume collected, will be assessed in future studies. The effects of insertion parameters, such needle gauge, insertion speed, and insertion angle, will also be investigated. Finally, collaborative features between the imaging system, the robot, and the operator will be further developed to facilitate clinical translation.
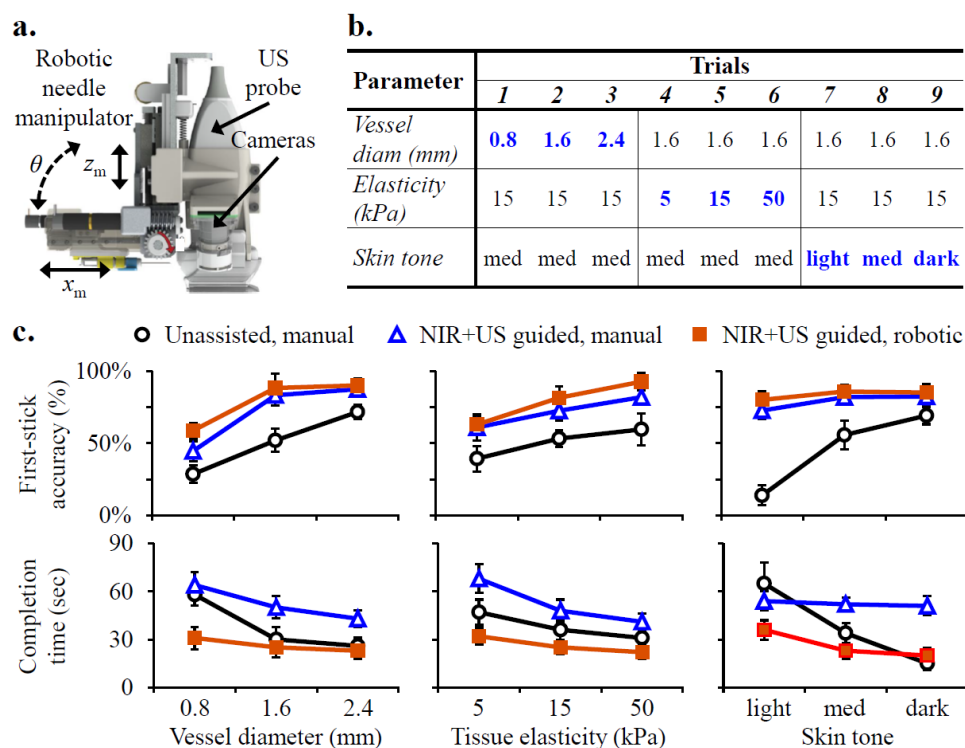
Figure 2-22. Cannulation testing in tissue phantoms. (a) NIR+US imaging system coupled with robotic needle manipulator. (b) Phantom conditions used to assess cannulation performance. (c) First-stick accuracy and completion times of unassisted, image-guided, and robotic cannulation. Error bars indicate deviations for 12 trials.

2.6.   Discussion

In general, imaging technologies such as NIR and US are typically used in the clinic if the practitioner has trouble locating a suitable vein for cannulation. While NIR is best suited for superficial veins, and US is ideal for deeper vessels, it remains controversial whether these imaging modalities significantly improve cannulation success rates and efficiency. To address the limitations of current imaging approaches, researchers have looked to methods that combine both imaging modalities to provide improved vessel visualization. For example, methods have been proposed that combine commercial US imaging systems with optical, laser, or electromagnetic sensors to track the position of the tissue structures and needle throughout the procedure[120–125].

However, these methods require expensive external hardware, specialized needles, and/or extensive calibration before use.

Alternatively, techniques based on visual tracking using sensors local to the US probe may require less expensive hardware and may be compatible with standard needles and probes. One such device[93] uses stereo cameras to infer the 6-DOF pose of the needle in real-world 3D space. The system then projects the pose information onto the 2D US image plane and the 2D view of each camera. The system is designed as an augmented reality device by providing guidance cues to the user in the form of alignment markers displayed on-screen. The user is then tasked with aligning the visible needle with the alignment markers simultaneously, as doing so would ensure the proper insertion trajectory. The computation of disparities between the stereo cameras is made more tractable with the use of structured light sensing, or active stereo, via a visible light digital projector coupled to the US probe. Nevertheless, while structured light sensing helps to texturize the images of the skin surface and allow for more accurate stereo correspondence, current digital projectors are fairly bulky. Even with the use of structured light, capturing reliable features reflected from the needle shaft for stereo correspondence will likely remain challenging, particularly in cluttered image scenes. Furthermore, even with the added visual cues, the system still requires good hand-eye coordination from the user such that they can adequately perform the alignment task. Thus, it remains to be seen whether the device will ultimately lead to improved clinical outcomes or completion times.

The bimodal 3D NIR+US imaging system described in Chapter 2.5.3 combines the advantages of both imaging modalities to improve visualization of the peripheral vasculature. We demonstrated that the NIR+US imaging system enhances the operator's ability to locate a suitable vein for cannulation by constructing a 3D map of the subcutaneous vessels, providing a cue to guide the operator in lowering the US probe over a selected cannulation site, segmenting the vessel and confirming blood flow via image processing of the B-mode US scan, and tracking the needle as it

is inserted into the tissue. When further coupled with a semi-automatic needle insertion mechanism, as described in Chapter 2.5.4, the NIR+US imaging system demonstrated improved cannulation success rates and completion times compared to manual needle insertions with and without the use of assistive imaging devices. The improvements were particularly notable in conditions where the vessel was embedded at depths exceeding approximately 3 mm beneath the skin surface and when the skin tone affected the vein visibility, i.e., in phantoms with dark skin.

In the NIR imaging studies described in Chapter 2.5.1, NIR light at 940 nm was observed to significantly improve the detection of peripheral upper limb veins compared to visible light. The improved detection at 940 nm is most likely due to the local deoxyhemoglobin absorption peak as well as reduced scatter at longer wavelengths. We did not evaluate the system at wavelengths above 940 nm due the rapid decline in quantum efficiency for CMOS cameras past this range. However, if a multi-bandpass filter is needed (for example if a lower NIR wavelength is desired for forearm skin imaging and a higher wavelength is desired for subcutaneous vessel imaging), then it may not be possible to use 940 nm as the illumination wavelength. For dual-wavelength imaging, we used a combination of 690 and 830 nm LEDs to accommodate the use of commercially available 688/828 nm dual bandpass filters. It is unlikely that using 830 nm as opposed to 940 nm would substantially affect the visibility of the vessels; however, a direct comparative study would need to be carried out to verify this assumption.

Meanwhile, in the comparative imaging studies in Chapter 2.5.2, we allowed the phlebotomist to utilize visual and tactile techniques to find veins. In the majority of cases, the phlebotomist identified the median cubital vein in the ACF as the primary target for blood draws, and veins along the anterior lower forearm for intravenous infusions. Currently, the device suggests a cannulation target based on an aggregated score of various image features and displays the decision on the touchscreen interface in an overlay of the real time video. The clinician can either agree with the decision or select an alternative site of cannulation. Incorporate higher level information such as

vein structure and anatomical prior knowledge, e.g., by optimizing the graph-based structure recognition approaches described in Chapter 2.4.3 for real-time operation and implementing them into the imaging device, may allow the device to more closely replicate the deductive reasoning of an experienced clinician. It may also be possible to introduce artificial intelligence approaches[126] that would allow the system to learn the correct clinical decisions by observing experts over time.

2.7. Supplementary – Algorithmic Approaches

2.7.1. Geometric camera calibration

In order to register the 2D camera coordinate frame to the 3D world coordinate frame, it is necessary to determine a set of camera parameters that describe the optimal mapping. Camera calibration is achieved by fitting a camera model to observations of a calibration target whose geometric properties are known. The measured positions serve as the control points in the calibration images. Typically, both the extrinsic (rotational and translational parameters) and intrinsic (projective transformations from the object frame to the image frame) camera parameters are estimated by non-linear optimization and minimization of a suitable cost function over the camera parameters.

Geometric camera calibration has been a major focus of computer vision research for the past few decades. A summary of camera models is presented by Kannala *et. al.*[127,128]. A review of the calibration methods can be found in Hartley and Zisserman[129]. In our implementation, the camera intrinsic and extrinsic parameters are automatically computed during device initialization. We used a pinhole camera model, which is a commonly used approximation that simplifies the optimization problem to a perspective projection followed by an affine transformation in the image plane. Each camera is represented by a 3x4 projection matrix P_i containing the 3x3 matrix R_i that describes the camera orientation, a 3x1 vector t_i that describes the camera position, and the camera intrinsic matrix A:

$$P_i = A \ [R_i \ \ t_i]$$

$$R = \begin{bmatrix} R_{x,x} & R_{x,y} & R_{x,z} \\ R_{y,x} & R_{y,y} & R_{y,z} \\ R_{z,x} & R_{z,y} & R_{z,z} \end{bmatrix}$$

$$t = [t_x \ \ t_y \ \ t_z]^{\mathrm{T}}$$

$$A = \begin{bmatrix} f_x & \gamma & c_x \\ 0 & f_y & c_y \\ 0 & 0 & 1 \end{bmatrix}$$

Then, given $x_{ij} = P_i X_j$ relating the 3D points to their 2D projections, P_i is numerically estimated, most often via Levenberg–Marquardt optimization. We obtain a maximum likelihood estimation (MLE) of P_i by minimizing the reprojection error, that is, the SSD between the measured 3D world points $X = [X \ \ Y \ \ Z \ \ 1]^{\mathrm{T}}$ and the 2D projected image points $x = [x \ \ y \ \ 1]^{\mathrm{T}}$. Isotropic and independent normally distributed measurement errors were assumed.

Our particular geometric calibration implementation is based on the method described by Heikkila[96] and utilizes the camera calibration toolbox developed by Jean-Yves Bouguet[130]. In our system, a motorized system was designed to position the cameras vertically to present a calibration grid with circular control points at 15 different depths. A planar grid with circular control points was machined to the base of the system. During the calibration, the grid is imaged by the stereo camera pair at different viewing heights to form a non-planar cubic calibration rig. The cameras are positioned vertically by the z-axis of the 3-DOF gantry system, and the centers of each circular control point are extracted using an OpenCV circle detection algorithm with sub-pixel accuracy. Each camera's intrinsic and extrinsic parameters are then computed, allowing the camera coordinates to be registered to the robot frame. The SSD reprojection error in our system is approximately ±0.1 mm, which translates to an image reconstruction error of approximately 0.2 mm in the x and y directions and an error of approximately 1 mm in the z direction.

2.7.2. *Arm segmentation based on active contours in NIR images*

To segment the arm in each of the left and right images, we implemented an active contours (snakes) approach based on the use of the GVF flow field as the external force. The traditional snake, first introduced by Kass[131], is a continuous parametric curve $f(s), s \in [0,1]$ that moves through the spatial domain of an image with the objective of coming to rest at the boundaries of the object to be segmented. Using the same notation as before but now in the context of segmentation, this snake should represent the *maximum a posteriori* (MAP) estimation of the joint probability

$$p(f) = e^{-\phi}e^{-\psi}$$

given data term ϕ and prior term ψ. For active contour segmentation, ϕ is taken to represent information derived from the image about the boundary of the object and ψ to represent information about the known shape of the object. Finding $\mathrm{argmax}[p(f)]$ is equivalent to minimizing the negative log of $p(f)$, which for the continuous snake is:

$$E(f) = -\log p(f)$$

$$= \int \phi(f) + \psi(f) \ ds$$

Kass defined the snake energy function in terms of an internal energy $E_{int}(f(s))$ and an external energy $E_{ext}(f(s))$ on the continuum $s \in [0,1]$:

$$E(f(s)) = \int_0^1 E_{int}(f(s)) + E_{ext}(f(s)) \ ds$$

$$= \int_0^1 \frac{1}{2}(\alpha|f'(s)|^2 + \beta|f''(s)|^2) + E_{ext}(f(s)) \ ds$$

where $E_{int}(f(s)) = \frac{1}{2}(\alpha|f'(s)|^2 + \beta|f''(s)|^2)$ contains weighting constants α and β that determine the snake's tension and rigidity, respectively. $f'(s)$ and $f''(s)$ are the first and second

derivatives of $f(s)$ with respect to s. E_{ext} is the external energy function derived from the image, and is formulated such that its values are smallest at the object boundaries.

The numerical method used to minimize E is based on solving the Euler equation

$$\alpha f''(s) - \beta f''''(s) - \nabla E_{ext} = 0$$

The main limitations of the traditional snake model are that it suffers from poor convergence, is highly dependent on where in the image the snake is initialized, and has extreme difficulty moving into concave regions. For arm segmentation, the latter is not presumed to be an issue, as the arm is generally convex. Nevertheless, the issues with convergence and initialization remain problematic.

Unlike the traditional snake, the GVF field[99,100] can capture the object boundary from an initialization within the region boundary or outside the region boundary, and it can force the contour into concave regions. The GVF field is recovered through the diffusion of the edge-driven information, that is, it points toward the object boundary when very near to the boundary but varies smoothly over image regions whose intensities are homogenous. The GVF field is defined in terms of a 2D edge function $g = -E_{ext}$, and its interpretation is also based on energy minimization. Specifically, the GVF is the 2D vector field $\mathbf{v} = (u, v)$ that minimizes the energy function

$$E(\mathbf{v}) = \iint \mu\left(u_x^2 + u_y^2 + v_x^2 + v_y^2\right) + |\nabla g|^2 |\mathbf{v} - \nabla g|^2 dxdy$$

where u_x^2, u_y^2, v_x^2, and v_y^2 are the spatial derivatives of the field and μ a smoothness parameter. When $|\nabla g|$ is small, $E(\mathbf{v})$ is dominated by the partial derivatives of the vector field, and the field is smooth. On the other hand, when $|\nabla g|$ is large, the second term dominates the integrand and is minimized by $\mathbf{v} = \nabla g$. The parameter μ determines the tradeoff between the first and second terms. The GVF can be found by solving a pair of Euler equations

$$\mu\nabla^2 u - (u - g_x)\left(g_x{}^2 + g_y{}^2\right) = 0$$

$$\mu\nabla^2 v - \left(v - g_y\right)\left(g_x{}^2 + g_y{}^2\right) = 0$$

where ∇^2 is the Laplacian operator. Revisiting the edge function $g = -E_{ext}$, we used the DOG operator, which will be described in the context of vessel segmentation in the next section. The choice of edge enhancement algorithm is not particularly important for the GVF computation, as any continuous edge detector may be used as the input with comparable results.

The resulting active contour $E_{min}(\mathbf{v}) = \min_{\mathbf{v}}(E(\mathbf{v}))$ is referred to as the GVF snake. In our system, near real-time computation of the GVF snake was made possible by an accelerated GPGPU implementation of the numerical optimization built on the OpenCL platform[101]. Once $\mathbf{v}$ is computed, we can replace $-\nabla E_{ext}$ in the snake Euler equation with $\mathbf{v}$, yielding:

$$\alpha f''(s) - \beta f''''(s) + \mathbf{v} = 0$$

Solving for $f(s)$ from the above is done in a similar fashion to the traditional snake, i.e., by numerical approximation via gradient descent.

One issue with the use of an edge function to drive the snake is that edges corresponding to vessels (rather than corresponding to the sides of the arm) may undesirably influence the snake. It is possible to define an internal force $E_{int}(f(s))$ with strong tension and rigidity parameters to force the snake through the vessels and out toward the sides of the arm. However, a delicate balance must then be struck so that $E_{int}(f(s))$ does not overwhelm the edge force exerted at the true boundary. We avoid this by using the lower NIR wavelength (690 nm) to capture the input image into the edge filter. Vessels are less pronounced at 690 nm compared to higher wavelengths such as 830 or 940 nm, and thus the edge strength along the vessels is substantially reduced. To initialize the snake in the first frame of the video, we input a region that is somewhat close to the actual

boundary based on simple image thresholding and morphological processing. In all subsequent frames, the GVF snake from the previous frame is used to initialize the snake in the next frame.

2.7.3. *Dense stereo correspondence based on belief propagation in NIR images*

A 3D representation of the forearm surface is essential to provide position information to the robotic system. For a simple 3-DOF Cartesian robot, the (x, y, z) position information is sufficient for robotic guidance. However, for more complex robotic systems that are capable of alignment with any given 6-DOF pose, rotations about the (x, y, z) position are also needed. One way to estimate 3D image information is based on binocular stereo. The basic principle of binocular stereo is to reconstruct a 3D scene from images acquired simultaneously by two aligned cameras. Depth is then computed from the positional disparity between each corresponding pixel in the left and right cameras. The process of identifying matching pixels is known as stereo correspondence, and is one of the most active areas of computer vision research; while a large number of algorithms for stereo correspondence have been developed, it remains highly challenging to resolve accurate disparity maps in the presence of image noise, occlusions, discontinuities, and ambiguity. When sophisticated algorithms are introduced that perform sufficiently compared to ground truth data (or even compared to human performance), it then becomes a challenge to implement them with sufficient computational efficiency. In particular, the development of stereo correspondence approaches that are both robust and real-time compatible remains a challenge. In this section, I describe our implementation of several real-time stereo algorithms using the OpenCV library and developed for general-purpose GPU processing on the CUDA platform. The focus here is on dense methods where every pixel of the first image is assigned a correspondence in the second image; we utilize dense stereo to approximate the 3D surface of the forearm.

Local (window) versus global (MRF) disparity: A comprehensive taxonomy of dense two-frame stereo correspondence algorithms is provided by Scharstein and Szeliski[132] in which methods

are categorized based on four main processing steps: matching cost computation, cost aggregation, disparity computation / optimization, and disparity refinement. For example, a local (window-based) approach based on SSD can be described by its:

i.   data cost ϕ = squared difference of intensities for each possible disparity

ii. support cost ψ = summing matching costs over windows with constant disparity

iii. disparity computation = selecting the minimal aggregated value at each pixel

Local methods are computationally efficient but suffer in performance from a simplistic representation of the disparity. While local methods are capable of modeling the matching costs associated with each possible disparity value for every pixel, they do not account for the supporting evidence provided by the disparities from neighboring pixels. Local methods based on adaptive windows or shiftable windows have been developed to overcome some of the limitations of fixed window approaches, but there is still no guarantee of arriving at an approximation of a defined global optimization criterion.

Alternatively, global algorithms make explicit smoothness assumptions in the disparity computation/optimization step in which "optimal" disparity at a given pixel is dependent not only on the local matching cost about the pixel but also on the disparity hypotheses of the neighboring pixels. Most recent global stereo algorithms model the disparity map as an MRF where the pixels of the map are represented by nodes in a graph $G = (V, E)$ with V the nodes and E the edges connecting each node[133,134]. To allow a tractable solution, the MRF is further defined to be pair-wise such that the value of each node is influenced only its immediate four-connected neighbors. The joint probability of this MRF given its likelihood $e^{-\phi}$ and prior $e^{-\psi}$ can be written as:

$$p(f) = e^{-\phi} e^{-\psi}$$

For the case of stereo correspondence, f is the function representing the disparity image. Using our earlier description, ϕ is then the data cost and ψ is the support cost. The dependence of ψ on neighboring pixel information in the MRF can be more explicitly stated by re-defining $p(f)$ as:

$$p(f) = \prod_i e^{-\phi(f_i)} \prod_{(i,j)} e^{-\psi(f_i, f_j)}$$

where $\phi(f_i)$ describes the penalty for the disparity value f_i at pixel i given the intensity difference between the left and right images at i, and $\psi(f_i, f_j)$ describes the penalty given the difference in disparities between neighboring pixels i and j. Put another way, $\psi(f_i, f_j)$ penalizes a lack of the smoothness between neighboring pixels of the disparity map. One important criteria of $\psi(f_i, f_j)$ is that it should be discontinuity-preserving, i.e., the boundaries between objects located at different depths should not be artificially blurred. For example, the edge between a subject's arm and the table on which the arm rests should remain sharp as opposed to blurred. The requirement of preserving discontinuity prevents simple quadratic regularizing functions to be used for $\psi(f_i, f_j)$.

The optimal disparities are found by maximizing the joint probability, that is, finding the disparity function f that gives $\max_f(p(f))$. This is typically done by MAP estimation, which is equivalent to minimizing the negative log of $p(f)$:

$$E(f) = -\log p(f)$$
$$= \sum_i \phi(f_i) + \sum_{(i,j)} \psi(f_i, f_j)$$

where $E(f)$ is the energy function acting on the disparity. The goal then becomes to find

$$E_{min}(f) = \min_f\big(E(f)\big).$$

Hierarchical loopy belief propagation (LBP): To solve the minimization problem, we utilized OpenCV implementations of two hierarchical dense global stereo correspondence algorithms based on hierarchical LBP first introduced by Felzenszwalb *et. al.* and Yang *et. al.*, respectively[135,136]. Both implementations are optimized for GPU using the CUDA platform and allows for computational speeds that are close to real-time (~5-20 FPS for a 320 x 240 image pair). In LBP, the influence of neighboring nodes is propagated iteratively by passing messages (conditional probabilities) around the MRF graph. Letting m_{ij}^t be the message sent from pixel i to pixel j at time t, new messages are computed at each iteration based on the messages arriving from neighboring nodes at time t–1. The min-sum algorithm is used to approximate the minimum cost labeling by:

$$m_{ij}^t \leftarrow \min_{f_i}\left(\phi(f_i) + \psi(f_i, f_j) + \sum_{k \in N(i)\backslash j} m_{ki}^{t-1}(f_i)\right)$$

where $k \in N(i)\backslash j$ represents all of the neighbors of i other than j. After T iterations, a belief vector is computed for each node:

$$b_j(f_j) \leftarrow \phi(f_i) + \sum_{i \in N(j)} m_{ij}^T(f_j).$$

Solving for $E_{min}(f)$ then becomes equivalent to finding the label that minimizes $b_j(f_j)$ individually at each node. With traditional LBP, the computation time is $\propto O(k^2)$, where k is the number of possible disparities. The methods of Felzenszwalb *et. al.* and Yang *et. al.* introduce strategies to substantially reduce the time needed to compute the message updates. Felzenszwalb *et. al.* simplifies the calculation of $\psi(f_i, f_j)$ using the truncated linear model,

$$\psi(f_i, f_j) = \min(s_\psi |f_i - f_j|, \psi_{max}).$$

Here, the cost increases linearly based on the distance between the disparities f_i and f_j according to a scaling constant s_ψ and up to a maximum cost ψ_{max}. Both methods use a hierarchical strategy in which the LBP algorithm passes the belief vectors down from coarser levels in order to constrain the search at finer levels. In Felzenszwalb *et. al.*, the coarse-to-fine scheme is applied in the spatial domain on an image pyramid. In Yang *et. al.*, the coarse-to-fine scheme is applied both to the spatial domain and to the depth domain, and the number of disparity levels is gradually reduced as the messages propagate down the hierarchy. With these reductions, the computational efficiency is improved to $\propto O(k)$.

Incorporation of additional priors: A major advantage of the Bayesian framework for stereo correspondence is that it allows additional constraints to be readily incorporated into the prior term:

$$p(f) = \prod_i e^{-\phi(f_i)} \prod_{(i,j)} e^{-\psi_0(f_i, f_j)} e^{-\psi_1(f_i, f_j)} \ldots e^{-\psi_n(f_i, f_j)} \ldots e^{-\psi_N(f_i, f_j)}$$

$$= \prod_i e^{-\phi(f_i)} \prod_{(i,j)} \prod_n^N e^{-\psi_n(f_i, f_j)}$$

where $e^{-\psi_0(f_i, f_j)}$ is the disparity prior and $\{\psi_1(f_i, f_j) \ldots \psi_N(f_i, f_j)\}$ is the set of additional constraints. The energy function, expressed as the negative log of $p(f)$, then becomes:

$$E(f) = \sum_i \phi(f_i) + \sum_{(i,j)} \sum_n^N \psi_n(f_i, f_j)$$

Currently, no additional priors are used in the computation of the disparity map. However, at the end of Section 2.4.3, we will describe our proposed approach for incorporating the intensity class labels resulting from the arm segmentation step, as well as the outputs of vessel segmentation and

motion tracking. Finally, we will describe a wrapping function that may be implemented fairly easily to automatically tune the parameters of the MRF from one frame of the image sequence to the next.

2.7.4.   *Vessel segmentation based on local curvature in NIR images*

Normalizing local intensities as a pre-processing step: Local intensity normalization helps to minimize differences in brightness across different areas of the image by equalizing the mean and variance of image patches of a predefined size. In adaptive local normalization approaches, the size of the image patch can vary for different parts of the image depending on the objective criterion. In our approach, the image patch is held constant, and the normalization is simply expressed by

$$g_i = \frac{f_i - m_i}{\sigma_i}$$

where f_i is the intensity value of the input image at pixel i, m_i is an estimation of the mean of a local window of f_i centered on i, σ_i is the standard deviation of the intensities in the local window, and g_i is the resultant normalized intensity at i.

Enhancing vessel structures using a DOG filter: The vessels are segmented based on the assumption that they have a curvilinear line- or tube-like geometric characteristic. As a first enhancement step, low contrast images of the forearm may be enhanced by treating peripheral veins as edges and applying edge detection schemes to them. For this, we employ a DOG transformation whereby an image f convolved with the Gaussian of variance $\sigma_1{}^2$ is subtracted from the image convolved with a Gaussian of wider variance $\sigma_2{}^2$, that is:

$$g(\sigma_1, \sigma_2) = G(\sigma_2) * f - G(\sigma_1) * f$$
$$= \big(G(\sigma_2) - G(\sigma_1)\big) * f$$

where $G(\sigma_1)$ and $G(\sigma_2)$ are the 2D Gaussian kernels. The resulting DOG image $g(\sigma_1,\sigma_2)$ contains only the spatial information that lies between the range of frequencies that are preserved in the two convolved images. Thus, the DOG functions as a bandpass filter that discards all but a handful of spatial frequencies that are present in the original grayscale image. Here, the input image f is the output of the local normalization step described in the previous section. It is worth noting that the selection of scales σ_1 and σ_2 is done in an ad-hoc manner, currently. It is possible to select the scales in a maximum-likelihood manner as is demonstrated in the second vessel enhancement step, described below.

Enhancing vessel structures using a Hessian directional ridge filter: Whereas $g(\sigma_1,\sigma_2)$ represents a first-order filter enhancing edges, vessels in the NIR image are in fact more appropriately thought of as convex ridges (or valleys), the representation of which requires modeling of the second-order structure of the image. Analyzing the second-order information has an intuitive justification for vessel detection in NIR images: as first observed by Frangi *et. al.*, vessels, being tubular, exhibit high local curvature in a principle direction and near-zero local curvature in the orthogonal direction[102]. Furthermore since vessels tend to be darker than surrounding tissues, the principle curvature will be negative. The magnitudes and principal directions of the local curvature of an image f are represented by the eigenvalues and eigenvectors of the 2D Hessian matrix $h(\sigma_h)$ at some scale σ_h (the subscript is used to distinguish this scale factor from scales described earlier). Let $\lambda_1(\sigma_h)$ and $\lambda_2(\sigma_h)$ be the first and second eigenvalues of $h(\sigma_h)$, respectively, and let $v_1(\sigma_h)$ and $v_2(\sigma_h)$ be the corresponding eigenvectors. $v_1(\sigma_h)$ represents the direction along with the second derivative is maximum, and $\lambda_1(\sigma_h)$ gives the maximum second derivative magnitude. $v_2(\sigma_h)$ is the direction orthogonal to $v_1(\sigma_h)$, with $\lambda_2(\sigma_h)$ its magnitude. The geometry of an ideal dark tubular structure, e.g., a vessel in a 2D NIR image, can then be modeled by a simple set of descriptors:

$$|\lambda_1(\sigma_h)| \approx 0 \qquad |\lambda_1(\sigma_h)| \ll |\lambda_2(\sigma_h)| \qquad R(\sigma_h) = \left|\frac{\lambda_1(\sigma_h)}{\lambda_2(\sigma_h)}\right|$$

These descriptors are grey-level invariant, and the geometric ratio $R(\sigma_h)$ describes whether a structure in $h(\sigma_h)$ is more ridge-like $(R(\sigma_h) \to 0)$ or more blob-like $(R(\sigma_h) \to 1)$. An additional distinguishing property of background pixels is that the magnitude of the derivatives (and thus the eigenvalues) is small. To quantify this, it is common to use the Frobenius matrix norm of $h(\sigma_h)$:

$$S(\sigma_h) = \frac{1}{\|h(\sigma_h)\|_F} = \frac{1}{\sqrt{\left(\lambda_1(\sigma_h)\right)^2 + \left(\lambda_2(\sigma_h)\right)^2}}$$

Frangi *et. al.* proposed to combine the two descriptors $R(\sigma_h)$ and $S(\sigma_h)$ to obtain an overall measure of the "vesselness" of each pixel of f given weighting constants α and β:

$$V(\sigma) = \begin{cases} 0, & \lambda_2 < 0 \\ e^{-\alpha R(\sigma_h)} e^{-\beta S(\sigma_h)}, & \lambda_2 \geq 0 \end{cases}$$

It is emphasized that the output image $V(\sigma_h)$ is directly dependent on the choice of scale. If all vessels of interest are expected to occur at a single scale, that is, the vessels are all of similar diameter, then $V(\sigma_h)$ is simply a function of a constant. However, if vessels of different sizes are expected, then the optimal scale will vary across the image and σ_h becomes a 2D function (rather than a constant) with $V(\sigma_h)$ its functional. Thus for a given range of possible scale values $\{1, \dots n\}$, there exists a particular scale function $\sigma_h^{max} \in \{1, \dots n\}$ that produces the maximum possible value of $V(\sigma_h)$ over all pixels, i.e., maximizes the likelihood of the output representing the true scale of local second-order vessel structure. Summing over all pixels, we can find the MAP estimate of vesselness with respect to scale:

$$V_{max}(\sigma_h) = \max_{\sigma_h}\left(\prod_i V_i(\sigma_h)\right)$$

$$E_{min}(\sigma_h) = \min_{\sigma_h}\left(-log\left(V_{max}(\sigma_h)\right)\right)$$

$$= \min_{\sigma_h}\left(\alpha \sum_i R(\sigma_h) + \beta \sum_i S(\sigma_h)\right)$$

Here we have implicitly modeled the prior distribution of σ_h over the image as uniform, reflecting a lack of knowledge about the real distribution; however, any prior distribution over σ_h may be used. In theory, it would be possible to find an approximate solution for $E_{min}(\sigma_h)$ by modeling the scale map as a pair-wise MRF and computing marginal distributions for hidden nodes, conditioned on the observed data, using methods such as LBP. This approach, which is analogous to our earlier approach for computing disparity maps in stereo correspondence, would take into account the influence of neighboring scales through the passing of messages between adjacent nodes in the MRF. However, to save on computational resources, we did not implement the MRF here. Instead, we simply calculated σ_h^{max} independently for each pixel using an accumulator. In future studies, we will investigate a method in which the MRF is applied only in the first frame of the NIR image sequence to obtain a locally connected scale map σ, which would then be used as the prior for MAP estimation in subsequent frames.

In our implementation, the input to the Hessian-based ridge filter was the result of the DOG edge filter $g(\sigma_1,\sigma_2)$ convolved with a third Gaussian kernel $G(\sigma_3)$. It was not our original intention to input an edge-enhanced image, particularly since the edge image exhibits bright side-bands along steep gradients, which are artifacts. However, we found that the use of the edge filter helped to stabilize the output $V_{max}(\sigma_h)$ when the range was defined over very small scales (3 to 5 pixels), which was the case given the diameter of the vessels relative to the pixel resolution of the NIR images. With higher resolution images, the edge filter may not be necessary. If this is so, then the input would simply be the locally normalized intensity image.

Segmenting the vessels and computing the medial axis skeleton: Given the fairly extensive steps taken to enhance the vessels, our segmentation approach is trivial: we simply mask the output of the Hessian vessel filter V_{max} with the parametric snake $f(s)$ representing the inner boundary of the arm, and apply a threshold at zero brightness. That is, for each pixel i, we define the binary segmentation by:

$$V_{seg}(i) = \begin{cases} 1, & V_{max}(i) \ f(s) > 0 \\ 0, & \text{else} \end{cases}$$

Finally, we compute the medial axis skeleton of V_{seg} using an optimized C++ implementation of an iterative thinning algorithm[137]. **Figure 2-18** shows representative images of the segmentation routine applied to forearm vessels of four patients with varying skin tones and body mass indices.

2.7.5. *Vessel motion tracking in NIR images*

Once the vessels are segmented and a target selected as the site of cannulation, the position of the vessel target must be tracked from one frame of the image sequence to the next. This is important as the robot brings the cannula near the target site to adjust to small motions of the patient's arm. Object tracking approaches may be generally categorized into feature-based approaches or optical flow-based approaches. Feature-based algorithms track a small number of salient features by finding the corresponding features in the following frame based on a similarity criterion. The features may represent single-pixel points in the image, a ROI, or a window. Typical feature-based tracking algorithms include multiple hypothesis tracking, mean shift tracking, Kalman filters, particle filters, and hidden Markov models. In contrast to feature-based algorithms, optical flow algorithms estimate a vector field that describes the change in image intensity or image gradient over time. Optical flow refers to the visible motion of an object in an image, and the apparent motion of pixels in an image resulting from 3D motion being projected onto a 2D image

plane. Numerous methods have been introduced to compute the 3D velocity from the image gradient, including the classic methods by Horn-Schunck[107] and Lucas-Kanade[105,138].

To compare the effectiveness of different strategies for vessel tracking, we implemented a correlation window-based tracker, several point-based feature trackers using different feature descriptors, a number of optical flow-based trackers, and an algorithm based on global shape contexts. We also implemented a Kalman filter that would allow position estimates from multiple trackers to be combined to produce a joint probability density estimate that is optimal in a maximum likelihood sense.

2.7.6. *Bayesian integration of segmentation, depth, and motion in NIR images*

In the previous sections, I described the various steps of 3D stereo correspondence, arm segmentation, vessel segmentation, and motion tracking as discrete steps. The inputs and outputs of each step are largely independent of the other steps. However, the desired world state (essentially the 6-DOF pose of a true vessel target) may be represented by a combination of the outputs of each of these steps. In this way, the outputs may be thought of as either independent or partially correlated opinions on the true state, with each opinion altering with some weighting factor the final opinion. The Bayesian framework provides a way to merge these different information sources by representing the opinions as prior probability densities influencing the posterior probability of the estimated true state. Here I will describe a general approach for coupling stereo, segmentation, and tracking results within a unified Bayesian model, which would be expected to represent the true state of the target vessel more accurately than a segregated "pipeline" approach. Currently, this Bayesian approach has not been implemented within the imaging system, as code optimization, e.g., by leveraging CUDA, would be essential to ensure real-time performance. Nevertheless, the concept represents an important direction for future work that will likely be a critical component of the final clinical system.

The particular method described here introduces the labeling information provided by the arm and vessel segmentation steps, as well as the motion vectors resulting from optical flow, as additional constraints in the computation of the stereo disparity function f. Specifically, these added constraints are incorporated in the prior term, which is passed around as messages from each node i to neighboring nodes j of the MRF during belief propagation (see Chapter 2.7.3). This approach was first proposed by Sun *et. al.*[133]. Others later extended the concept by implementing robust surface fitting using RANSAC as part of the initial segmentation, and then classifying each pixel as either occluded, stable, or unstable[139]. This particular approach takes the initial disparity function f (obtained from an initial pass of loopy belief propagation), the initial segmentation, the left image, and the pixel class memberships all as inputs into a second pass of loopy belief propagation. Neither of these previous studies incorporated motion information into the beliefs.

Expanding on the method of Sun *et. al.*, we can expand the basic stereo model to incorporate additional cues:

$$p(f) = \prod_i e^{-\phi(f_i)} \prod_{(i,j)} e^{-\psi(f_i, f_j)} e^{-\gamma(f_i, f_j)} e^{-\eta(f_i, f_j)} e^{-\varphi(f_i, f_j)}$$

And the energy function becomes:

$$E(f) = \sum_i \phi(f_i) + \sum_{(i,j)} \left(\psi(f_i, f_j) + \gamma(f_i, f_j) + \eta(f_i, f_j) + \varphi(f_i, f_j) \right)$$

Here, $\psi(f_i, f_j)$ is the disparity prior. The three added constraints $\gamma(f_i, f_j)$, $\eta(f_i, f_j)$, and $\varphi(f_i, f_j)$, are described below:

The first addition constraint, $\gamma(f_i, f_j)$, encourages disparity discontinuities to be aligned with segmentation borders based on the arm, vessel, and background class labels computed from the

arm segmentation and vessel segmentation steps (see Chapters 2.7.2 and 2.7.4). We define $\gamma(f_i, f_j)$ with a Potts model:

$$\gamma(f_i, f_j) = \begin{cases} 0 & \text{same segmentation label for } i \text{ and } j \\ s_\gamma & \text{different segmentation labels for } i \text{ and } j \end{cases}$$

More energy is needed to pass messages between neighboring nodes of the MRF when the messages must cross a segmentation border. The larger the value of s_γ, the greater this added cost; in other words, the influence from neighbors becomes smaller with increasing s_γ.

The second constraint, $\eta(f_i, f_j)$ is a truncated linear model that penalizes differences in the motion vectors $\omega(u, v)$ (see Section 2.7.5) between adjacent nodes i and j:

$$\eta(f_i, f_j) = \min(s_\eta \sum |\omega_i(u, v) - \omega_j(u, v)|, \eta_{max})$$

Here we introduce the intuition that piecewise smooth objects, for example the arm and the vessels, should demonstrate piecewise smooth optical flow. Note the similarity to the formulation of $\psi(f_i, f_j)$, as introduce by Felzenszwalb *et. al.* and described in Chapter 2.7.3. s_η is a scaling factor and η_{max} is the maximum cost.

The third constraint, $\varphi(f_i)$ penalizes the disparity value f_i according to the difference in the left and right motion vectors $\omega(u, v)$ at node i:

$$\xi(f_i) = \min\left(s_\xi \sum |\omega_{i,left} - \omega_{i,right}|, \xi_{max}\right)$$

This term asserts that in rectified stereo images, corresponding pixels should demonstrate corresponding motion. Note the similarity to the formulation of $\phi(f_i)$ in Chapter 2.7.3.

Together, these three constraints allow the segmentation and motion information to be applied toward inferring the disparity map. The constraints encourage the disparity discontinuities to be aligned with intensity and motion discontinuities.

Finally, it may be possible to efficiently incorporate a wrapping function that automatically tunes the parameters of the MRF from one frame of the image sequence to the next. For example, it has recently been shown that the parameters for MRF-based stereo algorithms may be estimated based on MAP inference by alternating between estimating the parameters based on an acquired disparity map and estimating the disparity map based on newly estimated parameters[140]. Their routine is designed to interface with the belief propagation solver, which was also the basis of our approach. By assuming independence between the disparity prior parameters, image parameters, and motion parameters, (which in our case would include the scaling factors (s_γ, s_η, and s_ξ) and thresholds (γ_{max}, η_{max}, and ξ_{max}) for Pott's and linear truncated models), alternating parameter optimization may then be performed based on the well-known Expectation-Maximization algorithm. Beyond optimizing the MRF parameters, it may also be possible to the above procedures to significantly reduce the disparity search space at each node of the MRF for each image frame beyond the first. Finally, it may be possible to incorporate the disparity map at each frame as prior terms in the segmentation and motion estimation steps.

2.7.7. *Vessel segmentation and tracking in B-mode US images*

The computational efficiency of motion tracking can be improved significantly by limiting the search space to the inside of the vessel lumen. This can be performed by segmenting the vessel from the background tissue. Many techniques exist for vessel segmentation and are discussed extensively in the literature. Generally, these can be classified into three groups, namely: (1) global optimization approaches based on Bayesian likelihood maximization or energy minimization; (2) region growing and merging techniques; and (3) snake and balloon methods, i.e., active contours.

It is also possible to combine these different categories of approaches within a single framework[112].

For segmentation of the vessel lumen from 10 MHz longitudinal B-mode US images, we implemented one segmentation approach from each category and compared their effectiveness on B-mode US video sequences acquired at 30 FPS, as described below.

Mean shift segmentation: As one method to segment the vessel lumen from the B-mode US image, we implemented the mean shift tracking algorithm available in OpenCV. Mean shift is an iterative, non-parametric feature-space analysis technique more generally applied to data clustering[141]. Mean shift works by modeling features as latent probability densities and iteratively attempts to identify the parameters of the probability densities, for example based on maximum likelihood criteria. If dense clusters are present in the feature space, then they correspond to local maxima of the probability density function. Given a kernel K, bandwidth parameter h, the kernel density estimator for a given set of d-dimensional points is:

$$f(x) = \frac{1}{nh^d} \sum_{i=1}^{n} K\left(\frac{x - x_i}{h}\right)$$

The weight of nearby points are determined for re-estimation of the mean. The weighted mean of the density in the window determined by K is:

$$m(x) = \frac{\sum_{x_i \in N(x)} K(x_i - x) x_i}{\sum_{x_i \in N(x)} K(x_i - x)}$$

where $N(x)$ is the neighborhood of x.

In the iterative step, the mean-shift algorithm sets $x \leftarrow m(x)$, and repeats the estimation via gradient descent until $m(x)$ converges. In the OpenCV implementation, the color histogram of the input image is used as the probability density function. Since the NIR images lack color

information, we instead used the grayscale image, the gradient magnitude image, and the Hessian image as the first, second, and third dimensions of the input three-channel image.

Region-grow segmentation: As a third method to segment the vessel lumen from the B-mode US image, a C++ implementation of the region growing segmentation algorithm[142–144] was employed in which the seed point is initialized based on the 3D location of the vessel center as estimated from the NIR images. However, using the standard region growing approach, we observed that in some circumstances the region boundary would expand far past the borders of the vessel. To minimize the likelihood of such errors, a modification to the region growing approach was made. Here, three shape properties - namely, the total area, eccentricity, and the convexity of the region - are calculated at each incremental step and represented as a 3x1 vector of scalar values between 0 and 1. Large changes in the direction or magnitude of the vector, which corresponds to sudden changes in shape, indicate that the region has likely expanded past the vessel boundaries. When this is detected, the iterative process is halted, and the boundary from the previous increment is used to compute the vessel centroid. Depending on whether the US transducer is oriented in the axial or longitudinal view, the shape properties will be different. However, because take into account only the change in shape from one incremental step to the next (and not the shape itself), the approach is equally suited to either transducer orientation.

Active contour segmentation: We also implemented the active contours segmentation approach with the GVF energy formulation[99,100], as described in Chapter 2.7.2 for arm segmentation. Here, we initialized the active contour in each frame of the video sequence using the result of the region grow segmentation. As in our previous implementations, the computation of the GVF was accelerated with a CUDA-optimized OpenCL implementation[101].

2.7.8. *Blood flow velocity estimation in B-mode US images*

The most common technique for blood flow detection is Doppler velocimetry, where the resulting color flow information is overlaid on the B-mode scan[145]. Typically, color flow imaging first detects the Doppler shifts of blood flow, and then makes a threshold decision on where to overlay the color pixels on the B-mode image. Since the threshold decision is imperfect, vessel wall overwrite may occur which can obscure important diagnostic information, while large tissue motions in the color flow overlay are displayed as artifacts that overshadow the true flow and anatomical data[145–147]. An additional limitation of Doppler imaging is the necessary trade-off between sensitivity and computational efficiency. By using large packets of longer transmit pulses and wall filtering, Doppler is able to visualize weak blood echoes. However, large packets limit the frame rate, and long transmit pulses degrade spatial resolution. Thus while Doppler imaging may be very sensitive to flow signals, its temporal and spatial resolution is limited. Finally, the measured Doppler frequency shift in a blood vessel varies inversely with the angle between the incident beam and blood vessel[148]. Thus, techniques that do not inherently depend on the Doppler angle may be particularly useful for visualizing blood vessels.

B-mode, by itself, may be useful for tracking the flow field, and a number of groups have focused on this area of research. There is much research into use of image analysis algorithms to improve the SNR and contrast of blood speckle in B-mode US images. The most common time-domain method for 2D speckle motion estimation consists of block-matching algorithms based on sum of absolute differences or normalized cross-correlation[149]. Block matching is efficient for detecting linear translations of tissues, but is known to be unreliable for more complex motions in which the displacement vectors vary significantly within the window, i.e., the gradient of the velocity field is large[150]. Methods that adjust the size, shape, or support weights of the window, depending on the correlation responses of neighboring speckle or on prior information about the velocity field[151–154], have been proposed but not implemented for blood flow tracking. An

alternative to block matching for blood speckle motion estimation is to apply techniques based on optical flow. Optical flow techniques have recently been used in tissue elastography, particularly to track myocardial motion[149]. Optical flow in US has been compared against correlation block matching and has been observed to reduce erroneous motion responses in complex, spatially or temporally invariant motions[150].

The accuracy of blood flow velocity estimation using B-mode alone is dependent on the frequency of the US signal. Previous work has demonstrated the feasibility of tracking speckle motions based on correlation windows using a 35 MHz probe[155]. Unfortunately, the cost of high frequency transducers US transducers has limited their clinical adoption. Meanwhile at lower frequencies, e.g., below 24 MHz, the contrast, resolution, and SNR of good features is much lower. As a result, the influence of speckle decorrelation is increased. Thus in order to attain reliable tracking at clinical frequencies, it becomes important to enhance the contrast of speckle and then to select reliable features.

We implemented a blood flow detection algorithm on B-mode scans using a feature extraction in conjunction with a differential motion estimation approach. To first detect the weak echoes from red blood cells, we enhance the speckle contrast using DOG. Speckle motion estimation is then computed using a pyramidal implementation of the Lucas-Kanade optical flow detector optimized for real-time CUDA processing. Spurious flow vectors are removed based on the identification of outliers in the motion probability distribution, and the parabolic flow profile is estimated from the remaining flow vectors. These steps are described in more detail below, and experimental results on test image sequences are shown.

Enhancing speckle contrast using DOG: As a prior step to feature extraction, speckle features in the vessel lumen are enhanced using the DOG filter. Given that red blood cells tend to aggregate into 50 to 100 μm long rouleaux, the scale constants σ_1 and σ_2 of the two Gaussian kernels

$G(\sigma_1)$ and $G(\sigma_2)$ can be estimated from the spatial resolution of the US image f. We found that maximizing the intensity differences between objects in the 3 to 5 pixel size range gave a resulting image function $g(\sigma_1, \sigma_2) = (G(\sigma_2) - G(\sigma_1)) * f$ such that the enhanced features could be tracked the most reliably given the feature extraction and motion tracking approach that we implemented (described below).

Speckle motion estimation based on optical flow: Optical flow in 2D images can be defined by

$$\vec{V} = \{U(x,y), V(x,y)\}$$

where U and V are the velocity vector components at the point (x, y) in the image. The optical flow algorithm assumes that if a point in the image changes by dx in the x direction, dy in the y direction, and dt in time, the brightness E of that point remains constant

$$E(x, y, t) = E(x + \delta x, y + \delta y, t + \delta t)$$

and leads to the brightness constraint:

$$E_x U + E_y V + E_t = 0$$

where E_x, E, and E_t are the partial derivatives of E with respect to x, y, and t. These partial derivatives can be estimated from adjacent pixels (in both space and time) from the image. The solution will not, however, determine the component of motion in the direction of constant brightness contours. An additional constraint is needed that assumes that the velocity field of the brightness patterns in the image varies smoothly almost everywhere. By minimizing the error in the departure from smoothness in velocity flow and the error in the rate of change of brightness, the velocity vector can be solved. The total error to be minimized can then be expressed as

$$E^2 = \int \int (\alpha^2 E_c^2 + E_b^2) dx dy$$

where α is a weighting parameter set equal to the noise in the estimate of $Ex + Ey$. The velocity vector can be solved with the minimization of E^2 and the estimated partial derivatives using iterative numerical methods. Once the velocity vector $V(x, y)$ is determined for each pixel (x, y), the direction and magnitude of the flow can be plotted at each pixel location.

Eliminating spurious vectors based on motion statistics: Spurious vectors are removed based on assumptions of flow velocity and direction. In the human superficial vein, blood flow velocity ranges from 12 to 100 cm/s (95% confidence interval), and thus vectors with magnitude velocities exceeding this range can be removed. Additionally, with an assumption of no backflow, vectors with velocity directions against the expected flow are removed. Finally, we assumed the remaining distribution of velocity vectors to form a normal distribution with respect to direction and magnitude. After determining the Gaussian parameters (m_{vec} and σ_{vec}) of the vector distribution, we eliminated all vectors following outside the 95% confidence interval of the distribution.

Computing the velocity field: Normal blood flow through a vessel follows a parabolic profile. In our study, the estimation of flow velocity is determined in two ways. First, individual velocity vectors are binned into 10 groups based on their vertical position in the image, where each bin represents a depth range of 5 mm. The mean velocity of each bin is then calculated. In the second method, the parabolic profile of flow is determined by applying a 2nd-order parabolic best-fit to the velocity distribution.

Experimental results on US test image sequences: **Figure 2-8** (provided in Chapter 2.4.3) shows the image enhancement steps applied to B-mode images acquired from left and right forearm superficial veins a healthy adult at 12 MHz using a mechanically-scanned single-element sector probe. In order to reduce the total computation time, a maximum of 1000 speckle features were tracked in each frame. The speed of the image analysis steps, namely mean-shift segmentation was compared when performed in Matlab and C++. In Matlab, the mean per-frame completion time

was 2.5 s (0.4 MHz), whereas in C++ mean completion time was 28.6 ms on the GPU. A Matlab GPU implementation was not evaluated. Using C++, the maximum analysis frame rate was 33 MHz, which is fast enough to keep up with the 30 MHz probe acquisition rate. Meanwhile, comparing flows before and after the removal of spurious vectors based on velocity magnitude and direction, we found that, on average, 12.3% of all flow vectors were determined to be spurious in the 12 MHz images. (In a separate study conducted using a 40 MHz US transducer, we found that the proportion of spurious flow vectors was reduced to 6.1%.)

Figure 2-9 shows estimated blood flow velocity fields from superficial forearm veins in eight healthy adults. Velocity fields were determined from the mean distance traveled per acquired frame. Mean velocities were calculated based on the axial position of each vector within the vessel. Position values were binned into one of 10 groups, each representing a 5 mm range of depth. A parabolic best-fit was also estimated over the distribution. The mean velocity at the vessel center was 21.4 cm s^{-1} across all of the human experiments, which is within the expected range for human blood flow in superficial veins[155,156].

2.7.9.   *Needle segmentation and tracking in B-mode US images*

Probabilistic estimation of needle shaft orientation and needle position: Inserting the needle into the center of the vein can be challenging if the depth of the vein is unknown to the clinician. Cannulating through the back of the vein wall can lead to complications like internal bleeding, whereas not reaching the vein, can result in extravasation of fluids. Hence, it is critical to know the true needle tip position as it traverses through the skin tissue *en route* to the center of the vein. As shown in **Figure 2-10 (a)** (provided in Chapter 2.4.3), the metallic needle typically appears as a salient line in the upper right-hand corner of the US image. Often, the needle is disconnected due to image artifacts. To extract the needle tip in the US image using the combined approach, the US image is first cropped to restrict the search area to where the needle should be based on the

kinematic output by the robot. In our system, the expected error by the robot was ±1.5 mm and ±2°. (for freehand US imaging, a more lenient search region would be needed, since the expected initial position of the needle in the US image would vary by a significantly greater amount). Based on this, a probabilistic map can be generated representing the prior distribution on the needle shaft orientation **Figure 2-10 (b)**. The log-Gabor directional wavelet filter is then applied to search for intensity gradients along the angle of insertion of the cannula (**Figure 2-10 (c)**). By filtering the image, extraneous lines that may result in false positives are eliminated, while lines that reside along the angle of insertion of the cannula are enhanced. Finally, to segment the needle, the probabilistic Hough transform is applied to search for the most prominent and continuous line segments in the image. If multiple lines are detected, as is commonly the case (**Figure 2-10 (d)**), the coordinates of each candidate line segment is weighted in the Hough parameter space by the probabilistic prior, and the MAP estimation is taken to represent the orientation of the needle shaft.

The needle tip position is determined separately because the bevel tip is not typically in line with the shaft. Candidate needle tip coordinates are extracted using a feature detector (in our case, the Shi-Tomasi feature detector) and weighted by a second probabilistic prior distribution to infer the true position based on MAP estimation (**Figure 2-10 (e)**). In this step, it would be straightforward to incorporate prior knowledge provided by the result of the probabilistic Hough transform as a prior into the needle tip extraction step, since the position offset of the needle tip is known given the needle gauge and the angle of the bevel. However, at present, the prior distribution is a function of only the robot's kinematic output. **Figure 2-10 (f)** shows the results of this method. The combined use of the probabilistic Hough transform line detector, log-Gabor directional wavelet filter, Shi-Tomasi needle tip detector, and pixel tracking based on pyramidal Lucas Kanade optical flow required a mean processing time of 40.4 ms, with the maximum time unlikely to exceed 52.9 ms. Meanwhile, error distances were still reasonably low: the insertion angle errors were <1° while needle tip extraction errors were <1 mm.

Comparison of different approaches to needle shaft detection, needle tip extraction, and motion tracking: The general approach described above may be adapted to using a wide range of line enhancement and detection techniques and feature extractors to localize the needle tip. To compare the accuracy and computation time of different feature detectors, we implemented a range of needle segmentation and tracking algorithms in Matlab, OpenCV, and LabVIEW. Some of the algorithms have been optimized for real-time GPU processing using the NVIDIA CUDA platform. Our goal was to identify an algorithmic approach that would result in a minimal error while maintaining a processing rate of 15 FPS. To acquire image data, B-mode longitudinal US images were acquired using an 18 MHz transducer during robotic cannulations on gelatin phantoms. For each trial, frame-by-frame image recordings were captured over a 10 second period at 15 FPS for a total of 200 acquired images per trial. For each set of images, we selected for analysis the frame corresponding to the time point at which the manipulator's needle insertion velocity returned to zero, indicating the completion of the cannulation, with the needle thought to be centered within the vessel. The needle orientation and needle tip positions in each of the selected US image frames were annotated manually, and served as the control for the study. Meanwhile, the needle orientation and needle tip positions predicted by the robot kinematics served as the ground-truth information. The needle segmentation and motion tracking algorithms were then applied to each of the images sequentially. Mean error distances were calculated (1) between the robot kinematic predictions and the needle tip positions computed by each algorithm, and (2) between the kinematic predictions and the manually annotated needle tip positions. The same approach was applied to the line segmentation algorithms to determine mean error distances in the estimated angular needle orientation. For the motion tracking algorithms, manual annotation was not performed; instead, the positions calculated by the tracking algorithms were compared only against the kinematic predictions.

Table 2-4 shows the mean error distances and completion times of a range of needle localization schemes. In total, we compared two methods for image enhancement (the directional log-Gabor filter and the Hessian line filter), three methods of line detection (the Hough transform, probabilistic Hough transform, and RANSAC algorithm), three methods of needle tip extraction (a rotationally invariant template matcher, the Harris corner detector, and the Shi-Tomasi corner detector), and three methods of motion tracking based on optical flow (a pyramidal implementation of the Lucas-Kanade algorithm[105], the Horn-Schunck method[107], and a variational calculus approach proposed by Brox *et. al.*[108]. The latter approach, uniquely, incorporates a coarse-to-fine warping scheme to efficiently perform the numerical optimizations needed to solve the Euler-Lagrange equations representing the flow functionals; the coarse-to-fine warping enables larger displacement steps and decreases the computational costs of the algorithm).

Shown in blue is the approach described above and in **Figure 2-10**. This method has been implemented in the NIR+US imaging system. We used the probabilistic Hough transform as the line detector because it was the most computationally efficient. However, we saw that RANSAC, in conjunction with the log-Gabor filter, resulted in the lowest positioning mean error and standard deviation. In these studies, we did not use a CUDA implementation of the RANSAC algorithm, which would have allowed the processing to be performed on the GPU. In future studies, we will compare a CUDA implementation of RANSAC to the CUDA implementation of the probabilistic Hough transform. We will also investigate the use of other robust parameter estimation algorithms such maximum likelihood estimation sample consensus (MLESAC), which has shown very strong potential for needle localization in US images. Similarly, we will compare other line detectors (the grayscale Hough transform, oriented diffusion filters, robust edge detectors, etc.), corner detectors (the Lucas-Kanade-Tomasi detector, Hessian-based detectors, DOG and LOG detectors, detectors based on level curves, etc.), and general descriptor-rich feature detectors (SIFT, SURF, SUSAN,

FAST, etc.). Other methods of frame-to-frame tracking, including alternatives to optical flow (for example, the mean-shift algorithm and the stochastic state observers) will also be explored.

Chapter 3 – Autonomous, image-guided robotic vessel cannulation

Parts of Chapter 3 were adapted from the publication listed below. All excerpts represent the original work of Alvin Chen, whose specific contributions as first author of the publication included: designing and conducting the described experimental studies; generating the presented data and corresponding figures; writing, editing, and revising the original text; and addressing reviewers' comments as corresponding author of the original manuscript submission.

A. Chen[†], M. Balter[†], T. Maguire, M. Yarmush. Real-time needle steering in response to rolling veins in a 9-DOF image-guided venipuncture robot. *IEEE Proceedings of the International Conference of Intelligent Robots and Systems* 2633–2638 (2015). [†]*Equal first author contribution.*

Parts of Chapter 3 were also adapted from the following publications. All excerpts represent the original work of Alvin Chen, whose specific contributions to the excerpted sections included: designing and conducting the described experimental studies; generating the presented data and corresponding figures; and writing, editing, and revising the original text.

M. Balter[†], **A. Chen**[†], T. Maguire, M. Yarmush. Adaptive kinematic control of an automated robotic venipuncture device based on stereo vision, ultrasound, and force guidance. *IEEE Transactions on Industrial Electronics* (*in press*). [†]*Equal first author contribution.*

M. Balter, **A. Chen**, T. Maguire, M. Yarmush. The system design and evaluation of a 7-DOF image-guided venipuncture robot. *IEEE Transactions on Robotics* 31, 1044–1053 (2015).

3.1. Overview

Medical robots have played a key role over the past decade in assisting practitioners to perform a wide range of interventions. These systems are primarily used to manipulate medical instruments, most commonly needles or sutures, within the operating workspace of the procedure. In many cases, the system's performance depends heavily on its ability to obtain accurate information about the spatial positioning of the instruments and the target. This positioning information may then be used as feedback in the robot's motion control scheme. To augment the needle insertion process, imaging modalities such as those described in Chapter 2 may be utilized before the procedure to plan the path of the needle or during the procedure to servo the needle in real-time.

In Chapter 3, I describe the development and evaluation of three robotic prototypes designed to perform real-time needle steering and vessel cannulation under image-guidance[58–61]. The earliest prototype comprised four DOF and uses only NIR imaging to perform basic positioning and insertion tasks. The accuracy of the system is evaluated on a commercial phlebotomy training arm. The second prototype comprised seven DOF, including a 3-DOF Cartesian positioning system and a 4-DOF articulated manipulator. The articulated design of the manipulator allows the needle to be advanced along a non-linear path that is in closer agreement with clinical best practices than standard linear insertion. A method to automate the attachment, release, and disposal of the needle is described. The results of workspace positioning studies and cannulation trials in gelatin phantoms are then reported. The second US prototype incorporates the bimodal 3D NIR+US imaging system described in Chapter 2, thereby allowing subpixel-resolution, depth-resolved images of the vessel lumen at depths below 3 mm. Finally, the most recent prototype comprises nine DOF to enable the automatic alignment of the end-effector with the 6-DOF pose of a target vessel over a large workspace of possible orientations. The system also incorporates a force-sensitive needle insertion mechanism that may be used for blood sample collection or for peripheral catheter placement. Image-guided control of the robotic using 3D NIR stereo vision, US, and force sensing is demonstrated experimentally. Finally, I discuss the implications of this work on the clinical translation and usability of the system. I then suggest methods to improve the speed, adaptability, and overall intelligence of the robot based on recent advancements in machine learning and dynamic control. Ongoing work to further miniaturize the system is also discussed.

3.2. Background and previous work

3.2.1. *Mechanical properties of human skin and vessels:*

Recent studies from the literature on the mechanical properties of the human skin layers, blood vessels, and blood are summarized in **Table 3-1** and described below.

Epidermis: The epidermis is the outermost skin layer and functions as a thin protective barrier $(\delta_{\text{epidermis}} \sim 0.1 \text{ mm})$[157]. Studies measuring the mechanical properties of the epidermis under uniaxial[158,159] and shear strains[160,161] have shown the epidermis tissue structure to be highly anisotropic, with $E_{\text{epidermis}}$ and $G_{\text{epidermis}}$ on the order of 1 MPa and 10 kPa, respectively $(E_{\text{dermis}}/G_{\text{dermis}} \sim 10^2)$.

Dermis: The dermis is the dense, vascularized connective tissue layer beneath the epidermis and comprises a network of collagen and elastin fibers anchoring a polysaccharide ground substance. Compared to the epidermis, forearm dermis is thicker $(\delta_{\text{dermis}} \sim 1.3 \text{ mm})$[162–167] and less mechanically stiff $(E_{\text{dermis}} \sim 50 \text{ kPa}, G_{\text{dermis}} \sim 5 \text{ kPa})$[160–162,168–170]. The tissue structure of the dermis is considerably more isotropic compared to the epidermis $(E_{\text{dermis}}/G_{\text{dermis}} \sim 10)$. At low strains $(\varepsilon < 0.1)$, the mechanical behavior of the dermis is governed predominantly by elastin fibers and follows a linearly elastic pattern. In contrast, the mechanical properties of collagen govern the behavior of dermis at higher strains, resulting a rapid nonlinear increase in stress for $\varepsilon > 0.3$.

Hypodermis: The hypodermis is the lowermost skin layer and consists predominantly of adipose. Thickness $\delta_{\text{hypodermis}}$ varies with the anatomical site, can range anywhere between 1 and 5 mm[163,171,172], and has been shown to correlate with body mass index. The hypodermis has the lowest Young's modulus and is the most isotropic of the skin layers ($E_{\text{hypodermis}} \sim G_{\text{hypodermis}} \sim 1 \text{ kPa}$), exhibiting nearly perfect symmetry in its tensile and compressive response[173–175]. Elasticity of the tissue is highly nonlinear for $\varepsilon > 0.1$ and changes rapidly with $\dot{\varepsilon}$ [176,177].

Adipose tissue, which makes up over 90% of the hypodermis, exhibits a non-linear response at high strains $(\varepsilon > 0.3)$[173,178]. Furthermore, adipose has a large dependency on strain rate; at low strain rates $(\varepsilon' < 1 \text{ s}^{-1})$, E is on the order of 10^0 to 10^1 kPa, whereas for $\varepsilon' > 1 \text{ s}^{-1}$, E increases rapidly

beyond 10^3 kPa[176,178]. This nonlinearity is seen to a much greater extent in the hypodermis than in the upper skin layers, and greatly affects the behavior of the hypodermis in response to external forces such as those created by a penetrating needle.

Blood vessels: Traversing the dermis and hypodermis are peripheral vessels, which have diameters d_{vessel} ranging from 1.2 to 3.2 mm (average $\sim$ 2 mm)[179,180]. The thickness δ_{vessel} is ~ 0.4 mm, with artery walls being $\sim$0.5 mm thicker than vein walls[180,181]. The constituent materials in the vessel wall are collagen, elastin, and vascular smooth muscle. Like the dermis, elastin governs the vessel mechanical behavior at low strains while collagen dominates at higher strains $(\varepsilon > 0.4)$[182]. Elastin, which may be readily extended to 250% of its original length, dominates vessel mechanical behaviors at low stresses and strains. In contrast, at higher deformations, the mechanical properties of collagen dominate, and vessels become much stiffer. Arteries contain more elastin than collagen (2:1 ratio in major arteries), resulting in greater compliance $(E_{\text{artery}} \sim 0.3 \; to \; 0.5 \; \text{MPa})$, whereas veins have a lower fraction of elastin than collagen (1:3 ratio), resulting in stiffer walls $(E_{\text{vein}} \sim 1 \; to \; 1.5 \; \text{MPa})$[183–186].

Table 3-1. Summary of the mechanical properties of human skin and vessel tissue layers.

Tissue Layer	Values used for phantom designs (see Chapter 4.2)	Value(s) from Literature	Body Location (Measurement Technique)	Ref.
Tissue thickness, δ (mm)				
Epidermis	~0.1	0.75 ± 0.16 0.95 ± 0.05 1.38 ± 12.7	forearm forearm forearm	[157] [159] [168]
Dermis	1.3	0.92 ± 0.12 1.14 ± 0.20 1.16 ± 0.16 1.35 ± 0.10	forearm forearm forearm forearm	[162] [167] [164] [166]
Hypodermis	1 to 5 *(varied by design)*	1.21 ± 0.32 2.15 ± 0.64 2.49 ± 0.64	forearm forearm forearm	[164] [171] [187]
Vessel wall	$1.2–3.2$ (d_v) $0.3–0.5$ (δ_v) *(varied by design)*	2.1 ± 1.1 (d_{vein}) 3.0 ± 0.8 (d_{artery}) 0.31 ± 0.07 (δ_{vein}) 0.40 ± 0.08 (δ_{artery})	forearm	[181]
Elastic modulus, E (kPa)				
Epidermis	$2 \cdot 10^3$	$1–2 \cdot 10^3$	abdomen (indentation)	[159]
Dermis	50	35 56 ~50 $(\varepsilon < 0.1)$	forearm (indentation) forearm (suction) buttock, porcine (compression)	[169] [168] [176]
Hypodermis	2	2 1.6 $(\varepsilon < 0.1)$ 1–2.5 $(\varepsilon < 0.1)$	forearm (indentation) abdomen (tensile) abdomen, porcine (compression)	[169] [171] [164]
Vessel wall	$4 \cdot 10^3$ (vein) $12 \cdot 10^3$ (artery)	$0.4 \cdot 10^3$ (vein, $\varepsilon < 0.4$) $1.2 \cdot 10^3$ (artery, $\varepsilon < 0.4$)	porcine (tensile)	[181]
Shear modulus, G (kPa)				
Epidermis	not assessed	~10	abdomen (rheometry)	[160]
Dermis	5	~2	forearm (rheometry)	[174]
Hypodermis	1	~1	abdomen, porcine (rheometry)	[174]
Vessel wall	not assessed	~75	aorta, porcine (torsion test)	[188]

3.2.2. Limitations of current methods of robotic venous access

Robotic systems that automate needle insertion and catheter guidance procedures have been the focus of many research groups[54–56], and some systems have recently achieved regulatory approval in the U.S. and the European Union[52,53]. Nevertheless, while robotic devices have been shown to improve the accuracy, treatment time, and outcome of various surgical operations32,33, the majority of research in needle insertion robotics has, to date, focused on complex surgical procedures. Fortunately, the continued miniaturization of imaging technologies, coupled with the rapid improvement in the computing power of embedded hardware and the advancement of image-guidance techniques, has made it possible to develop portable, miniaturized, or even microscale robotic platforms[47,189–191]. Such platforms may be particularly suited for utilization in more routine interventions that occur outside of the operating room. As a result of these technological advancements, image-guided robotic systems developed for peripheral vascular access have received increased attention over the past few years. The most relevant research in the area of robotic vessel cannulation is summarized below.

Zivanovic *et. al.* first described a robotic mechanism designed to take blood samples from the arm[192]. To locate a vein, a force sensor was pressed against the surface of the forearm in multiple locations, and force/position profiles were analyzed to identify the presence of a vein. Force sensing was also utilized during the needle insertion to prevent overshoot of the needle. The success rate for locating a vein was 78% on a single human subject; cannulation accuracy has not been assessed.

Sørensen *et. al.* developed a robotic system for tactile vessel sensing based on the use of a voice-coil linear actuator as the end-effector of a 6-DOF KUKA industrial robotic arm[193]. The voice-coil actuator was used to measure the elasticity of tissue below the skin surface. The success rate for identifying a blood vessel below the skin with this method was 40% in a study on 50 adults. Their group has also investigated several methods for processing NIR video images on GPUs to

enhance venous structure, including correlation-based 2D matched filtering. However, the work has not yet culminated in an integrated prototype amenable for needle insertion.

Boer *et. al.* developed a benchtop system for robotic venous access using US guidance[194]. The US probe was swept across the surface of the hand to identify veins, and the needle was aligned mechanically with a targeted vein. A uniaxial force sensor was used to detect the reaction force from the vessel to prevent overshoot, and an algorithm was developed to halt needle advancement upon detecting a puncture event based on forces. Needle insertion experiments were performed on phantom and porcine tissues to evaluate the force detection algorithm and to assess the effects of insertion speed and insertion angle on tissue deformation. However, the accuracy of the system was not evaluated, and methods to automate the motion of the robot have not yet been developed.

Carvalho *et. al.* described a benchtop system using a monocular NIR camera to scan for peripheral veins and a uniaxial force sensor coupled to the insertion mechanism to detect depth[195]. Veins were modeled as straight lines in the NIR image and segmented using a Hough transform line detector in conjunction with image post-processing. The accuracy of the image analysis approach has not yet been evaluated. Likewise, the mechanical system has not yet been evaluated in any experimental studies.

Brewer *et. al.* developed a sophisticated, industrial-sized, two-arm dexterous robot with 17 total DOF using NIR imaging to guide the needle insertion[196,197]. The system was designed to perform blood sampling and intravenous catheter placement in the dorsal veins of the hand. An algorithm was developed to localize vein bifurcations and estimate pose, though performance was not shown to be better than manual vessel detection. A phantom with realistic vessel geometries was used to obtain proof-of-concept for the robot, though the cannulation performance has not been evaluated, particularly in comparison to manual cannulation. Integration of the imaging and robotic components has not yet been demonstrated.

Finally, a medical device startup company, Veebot, has been working to develop an industrial-sized robotic arm that uses monocular NIR imaging and laser range-finding to localize peripheral forearm vessels[198]. US imaging is then used to confirm blood flow. The system incorporates an EPSON arm to provide 6-DOF positioning of the needle. The imaging approach was found to identify suitable vessels in 83% experimental trials, though the accuracy of the image analysis methods were not evaluated. Similarly, no measure of success has been provided for needle insertion, and the work has yet to be published in a peer-reviewed journal.

3.3. Rationale and approach

Our goal was to design a device that was capable of supervised, autonomous, image-guided cannula insertion into peripheral veins and arteries in the forearm and hand. Furthermore, the device was to be developed for use in hospitals, diagnostic labs, and other clinical environments. Ultimately, the system would have to be manufactured at scale with an acceptable price point. To further guide the design of the device, we observed blood draw and intravenous catheter insertions at a number of hospitals and diagnostic blood testing facilities in the U.S. (see **Appendix**). Based on these studies, a number of design constraints were established:

i. Device should be portable; the system should be designed for table tops, mobile crash carts, and bedside procedures.

ii. Device must have sufficient mechanical dexterity to align the needle along the expected 6-DOF orientation of all common vessels in the forearm and hand.

iii. Device must demonstrate sufficient imaging resolution and robotic precision to cannulate 1 mm diameter vessels at least 3 mm in depth beneath the skin surface.

iv. Device must be able to make adjustment to patient arm movement and vessel motion.

v. Device should be able to withdraw a blood sample or deliver an intravenous fluid immediately following cannula insertion and/or catheter placement.

vi. The venipuncture procedure, including vessel imaging and cannula insertion but not the blood collection or fluid infusion, must not exceed 120 seconds (the maximum time for tourniquet application) and should ideally be less than 60 seconds (the recommended time for tourniquet application).

vii. The materials cost for the device should ideally be below $25,000 USD (current NIR and US imaging devices are priced in the range of $10,000 to $30,000 USD).

The design, development, and evaluation of the three robotic prototypes are described in the following sections. Differences in the design of each system are highlighted with respect to the design criteria and clinical workflow summarized here.

3.4. First-generation 4-DOF robot using 3D NIR guidance

3.4.1. Methods

3.4.1.1. Device workflow and architecture

The envisioned workflow for using the device is as follows. Before the procedure, the patient places his or her arm in a padded, inflatable arm cuff sleeve. The needle is automatically loaded into the device without requiring manual intervention. The device then scans the arm to identify forearm veins. After a vein is selected by the clinician, the device maneuvers the US probe over to the cannulation site to confirm blood flow. The device then positions the needle along the direction of the vein, inserts the needle tip into the center of the vein, and draws blood into standard collection vials. In the insertion process, the needle begins at a steeper angle (30º) until the tip punctures the vessel wall. The insertion angle is then gradually reduced to 15º as the needle is inserted further within the vessel lumen. Catheter advancement is likewise performed at the shallower angle. After the procedure, the used needle is automatically disposed in a sharps container within the device.

The cuff sleeve can be tightened to secure the arm, includes a strap at the proximal end that serves as a tourniquet, and can be easily disinfected between use.

Not all elements of the workflow were implemented in the first-generation device. In particular, the first-generation system relies only on NIR stereo imaging and does not incorporate US imaging. Thus the 3D vessel position information is used directly to guide the needle insertion rather than to position the US transducer. Likewise, not all aspects of the image analysis framework described in Chapter 2 were implemented in the first-generation system. Here, the focus was on robust and real-time vessel segmentation and dense stereo correspondence; some of the other algorithmic approaches, including arm segmentation, sparse vessel stereo registration, and 6-DOF vessel pose estimation, are introduced in subsequent systems. The first-generation system is not capable of placing a catheter and instead is designed only for inserting steel needles for blood collection. Finally, the automated needle handling capabilities have not been built into the system; this functionality will be introduced in the second-generation device.

Device design and control software: The 4-DOF robot was designed for early preclinical evaluation on *in vitro* models containing straight vessels. The system comprises several major components, shown in **Figure 3-1**. These are: (1) an NIR imaging system for vessel detection, (2) image analysis software for vein enhancement and segmentation; (3) 3D vessel reconstruction software based on stereovision; (4) a vessel selection algorithm; (5) robotic motion control system; and (6) a 4-DOF robot manipulator that positions the needle. The robot couples a 2-DOF (x, y) Cartesian gantry system that translates the NIR cameras and the needle insertion mechanism. The needle insertion mechanism itself supports two DOF. The host processor for the robot is a Dell Precision M6400 workstation laptop.
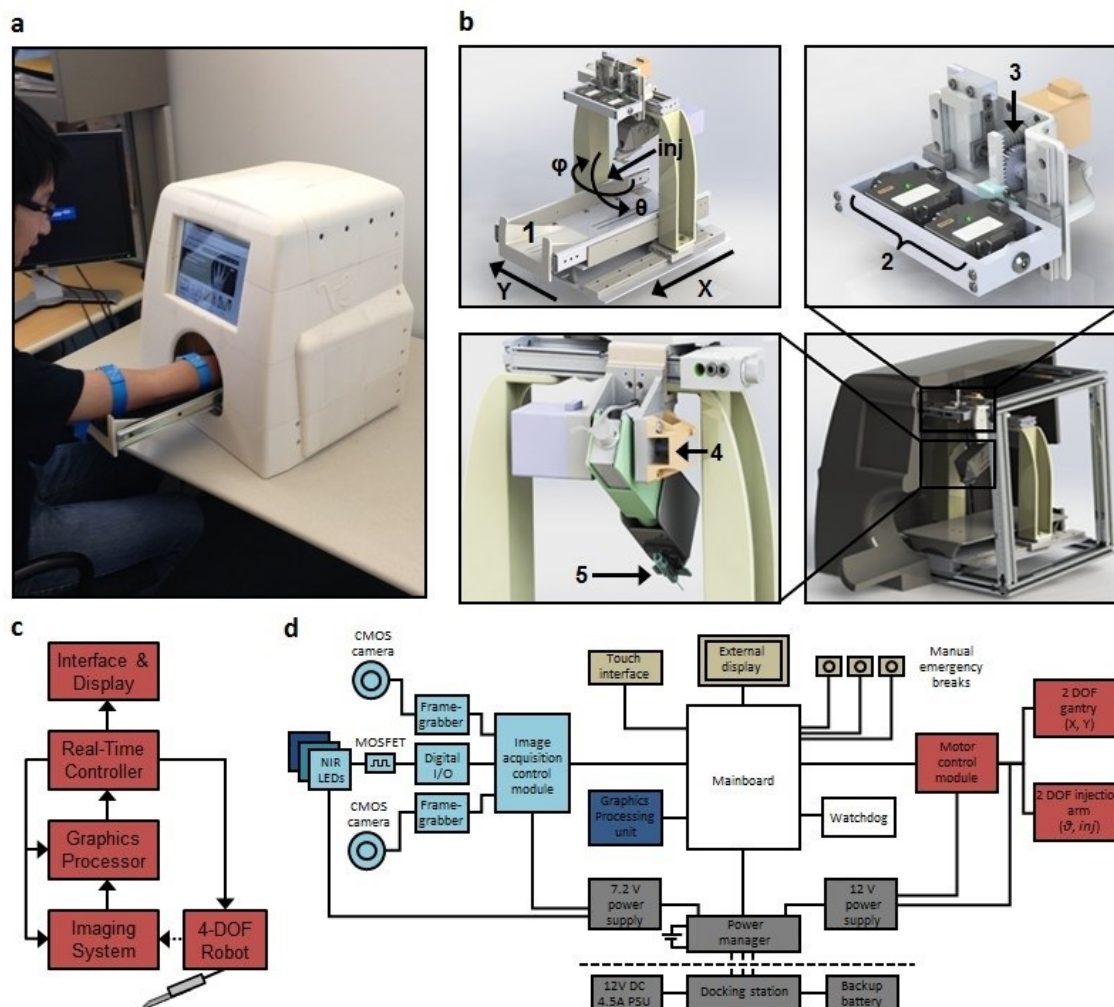
Figure 3-1. Design of first-generation 4-DOF automated venipuncture device. **(a)** Functional prototype. The device measures 18 in^3, weighs 13 kg, and features a detachable unit for sterilization, a removable blood tube holder, spring-loaded safety needles, a touchscreen interface, and a rechargeable battery. **(b)** Major functional components. Top left: 4-DOF mechanism (x, y, θ, and inj). A fifth DOF (φ) is was not used in the cannulation studies performed to evaluate system accuracy but will be critical in future studies on non-parallel and curve vessels. Top right: imaging system; Bottom left: injection arm; Bottom right: full assembly. *Labels:* (i) patient arm constraint; (ii) stereo cameras; (iii) motorized camera positioning and calibration; (iv) motor encoder feedback; (v) needle with automated detachment. **(c)** Device data flow. Image information is passed to a graphics processing unit for analysis and then to the control system that guides the robot. User input/output is provided through a touchscreen interface. **(d)** Hardware architecture grouped by function. The mainboard (white) directs communication between the stereo imaging system (light blue), GPU (dark blue), motors and controllers (red), power system (gray), and interface (tan).
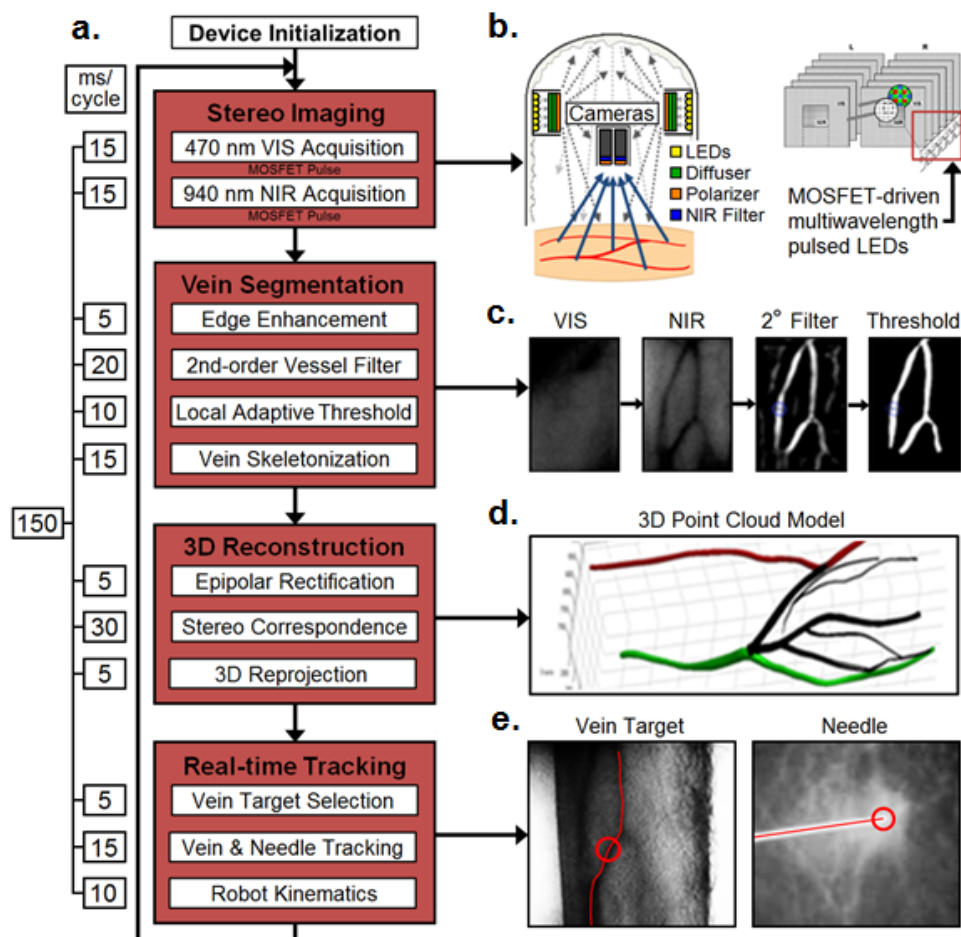
Figure 3-2. Real-time vision-based robot guidance. **(a)** The real-time control system operates at ~150 ms. Shown also are the computation times for individual processing steps in each cycle. **(b)** Multispectral stereo image acquisition under VIS and NIR light. **(c)** Image processing and vein segmentation steps. **(d)** 3D reconstruction of subcutaneous forearm veins. **(e)** Selection of a vessel target via the GUI, and segmentation of the needle and needle tip in the NIR image prior to skin puncture (once the needle is within the skin tissue, the needle tip is no longer visible in the NIR images).

The overall control software is written in LabVIEW and directs communication between the imaging, analysis, and robotic components. Image acquisition is performed on the National Instruments CompactRIO-9025 real-time controller with precise clock-control and runtime determinism. Connected to each of two CompactRIO-compatible frame grabbers (MoviMed AF-1501) is low light CCD snake camera (PC229HRXP, SuperCircuits Inc.) with extended sensitivity in the NIR range (1/3" Sony Ex-View sensors). The cameras are placed 16 cm above the arm and

installed with wide-angle (100°) lenses to allow an FOV from the wrist to the elbow. Images are captured at 60 Hz and transmitted to the GPU for processing. Graphical processing is executed on an NVIDIA Quadro FX 3700M GPU. Machine vision software is implemented using OpenCV. A watchdog software protocol is used to activate fail-safe circuitry and force all control outputs to safe states when a fault is detected. The watchdog is also used to regulate the activity and electrical state of the system. The watchdog software is implemented on an embedded FPGA to ensure real-time deterministic monitoring. The GUI guides the clinician through the process and allows the clinician to select the cannulation site.

3.4.1.2.   *Robot mechanical design*

The prototype measures 25.8 x 20.2 x 22.5 cm and weighs 13 kg. The system contains a 2-DOF gantry system and a 2-DOF needle insertion mechanism. The gantry comprises two linear ball-screw stages (Zaber T-LSM 100/200) giving X and Y translation. The 10.3 cm needle insertion mechanism contains a stepper motor (Zaber T-NM17A04) to control the needle insertion angle and a linear actuator (Zaber T-NA08-25) to drive the insertion. The linear stages have a peak velocity of 7 mm/s and step size of 0.0476 μm, and the steppers provide a maximum torque of 30.7 N-cm and angular step size of 0.0191°. Both the needle insertion mechanism and the cameras are mounted such that the needle is always within the FOV. A separate *z*-stage is used to calibrate the cameras. A fifth DOF (φ) is not currently used but will be critical in future studies on non-parallel and curve vessels. The workspace is 20 x 15 cm, which is sufficient to scan the length of the forearm and elbow. The step precision of the linear actuators is 0.05 μm and the step precision of the rotational actuators is 0.3°, which is sufficient given the camera spatial resolution (0.1 mm) and the desired injection precision (0.25 mm).

3.4.1.3.   *Robot motion control*

The robotic guidance approach is shown in **Figure 3-2**. At a rate of 15 FPS per camera, NIR images are sent to a programmable logic controller (National Instruments CompactRIO 9025) for analysis. Two cameras placed 11 mm apart form a stereo configuration. Continuous image segmentation, stereo correspondence, and motion tracking routines, as described in Chapter 2, were implemented to allow the 3D position coordinates of the vessel to be computed and updated in real-time. The position coordinates are then translated to motor displacement commands to allow continuous robotic position adjustment.

The overall motion control process consists of two phases: moving to the cannulation site, and tracking the site as the needle descends. The first phase involves one cycle through the acquisition process and ends with an interactive dialogue box asking the user for his agreement with the cannulation site that the program has chosen. The user may disagree and manually choose an alternative site via point-and-click selection, or he may agree. Agreement brings the system into the real-time tracking phase, which involves a single large translation to transport the needle to the cannulation site, followed by subsequent millimeter or micrometer dynamic movements to track small vein displacements that may occur as the needle rotates downward and then inserts into skin. The duration for one cycle from acquisition to motion is 0.2 s (5 s^{-1} cycle rate).

Needle steering is modulated by comparing the responses of an open-loop controller and a closed-loop controller. The open-loop controller measures the stepper motor response to calculate needle pose directly. The closed-loop controller determines the needle pose by relating the coordinate frames of the calibrated cameras to the target frame (the vessel orientation), end-effector frame (the needle orientation), and robot base frame:

$$R(\theta, \phi) = \begin{bmatrix} \cos\theta & \sin\varphi\sin\theta & \cos\varphi\sin\theta \\ \cos\varphi & 0 & -\sin\ \varphi \\ -\sin\theta & \sin\varphi\cos\theta & \cos\varphi\cos\theta \end{bmatrix}$$

$$T = [T_x \quad T_y \quad T_z]^{\mathrm{T}}$$

$$J(x, y, z, \theta, \varphi) = \begin{bmatrix} R(\theta, \varphi) & T \\ [0 \quad 0 \quad 0] & 1 \end{bmatrix}$$

The pose of the vein governs the needle trajectory **(Figure 3-3)**: vein orientation (θ_v, φ_v) is first calculated from the 3D reconstruction, after which the needle trajectory is computed along the vessel axes (x_v, y_v, z_v) at an incident angle θ_{n-v}^f. At each cycle of the real-time loop, the needle pose computed by the closed-loop controller is compared to the open-loop response. Agreement to within 0.2 mm is considered acceptable, otherwise the action is flagged and the pose is reevaluated. A continuous flag period of t > 1 sec results in termination and a request by the device for recalibration. The mean cycle rate is ~10 Hz, depending primarily on the amount of translation at each cycle.
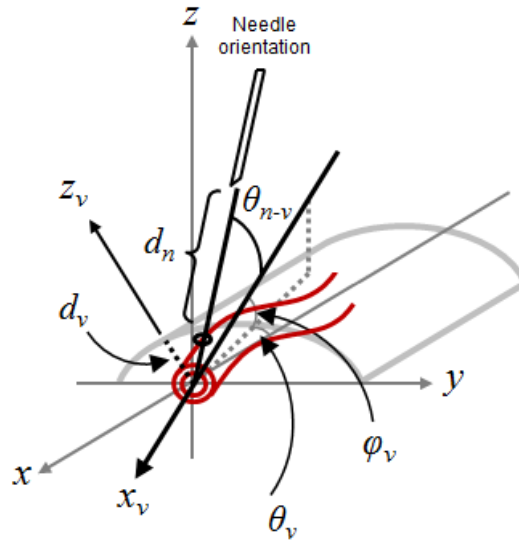
Figure 3-3. Needle pose determined based on vessel position and orientation in 6-DOF space. The angular vessel orientation $(\boldsymbol{\theta_v}, \boldsymbol{\varphi_v})$ is first calculated based on normal vector about the 3D vessel position (x_v, y_v, z_v), which is estimated from the surface map of the forearm. The needle trajectory is then determined based on a desired starting angle $\boldsymbol{\theta_{n-v}^0}$ (most commonly, 30°) and a desired final incident angle $\boldsymbol{\theta_{n-v}^f}$ (most commonly, 15°). Needle rotation $\boldsymbol{R} = (\boldsymbol{\theta_v}, \boldsymbol{\varphi_v})$ and translation $\boldsymbol{T} = (\boldsymbol{T_x}, \boldsymbol{T_y}, \boldsymbol{T_z})$ are determined by comparing the current needle orientation to the desired final orientation.

Device safety: Safety mechanisms are distributed across the device's sensor, effector, computer, and operator components. Electronic safety is monitored by a watchdog that activates fail-safe circuitry when a fault is detected.   Mechanical safety is provided by ensuring that all DOF are locked when electrical torque is removed, in order to inhibit "free" robot motion. A detachable spring-locked needle is used which can be quickly disengaged from the robot. Finally, the GUI is designed to allow the clinician to operate the device with minimal training.

Blood collection: Standard collection vials are loaded onto a housing unit prior to the phlebotomy. After the blood draw, the vials can be unloaded for analysis or storage, while the housing unit can be removed for sterilization.

3.4.2.   Results

3.4.2.1.   Cannula insertion accuracy on phlebotomy training model

We evaluated device accuracy and speed on a dark-skinned phlebotomy training model (NASCO LF01126U-Black). The model is well-known in the field of phlebotomy training and is classified as an "advanced" training arm. The model provides venous access for intravenous therapy and phlebotomy at all primary and secondary locations, including the ACF, forearm, wrist, and hand. The model comes with a skin layer with dark pigmentation, as well as an external fluid bag supplying artificial blood to the veins. Veins are positioned at varying diameters and depths beneath the skin surface to simulate different age groups and levels of difficulty. As in the imaging studies, we employed orthogonal experimental design (**Figure 3-4**)[113,114] to systematically determine the device settings that maximize cannulation accuracy. In 270 trials, the device was able to successfully cannulate the center of the target vein on the first try 100% of the time. On average, the mean distance of the needle tip from the vein center was 0.43 ± 0.21 mm. Mean distance was observed to change with different needle bevel orientations over all three vein diameters (**Figure 3-5 (a)**). Mean distance was observed to decrease as vein diameter decreased, possibly indicating

that small veins are more likely to roll upon contact (**Figure 3-5 (b)**). Neither the angle nor speed of insertion was observed to significantly affect accuracy on the model. Needle diameter did not affect accuracy either, though veins smaller than 2.4 mm would necessitate higher gauge (lower diameter) needles. No needle deflection was observed in the study. The mean completion time per trial was 28.4 seconds (**Figure 3-5 (c)**). Time to completion did not vary significantly due to any of the test conditions. Individual time durations for the major steps in each cycle of the real-time process are shown in **Figure 3-5 (d)**.

Summary of statistical approach: Like the methodology used to optimize the device's imaging parameters, the device cannulation was assessed using a Taguchi experimental approach (**Figure 3-4**). A 4-variable 3-level L9 orthogonal array of device parameters was used in the study. Veins with outer diameters of 2.4, 3.2, and 4.0 mm were tested at a depth of 3 mm from the skin surface. 10 replicates were conducted per trial, and the run order was again randomized. The four control parameters were: needle orientation, in which the bevel tip faced upward, sideways, or downward; needle diameters of 0.91, 0.64, and 0.36 mm; injection angles of 15°, 30°, and 45°; and injection velocities of 10, 20, and 30 mm/s. Cannulation accuracy was measured by the distance (d) of the needle tip from the vein's central axis (the greater the distance, the lower the accuracy). Distances were then used to derive the robustness measure, namely the Taguchi SNR = $-10 \log (\bar{d}^{\,2} / \sigma^{\,2})$. One-way ANOVA was used to assess whether vein diameter or any the control parameters had a significant effect on device performance. Post-hoc analysis using F-LSD was conducted following the ANOVA to identify the experimental levels between which the performance difference was significant. Of the control parameters, only the orientation of the needle bevel was found to significantly affect d and SNR (two-tailed p-value < 0.05 (*))**.** Of all the parameters tested, vein diameter had the most significant effect on d and SNR (two-tailed p-value < 0.05 (*), 0.01 (**)). Time to completion was also measured in the study, but was not found to vary significantly due to any of the test conditions (one-way ANOVA, $p < 0.05$, data not shown).

a.

Inner array (device settings)	Units	1	2	3
Needle diameter	mm	0.9081	0.6414	0.362
Needle bevel orientation	degrees	upward	downward	no bevel
Injection angle	degrees	15	30	45
Injection velocity	mm/sec	20	40	60

Outer array (test parameters)	Units	1	2	3
Vein diameter	mm	2.4	3.2	4.0

					1	2	3
				Vein diameter	−	o	+
Inner Array (L9)	Needle bevel	Needle diameter	Injection angle	Injection velocity			
1	−	−	−	−			
2	−	o	o	o			
3	−	+	+	+		*4 device parameter (9 runs)*		
4	o	−	o	+		*1 demographic parameters (3 runs)*		
5	o	o	+	−		*10 replicates*		
6	o	+	−	o		*270 total trials*		
7	+	−	+	o				
8	+	o	−	+				
9	+	+	o	−				

b.
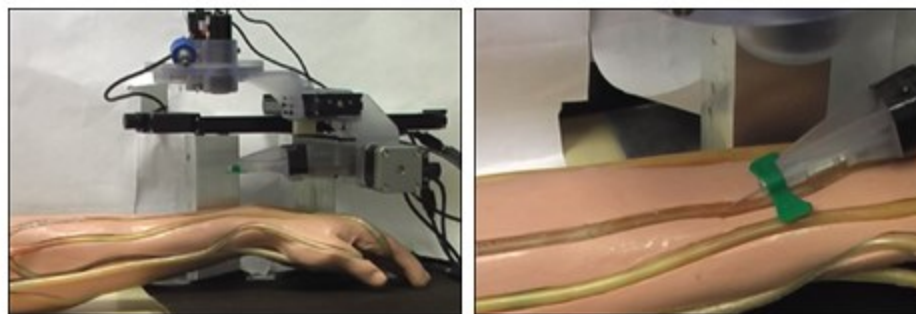
Figure 3-4. Optimization of device cannulation parameters. **(a)** Taguchi experimental design comprising a 4-variable 3-level L9 orthogonal array of device parameters. In total, 270 trials were carried out on a phlebotomy training model with 3 different vessel diameters. Cannulation accuracy was defined as the distance (d) of the needle tip from the vein's central axis. The statistical outcome score was defined by the nominal Taguchi SNR $= -10 \log (\bar{d}^2 / \sigma^2)$, where σ is the standard deviation in the set. **(b)** 4-DOF robotic prototype performing autonomous cannulation on phlebotomy training arm (skin removed for visualization).
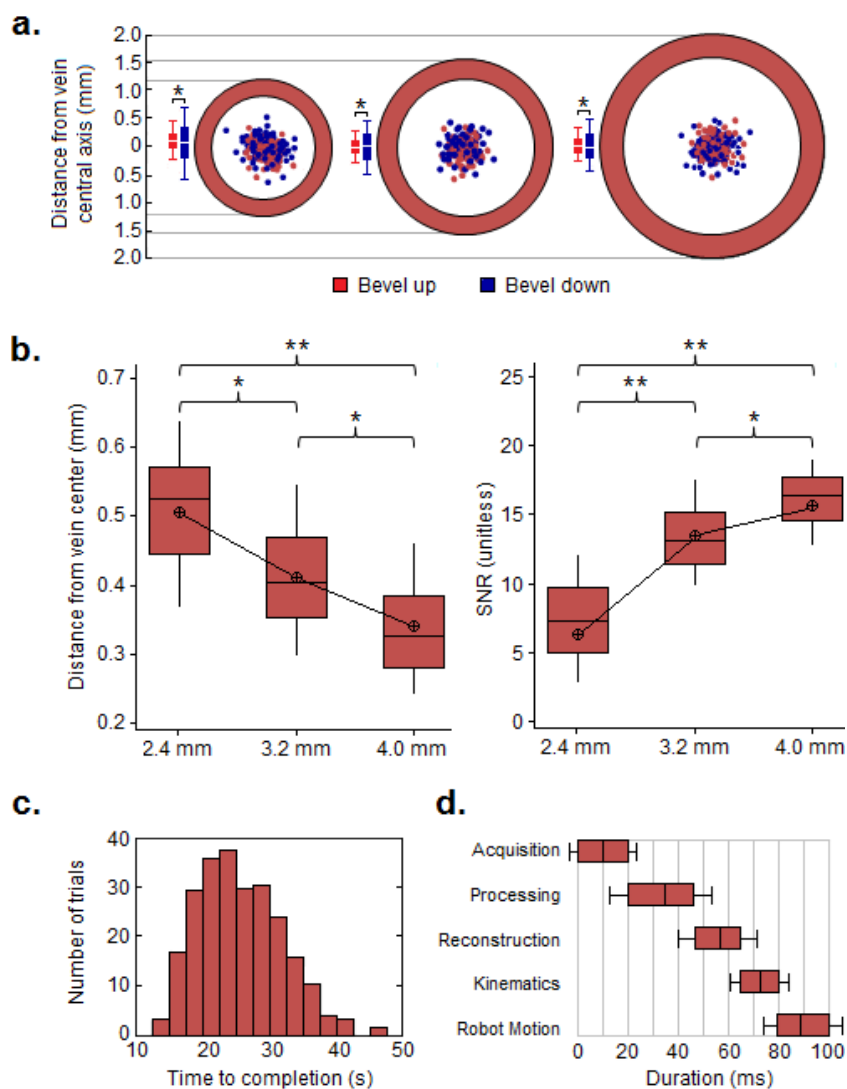
Figure 3-5. Device demonstrates 100% first-stick accuracy in 270 cannulation trials on commercial phlebotomy training models. **(a)** Cross-sectional representation of major veins of the model. Final needle tip positions within vessels are shown for each trial. *Red:* needle bevel oriented upward; *Blue:* needle bevel oriented downward. Significant differences between means indicated by asterisks (two-tailed p-value < 0.05 (*)). **(b)** Device accuracy (measured by distances from vessel centers) and robustness (measured by the Taguchi SNR) for 2.4, 3.2, and 4.0 mm diameter vessels. Box-plots show the median distances as well as the upper quartiles, lower quartiles, and extremas. Circles show mean distances. Significant differences indicated by asterisks (two-tailed p-value < 0.05 (*), 0.01 (**)). Mean distance from the vessel center was 0.43 ± 0.21 mm. **(c)** Distribution of device completion times across all 270 trials. *Mean completion time:* 28.4 sec; *min:* 13.1 sec; *max:* 47.5 sec. **(d)** Duration of for one cycle from acquisition to actuation is 0.1 seconds (10 s^{-1} cycle rate). Box-plots show the mean duration for each step, as well as the upper quartiles, the lower quartiles, and the minimum and maximum observed times.

3.5. Second-generation 7-DOF robot using 3D NIR+US guidance

The first-generation 4-DOF robotic prototype described in Chapter 3.4 demonstrated the ability to significantly increase vein visualization compared to manual visualization by a trained clinician. The system also demonstrated a 100% first-stick cannulation success rate on a phlebotomy training arm. Nevertheless, several limitations were observed. First, the system lacked three DOF needed to adapt the cannulation parameters from patient to patient. Without these DOF, the system would not have been able to: (1) align the needle along the axis of the vein; (2) adjust the insertion angle according to deformations in the tissue; or (3) adjust the vertical height of the needle manipulator. Second, the handling of the needle was still performed manually by the clinician, and as such, the device did not have any means to minimize risks associated with accidental contact with used sharps. Finally, the first-generation device relied only on NIR imaging to estimate vessel depth.

To address the limitations of the first-generation prototype, we developed a second system that incorporates seven DOF and extends the operating workspace (**Figure 3-6**). The major mechanical change is the implementation of a miniaturized 4-DOF articulated serial manipulator capable of inserting the needle along curved trajectories. The device also integrates the bimodal 3D NIR+US imaging system described in Chapter 2. Accuracy and precision are evaluated through tracking, free-space positioning, and *in vitro* experiments. The results indicate that sub-millimeter accuracies can be achieved throughout the operating workspace of the manipulator. Mechanical instabilities in the serial manipulator design are quantified, and methods of improvement are suggested.

3.5.1. *Methods*

3.5.1.1. *Device workflow and architecture*

Figure 3-7 shows the physical device, which is smaller (30 × 25 × 25 cm in volume, 3.5 kg in mass) than the first-generation system (46 × 46 × 46 cm in volume, 10 kg in mass). The open half-

shell design allows the device to be easily integrated into the existing phlebotomy work flow, which has been modified from the workflow for the first-generation system. A GUI is incorporated into the device (**Figure 3-8**) to allow the clinician to oversee the procedure. The GUI directs the clinician through the protocol to ensure safe operation throughout the procedure. The key elements in the system architecture include the NIR+US imaging system, host computer, GPU, and the mechanical robot (**Figure 3-9**). The device is controlled on a Dell Precision M4600 laptop computer. Several software-based safety systems, including a watchdog protocol, were implemented to monitor the activity of the processing unit, controls, and electronics.
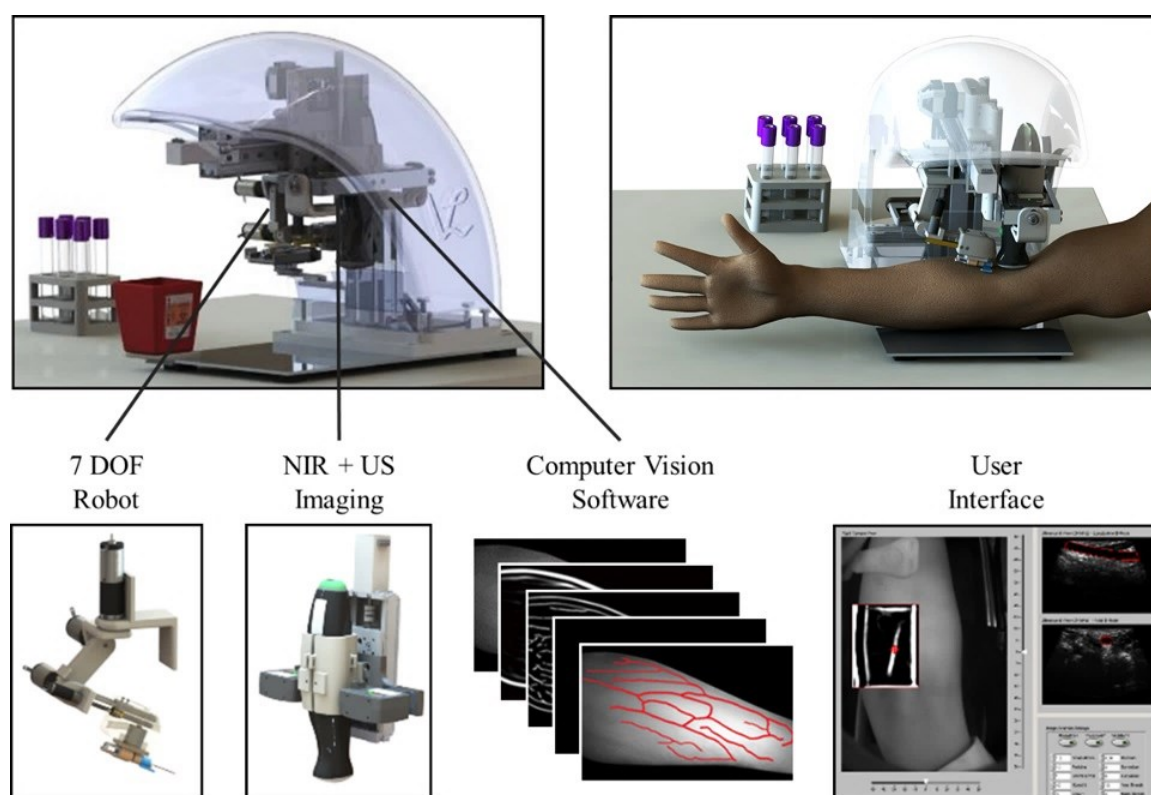
Figure 3-6. Design of second-generation 7-DOF automated venipuncture device. The device comprises a 3-DOF Cartesian positioning system and a miniaturized 4-DOF articulated manipulator arm. The device also incorporates the bimodal 3D NIR+US imaging system and computer vision algorithms described in Chapter 2. A GUI was also developed to allow the clinician to select a suitable vessel for cannulation based on clinical judgment.
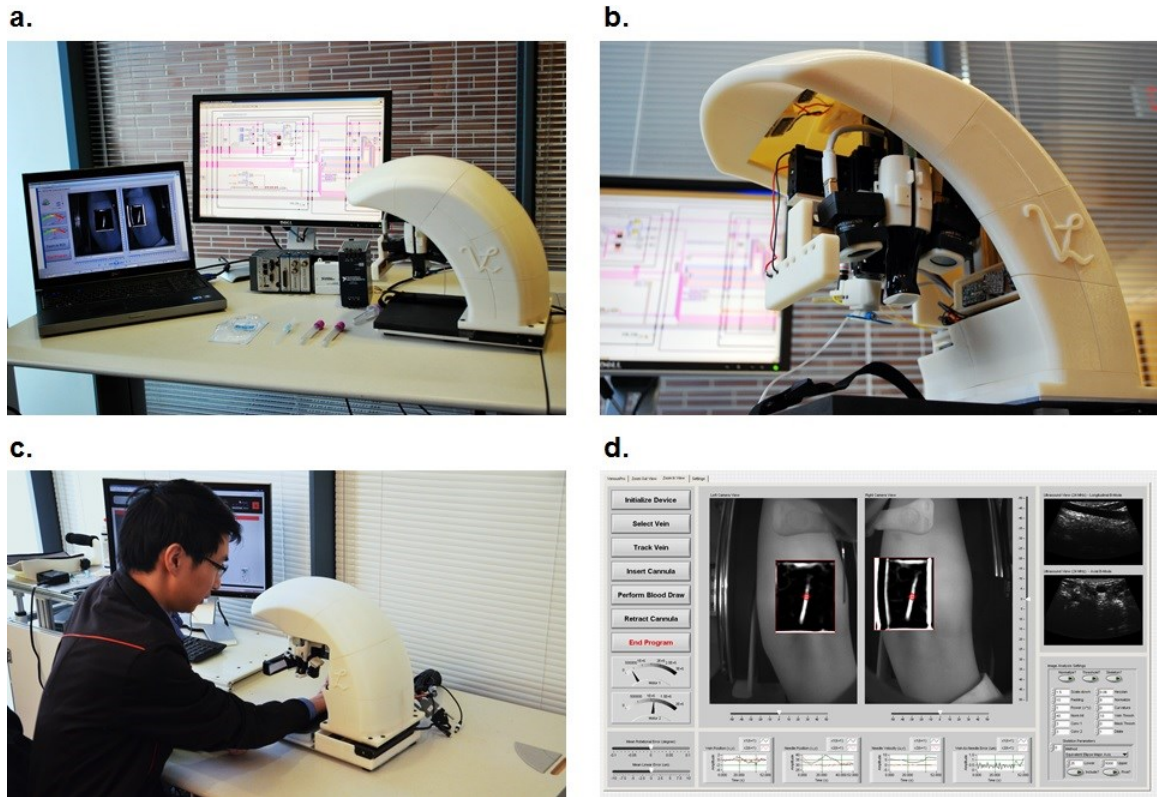
Figure 3-7. Physical prototype of 7-DOF device with key systems highlighted. **(a)** The prototype measures 30 × 25 × 25 cm and weights 3.5 kg. The device is run on a Dell Precision M4600 laptop computer. **(b)** The bimodal NIR+US imaging system can be seen within the device. **(c)** The open half-shell design allows the device to be more easily integrated into the existing phlebotomy work flow compared to the closed design of the first-generation device. The open design also allows the patient to place their arm more easily, and allows the clinician better access to the patient's arm. **(d)** The GUI allows the clinician to oversee the full robotic venipuncture and intervene if necessary. In addition, the GUI directs the clinician through the protocol steps by prompting checks and reminders to ensure that both the patient and practitioner remain safe.
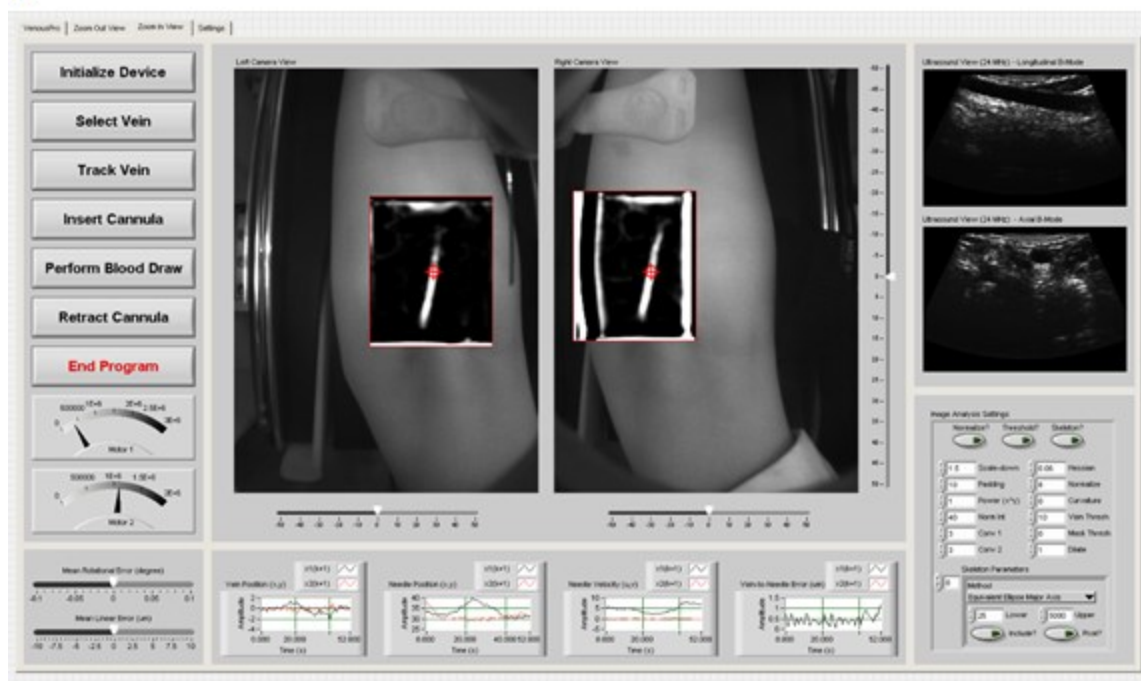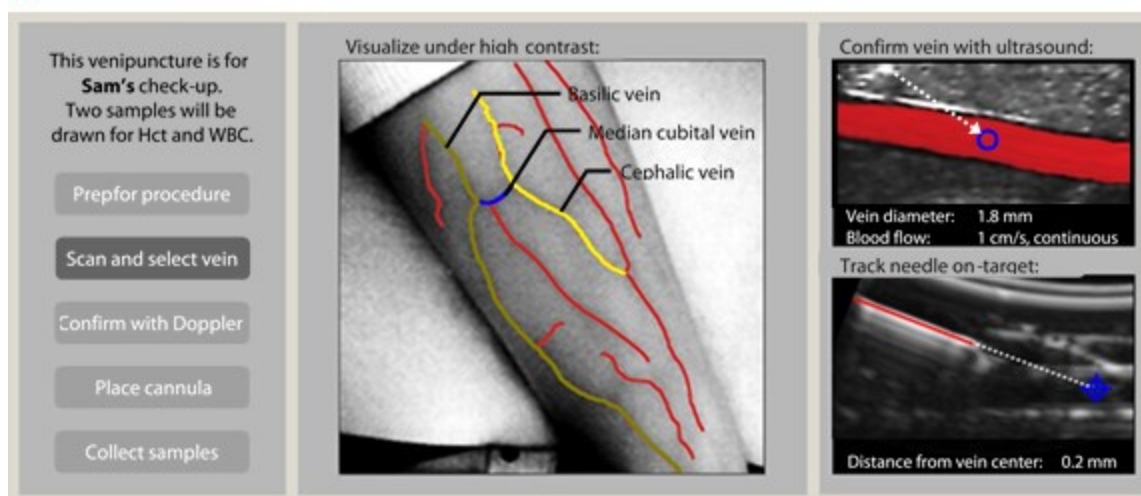
Figure 3-8. Graphical user interface and visual display. **(a)** Current GUI for second-generation system. Stereo NIR images are displayed along with registered vessel targets in each image. B-mode US images are shown in either the longitudinal or the transverse view. **(b)** Design of the GUI incorporating software to suggest suitable cannulation sites based on vessel structural recognition. Here the interface serves to assist the clinician through the major steps of the procedure (left panel) and displays segmented NIR and DUS images in real-time on the screen (center and right panels). The three veins most commonly used for venipuncture, i.e., the median cubital, basilic, and cephalic veins, are labeled and shown.
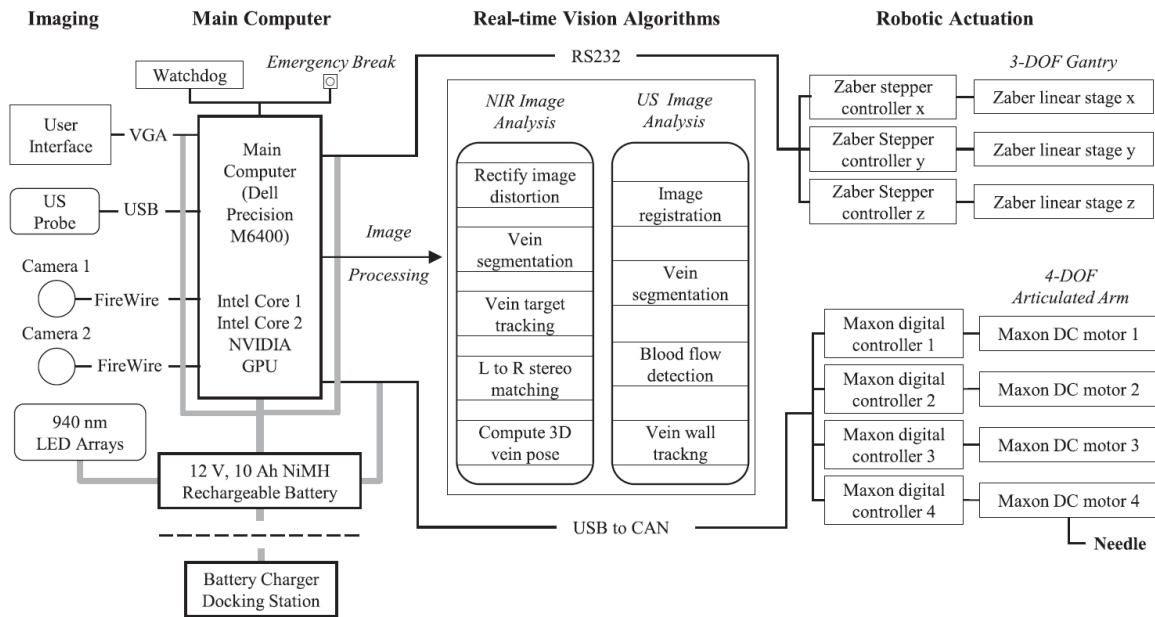
Figure 3-9. Hardware and software architecture of second-generation device. Real-time communication between imaging and robotic control systems allow closed-loop servoing of the needle.

3.5.1.2.   *Robot mechanical design*

3-DOF base positioning system: The robotic assembly is comprised of a 3-DOF Cartesian gantry and a miniaturized 4-DOF serial needle manipulator arm. The Cartesian gantry system consists of precision lead-screw linear stages that function to translate the NIR imaging system, the US transducer, and the 4-DOF serial arm across the rectangular workspace of the device. The x and y translations allow the subsystems to be positioned above the cannulation site, while the z translation serves to lower the US transducer down onto the arm surface. The gantry system demonstrates a step resolution of 0.1905 μm in all three directions.

4-DOF articulated serial needle manipulator: The design of the serial needle manipulator arm overcomes limitations of the 2-DOF end-effector in the first-generation device. There, the device was limited to linear insertions. More importantly the insertions could only be performed in a single direction, since the end-effector could not rotate. Thus the device was not able to align the needle with the orientation of the vein. Furthermore, since translations were only possible in the x and y

directions, the insertion angle was directly dependent on the z position of the target, and could not be adjusted according to other parameters. Finally, since non-encoder stepper motors were used in all joints in the earlier device, closed-loop position feedback was not possible.

The compact 4-DOF serial arm overcomes these limitations by allowing nonlinear trajectories, alignment with the vessel, control of the insertion angle, and position feedback from incremental motor encoders. In its initialized position, the arm is folded such that the needle remains hidden away from the patient until immediately before the venipuncture. This design substantially reduces the risk of patient or practitioner injuries resulting from unintended contact with the needle tip, which was somewhat of a concern in the earlier device. In its folded state, the manipulator has a volume of $2 \times 2 \times 6$ cm. When fully extended, the manipulator can extend the needle up to 10 cm from the initial hidden position. The overall reachable workspace of the manipulator is 175 cm^3. The total weight of the manipulator is 250 g.

The manipulator consists of three rotational joints that control angle and trajectory and a linear needle insertion mechanism on the distal end of the arm. The rotational joints are driven by DC brushed motors (A-max 16, Maxon Motors) with integrated gear heads (GS16VZ, Maxon Motors) having very low backlash (<0.3°). 512 cpt quadrature encoders on each motor ensure a rotational positioning resolution of 0.002°. The insertion mechanism consists of a linear spindle motor (RE 8, Maxon Motors) with backlash of 1.8° and resulting positioning accuracy of 0.112-mm. The spindle drive outputs a maximum force of 8N, which exceeds the typical forces needed to penetrate human skin and superficial vessels. For motor control in the 4-DOF arm, independent proportional-integral-derivative (PID) controllers (EPOS2, Maxon Motors) for each joint were used.

Automated needle handling and US solid gel application: We implemented a method for the device to manage all of the pre- and post-operative tool handling steps involved in the venipuncture procedure. Specifically, the automation system allows the needle to be attached to the distal link of

the serial manipulator arm and a plastic clip, containing solid US coupling gel, to be attached to the US transducer head. Both consumable items are packaged together in a single sterile disposable unit. The clinician places the package in an indicated holder behind the device and, after peeling off the plastic cover, allows the device to load both items automatically. Mechanically, the device's gantry system positions the needle manipulator directly over the pre-packaged consumable unit. In one actuated motion, the needle manipulator then engages the needle via an electromagnet attachment mechanism while securing the US gel clip via a press-fit mechanism. After the procedure, the needle, needle clip, and US clip are disposed into a sharps container built within the device. Together, the added functionally to completely remove practitioner contact with exposed sharps and thus significantly reduces the risk of needlestick injuries. It also eliminates the need to apply liquid-based US gels, which would add to the procedure time and potentially affect the visibility of the vessels in the NIR image.

3.5.1.3.   *Robot motion control*

The motor control scheme consists of a NIR stereo vision-based positioning set and US-based needle adjustment step. Both steps operate based on real-time image feedback. In the NIR-based positioning step, the 3D position of the target cannulation site is determined from the disparity map estimated from the images. The position information is then used by the robot gantry system to position the US transducer over the cannulation site and lowered to make contact with the arm surface. In the second step, smaller position adjustments are made based on the US image. The position of the target vessel in the US image is then used to determine the rotations of each joint in the serial manipulator arm, given a set insertion distance (which remains constant across all procedures). A trajectory is computed for the needle based on a desired starting angle (typically 30°), a desired ending angle (typically 15°), and an insertion speed (typically 10 mm/s). The joint angles are derived from the kinematics of the robot. The manipulator has the potential to steer the needle in real time by tracking the cannulation site and vessel walls in the US image, which would

allow the device to adapt to patient arm movement, vein/tissue deformation, and vein rolling. During the cannulation, the insertion angle is gradually decreased from the starting angle to the ending angle as the needle is introduced into the vessel.

The kinematic equations for the manipulator arm were derived using the Denavit–Hartenberg (DH) convention[199]. The parameters in the DH table link the manipulator origin frame to the wrist frame at the distal end of the end-effector. The needle tip position is then computed using a wrist-to-tool transform:

$$ {}^0_W T = {}^0_1 T(\theta_1) * {}^1_2 T(\theta_2) * {}^2_3 T(\theta_3) * {}^3_W T(\theta_W) $$

$$ {}^0_1 T(\theta_1) = \begin{bmatrix} C_{\theta 1} & -S_{\theta 1} & 0 & 0 \\ S_{\theta 1} & C_{\theta 1} & 0 & 0 \\ 0 & 0 & 1 & 0 \\ 0 & 0 & 0 & 1 \end{bmatrix} \quad {}^1_2 T(\theta_2) = \begin{bmatrix} C_{\theta 2} & -S_{\theta 2} & 0 & 0 \\ 0 & 0 & -1 & 0 \\ S_{\theta 2} & C_{\theta 2} & 0 & 0 \\ 0 & 0 & 0 & 1 \end{bmatrix} $$

$$ {}^2_3 T(\theta_3) = \begin{bmatrix} C_{\theta 3} & -S_{\theta 3} & 0 & L_2 \\ S_{\theta 3} & C_{\theta 3} & 0 & 0 \\ 0 & 0 & 1 & 0 \\ 0 & 0 & 0 & 1 \end{bmatrix} \quad {}^3_W T(\theta_W) = \begin{bmatrix} 1 & 0 & 0 & L_3 \\ 0 & 1 & 0 & 0 \\ 0 & 0 & 1 & 0 \\ 0 & 0 & 0 & 1 \end{bmatrix} $$

3.5.2.   *Results*

3.5.2.1.   *Free-space positioning accuracy*

To test the positioning accuracy, precision, and operating workspace of the needle manipulator, we conducted studies in which we positioned the needle tip on the center of ø4 mm circles on a calibration grid (**Figure 3-10**). The circles were oriented on a flat plane in a 7 × 7 grid separated by 7 mm center-to-center. The grid structure was rigidly mounted to the base of the robot (**Figure**

3-10 (a)); hence, we could relate the coordinates of the circles with the robot coordinate frame by extracting the dimensions from the CAD model. In all experiments, the robot arm was initially set on the gantry; therefore, the needle was in-plane with the middle circles along the y-axis. For each trial, the experimental protocol included extracting the center of the circle (x, y, z) via the robot frame, then using this coordinate as the input into the inverse kinematic controls of the manipulator to set the required joint parameters to position the needle tip on the center of the circle. Finally, the desired circle center location extracted from the CAD model was compared to the actual needle tip position using the fixed cameras on the robot. Needle tip segmentation was achieved using a region grow formula with a Canny edge detector. To ensure minimal errors, we manually selected the needle tip in the post-processed images. **Figure 3-10 (b)** shows stereo images of the needle tip at the center of a test circle on the calibration grid as well as the resulting needle tip segmentation.

To first test the repeatability of the needle manipulator, we ran 50 trials on the five yellow outlined circles labeled in **Figure 3-10 (a)** and compared the actual versus desired needle tip position. The average 3D positioning error (mean ± standard deviation) was 0.81 ± 0.02, 0.79 ± 0.01, 0.94 ± 0.02, 0.66 ± 0.02, and 0.52 ± 0.02 mm for the front, middle, back, left, and right circles, respectively. These circles were chosen to test the repeatability of the manipulator across the workspace area.

To further test the free-space positioning accuracy, the calibration grid was removed, and the needle tip was then placed at the coordinate of every circle within the inner 5×5 grid, as indicated by the black square outlined in **Figure 3-10 (a)**. During the experiment, the height of the grid was varied over seven heights at vertical increments of 4 mm. This way, the accuracy of the robot was evaluated over 175 evenly spaced positions within a $28 \times 28 \times 24$ mm work volume. By determining the exact offset of the manipulator at each grid point, and then interpolating at every position in between, dense error maps were created at different heights. **Figure 3-11** shows the error maps at a z position of 78 mm. **Table 3-2** presents the quantitative results across the seven

heights. Because of the high repeatability in the serial arm, we were able to input these error maps into our motor control algorithms to compensate for the subtle positioning inaccuracies. As can be seen, the robot exhibited significantly reduced errors after repeating the workspace positioning experiments following error correction (3D magnitude error = 0.201 mm) compared with before (3D magnitude error = 1.824 mm). Overall, the results indicate that the manipulator is able to position the needle at a desired location both with high accuracy (mean positioning error = 0.21 mm) and precision (standard deviation = 0.02 mm) over the required 3D workspace.
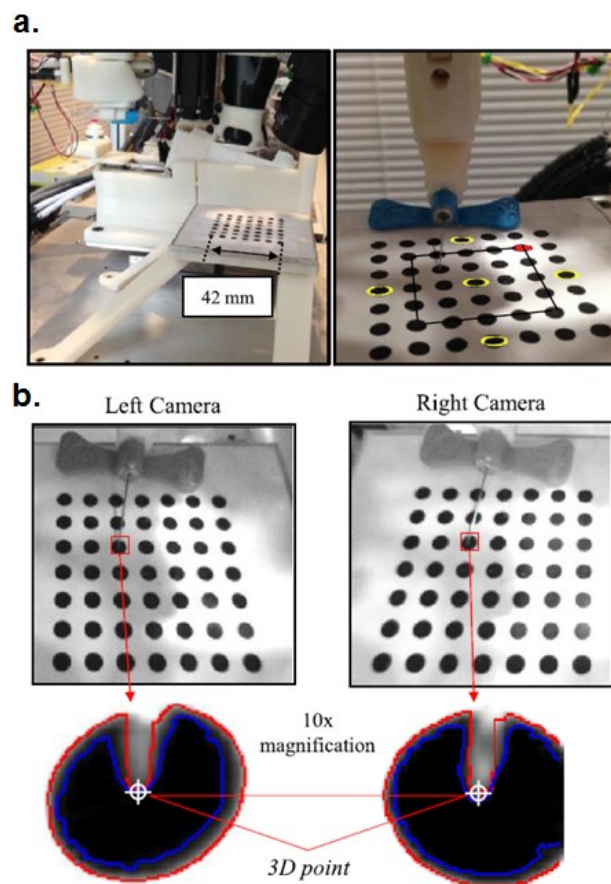
Figure 3-10. Experimental setup for device free-space positioning studies. **(a)** *Left:* needle positioning testing setup. *Right:* robot calibration grid. Yellow circles denote those used for repeatability testing; inner 5 × 5 grid outlined in black, indicates circles used for positioning studies; and red circle indicates plot origins. **(b)** Rectified stereo images with the needle tip outlined in red, and (lower) 10x magnified images illustrating the region grow (blue) and edge detection (red) algorithms to segment the needle tip. Final needle tip selection was performed manually. The 10× images have a pixel resolution of 0.1 mm.

The needle tip extraction method used to determine the actual needle tip location had an accuracy of 0.1 mm due to the resolution in our NIR images (1 mm in x and y, 2 mm in z). Thus methods to improve the needle tip extraction accuracy would be useful in reducing apparent positioning errors. Additionally, errors may have stemmed from inaccuracies in the fabrication and machining of our robotic components; these errors are expected to decrease significantly in later prototypes developed under strict design and manufacturing controls.

Table 3-2. Mean needle tip positioning errors from kinematic workspace studies. dx, dy, and dz refer to the needle tip error in the x, y, and z dimensions, respectively.

Platform Height (mm)	Before Error Compensation				After Error Compensation			
	dx (mm)	dy (mm)	dz (mm)	3D (mm)	dx (mm)	dy (mm)	dz (mm)	3D (mm)
66	0.332	2.80	0.709	2.95	0.0780	0.0610	0.1728	0.211
70	0.283	1.745	0.488	1.871	0.0990	0.1601	0.0980	0.237
74	0.362	1.115	0.607	1.405	0.0840	0.0870	0.1214	0.1974
78 (ref)	0.722	0.1099	0.583	0.949	0.0850	0.0850	0.0770	0.1592
82	0.351	0.952	0.549	1.236	0.0900	0.1075	0.1167	0.207
86	0.284	1.969	0.698	2.17	0.0930	0.1398	0.1234	0.226
90	0.326	2.01	0.641	2.19	0.1446	0.0980	0.1156	0.224
Avg	0.380	1.529	0.611	1.824	0.0960	0.1054	0.1178	0.201
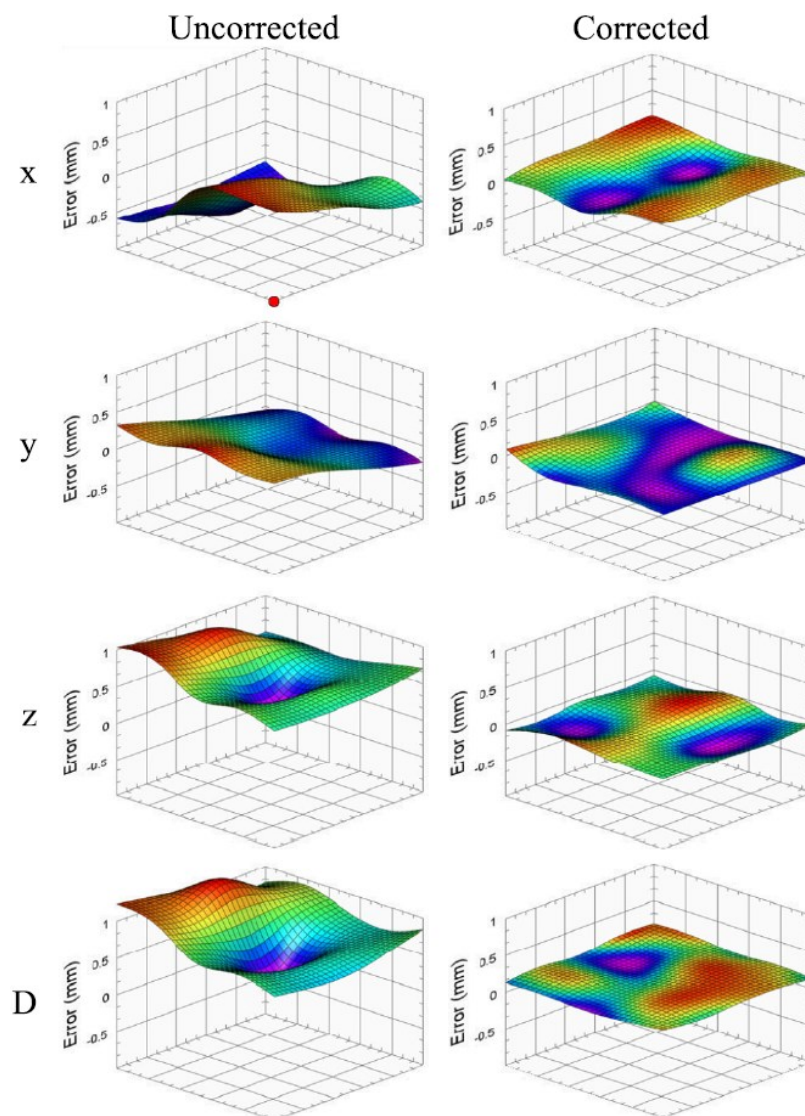
Figure 3-11. Results of free-space positioning experiments. Surface maps show needle tip positioning error over the kinematic workspace in the uncorrected (left) and corrected (right) states for *x*, *y*, *z*, and 3D at a 78-mm calibration platform height. Bi-cubic interpolation was used to estimate errors between dots in the calibration grid. Significantly greater accuracy was observed after error compensation in *x*, *y*, *z*, and 3D ($p<0.001$, two-sample t-test). Red circle in top left plot indicates the robot origin (0,0).

3.5.2.2. US-guided cannula insertion accuracy

Finally, we evaluated the image guided needle positioning accuracy of the venipuncture robot on a skin-mimicking phantom model embedded with surrogate veins. The phantom, which measured $80 \times 50 \times 10$ mm, was fabricated out of gelatin (12 g/100 ml) to provide an elastic skin-

like matrix. The surrogate veins consisted of silicone tubing (Silastic silicone elastomer tubing, Dow-Corning) of two diameters (3.2 and 1.8 mm). The elastic modulus of the tubing (9.5 kPa) closely matched that of typical adult peripheral veins (7–10 kPa). A fluid with blood-like optical absorption and viscosity (black India ink, diluted to 0.45 ml/100 ml and mixed with dextran-40) was introduced into each vein prior to the experiment.

Figure 3-12 (a) illustrates the experimental setup, with the phantom model contained in a 3D printed enclosure in which all veins lay 2 mm beneath the surface of the gelatin matrix. In total, 16 phantom vein cannulation trials were performed – eight for each vein diameter. The study evaluated the complete device workflow, including the NIR images (**Figure 3-12 (b, upper)**), the longitudinal US images (**Figure 3-12 (b, lower)**), and the 3-DOF gantry and 4-DOF manipulator controls. Briefly, the device imaged and segmented the phantom veins using 3D NIR imaging and tracked the center of the selected vein using the US system. The robot then inserted the cannula bevel-up at 15° under US image guidance until the needle tip reached the center of the vein. Between each trial, the needle was retracted, the robot was homed, and then, the cannulation was repeated after shifting the cannulation site 10 mm along the length of the vein. After the study, the recorded US images were manually segmented and analyzed. The center of the vein was determined as the equidistant point between the upper and lower vessel walls. The final needle insertion position was determined as the center of the cannula opening at the bevel tip. Cannulation results are presented in **Figure 3-12 (c)**. The RMS errors were 0.3 ± 0.2 mm and 0.4 ± 0.2 mm for the 3.2 and 1.8 mm diameter veins, respectively. In all 16 trials, the robot was able to successfully cannulate the vein target on the first insertion attempt. In each of the eight trials on the 3.2 mm vein, the final needle tip position was closer to the vein center than to either vein wall, while this was true in six of the eight trials on the 1.8 mm vein.
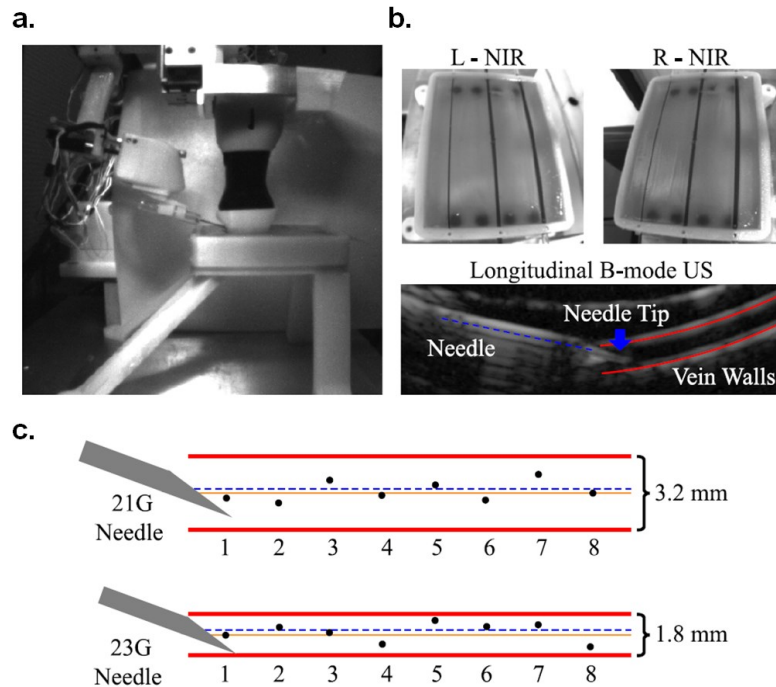
Figure 3-12. Assessment of device cannulation accuracy in gelatin phantoms. **(a)** Experimental setup for phantom cannulation testing. **(b)** Left and right NIR images of an in vitro tissue phantom (top), and longitudinal US image during a needle insertion on the 1.8 mm vein (bottom). **(c)** Results from the cannulation study – orange solid line refers to the desired vein center and black dots indicate the actual location of the needle (at the center of the cannula opening) for each trial. The dashed blue line indicates the average position of the needle within the vein over the eight trials.

3.5.2.3.   Robot servoing in response to tissue motion and vessel deformation

Finally, we investigated the mechanics of vessel rolling and deformation in response to needle insertions performed by the robot, and we evaluated how the robot can make real-time adjustments under image guidance to compensate for subtle vessel motions during cannula insertion. To simulate needle insertions into a blood vessel, while accounting for the nonlinear behavior of the tissue caused by on- and off-axis loads during needle insertion, we implemented finite element (FE) models of a typical adult median cubital vein and a dermis/hypodermis support layer (**Figure 3-13 (a)**). The results of the computational approach were then compared to those of in vitro robotic cannulation experiments performed on gelatin phantoms containing synthetic vessels.

Table 3-3. Comparison of the material properties used for the finite element models and the phantoms.

Tissue Layer	Material Parameter	Unit	Finite Element Model	In Vitro Phantom Model
Vein	Material	–	Elastin	Silicone
	Outer vein diameter, d_v	mm	3.2	3.2
	Wall thickness, t_v	mm	0.55	0.6
	Vein length, l_v	mm	80	80
	Elastic modulus, E_v	MPa	10	9.5
	Shear modulus, G_v	MPa	5.2	–
	Poisson ratio, ν_v	–	0.48	0.48
	Compression strength, σ_{cv}	MPa	20	–
	Yield strength, σ_{yv}	MPa	3.1	3.8
	Tensile strength, σ_{tv}	MPa	9	9.3
Dermis, Hypodermis	Material	–	Adipose	Gelatin
	Dimensions, l_t, w_t, h_t	cm	8x3x1	8x3x1
	Elastic modulus, E_t	MPa	1	1
	Shear modulus, G_t	MPa	0.5	–
	Poisson ratio, ν_t	–	0.48	0.49
	Compression strength, σ_{ct}	MPa	0.75	1
	Yield strength, σ_{yt}	MPa	–	–
	Tensile strength, σ_{tt}	MPa	–	–

Table 3-3 summarizes the mechanical properties of the FE models. In the first of three simulations, the needle was aligned with the medial axis of the vein. Here, only downward vessel displacements were expected. This condition is representative of an ideal venipuncture. In the second simulation, the needle was positioned off-axis, and slip was allowed at the contact interface between the needle and the vein. This condition, where the vein slides away from the needle tip immediately upon contact, is observed in patients with poorly anchored or rolling veins. The needle was likewise positioned off-axis in the third simulation. However, a no-slip condition was enforced between the needle and the vein. In this condition, which may be observed in patients with hardened veins, high strains are exerted on the vessel wall that may lead to significant deformation or vessel rupture[200]. In all simulations, we used a 25 G needle and an angle of insertion of 15°. As in the beam detection model, the applied loads were maintained below the minimum puncture force.

Robot cannulation trials were then conducted *in vitro* to investigate vessel deformation and device accuracy. Here, phantom models with mechanical properties similar to those of the human forearm were utilized (**Figure 3-13 (b)**). To keep consistent with the geometry of the FE models, we fabricated each phantom within an 8 x 3 x 1 cm container. Like the FE models, each phantom comprised a surrogate vein (Dow-Corning Silastic silicone tubing) with the bottom half embedded in support tissue. The support tissue was formed from porcine gelatin, whose mechanical properties can be controlled to resemble those of the dermis and hypodermis. For example, a support tissue with elastic modulus E = 50 kPa (concentration 20% m/v) may be used to model mechanically rigid tissues such as dermis. In contrast, the phantoms used in this study (**Table 3-3**) were significantly more compliant (E = 0.5 kPa, concentration 2.5% m/v) to mimic adipose tissue. Here, rather than provide support, the tissue would more likely deform on needle contact and cause the vein to roll.

Phantoms were constructed to investigate the three needle insertion conditions simulated earlier, namely the on-axis, off-axis slip, and off-axis no-slip conditions. In a first set of trials, vessel deformations predicted by the simulations were compared with experimental observations of the three conditions. To ensure that the mechanical properties of the phantom would be affected only by the applied load of the needle, we did not utilize US imaging here. Instead, the robot kinematics were computed directly from the 3D coordinates provided by the stereo NIR imaging. Furthermore, the computational and experimental insertion parameters were kept consistent, i.e., the needle was inserted at a constant 15° angle with a 10 mm travel distance and 10 mm s^{-1} speed.

Figure 3-14 shows time-lapse images comparing the FE simulations and experimentally observed vessel deformation patterns for the on-axis, off-axis slip, and off-axis no-slip cannulation conditions. The vessel detection predicted by the beam bending model for the on-axis applied load is also shown (**Figure 3-14 (a)**, solid black line) with maximum displacement d_{max} = 12.95 mm. For the on-axis FE and experimental trials, (**Figure 3-14 (a, b)**), vessel displacement was observed to occur primarily in the longitudinal (x) and vertical (z) directions, whereas minimal vessel

displacement was observed in the lateral (*y*) direction. On the contrary, significant lateral (*y*) vessel

displacement was observed when the needle was introduced off-axis. In the slip condition (**Figure 3-14 (c, d)**), the asymmetrically distributed forces applied to the vein side wall caused the vein to

roll under and away from the axis of insertion shortly after initial contact with the vein. Finally, in

the no-slip simulation, significant deformations occurred along the distal portions of the vein. In

the simulations, the applied stress on the vein side wall was found to exceed the material yield

stress after the needle was inserted 5 mm (**Figure 3-14 (e, f)**). Similarly, in the phantom experiment,

the vessel side wall was observed to rupture shortly after 5 mm of insertion.
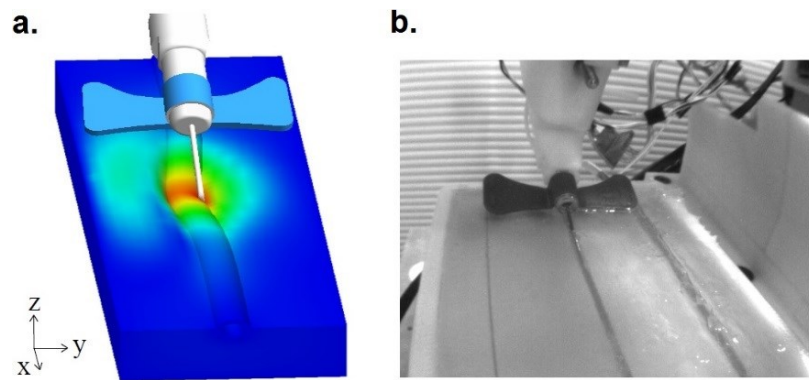
Figure 3-13. Modeling vessel rolling and deformation in response to needle insertion. **(a) (b)** Finite element model of off-axis needle insertion. Vertical and lateral deflections due to applied needle forces can be observed. The colors indicate reaction force magnitudes. **(b)** Setup for phantom cannulation experiments.
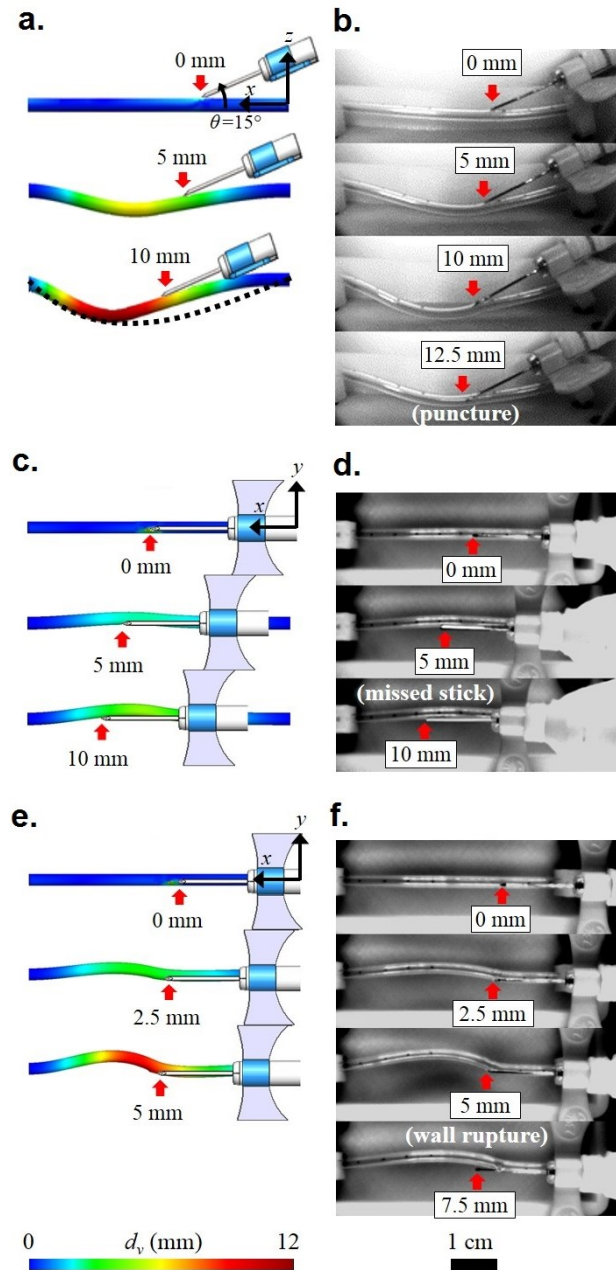
Figure 3-14. Vertical and lateral vessel deflections observed during FEM simulations and phantom cannulation experiments. Shown are time-lapse images comparing the simulated (left) and experimentally observed (right) vessel deformation patterns for **(a)** on-axis, **(b)** off-axis low friction, and **(c)** off-axis high friction cannulation conditions. Red arrows indicate the needle tip position and total needle insertion distance along the axis of cannulation. Vessel displacement dv (mm) is also shown via the color map. Insertion parameters between the simulations and experiments were kept consistent, that is, the needle was inserted at a constant 15 angle with a 10 mm maximum travel distance and speed of 10 mm/s.

Finally, we evaluated the ability of the robotic system to adapt to tissue deformation during insertion by adjusting the angle of the needle relative to the target vessel. In these studies, the US imaging system was utilized to locate and track the center of the vein in each image frame. Additionally, the robot was allowed to adjust the position and orientation of the needle tip based on the image feedback. In this way, we were able to evaluate the robot's ability to guide the needle into the vein in the presence of vein movement and deformation. Longitudinal B-mode US images of needle insertion and vessel deformation are shown in **Figure 3-15**. The adjustment of needle orientation in response to the deforming vessel can be observed. The insertion distance was 5 mm. The time to lower the needle from its starting angle of 25° (**Figure 3-15 (a)**) to 18° (**Figure 3-15 (b)**) on first contact with the vessel wall, and finally to 10° (**Figure 3-15 (c)**), was 0.5 s.
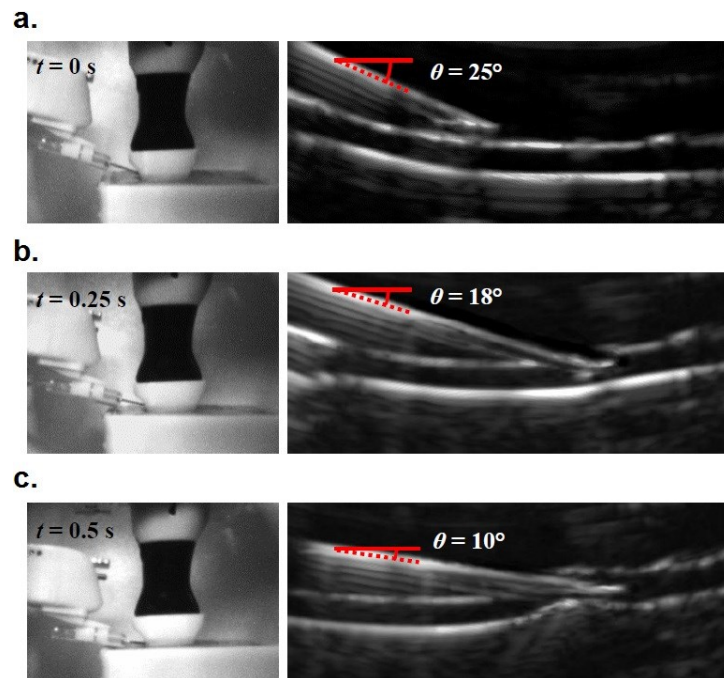
Figure 3-15. Longitudinal B-mode US images showing robotic needle guidance and vessel deformation in a phantom. The adjustment of the needle angle in response to the vein target can be observed. The insertion angle was lowered from **(a)** its starting angle of $\theta = 25°$ to **(b)** an intermediate angle of $\theta = 18°$ on first contact with the vessel wall, and finally **(c)** to a final shallow angle of $\theta = 10°$.

3.6. Third-generation 9-DOF robot using 3D NIR+US and force guidance

Two early prototypes of the robotic system have been described so far. The most recent consisted of seven DOF and demonstrated sub-millimeter accuracy in free-space positioning experiments. However, despite these promising results, several limitations in the robotic design were observed. First, the previous systems lacked the ability to align both the needle insertion and imaging subsystems with the vessel since the imaging components were positioned by a gantry system. Thus, while the device could be tested on phantoms with parallel, unidirectional vessels, human cannulations would have been difficult due to the wide range of vessel orientations in people. Second, the previous devices lacked a radial degree of rotation allowing the robot to reach lateral vessels on the sides of the forearm. As a result of the missing DOF, the previous prototypes were unable to fully utilize the combined NIR and US image information to adjust the position and orientation of the needle in 3D space. This kinematic control is critical in allowing the system to adapt to gross arm motions and subtle vessel movements during the insertion.

In Chapter 3.6, I describe the development of a third-generation robotic device (**Figure 3-16**) that addresses the limitations of the previous systems. The advancements introduced in the third-generation device include the following. First, the mechanical configuration of the system is redesigned to incorporate the added DOF without compromising portability. Second, the NIR, US, and needle insertion subsystems are integrated into a compact end-effector unit that allows each subsystem to remain aligned regardless of the end-effector orientation. Third, a force sensor is coupled to the motorized needle insertion mechanism as an added method of feedback during the venipuncture. Fourth, a new kinematic model is introduced to reflect the eye-in-hand configuration of the camera system, and separate motion control schemes are implemented that utilize the stereo vision, US, and force measurements to adjust the needle orientation in real-time. To assess the

positioning accuracy and speed of the device under NIR, US, and force-based guidance, a number of real-time robotic tracking and cannulation experiments are carried out. The positioning experiments indicate sub-millimeter accuracy and repeatability over the operating workspace of the system, while tracking studies demonstrate real-time needle servoing in response to moving targets. The robotic phantom cannulations demonstrate the use of multiple system states to confirm that the needle has reached the center of the vessel.
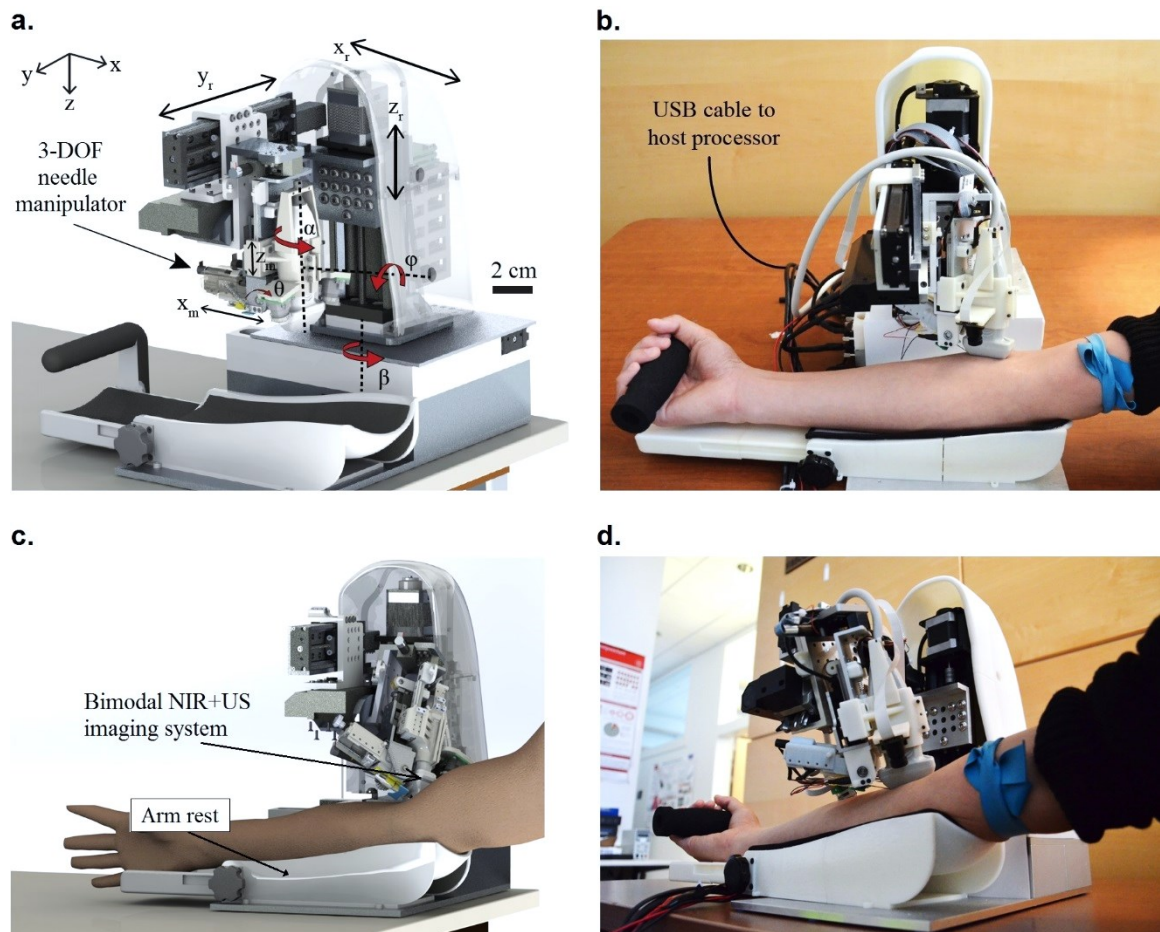
Figure 3-16. Design of third-generation 9-DOF autonomous venipuncture device. **(a, c)** Conceptual designs (CAD renders) of the robotic system. **(b, d)** Physical device prototype.

3.6.1. *Methods*

3.6.1.1. *Device workflow and architecture*

The protocol to perform a cannulation procedure using the device is similar to the protocols for the previous systems. The procedure begins with disinfecting the forearm and applying a tourniquet. The device then scans the patient's forearm, using the NIR system to create a 3D map of the vessels and estimate their depth below the skin. Once a cannulation site is selected by the clinician via the GUI, the US probe is positioned over the site to provide a magnified cross-sectional view of the vessel and confirm blood flow. The coordinates of the cannulation site are directed to the robot, which then orients and inserts the needle. The device is comprised of three main subsystems: the host processor, base positioning system, and compact manipulator unit, which contains the imaging and needle insertion components.

The device runs off a laptop computer (i7-4710HQ 2.5 GHz CPU) serving as the host processor, communicating with the actuators and sensors via a USB bus. The image processing steps are accelerated on a general purpose GPU (NVIDIA Quadro K2200M), whereas all other tasks, i.e., the path planning, motor and electronics control, and GUI functions, are executed on the CPU. The main processor subsystems are the CPU and GPU, camera and DUS controllers, PID motor controllers, power management system, and display (**Figure 3-17**). With this architecture, the computer can perform the imaging and robotics computations at real-time frame rates using 800 MB and 500 MB of CPU and GPU memory respectively. 100 MB/s of data is communicated between the laptop and the robot via a single USB 3.0 cable. Inside the robot, a receiver hub splits the input into four independent outputs that connect to the cameras, US system, base positioning system, and manipulator unit. The device measures $35 \times 24 \times 21$ cm and weighs 8 kg.
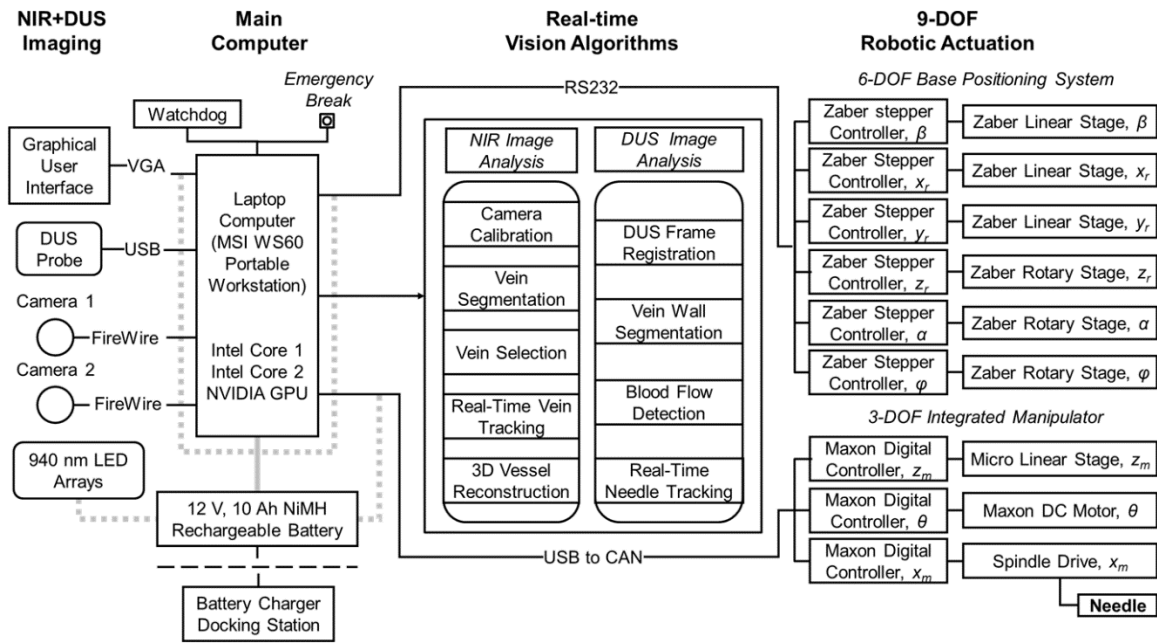
Figure 3-17. Hardware and software architecture of third-generation robotic device. Main hardware subsystems are the CPU and GPU, camera and DUS controllers, positioning controllers for the 9-DOF robot, power management system, and display. Main software subsystems include the GUI (run asynchronously on the CPU), real-time vision algorithms (deployed to the GPU), robotics processing (deployed to the CPU or the individual controllers), and the safety monitoring systems (run on the CPU).

3.6.1.2. *Robot mechanical design*

6-DOF base positioning system: The base positioning system serves to orient the imaging and needle insertion end-effector unit over the target vessel. As illustrated in **Figure 3-16 (a)**, the gantry includes six DOF: three prismatic joints and three revolute joints. The prismatic joints form a Cartesian positioner (x_r, y_r, and z_r), whereas revolute joints α and φ) allow the robot to align with the vein. β allows the entire robot to rotate before and after the procedure, but is not part of the kinematic geometry during the needle insertion. The α rotation is actuated by a miniature rotary stage (3M-R, NAI) positioned directly above the US probe, while the φ rotation is controlled by a goniometer cradle (BGS50, Newport). The use of a goniometer allows the axis of rotation to be offset from the stage and aligned with the axis of the forearm. This design is key to

providing circumferential motion around the forearm to reach vessels at either side, without increasing the size of the device.

3-DOF needle manipulator: In previous designs, the base rotational joint of the serial arm manipulator, was positioned a large distance from the needle tip (approximately 10 cm when the arm was fully extended) (**Figure 3-18 (a)**). Though extending the operating workspace of the manipulator, the articulated arm compromised joint stability, as minute rotational errors (<0.1°) at the joints could lead to large positioning errors at the needle tip (>1 mm). While our previous studies showed that these errors could be minimized after calibrating the robot, relying on calibration before each use may be impractical. Furthermore, because the manipulator was not kinematically coupled with the imaging system, lateral rotations by the manipulator to align with the vessel would bring the needle out of the US image plane during the cannulation. Similarly, the insertion angle of the needle was constrained by the height of the US probe and could not be adjusted once the probe was positioned over the vessel.

Figure 3-18 (b) shows the design of the miniaturized 3-DOF manipulator developed for the third-generation device. The 3-DOF manipulator fully couples the NIR imaging system, the US transducer, and the needle insertion mechanism into a single, compact unit. Without any added positioning by the robot's base gantry system, the redesigned manipulator has a reachable workspace that allows the needle to be inserted anywhere within the imaging field of the US probe. The manipulator, which has an approximate volume of 7 x 3 x 8 cm, is mounted directly to the base positioning system, as can be seen in **Figure 3-16 (b)**. (Alternatively, the manipulator may be used as a standalone image-guided cannula placement device.) There are five major design changes in comparison to the articulated serial needle manipulator in the previous designs:

1. The new kinematic geometry allows the insertion angle (θ_m in **Figure 3-18 (b)**) to be controlled independently of the other DOF. This is made possible by a linear stage that

adjusts the height of the needle (z_m) without affecting the height of the US probe. Combined with a servo motor that sets the insertion angle and a spindle drive that translates the needle (x_m), the manipulator is able to target vessels at depths ranging from 1–10 mm below the skin surface at insertion angles of 0–30°.

2. The distance between the needle tip and the needle's center of rotation (curved black arrow in **Figure 3-18 (b)**) is minimized to increase joint stability. The center of rotation of the redesigned manipulator remains adjacent to the needle tip regardless of the insertion position or angle. This design change dramatically improves the joint stability and needle tip positioning accuracy of the robot.

3. The lateral rotation (θ_1 in the second-generation manipulator as shown in **Figure 3-18 (a)**) has been incorporated into the base positioning system (α in **Figure 3-18 (a)**), allowing the US probe and needle to rotate together and thereby remain in alignment at all times.

4. As opposed to the direct-drive mechanism of the previous manipulator, a worm-gear drive train is built into the motor controlling the insertion angle to ensure self-locking of the joint. This prevents free, unconstrained motion by the robot when electrical power is not being supplied to the system.

5. The redesigned manipulator may be adapted for intravenous catheter placement with little change to the form factor or cost of the insertion mechanism. **Figure 3-18 (c)** shows prototype designs of needle insertion end-effectors with similar form factors, with one end-effector adapted for blood collection (top) and the other for catheter placement (bottom).
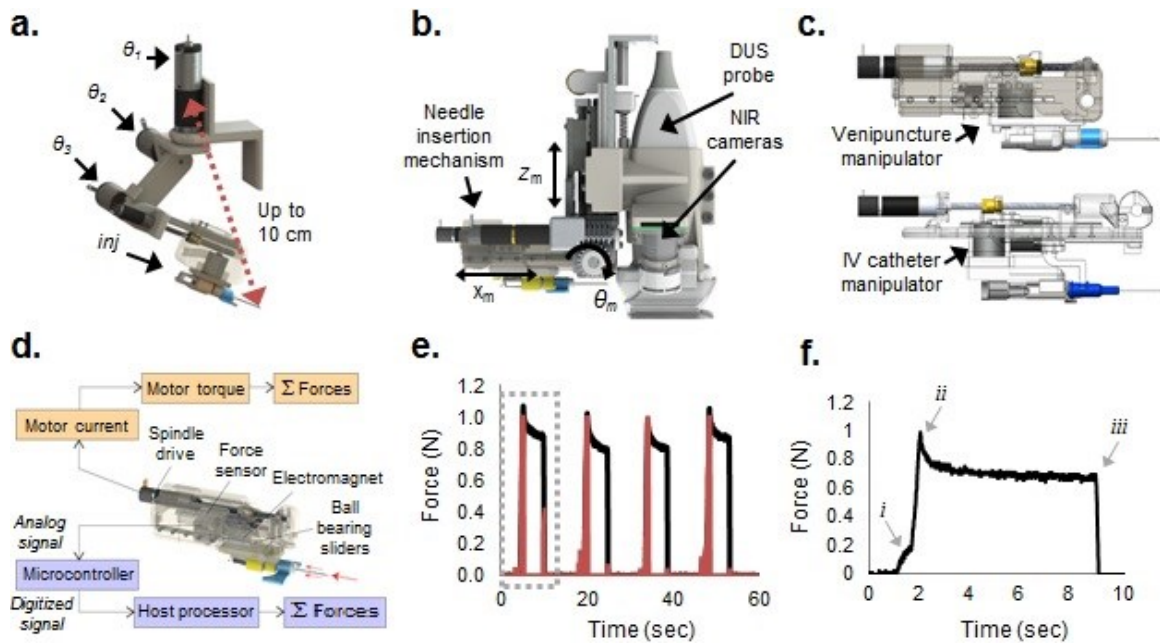
Figure 3-18. Compact integrated manipulator with force-sensitive needle insertion. **(a)** Previous 4-DOF articulated needle manipulator, decoupled from the NIR and US imaging systems. The distance between the base joint and needle tip (dotted red arrow) reached up to 10 cm at full arm extension, which reduced the overall joint stability. **(b)** Compact, integrated manipulator coupling a redesigned needle insertion mechanism with a miniaturized bimodal NIR+DUS imaging system. **(c)** Comparison of needle insertion mechanisms for blood draws (upper) and intravenous catheter insertions (lower). The upper mechanism is designed for Butterfly needles commonly used for venous blood collection. The lower mechanism is adapted for inserting catheters. **(d)** Needle insertion mechanism incorporating dual force-current sensing to extrapolate the needle tip position during the venipuncture. **(e)** Representative force profiles observed during controlled cannulations into silicone phantom vessels. Red lines show corresponding measurements of current running through the windings of the DC brushed motor. **(f)** Force profile of the temporal window outlined by the gray box in (e). Distinct patterns in the profile are can be seen when the needle pierces the top skin layer *(i)* and vein wall *(ii)*, as well as when the cannula is removed *(iii)*.

The stereo imaging system is calibrated using a fixed planar grid with circular control points (see Section 2.7.1). Rather than needing a separate motorized stage to adjust the height of the grid, the cameras are moved vertically via the existing z_r stage, allowing the intrinsic and extrinsic camera parameters to be computed within the workspace of the robot. The system utilizes the 18 MHz Telemed linear array transducer for B-mode and Doppler imaging. The transducer has been reoriented on the device to provide transverse, cross-sectional imaging. In the earlier prototype, the image plane of the US probe was oriented longitudinally with respect to the vessel. However,

vessels tend to roll in the axial direction during the needle insertion. In these cases, the vessel would roll out of the US image plane, making it impossible for the robot to track. In contrast, the transverse orientation of the US probe allows the target vessel to be tracked over a larger cross-sectional range.

3.6.1.3.   *Force sensitive needle insertion mechanism*

In addition to visualizing the needle in the US image, we also implemented a force sensor in the manipulator to detect when the needle punctures the skin and vessel wall (**Figure 3-18 (d)**). Axial forces along the needle vary throughout the insertion due to the natural inhomogeneity of human skin tissue. The sensor measures these forces, relaying information to the robotics to help compute the position of the needle tip. The force-sensitive insertion mechanism consists of a linear stage actuated by a lead screw spindle drive (RE 8, Maxon Motors) and supported by ball bearing sliders. As the spindle translates to advance the cannula, normal and friction forces acting on the needle cause it to push against a force sensor (FSG-5N, Honeywell) embedded in the manipulator. This generates an analog signal which is then digitized by a 12-bit analog-to-digital converter. The computer simultaneously monitors the forces applied against the sensor and the electrical current running through the windings of the DC brushed spindle drive to determine puncture events. **Figure 3-18 (e)** provides preliminary results demonstrating the use of the force-current approach in controlled phantom experiments. Peaks in the current profile (red lines) are observed to occur in unison with peaks from the force sensor (black lines). **Figure 3-18 (f)** shows in greater detail the force profile during cannulation. By observing the peaks in the force profile during the cannulation, puncture events can be detected, including: (*i*) tissue deformation, which begins when the needle contacts the tissue and continues until the insertion force reaches a local maximum; (*ii*) puncture, which occurs when a crack propagates through the tissue following the force peak; and (*iii*) removal of the needle from the tissue. In this way, the force sensor serves as an important secondary measurement of vessel puncture, particularly when speckle artifacts in US image prevent the needle tip from being clearly visualized, segmented, and tracked.

3.6.1.4.   Device calibration

Joint calibration of the stereo camera configuration, the US transducer, and the robot is shown in **Figure 3-19**. Briefly, the intrinsic camera parameters were calibrated as shown in **Figure 3-19 (a)** to correct for nonlinear lens distortions. Similarly, the US image was calibrated to minimize distortions due to differences in sound speed (**Figure 3-19 (b)**). The extrinsic camera and US parameters were then related to the robot coordinate frame based on a series of linear transformations, i.e., rotations and translations. Finally, the kinematic joint parameters of the robot were calibrated through positioning experiments as described later in this chapter following DH conventions (**Figure 3-19 (c)**). A fully automated calibration routine was developed to allow joint correction of the intrinsic camera and US image parameters, the extrinsic camera-to-robot and US-to-robot parameters, and the kinematic joint parameters of the robot manipulator chain. An outline of the calibration process is shown in **Figure 3-19 (d)**.

3.6.1.5.   Robot motion control

The motion control scheme of the robot (Error! Reference source not found.) consists of three p hases: NIR stereo vision-based servoing, US-based servoing, and force feedback. The first phase involves extracting the 3D position of the insertion site from the stereo images, and directing this coordinate to the robot. This positions the end-effector unit over that location, aligning the needle with the vessel orientation. Desired joint angles are derived from the kinematics of the eye-in-hand camera configuration, and low-level position commands are sent to the motor drivers. The Cartesian gantry utilizes bipolar stepper motors and controllers capable of high-resolution micro-stepping (0.19 μm) and high repeatability (<4 μm). Attached encoders provide the position and velocity about each joint. Conversely, the rotary stages in the gantry contain DC-brushed motors, actuated via positioning controllers (EPOS, Maxon Motors). In the second phase, the 6-DOF on the base positioning system are further utilized to make fine position adjustments once the US probe is lowered, to enhance visualization of the vessel.
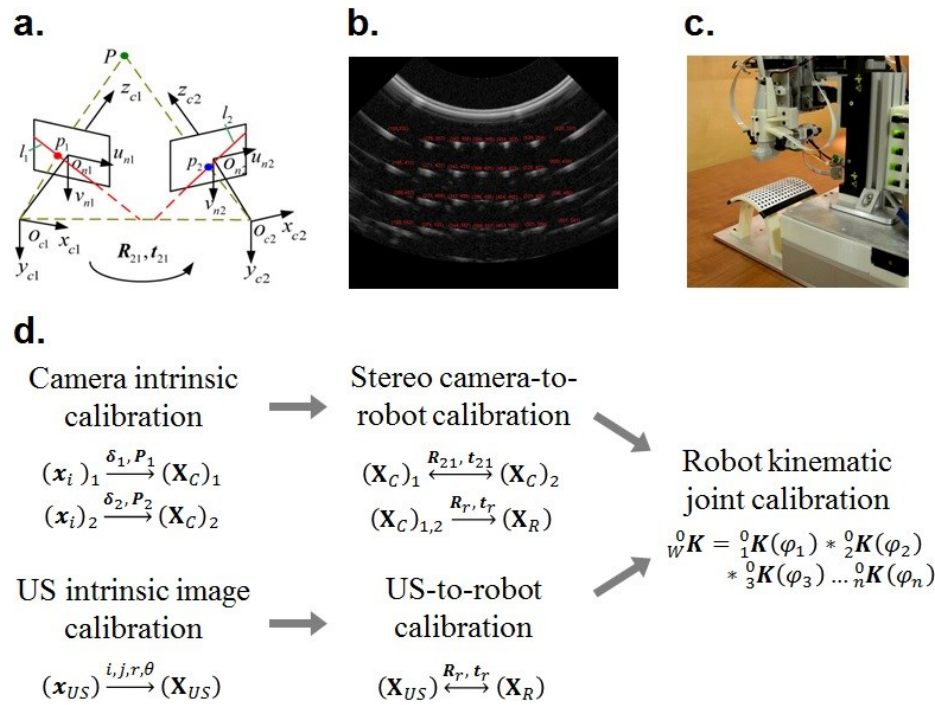
Figure 3-19. Joint calibration of stereo camera, ultrasound, and robot parameters.

Once each actuator reaches the set point wherein the US probe is oriented and centered over the target vessel, the robot then finely positions the needle via the 3-DOF on the manipulator. At this point, the US probe is lowered over the forearm to display a clear image of the vessel. The needle orientation is then adjusted in real-time based on inputs from the US image and force sensor to position the needle tip in the center of the vein. Extrapolating the vein center coordinates from the US image, and tracking the needle tip during the insertion, the desired needle tip position is modified to accommodate subtle tissue motion during the procedure. Finally, in the third phase, force and current signals measured during the needle insertion are registered with the US image data to confirm the puncture of the target vessel. Position-based visual servoing was implemented as opposed to an image-based approach for several reasons. Namely, the needle is not in the FOV of the cameras, thus there is no way to use an image-based servoing scheme for vision-guided tasks. For US-guided tasks, where the needle is in the FOV during the venipuncture, image-based servoing has several drawbacks[41,201]. First, task singularities can arise in the interaction matrix

potentially resulting in unstable behavior. Second, the needle may appear disjointed in the US image due to noise; thus the accuracy of an image-based servoing scheme that is fully reliant on accurate needle tip position extraction would suffer dramatically due to these errors.

3.6.2. Results

3.6.2.1. Kinematic workspace analysis

The forward kinematics model of the robot is used to extract the needle tip position from the joint parameters, whereas the inverse kinematics are used to calculate the joint angles required to position the needle tip at the desired location. The kinematic joint space of the robot, and the travel range of each actuator in the system, is shown in **Table 3-4 (a)**. Kinematic equations were derived using a series of matrix transforms linking the Cartesian (x_r, y_r, and z_r) and rotational joints (α and φ) of the gantry with the manipulator joint frames (z_m, θ, and x_m) based on standard DH convention (**Table 3-4 (b)**). For the base positioning system, the parameters specified in the DH table link the origin frame at the base of the system to the wrist, which is coupled to the US transducer. Meanwhile, the DH parameters for the needle manipulator link the manipulator origin frame, with a constant offset from the US transducer frame, to the distal end of the end-effector. The needle tip position is calculated using a wrist-to-tool transform. As mentioned earlier, the β revolute joint is independent of the needle insertion kinematics. Instead, it functions to rotate the device away from the patient, providing space for the clinician to disinfect the forearm and apply a tourniquet before the procedure and clean the device afterward.

Forward and inverse kinematics experiments were conducted to evaluate the workspace of the system. To ensure that the device is able to operate along the length and upper circumference of the forearm, we computed the operating work envelope of the robot based on the derived kinematic equations. The travel ranges of the x_r, y_r, and z_r prismatic joints provide a base rectangular work volume of 10 x 10 x 7.5 cm, and the rotational range of the revolute joints (α: ±90° and φ:

±30°) provides an additional envelope of 90 cm^3 from any given position within the base work volume. The manipulator adds a planar 14 cm^2 range of motion lying parallel with the axis of insertion. In total, the operating workspace allows the robot to cannulate any vein in the anterior forearm, spanning from the wrist to the ACF region of the elbow. Additionally, unlike earlier generations, the current robot is able to align with angled vessels and reach lateral or side veins.

Table 3-4. Kinematic joint space of the robotic system. **(a)** Joints 1–6 comprise the base positioning system; 7–9 for the manipulator. **(b)** DH parameters. Joints: 1–7 for the base; Joints: 8–11 for the manipulator.

a.

Joint	Motion	Travel Range
$1 - \beta$	Base rotation	0–90°
$2 - x_r$	Scan along arm length	0–100 mm
$3 - y_r$	Scan across arm width	0–100 mm
$4 - z_r$	Adjust manipulator height	0–100 mm
$5 - \phi$	Roll rotation (about x)	-30–30°
$6 - \alpha$	Yaw rotation (about z)	-45–45°
$7 - z_m$	Adjust needle height	0–25 mm
$8 - \theta$	Adjust insertion angle	0–30°
$9 - x_m$	Needle insertion length	0–35 mm

b.

i	Type	α_{i-1}	a_{i-1}	d_i	θ_i
1	Revolute, β	0	0	0	0
2	Prismatic, z_r	90°	0	0	0
3	Prismatic, x_r	90°	0	0	0
4	Prismatic, y_r	90°	0	0	0
5	Revolute, ϕ	-90°	0	0	0
6	Revolute, α	-90°	0	40 mm	0
7	US probe offset, p	0	0	95 mm	0
8	Prismatic, z_m	90°	0	0	0
9	Revolute, θ	90°	0	0	0
10	Prismatic, x_m	0	0	25 mm	0
11	Needle, n	0	0	-56 mm	0

3.6.2.2. Free-space positioning accuracy

Free-space needle positioning experiments similar to those described in Chapter 4.2 were conducted on a calibration platform to assess the accuracy and repeatability of the robot over its reachable workspace (Error! Reference source not found. **(a)**). The actual needle tip position was manually extracted from the stereo images after applying an ellipse detector to segment the target, and a line detector to highlight the needle. Specifically, the ellipse detector was implemented to segment and compute the centroid of each target, from which the 3D coordinates were calculated based on the extrinsic camera parameters and the robot kinematic geometry. The needle tip was then extracted manually from each image and used to compute the 3D needle tip location. Actual needle tip positions were compared to the desired and estimated 3D target positions to determine the error (accuracy) and standard deviation across trials (repeatability). Target positions were also

estimated from the right and left images acquired by the stereo imaging system (Error! Reference source not found. **(b)**).

The calibration platform comprised 192 circular targets (4 mm diameter, 7 mm center-to-center spacing) uniformly spaced over a cylindrical grid, with each target defining a unique, known 6-DOF pose (*x*, *y*, *z*, *pitch*, *yaw*, and *roll*). The sixth DOF (*roll*) was varied from -45 to 45° across the circumference of the platform. To evaluate repeatability, three positioning trials were conducted for each of the circle targets. For each trial, the robot started in its home position, moved the needle tip to the desired 6-DOF pose, and returned to the home position. The desired 3D position of each target was obtained from the CAD model of the robot.

Table 3-5 presents the error between the circle positions in the computer-aided-design model and the positions estimated from the stereo imaging (row 1); the error between the desired and actual positions of the needle tip (row 2); the repeatability of the needle tip positioning (row 3); and finally the repeatability of the needle tip detection alone (row 4). The detection repeatability indicates the error inherent in the manual needle tip extraction process, which adds to the positioning repeatability. Over three trials, the 3D positioning error was 0.22 ± 0.05 mm, with the needle tip detection repeatability being 0.03 mm. These results imply that the robot has sufficient accuracy and precision to position the needle tip in vessels as small as 1 mm in diameter, as is commonly found in neonatal and pediatric patients. In addition, because these positioning studies were conducted using a cylindrical testing platform that mimicked the curvature of an adult human forearm, we were able to evaluate the performance of the robot over the operating workspace of the needle insertion task. This testing differed from positioning studies conducted on previous prototypes in that each target in the cylindrical calibration grid defined a unique 6-DOF pose for the robot to manipulate the needle. In comparison, previous studies used a planar calibration grid and only specified a 3D Cartesian pose for the robot.

Table 3-5. Needle tip positioning errors (n = 3 trials). Units in mm.

	dx	dy	dz	3D
Mean – estimated vs. known position	0.05	0.08	0.07	0.13
Mean – needle tip vs. known position	0.09	0.15	0.08	0.22
Repeatability – needle tip positioning	0.05	0.04	0.07	0.05
Repeatability – needle tip extraction	0.02	0.03	0.03	0.03

3.6.2.3.   Robot control based on stereo vision guidance

Tracking experiments were then conducted to evaluate positioning accuracy under stereo vision-guided servoing. The first set of experiments evaluated the needle pose errors as the robot positioned the needle to follow a moving calibration target (**Figure 3-20 (a)**). The calibration target comprised a grid of four circles lying on a plane (**Figure 3-20 (b)**). As the target was moved by freehand under the FOV of the cameras, the plane parameters were calculated based on the 3D coordinates of each circle, which were extracted in real-time via an ellipse detector provided in LabVIEW. The plane parameters were then used to compute the 6-DOF pose of the circle target and, in turn, the desired pose of the needle.

Figure 3-20 (c) displays the desired and actual positions of each robot degree-of-freedom over a 60 sec period during the experiments. **Figure 3-20 (d)** displays the following errors as a function of the speed of the moving target. Both the linear and rotational errors were observed to increase with movement speed. At speeds of 10 mm/s and 10°/s, the following error was 0.4 mm and 0.5°, respectively. Particularly at high speeds, stochastic state estimation filters (for example, the unscented Kalman filter or the Monte Carlo-based particle filter, both of which are commonly used in navigation robots[202–204]) may help to reduce following errors by predicting future positions based on current system states.

Next, tracking experiments were repeated on veins identified on the forearm of a human subject by the NIR imaging system (**Figure 3-20 (e)**). To measure following errors over a range of speeds,

the subject was asked to move their arm randomly under the device for a 60 sec period. During the experiment, the plane tangent to the forearm surface around the vessel target was estimated from the 3D position of the vessel and the surrounding feature points (**Figure 3-20 (f)**). Similar to the previous tracking experiments on the calibration target, the plane parameters were used to determine the 6D vessel pose and the desired needle pose. Unlike the previous experiments, which relied solely on ellipse detection, the feature points in the forearm images were extracted via the scale-invariant feature transform (SIFT) detector. Only features present along the epipolar lines in both cameras were used in the pose calculations. Meanwhile, the actual vessel target was tracked using pyramidal Lucas-Kanade optical flow estimation.

The desired and actual positions of each degree-of-motion during the human vessel tracking experiments are shown in **Figure 3-20 (g)**, and presented with respect to vessel movement speed in **Figure 3-20 (h)**. As before, following errors were higher when the motions were faster. At speeds of 10 mm/s and 10°/s, the following error was approximately 1.0 mm and 0.9°, respectively. The increased error compared to the calibration tracking experiments is most likely due to errors in the SIFT detector and optical flow tracking approach. In future studies we will evaluate following errors over a range of object tracking algorithms[205]. We will also assess whether the use of dense stereo correspondence algorithms or active stereo vision approaches, e.g., based on structured lighting, may improve the quality of the 3D reconstruction and thus reduce errors during tracking.

a. Stereo tracking of calibration target

b.

c.

d.

e. Stereo tracking of human forearm vessel

f.

g.

h.
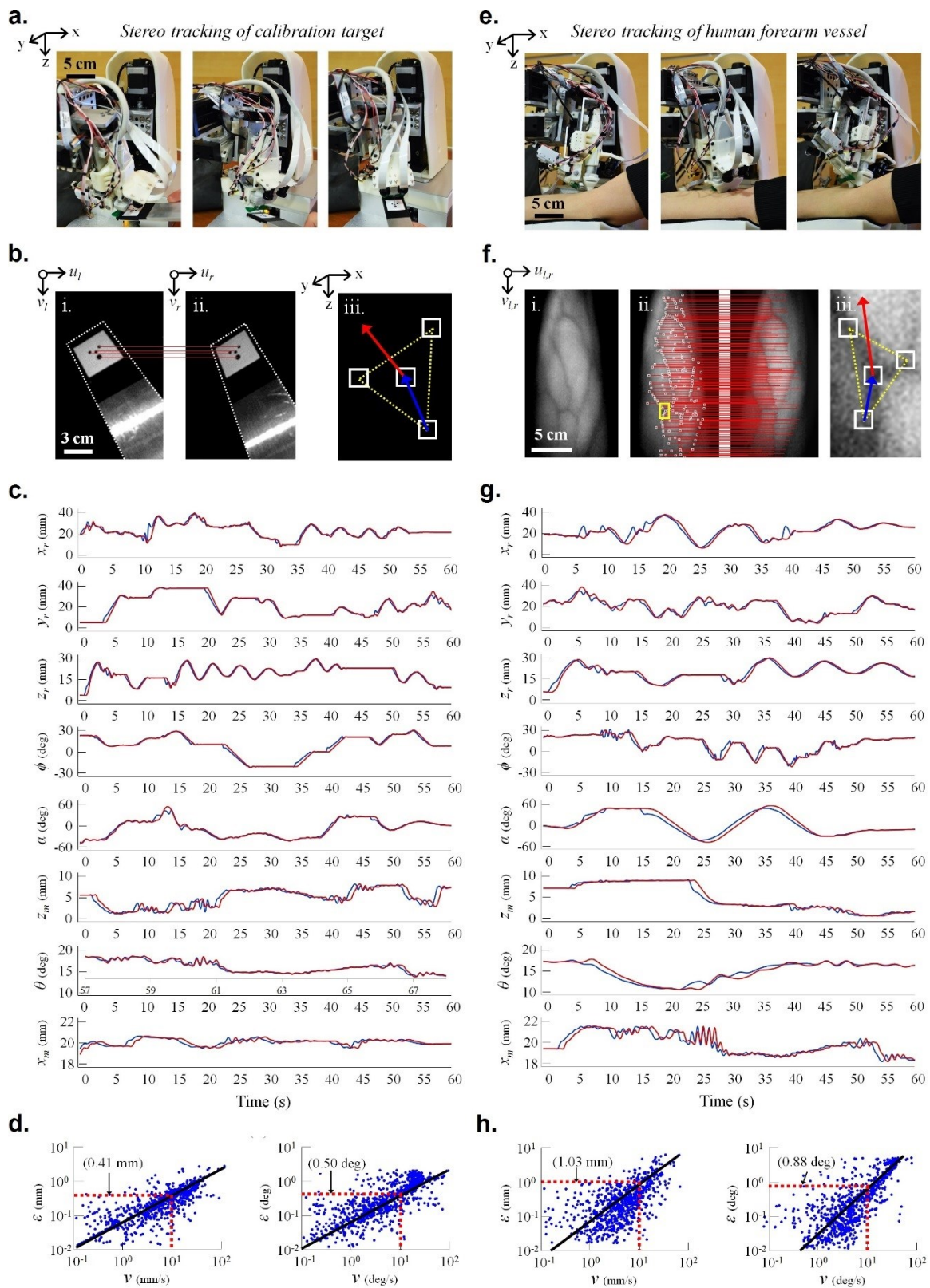
Figure 3-20. 6-DOF real-time robot tracking based on NIR stereo guidance. **(a)** Robot tasked with tracking a moving calibration target moved by freehand under the FOV of the stereo imaging system. **(b)** Stereo image pair showing the calibration target (*i, ii*); the epipolar correspondence lines between the circular control points on the target (red lines); and the 3D orientation of the target calculated from the plane parameters (*iii*). **(c)** Desired and actual positions of each robot degree-of-motion over 60 sec of freehand calibration target tracking. **(d)** Linear (left) and rotational (right) following errors with respect to the speed of the moving target. **(e)** Robot tracking experiments repeated on human subject. **(f)** NIR contrast image highlighting veins in the forearm (*i*); epipolar correspondence lines between SIFT features extracted from the left and right stereo images (*ii*, red lines); and SIFT feature points used to determine the 3D position and orientation of the vessel target based on the tangent plane parameters (*iii*). **(g)** Desired and actual positions of each degree-of-motion over 60 sec of human vessel tracking. **(h)** Following errors with respect to forearm movement speed.

3.6.2.4.   *Robot control based on ultrasound guidance*

Next, we evaluated US-based visual servoing in an *in vitro* blood vessel phantom. The phantom consisted of a flexible 3 mm diameter silicone tube simulating the vessel, embedded within a compliant hydrogel comprising 10% gelatin and 0.2% agarose. The phantom was contained in a 3D printed enclosure, which was further mounted to the device. Vessel motions were simulated by moving the vessel laterally (**Figure 3-21 (a, left)**, y-axis) within the phantom over time periods of 60 s. Controlled motion patterns were generated at varying speeds using a secondary motorized positioning system. The robot was then tasked with maintaining the needle tip position 1 mm above the moving vessel over the duration of the experiment. Frame-to-frame position changes of the vessel wall were tracked in each US image using optical flow. **Figure 3-21 (a, right)** shows a representative transverse US image of the surrogate vessel within the phantom (red dotted circle) and the tip of the needle passing through the transverse US imaging plane (yellow dotted circle). Also shown is the vessel's lateral range-of-motion within the phantom (green dotted line).

Table 3-6. US-based vessel tracking results averaged over four square wave cycles (error units in mm).

Speed (mm/s)	US Tracking Error	Following Error
0.5	0.004	0.003
2	0.006	0.046
10	0.004	0.794
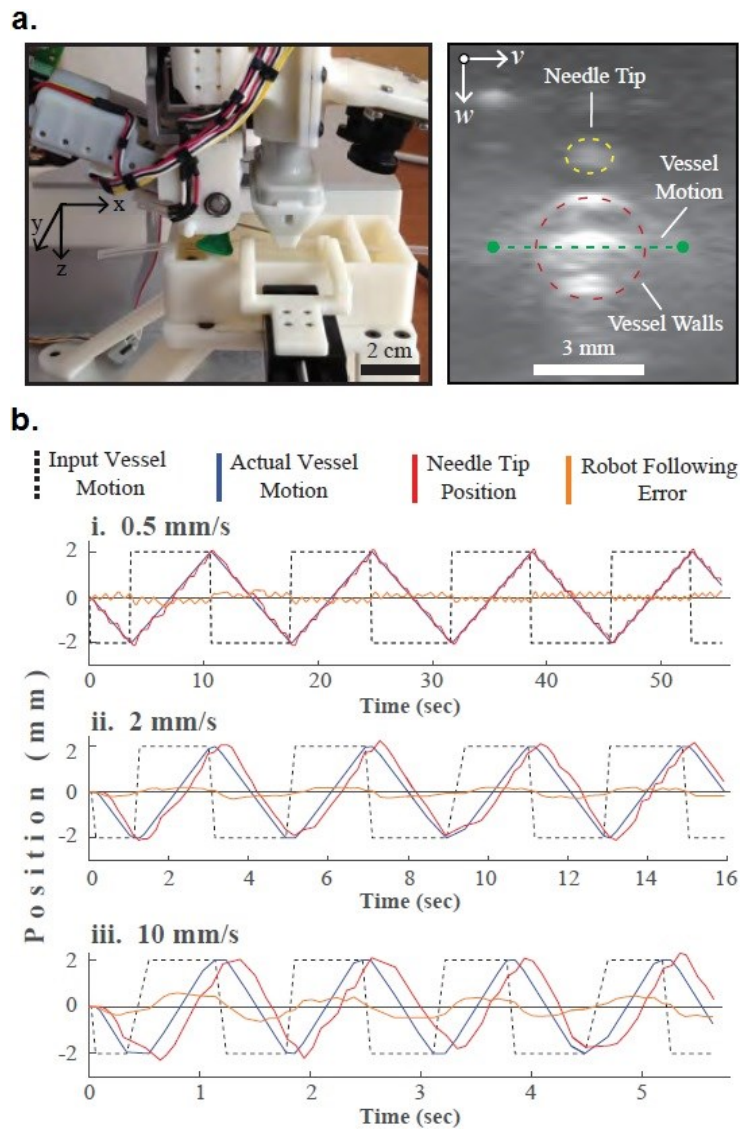
Figure 3-21. US-guided lateral vessel tracking. **(a)** *Left:* experimental setup showing the motorized phantom rig used to laterally displace the surrogate vein. *Right:* transverse US image depicting the vessel cross-section (red) and needle tip (yellow). **(b)** Robot following errors observed during side-to-side vessel tracking at (*i*) 0.5, (*ii*) 2, and (*iii*) 10 mm/s. Errors refer to the difference between the known vessel location (determined from the vessel positioning stage) and the needle tip position (computed from the robot kinematics).

Figure 3-21 (b) compares vessel and needle tip positions at three lateral movement speeds (0.5, 2, and 10 mm/s). **Table 3-6** summarizes the mean US tracking error (the error between the known vessel location, as set by the secondary positioning system, and the location estimated from the US

images) and the mean robot following error (the error between the known vessel location and the needle tip position) at each speed. The US tracking errors were negligible at all three speeds, indicating that the frame rate of the US imaging system was sufficient within the tested speed range. Robot following errors, meanwhile, were observed to increase with movement speed; the mean error at 0.5 mm/s (0.003 mm) was about two orders less than the error at 10 mm/s (0.8 mm). As with the vision-based tracking experiments, incorporating state estimation filters may help to reduce the following errors at high speeds.

3.6.2.5. *Robot control based on force guidance*

In a fourth set of experiments, we evaluated needle insertion under real-time force guidance using the same blood vessel phantom as described earlier. Again, the 3 mm diameter vessel was laterally displaced using the motorized stage (square wave, 2 mm diameter, 2 mm/s speed), and the robot was tasked with following the moving vessel target using the US image. For these studies, the robot positioned the needle tip directly above the vessel for three motion cycles, and then the insertion system introduced the needle into the center of the vessel at 10 mm/s and 15°. Both the needle insertion and vessel motion were halted once the force sensor detected the venipuncture. The robot then retracted the needle (at the same speed and angle as the insertion) and moved forward 2 mm in the x-direction to introduce the cannula on a new section of the vessel. In total, this process was repeated over five trials.

Figure 3-22 (a) displays a series of US image frames depicting the needle insertion steps. In addition to the force and current readings, we also monitored the vertical displacement of the vessel from the US images during the needle insertion (**Figure 3-22 (b)**). The vertical position measurement is the displacement from the original vessel position, as measured by optical flow. Thus, a downward vessel movement results in a positive peak in the plot. There was no observable time latency between the force, current, and z-position readings during the needle insertion.

Immediately following each vessel puncture event, a relaxation phase was observed in the vertical position of the vessel. Similarly, sharp negative peaks can be seen immediately following the withdrawal of the needle from the vessel, coinciding with a return of the axial force to baseline magnitudes. The average axial force for vessel puncture was 2.2N, which is higher than the typical force response for a human peripheral vein (~400 kPa) or artery (~1 MPa). This was unsurprising, as silicone rubber has a higher elastic modulus than the collagen and elastin found in human vessels.
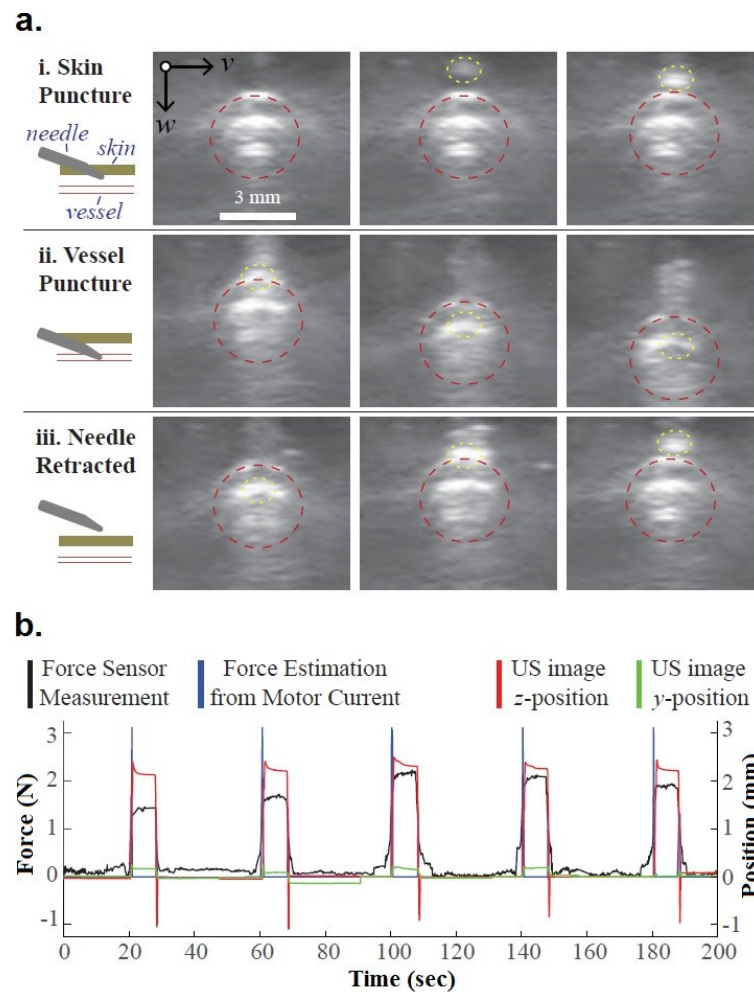
Figure 3-22. Needle insertion with simultaneous US, force, and motor current feedback. **(a)** US image frames depicting the needle insertion: (*i*) needle pierces top phantom layer; (*ii*) needle cannulates top vessel wall; and (*iii*) needle is retracted. Vessel wall and needle tip highlighted with a dotted red and yellow border respectively. **(b)** Vertical displacement of the vessel coincides with force and current responses observed as the needle punctures the vessel wall.

In these experiments, the phantoms we used consisted of a single homogenous gelatin layer with no addition of optical or acoustic absorbers and scatterers. The lack of modifiers made it relatively easy to visualize the vessels, since few image artifacts were seen in the US images. In Chapter 4, I will describe the development of more realistic, multi-layered tissue-mimicking phantoms that can be tuned to accurately simulate a range of human tissue properties.

3.7. Discussion

The key challenge of the work described in Chapter 3 involved designing a robotic system that was conducive to use in everyday clinical environments. Due to their size, cost, and complexity, current medical robotic systems have been limited to the operating room. For the venipuncture device to see broader adoption, the system would need to be portable. In a hospital setting the device would most commonly be moved from bed to bed on a mobile crash cart. The device may also need to be attached to bed railings to accommodate patients who must lie prone during the procedure. Meanwhile in a diagnostic testing facility, the device would most likely rest on a small table top or cart next to the phlebotomy chair. These requirements place practical constraints on the size and weight of the device. On the other hand, the required workspace is governed by the expected length and girth of an adult human forearm and the range of vessels that must be reached. In order to perform venipuncture on both forearm and hand vessels, the device would need to mechanically translate along the full length of the lower forearm, i.e., between the anterior cubital fossa in the elbow region and the wrist or back of the hand. Alternatively, the device would need to image a large FOV and provide cues for the patient to reposition his or her arm so that the device can reach a selected cannulation site. The first approach would be more convenient and allow greater autonomy, whereas the second approach would likely result in a smaller and simpler device. Beyond the workspace requirements, the dexterity of the robot also provided a challenge to its design. To accommodate the full range of expected vessel orientations in the forearm, hand, and wrist, at least six DOF are needed (three translational DOF and three rotational DOF). At least one

additional DOF is required on the end-effector to insert the needle. For catheter placement, two independent DOF are needed on the end-effector. If using US imaging as a detection modality, several of the DOF used to control the needle must then be decoupled from the US probe, since the probe stationary during the needle insertion; at least two more DOF are needed for decoupling. In total, it is estimated that at least eight DOF are needed if the goal is to achieve fully autonomous needle positioning, and a complete clinical system with ancillary functionality would likely require upwards of ten DOF. Thus the challenge was to develop a dexterous robotic system with high kinematic complexity and relatively large workspace requirements, and yet to do so in a way that remained practical for the most common clinical settings.

In Chapter 3, I presented three prototype generations with increasing complexity but decreasing overall form-factor. I also described a number of engineering bench studies conducted to evaluate robotic performance. The cannulation studies conducted on the commercial phlebotomy training arm to evaluate the first-generation device provided evidence NIR stereo vision could achieve the 3D precision necessary to robotically place a needle inside of vessels with diameters 2.4 mm or greater. The cannulation studies also demonstrate that the image analysis and robotic functions can be performed in real-time. However, in the first-generation device, US had not yet been incorporated, and limitations were observed when vessels were deeper than 3 mm beneath the skin surface. At these depths, optical scatter in the tissue caused the vessels to become difficult or impossible to detect. Additionally, vessels below 2.4 mm in diameter were more challenging to accurately cannulate due to the resolution of the NIR stereo imaging system in the z-direction. Specifically, depth resolution decreases with the distance of the target from the cameras; in our system, the depth resolution was 1.1 mm, which may be insufficient for small (~1 mm) vessels. Finally, the device comprised only four DOF and thus could not align the needle with all vessels.

The second-generation 7-DOF device overcame a some of the limitations in the first device and incorporated US as a second means of vessel imaging. We also implemented an automated

needle handling mechanism to minimize practitioner contact with used sharps. The results of the frequency tracking, free-space positioning, and cannulation experiments demonstrated that the device has the accuracy needed to cannulate smaller peripheral vessels. In particular, the addition of US allows for imaging resolutions of approximately 100 μm laterally and in depth. Meanwhile, kinematic calibration of the robot over its operating workspace reduced positioning errors to approximately 0.1 mm. Nonetheless, the second-generation system lacked several critical rotational DOF and exhibited some mechanical instabilities due to the design of the serial manipulator arm.

In the third-generation device, the two rotational DOF were added, and the needle manipulator unit was redesigned to eliminate mechanical instabilities found in the previous articulated arm. The stability issues were resolved by combining the imaging system and the robotic end-effector within a tightly integrated and compact manipulator unit. The end-effector was redesigned for both blood collection and catheter placement. Ancillary functions such as force feedback and automated needle handling were also implemented. A fully automated device calibration routine was developed to allow joint estimation of the intrinsic camera and US image parameters, the extrinsic camera-to-robot and US-to-robot parameters, and the parameters of the robot's kinematic chain. Real-time image guidance was evaluated through a series of tracking experiments based on stereo vision, US, and force feedback. Position-based servoing was used as opposed to an image-based approach because the needle was not in the FOV of the cameras during vision-guided tasks, and was occasionally occluded in the image during US-guided tasks.

We did notice some limitations in the design of the third-generation device when we investigated the effects of motion velocity on positioning accuracy. We found that high translational (> 10 mm/s) and rotational (>15 °/s) speeds would have been needed to adjust the needle to rapid vessel or arm movements. However, since robotic guidance was based on kinematic rather than dynamic controls, increased tracking errors were observed at these higher speeds. Robotic accuracy and responsiveness may thus be improved with the implementation of nonlinear

needle insertion dynamics and a more sophisticated control system, potentially allowing the device to adjust to higher-order parameters, such as acceleration, and to adapt to sudden variations in speed[206–209]. It is also possible that state estimation functions may be implemented to predict future positions based on current trajectories[202–204,210], and that this may help to reduce following errors at high speeds. Additionally, part of the tracking error is due simply to the maximum permissible speed of the translational stages in the base positioning unit. Faster stages would substantially reduce the following errors in the tracking experiments. Currently, the maximum allowable speeds are constrained by the load and precision requirements of each actuating component, and these constraints limit the response of the robot to rapid vessel motions[61]. As such, an important focus of future research will be to investigate alternative mechanical designs that can accommodate the dexterity requirements of the task while minimizing size and complexity. As one example, parallel manipulators with hexapod or delta mechanisms have been used in many industrial automation tasks. When the load requirements are low, parallel robots may be developed exhibiting very compact form factors, and some systems have been developed in recent years for clinical interventional tasks[211–213]. As we continue to miniaturize the venipuncture device, particularly around the needle and the end-effector, the load requirements are expected to decrease substantially; in combination with the implementation of dynamic and/or stochastic control systems, the reduced loads will allow us to explore a much broader range of robotic mechanisms.

Though not directly measured in these studies, a second source of inaccuracy that we observed was due to errors in 3D localization using the NIR stereo vision approach. Currently, the system as a whole relies on robust stereo correspondence to provide accurate estimations of the disparity map in real time and then compute 3D arm and vessel positions. In the third-generation device, the distance between the cameras and the surface of the patient's arm is much smaller (~5 cm) than the distance in the first-generation device (~20 cm). While a decrease in depth improves vertical resolution, it also increases the total disparity range and increases the likelihood of occlusion and

ambiguity during stereo matching. Inaccurate disparity estimates then lead to inaccurate positioning of the US probe, and if the vessel is not initially observed in the US image, the device has no means of automatically searching for the vessel; instead, the clinician must manually reposition the probe. One possible approach to alleviating difficulties with stereo correspondence involves making use of structured illumination, as described in Chapter 2.4.3. Specifically, it may be possible to implement a pattern projector in conjunction with a stereoscopic detection configuration. "Active stereo" techniques based on structured illumination have shown great promise in providing highly accurate dense disparity maps[214–216], and recent methods have achieved real-time rates[217–221].

Likewise, it may be possible to indirectly estimate the position of the target vessel with the NIR stereo vision system even after the probe is lowered over the forearm. This could be done by tracking surrounding passive or active landmarks on the skin surface and then inferring the position of the target vessel using registration techniques[93]. Alternatively, approximate 3D reconstructions of the vessel may be generated by rapidly steering the probe across a small length of the target vessel and using the segmented vessel in the NIR images as an input into the global path planner[222]. An intensity based servoing scheme using the US image (rather than the NIR images) could also be used to sweep across the vein[223–227]. Finally, it may be possible to incorporate a 3D US transducer as opposed to a conventional 2D imaging system, though the added cost would have to be considered. Regardless of the approach, the capability to servo the probe about all six DOF in real time, as opposed to being limited to two DOF of tracking (y and z) from the US image, would allow the device to more readily compensate for arm motions and vessel deformation.

Finally, the added DOF and functionality, while important for autonomous performance, also increases the cost of the device. Increased complexity may also make the device more difficult to operate and maintain. Previously, in Chapter 2, I described a semi-autonomous system that combined active and passive robotic components to maintain kinematic dexterity while reducing cost and complexity. There, a passive gantry arm was used in place of the 6-DOF actuated base

positioner. The 3-DOF manipulator could still be used to robotically introduce the needle, but the passive gantry system would require fewer actuators compared to the current motorized positioner. The semi-automated robotic assist device may be able to carry out the more difficult aspects of venipuncture while allowing simpler tasks, for example coarse positioning and alignment, to be performed by the operator. Nevertheless, in those earlier experiments, we only assessed the usability of the semi-autonomous device in phantoms with straight, parallel vessels. We later found that manual alignment with the target vessel remained challenging for the operator to perform, even with the increased stability provided by the passive arm. To reduce the need for coarse manual alignment, it may be possible to add rotational capabilities to the semi-automated device, bringing its total DOF to five. However, since large translations are no longer needed, the semi-automated device can still remain significantly smaller than the fully autonomous system. Whether such an approach is more or less clinically feasible compared to the fully autonomous system remains to be seen. More generally, further studies are needed to identify optimal designs based on expected trade-offs between device automation, cost, and complexity.

Chapter 4 – *In vitro* and *in vivo* device validation in phantom and animal models

Parts of Chapter 4 were adapted from the publication listed below. All excerpts represent the original work of Alvin Chen, whose specific contributions as first author of the publication included: designing and conducting the described experimental studies; generating the presented data and corresponding figures; writing, editing, and revising the original text; and addressing reviewers' comments as corresponding author of the original manuscript submission.

A. Chen, M. Balter, M. Chen, D. Gross, K. Alam, T. Maguire, M. Yarmush. Multilayered tissue-mimicking skin and vessel phantoms with tunable mechanical, optical, and acoustic properties. *Medical Physics* 43, 212–226.

Parts of Chapter 4 were also adapted from two manuscripts under review at the time of publication of this dissertation. All excerpts represent the original work of Alvin Chen, whose specific contributions as first author of these manuscripts included: designing and conducting the described experimental studies; generating the presented data and corresponding figures; and writing, editing, and revising the original text.

A. Chen, M. Balter, A. Davidovich, T. Maguire, M. Yarmush. Performance of an image-guided robotic vessel cannulation device on tissue-equivalent phantoms in comparison to manual cannula insertion. *IEEE Transactions on Medical Imaging* 2016 (*submitted for review August 12, 2016*).

A. Chen, M. Balter, G. Yarmush, T. Maguire, M. Yarmush. Automated lateral tail vein blood collection and fluid delivery in rats using a portable, image-guided, robotic vessel cannulation device. *Physics in Medicine and Biology* 2016 (*submitted for review September 01, 2016*).

4.1. Overview

The validation of medical robotic devices has traditionally been challenging due to a lack of suitable *in vitro* or *in vivo* models that reproduce the physiological diversity of real human patients. For robotic devices designed to perform vessel cannulation procedures, the majority of preclinical testing, including the cannulation experiments described in Chapters 2 and 3, has been carried out on commercial phlebotomy training models[58], simple phantoms[59–61,194–196], or engineering testing setups. However, while these previous studies by our group and others provide promising evidence of technical feasibility, their clinical relevance is limited in several regards. First, the performance of these systems has not been evaluated across the broad range of demographic factors that

contribute to failed vascular access procedures in the clinic; existing test models are unable to simulate the full extent of human variability. Second, the insertion parameters themselves have not been fully investigated; there is evidence that optimal insertion settings vary based on a number of tissue mechanical properties[200,228–230], and this knowledge could be used to greatly improve robotic performance. Third, evidence has not been presented that an improvement in insertion accuracy actually leads to a higher rate of success in blood sample withdrawal or fluid delivery. Finally, the accuracy and speed of robotic vessel cannulation devices has never been compared, *in vitro* or *in vivo*, to results obtained from manual techniques. As such, the clinical potential of automated vascular access remains a matter of question.

In Chapter 4.2 I describe the design and development of customizable, multilayered phantom models that simulate the mechanical, optical, and acoustic properties of human skin and vessels[62]. The phantom models comprise epidermis, dermis, and hypodermis skin layers, blood vessels, and blood-mimicking fluid (BMF), and each tissue component may be individually tailored to a range of physiological conditions. The models are characterized through uniaxial mechanical testing, rheometry, diffuse reflectance spectroscopy, and acoustic measurements. The results are compared with *in vivo* and *ex vivo* human tissue properties found from the literature.

In Chapter 4.3, I compare the accuracy and speed of automated peripheral vascular access to that of manual cannula insertion using the tissue phantom models[63]. The third-generation device introduced in Chapter 3.6 is used for these studies. Needle insertion parameters and tissue material properties are assessed over broad range of physiological and demographic variables. Device performance is then evaluated against results obtained from unassisted, NIR-guided, and US-guided manual cannulations.

In Chapter 4.4, I evaluate the *in vivo* performance of the device in comparison to unassisted manual cannulations[64]. NIR and US guided cannulations are carried out on the lateral tail veins of

adult Sprague-Dawley rats. The typical diameter of the rat lateral tail vein ranges from 500 to 800 μm, which is smaller than a neonatal peripheral hand or forearm vessel. A number of imaging and robotic configurations are compared, and needle insertion and blood collection success rates are assessed. Then, based on our observations during these studies, a low-cost, handheld cannula insertion device is developed specifically for use in rodents; whereas the human device can potentially improve clinical outcomes, the animal device may alleviate some of the materials costs, labor costs, and experimental errors associated with unsuccessful manual tail vein cannulations in the preclinical research setting. Together, the studies described in this chapter provide *in vitro* and *in vivo* evidence that automated, image-guided venipuncture can outperform manual techniques, particularly in difficult conditions.

4.2. Tunable, multilayered tissue-mimicking skin and vessel phantoms

Tissue-mimicking models (TMM) of human skin and blood vessels have been widely used as test systems for a variety of peripheral imaging techniques and image-guided interventions. These TMM consist of a skin mimicking material surrounding a vessel through which BMF is perfused. An important criterion for the design of the TMM is that the individual components should have similar material properties to soft tissue, vessel tissue, and blood. Of particular interest are models designed to evaluate multimodality imaging techniques and percutaneous needle insertion experiments[231–233]. For such applications, the mechanical, optical, and acoustic properties of the peripheral tissues must all be reproduced, and this greatly increases the complexity of the models.

The literature on the materials used in the design of the TMM is extensive[234–236], and over the years a number of customizable multimodal models have been described. Recently, Lamouche *et. al.* provided a comprehensive review of TMM with controllable optical, mechanical, and structural properties for optical coherence elastography[237]. Their focus was on the effects of different substrates (silicone, fibrin, and polyvinyl alcohol) on optical scattering behavior and mechanical

strength. Madsen *et. al.* demonstrated the use of gelatin/agar TMM for US elastography. They investigated the effects of India ink, Intralipid-20% (IL-20), glycerol, and graphite powder on the acoustic and mechanical properties of the models[238,239]. Cook *et. al.* reported on the design of gelatin-based TMM for photoacoustic imaging[240]. The models used India ink and dyes as the optical absorbers, IL-20 as the optical scatterer and acoustic attenuator, and silica microspheres as the acoustic backscattering agent. In their study, the models were developed as single-component, homogenous bulk materials, and the mechanical properties were not investigated. Hungr *et. al.* developed a deformable polyvinyl chloride prostate TMM for multimodal imaging and percutaneous needle insertion procedures, and characterized the sound velocity, mechanical properties, and effects of long-term storage[241]. In addition to general tissue-mimicking materials, models with vessel-like geometries have also been introduced using materials such as thin-walled silicone tubing[242], polyvinyl alcohol gels[243,244], and gelatin/agar hydrogels[245,246].

Here, I describe the design, fabrication, and characterization of multilayered TMM that mimic the mechanical, optical, and acoustic properties of five peripheral tissues, namely the epidermis, dermis, hypodermis, blood vessels, and blood (**Figure 4-1 (a)**). Each tissue component may be individually tailored to a range of physiological and demographic conditions with the addition of a wide range of modifiers. In this way, the TMM are uniquely suited to serving as test systems for multimodal imaging techniques and image-guided interventions. The TMM are characterized through uniaxial compression and tension experiments, rheological frequency sweep studies, diffuse reflectance spectroscopy, and acoustic pulse-echo measurements. Specifically, the uniaxial compression and tension experiments are performed to measure the Young's modulus E of each phantom tissue component at strains up to 1.0 and strain rates of 10^{-3} to 10^1 s^{-1}. The rheological frequency sweep experiments are conducted to determine dynamic shear modulus G at shear strain rates of 10^{-2} to 10^2 s^{-1}. The diffuse reflectance spectroscopy experiments are conducted to measure the optical absorption μ_a and scattering μ_s' of the tissue layers in the wavelength range

of 400 to 1100 nm by. Finally, acoustic attenuation α, backscatter β, speed of sound c, mass density ρ, and acoustic impedance Z are determined in the frequency range of 2 to 9 MHz using a scanning acoustic microscopy setup with single-element transducers. The results of these studies are then compared with *in vivo* and *ex vivo* tissue data from the literature.

4.2.1. *Methods*

4.2.1.1. *Nomenclature*

δ	=	thickness (mm)		μ_a	=	optical absorption coefficient (cm^{-1})
d	=	diameter (mm)		μ_s	=	optical scattering coefficient (cm^{-1})
E	=	Young's modulus (kPa)		μ_s'	=	optical reduced scattering coefficient (cm^{-1})
G	=	shear modulus (kPa)		λ	=	wavelength (nm)
σ	=	uniaxial stress (kPa)		φ	=	percent volume fraction (%)
ε	=	uniaxial strain (unitless)		ρ	=	mass density (kg m^{-3})
$\dot{\varepsilon}$	=	uniaxial strain rate (s^{-1})		c	=	velocity of sound (m s^{-1})
τ	=	shear stress (kPa)		Z	=	acoustic impedance ($10^6 \cdot$ kg m^{-2} s^{-1})
γ	=	shear strain (unitless)		α	=	acoustic attenuation (dB cm^{-1})
$\dot{\gamma}$	=	shear strain rate (s^{-1})		β	=	acoustic backscatter (sr^{-1} cm^{-1})
η	=	viscosity (kg m^{-1} s^{-1})		f	=	frequency (MHz)

4.2.1.2. *TMM design and fabrication*

Table 4-1 and **Table 4-2** summarize the design and material composition, respectively, of each TMM component. The tissue components were fabricated in 3D-printed square containers (120 x 120 x 21 mm) (**Figure 4-1 (b)**). Flexible and transparent thin-walled PDMS tubing (Sylgard-184 Silicone Elastomer Laboratory Tubing, Dow-Corning Corp., MI, U.S.) were cut to 150 mm in the length and used as blood vessel substitutes. The vessels had diameters ranging from 1 to 3.2 mm and a wall thickness of 0.4 mm (**Figure 4-1 (c, d)**), and were anchored by slots cut into two opposing walls of the phantom container. The depth of each vessel was fixed between 2 and 6 mm from the top of the container and was determined by the position of each slot. The skin mimicking layers were then fabricated and introduced.
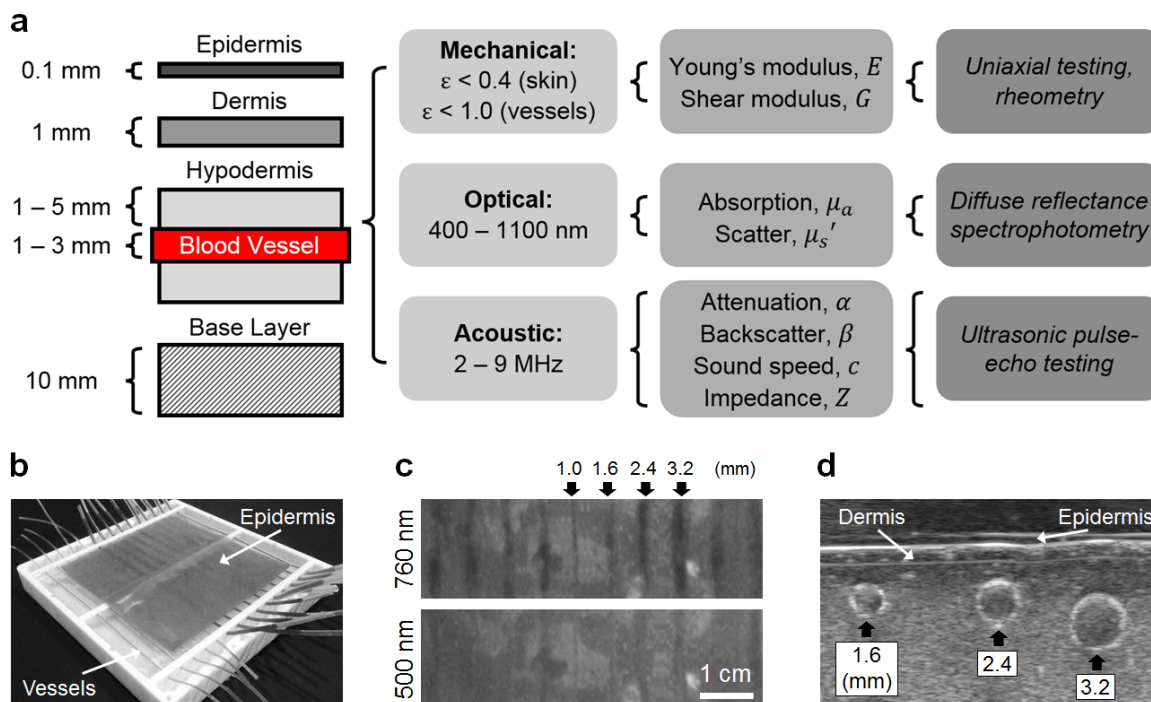
Figure 4-1. Design and characterization of skin and vessel mimicking TMM. **(a)** *Far left:* The TMM comprise a 0.1 mm thick epidermis mimicking layer, a 1 mm thick dermis layer, and a 10 mm thick hypodermis layer. Blood vessel substitutes with diameters between 1 and 3 mm are embedded at varying depths within the hypodermis. Blood mimicking fluid is perfused through the vessels. *Left center:* The TMM simulate the mechanical properties of human skin and vessel tissues for strains up to 0.4 and 1.0, respectively; optical properties between 400 and 1100 nm; and acoustic properties between 2 and 9 MHz. *Right center:* Eight material properties were assessed, and the results were compared to human tissue values from the literature. *Far right:* Experimental techniques used to characterize the material properties of each phantom model tissue component. **(b)** Completed models containing 15 vessels. To aid in visualization of the embedded vessels, absorbers and scatterers were not added to the dermis or hypodermis layers in the photographed phantom and the epidermis layer was cut to a smaller size. **(c)** Images taken at 500 and 760 nm showing vessels with varying diameters embedded at a depth of 3 mm. The difference in image contrast can be observed. **(d)** Transverse US image of phantom acquired at 18 MHz showing the skin layers and vessels.

4.2.1.3. Modification of TMM mechanical properties

Controlling mechanical properties in TMM epidermis layers: Epidermis mimicking films with thickness of 0.1 mm were prepared by dissolving 10g gelatin powder (Type A porcine powder, 300g Bloom, Sigma-Aldrich, Corp., MO, U.S.) and 5g glycerol (49781, ≥98% purity, Sigma-Aldrich) in 100 ml of distilled water. 0.01 to 0.1% glutaraldehyde (G5882, ≥99.5% purity, Sigma-Aldrich) was then added to the solutions, along with varying concentrations of synthetic melanin

(described later). The solutions were poured onto a 12x12 cm Plexiglas plate and dried for 48 hours at 21°C and 28% relative humidity to obtain the thin films.

Controlling mechanical properties in TMM dermis and hypodermis layers: The dermis mimicking layer was fabricated from a mixture of 24% gelatin and 1% agar (A1296 powder, Sigma-Aldrich), while the hypodermis mimicking layer consisted of 2% gelatin and 0.2% agar. A base layer of 8% gelatin was also formed. The gelatin and agar powders were dissolved in separate beakers and then combined, and optical and acoustic modifiers were added (described later).

Table 4-1. Summary of the material properties ($E, G, \mu_a, \mu_s', \alpha, \beta, c, Z,$ and η) investigated. Also shown are the constituent materials that make up the peripheral tissue layers in both humans and TMMs.

Tissue Layer	Material Property	Human Tissue Components	TMM Modifiers
Epidermis	E, G	keratin	gelatin (films)
	μ_a	melanin	synthetic melanin
	μ_s'	melanin	synthetic melanin
	α	keratin, melanin	IL-20, BSA
	β	keratin, melanin	40 μm silica beads
	c, Z	keratin, melanin	glycerol
Dermis	E, G	collagen/elastin	gelatin, agar
	μ_a	hemoglobin	India ink, 552 nm dye
	μ_s'	collagen/elastin	IL-20
	α	collagen/elastin	IL-20, BSA
	β	collagen/elastin	40 μm silica beads
	c and Z	collagen/elastin	methanol
Hypodermis	E, G	adipose	gelatin, agar
	μ_a	adipose, hemoglobin	India ink, 935 nm dye
	μ_s'	adipose	IL-20
	α	adipose	IL-20, BSA
	β	adipose	40 μm silica beads
	c and Z	adipose	methanol
Vessel wall	E, G	collagen/elastin	PDMS
	μ_a	hemoglobin	negligible
	μ_s'	collagen/elastin	negligible
	α	collagen/elastin	PDMS
	β	collagen/elastin	negligible
	c and Z	collagen/elastin	PDMS
Whole blood	η	RBCs	glycerol, dextran
	μ_a	hemoglobin	552 / 757 / 912 nm dyes
	μ_s'	RBCs	negligible
	α	hemoglobin, plasma	negligible
	β	RBCs	5 μm polyamide beads
	c and Z	RBCs, plasma	glycerol, dextran

Table 4-2. Percent concentrations of TMM components used for each tissue mimicking layer.

Tissue Layer	Gelatin (% v)	Agar (% w/v)	Melanin (% w/v)	Absorbing dyes (% w/v)	India ink (% v/v)	IL-20 (% v/v)	BSA (% w/v)	Silica beads (%w/v)	Other
Material properties affected	E, G μ_a α	E, G	μ_a, μ_s'	μ_a	μ_a	μ_s' α	α μ_s'	β μ_s'	
Epidermis	5	-	0.0003 (1% φ_{mel}) 0.0015 (5%) 0.0030 (10%) 0.0047 (15%) 0.0102 (30%) 0.0216 (45%)	-	-	-	-	-	0.01 – 0.1% glutaraldehyde
Dermis	24	1	-	0.058 (552 nm)	0.0182	28.5	35	1.0	15.31% methanol
Hypodermis	2	0.2	-	0.073 (552 nm) 0.047 (935 nm)	0.0202	7.8	15	0.5	23.45% methanol
Vessels	-	-	-	-	-	-	-	-	Commercial PDMS tubing
Blood (venous)	-	-	-	23.19 (552 nm) 1.373 (756 nm) 0.214 (935 nm)	0.0301	-	-	-	Commercial BMF
Blood (arterial)	-	-	-	26.09 (552 nm) 0.374 (935 nm)	0.0301	-	-	-	Commercial BMF
Notes	Gelatin concentration for epidermis layer based on weight % before drying	Calculated as weight % of Sigma-Aldrich A1296 agar powder	Calculated as weight % of Sigma-Aldrich M0418 synthetic melanin powder, ≥97% purity	Absorptivity at 552, 756, and 935 nm: 138, 52, and 187 L g^{-1} cm^{-1}, respectively	Calculated as volume % of undiluted Higgins Waterproof Black Ink	Calculated as volume % of undiluted Fresenius-Kabi IL-20	Calculated as weight % of Roche lyophilized BSA, ≥95% purity	Calculated as weight % of 40 μm diameter MIN-U-SIL silica microspheres	

Table 4-3. Relative composition of human tissues used to inform TMM designs.

Tissue Layer	Volume Percentages (φ) of Tissue Components				
	Melanin	*Collagen, elastin*	*Lipid*	*Hemoglobin*	*Water*
Epidermis	0 to 45%	40%	0%	<1%	15 to 60%
Dermis	0%	50%	0%	<1%	50%
Hypodermis	0%	0%	80%	<1%	20%
Vessel wall	0%	25%	0%	<1%	75%
Whole blood	0%	0%	0%	2%	98%

1.5% Germall-Plus (International Specialty products, Wayne, NJ, U.S.) was also added to serve as an antimicrobial agent[239]. The final solutions were then cooled to 40°C under constant stirring and introduced into the phantom container sequentially. The base layer was first introduced by pouring 8% gelatin solution through a 100 μm sieve (BD Falcon™ Cell Strainer) until a 10 mm thick viscous layer was formed at the bottom of the container. Depending on the height of the vessels, between 1 and 5 mm of spacing remained between the base layer and the vessels. Once the base layer was fully gelled, the hypodermis solution was then added to a total height of 20 mm, allowing the vessels to be fully submerged. After the hypodermis layer was gelled, the dermis solution was added to form a 1 mm layer. Finally, once the dermis layer was gelled, the epidermis film was placed above the dermis to form the topmost layer of the phantom.

Introduction of BMF: A commercial BMF (Model 046 Blood Mimicking Fluid, CIRS Inc., VA, U.S.) described by Ramnarine *et. al.*[247,248] was used here. The BMF consists of a water/glycerol/dextran base and 10 μm polyamide microspheres that mimic the acoustic backscatter of RBCs. The BMF may be passed through the vessels at controlled velocities during experiments, using for example a syringe pump to simulate continuous blood flow in the veins or a peristaltic pump to simulate pulsatile flow in the arteries.

4.2.1.4. *Modification of TMM optical properties*

The main component materials that affect the optical properties of peripheral tissues include melanin in the epidermis, collagen and elastin in the dermis, lipid in the hypodermis, hemoglobin in blood, and water[67,68] (**Table 4-3**). Optical absorption over the wavelength range of 400 to 1100 nm may be estimated as the sum of the individual absorption profiles μ_a^m of each component material m in the tissue and their relative percent volumes φ_m, that is, $\mu_a = \sum_m^n \varphi_m \ \mu_a^m$ [Eqn. 1]. Unlike with absorption, total optical scattering in the tissue is not necessarily equal to the sum of the individual scattering components. Rather, scattering in tissues may be approximated by a

power law expression, $\mu_s' = \mu_{s_1}'(\lambda/500)^{-n_s}$, where μ_{s_1}' is the reduced scattering coefficient at 1 nm and n_s is the power law constant describing the dependence on wavelength[68].

Controlling optical absorption and scattering in the TMM epidermis: Absorption and scattering in the epidermis is primarily due to melanin[76]. In the TMM epidermis layer, synthetic melanin powder (M0418, ≥97% purity, Sigma-Aldrich Corporation, U.S.) was added at concentrations ranging from 0.0003% to 0.0216% to simulate different skin tones. The optical properties of the brand of melanin used in this study has been described in detail by Bashkatov *et. al.*[249]. An advantage of using synthetic melanin is that its index of refraction (~1.65) is relatively similar to that of epidermis tissue (~1.44) compared to other absorbers[250]. Furthermore, because melanin is a strong optical scatterer, additional scattering materials are not needed.

Controlling optical absorption in the TMM dermis and hypodermis: Dermis tissue consists of weak absorbers (collagen, elastin, and minor amounts of hemoglobin), and so absorption is relatively low (<1 cm^{-1})[32]. In hypodermis tissue, absorption is highest at the fat absorption peaks, e.g., at 935 nm, and low elsewhere[74]. We used India ink (Higgins Waterproof Black, Sanford, U.S.) as the broad-spectrum absorber in the TMM dermis and hypodermis layers, and molecular absorbing dyes (QCR Solutions Corp., FL, U.S.) to simulate local absorption peaks. Specifically, 0.0182% of India ink and 0.058% of 552 nm dye were added to the dermis, while 0.0182% of India ink 0.047% of 935 nm dye were added to the hypodermis. The 552 nm and 935 nm dyes were added to simulate the increase in absorption due to hemoglobin and lipid, respectively. The India ink concentrations were determined based on absorption measurements reported by others using the same brand of ink[251], while the dye concentrations were determined from material data sheets.

Controlling optical scattering in the TMM dermis and hypodermis: The presence of collagen and elastin fibers leads to strong optical scattering in the dermis[32], while in the hypodermis the main scatterers are the lipid droplets[74]. To simulate the scattering profile of human skin, 28.5% and 7.8%

Intralipid-20% (IL-20, Fresenius Kaby AB, Sweden) were added as the optical scatterer in the dermis and hypodermis, respectively. Cook *et. al.* have characterized the scattering properties of IL-20, noting that μ_s' is diminished in gelatin compared to water and thus higher concentrations are needed[240]; this decrease in scattering was accounted for when determining IL-20 concentrations for the TMM tissue components. Meanwhile other studies have shown that absorption of IL-20 is negligible, that minimal variability (<2%) is exhibited between brands, batches, and over time, and that IL-20 does not affect the absorption properties of India ink, nor vice versa[252,253].

Controlling optical absorption in BMF: To reproduce the optical absorption of venous and arterial blood, molecular absorbing dyes (QCR Solutions Corp., FL, U.S.) and India ink were added to the commercial BMF. Specifically, dyes with absorption maxima at 552, 757 and 912 nm were used, while India ink provided the baseline absorption (colored inks such as Congo Red and Evans Blue may be used as low-cost alternatives to the molecular dyes[240]).

4.2.1.5.   Modification of TMM acoustic properties

Acoustic attenuation in most human tissues is known to increase with frequency following the power law function $\alpha = \alpha_1 f^{n_\alpha}$ dB cm^{-1}, where α_1 is the attenuation coefficient at 1 MHz, n_α is the power constant, and f is the frequency[77]. Similarly, acoustic backscatter may be modeled as $\beta = \beta_1 f^{n_\beta}$ [sr^{-1} cm^{-1}], where β_1 is the backscatter coefficient and n_β is the power constant. On the other hand, we assumed that speed of sound and acoustic impedance were constants with respect to frequency (valid for human tissues).

Controlling acoustic attenuation and backscatter in TMM tissues: Gelatin, agar, and IL-20 are all weak acoustic attenuators[239,240,254], and thus the addition of a modifier with strong attenuating properties is needed. Unfortunately, most attenuators affect the optical and/or mechanical properties of the materials to some extent. An exception is bovine serum albumin (BSA), which is optically transparent when dissolved in aqueous solution. The attenuation coefficient α_1 of 1%

BSA is ~0.02 dB cm^{-1} MHz^{-1} and   increases linearly with concentration[255,256]. Here we added 35% lyophilized BSA (≥95% purity, Roche Diagnostics, U.S.), which was expected to raise α_1 in the dermis layer from ~0.5 to ~1.1 dB cm^{-1} MHz^{-1}. Similarly, 15% BSA was added to the hypodermis layer to raise α_1 from ~0.3 to ~0.6 dB cm^{-1} MHz^{-1}. In both layers, BSA was slowly dissolved into solution at 30°C, which is well below its denaturing temperature. BSA was not added to the epidermis layer, vessels, or blood.

To modify the acoustic backscatter parameters in the dermis and hypodermis, 40 μm diameter monodisperse silica microspheres (MIN-U-SIL-4, Sigma-Alrich) were added at 0.5% and 1%, respectively. At such concentrations, the backscatter coefficient β_1 was expected to be on the order of 10^{-3} sr^{-1} cm^{-1} MHz^{-1}, which is in the range of human skin and fatty tissues[240]. As with BSA, the silica spheres were chosen over alternative materials due to their optical transparency.

Controlling speed of sound (and acoustic impedance) in TMM tissues: Varying the gelatin concentration from 2 to 24% has been shown to increase speed of sound linearly from 1490 to 1560 m s^{-1} (increase of ~3.2 m s^{-1} for each percent of gelatin added)[240]. Similarly, increasing the agar concentration from 0.2 to 2% increases speed of sound linearly from 1482 to 1500 m s^{-1} (~1 m s^{-1} per 0.1% agar)[254]. Likewise, BSA has been observed to increase speed of sound by ~3 m s^{-1} for each percent added[255,256]. In contrast to the above materials, IL-20 has minimal effect on sound speed[240], and the other modifiers (India ink, absorbing dyes, and silica beads) were all present in very low concentrations (≤1%) and thus were not expected to significantly affect speed of sound.

Based on the material composition of the TMM skin layers, the estimated speed of sound and acoustic impedance in the dermis layer (c ~ 1642 m s^{-1}, Z ~ 1.7×10^6 kg m^{-2} s^{-1}) and hypodermis layer (c ~ 1522 m s^{-1}, Z ~ 1.7×10^6 kg m^{-2} s^{-1}) were expected to be higher than measurements on human dermis (c ~ 1595 m s^{-1}, Z ~ 1.7×10^6 kg m^{-2} s^{-1}) and hypodermis (c ~ 1450 m s^{-1}, Z ~ 1.7×10^6 kg m^{-2} s^{-1})[78,79]. To compensate for this, methanol was introduced into the dermis and

hypodermis layers at concentrations of 15.31% and 23.45%, respectively. Methanol is known to decrease speed of sound by 3.77 m s^{-1} for each percent added, and like BSA causes no measurable changes to the optical or mechanical properties of the material[236,238].

Meanwhile, the estimated speed of sound and impedance in the epidermis layer ($c \sim 1625$ m s^{-1}, $Z \sim 1.7 \times 10^6$ kg m^{-2} s^{-1}) was expected to remain in range of measurements on human epidermis ($c \sim 1645$ m s^{-1}, $Z \sim 1.7 \times 10^6$ kg m^{-2} s^{-1})[78]. Finally, in the vessels, acoustic properties were determined entirely by Sylgaard-184 PDMS ($c \sim 1030$ m s^{-1}, $Z \sim 1.7 \times 10^6$ kg m^{-2} s^{-1}). These values are lower than measurements on human vessel wall tissue ($c \sim 1575$ m s^{-1}, $Z \sim 1.7 \times 106$ kg m^{-2} s^{-1}), and this disparity is a potential limitation of the commercial vessel substitutes. In this study, the mass densities of the phantom tissue components were not independently modified. To the best of our knowledge, changes in mass density with respect to gelatin, IL-20, and BSA concentration have not yet been fully characterized in the literature.

4.2.1.6. Packaging and storage

The crosslinked epidermis layer helps to reduce drying of the dermis and hypodermis layers below. The addition of Germall-Plus further prolongs the shelf-life by mitigating microbial or fungal infiltration. The models, once fully gelled in the 3D-printed containers, are wrapped in Saran Wrap and packaged in vacuum-sealed bags (FoodSaver V2244 Sealing System). The TMMs are then stored at room temperature (21°C).

4.2.2. Results

4.2.2.1. Characterization of TMM mechanical properties

Elasticity of gelatin and agar gels at varying concentrations: We first measured the true stress vs. strain responses of 2, 4, 8, 12, 16, 20, and 24% gelatin (**Figure 4-2 (a)**) and 0.1, 0.5, 1, and 2% agar (**Figure 4-2 (b)**). Measurements were obtained from unconfined uniaxial compression tests

(ElectroForce 3200 Test Instrument, Bose Corp., MA, U.S.), and the gels were assumed to be incompressible. The gels were compressed to a strain of 0.5 at five strain rates (10^{-3} to 10^{-1} s^{-1}), and Young's modulus was defined as the slope of the stress response in the low strain regime ($\varepsilon < 0.2$). For both types of gels, Young's modulus was seen to depend on gel concentration and strain rate.
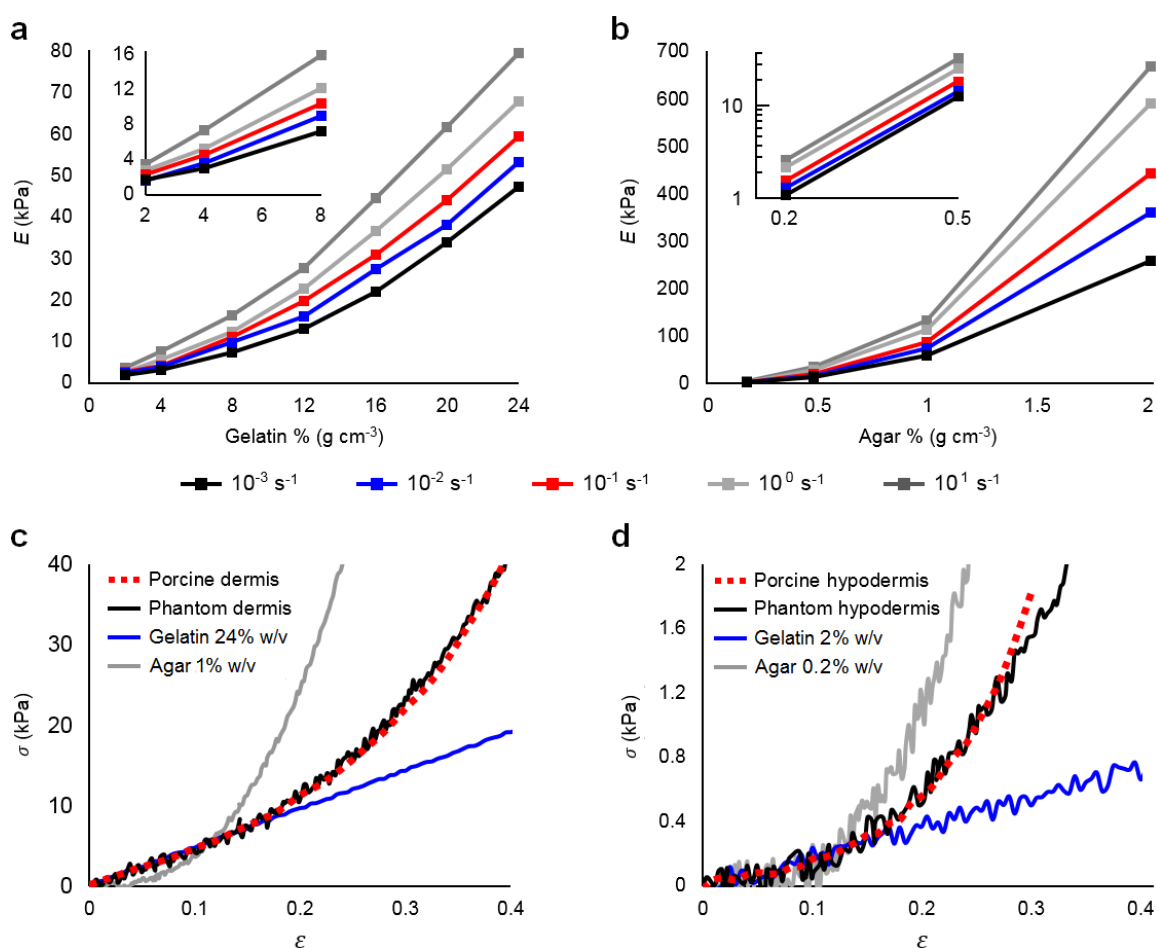
Figure 4-2. Mechanical characterization of gelatin, agar, and TMM skin layers. **(a)** Young's moduli E for 2 to 24% gelatin, measured during uniaxial compression over five strain rates ($\dot{\varepsilon} = \mathbf{10^{-3}}$ **to** $\mathbf{10^{1}}$ **s^{-1}**). **(b)** Young's moduli E for 0.2 to 2% agar ($\dot{\varepsilon} = \mathbf{10^{-3}}$ **to** $\mathbf{10^{1}}$ **s^{-1}**) from uniaxial compression. **(c)** Compressive true stress vs. strain curves for dermis mimicking layer in comparison to *ex vivo* porcine dermis[176]. Phantom and human measurements were both obtained from unconfined uniaxial compression tests at $\dot{\varepsilon} = \mathbf{10^{-1}}$ **s^{-1}**. Pure gelatin exhibited perfectly linear elasticity for $\boldsymbol{\varepsilon < 0.5}$ (blue line), while pure agar exhibited a highly nonlinear stress vs. strain relationship (gray line). Phantoms combining 24% gelatin and 1% agar (black line) were found to most closely mimic porcine dermis tissue (red dotted line). **(d)** Compressive true stress vs. strain curves for TMM hypodermis compared to *ex vivo* porcine hypodermis tissue[173]. Measurements were at $\dot{\varepsilon} = \mathbf{10^{-1}}$ **s^{-1}**. Phantoms combining 2% gelatin and 0.2% agar most closely mimicked porcine hypodermis tissue.

Thickness and elasticity of TMM dermis and hypodermis: Mean thickness values for the TMM dermis and hypodermis layers were 1.4 and 2.1 mm, respectively (**Table 4-4**). Measurements were made on four dermis samples and four hypodermis samples from B-mode images acquired with an 18 MHz US transducer ((L1830, Telemed UAB, Lithuania). Stress vs. strain responses were then obtained for the dermis and hypodermis samples (**Figure 4-2 (c, d)**). At low strains ($\varepsilon < 0.2$), the stiffness of the layers was provided by the gelatin component, and the stretch behavior was linearly elastic. Young's modulus of the TMM dermis was ~50 kPa for strains below 0.2 (**Table 4-5**) and approximated that of porcine dermis[176]. Similarly, the hypodermis TMM tissue was linearly elastic for strains below 0.2, and Young's modulus (~2 kPa) approximated that of porcine hypodermis tissue[173]. In contrast, for $\varepsilon > 0.2$, rapid strain hardening was observed in both the TMM and porcine skin tissues. In the TMM, this nonlinear behavior was predominantly due to the agar component.

Following the addition of 28.5% IL-20 and 35% BSA, the Young's modulus of the dermis layer decreased by a mean of 0.81 kPa over four samples. Similarly, the Young's modulus of the TMM hypodermis decreased by 0.22 kPa after adding 7.8% IL-20 and 15% kPa. However, in both cases, the differences were smaller than the variability between samples and thus were likely to be insignificant. The other modifiers were present in very low concentrations (≤1%) and were not expected to measurably alter the mechanical properties of the models.

Dynamic shear properties of TMM dermis and hypodermis: **Figure 4-3** shows the frequency dependence of shear modulus in the dermis and hypodermis mimicking phantoms. Measurements were obtained from rheometry experiments (Ares G2 Rheometer, TA Instruments, U.S.) at a shear strain of 0.5 and shear rates ranging from 10^{-2} to 10^{2} s^{-1}. The shear modulus of the TMM were comparable to measurements on human skin tissues[160,174] (

Table 4-6).

Thickness and elasticity of TMM epidermis: The mean thickness of the epidermis films over four samples was measured by US to be 0.12 mm, which is comparable to the thickness of the human epidermis[157,159,168]. Each film contained 0.0102% melanin, which corresponds to a melanin volume fraction φ_{mel} of 30% (see **Table 4-3**). **Figure 4-4** shows the Young's modulus of epidermis films crosslinked with 0.01, 0.025, 0.05, 0.075, or 0.1% glutaraldehyde. All films exhibited linearly elastic behavior under tensile stress until fracture at a strain of 0.2. The addition of 0.025% glutaraldehyde produced films with Young's modulus of ~1 MPa, which is comparable to indentation results on *ex vivo* human epidermis[159].

Diameter, wall thickness, and elasticity of TMM blood vessels: **Figure 4-5** shows the results of uniaxial tension experiments performed over varying strain rates on the TMM vessels. Results were compared to tensile measurements on *ex vivo* human venous and arterial wall[186]. At strains below 0.5, the vessels were linearly elastic and Young's modulus was ~1 MPa. At strains above 0.5, strain hardening was observed.
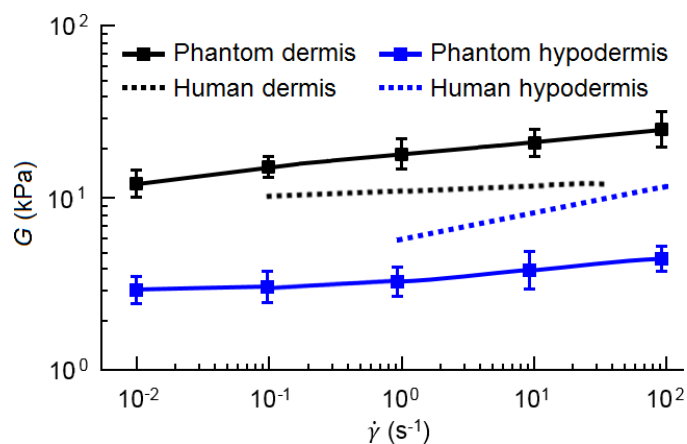
Figure 4-3. Shear modulus *G* of TMM dermis (black) and hypodermis (blue). Measurements were obtained from rheological frequency sweep at a shear strain γ of 0.5. Shear strain rates were increased from $\mathbf{10^{-2}}$ **to** $\mathbf{10^{2}}$ $\mathbf{s^{-1}}$. The magnitude and strain rate dependence of the TMM skin layers are comparable to those of human skin tissues (dotted lines)[160,174].
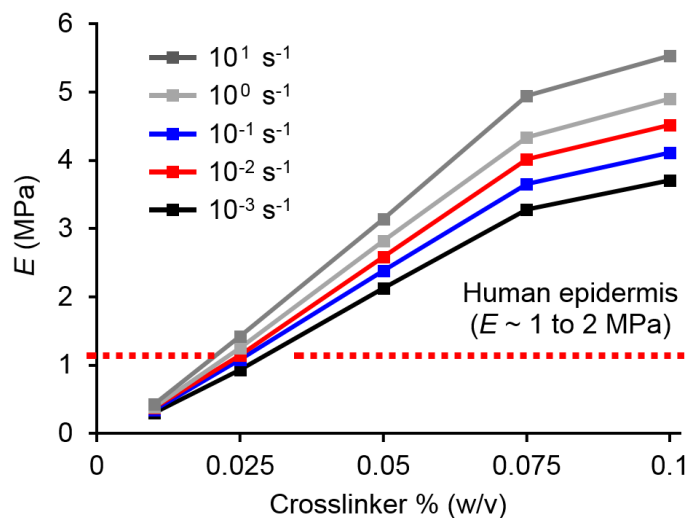
Figure 4-4. Young's modulus E of epidermis mimicking gelatin sheets. The TMM epidermis tissues were crosslinked 0.01 to 0.1% glutaraldehyde. Young's modulus was measured from tensile experiments over five strain rates ($\dot{\varepsilon} = 10^{-3}$ to 10^{1} s^{-1}). For $\varepsilon < 0.2$, E was closest to that of human epidermis (~1.2 MPa, red dotted line)[159] using 0.025% glutaraldehyde.
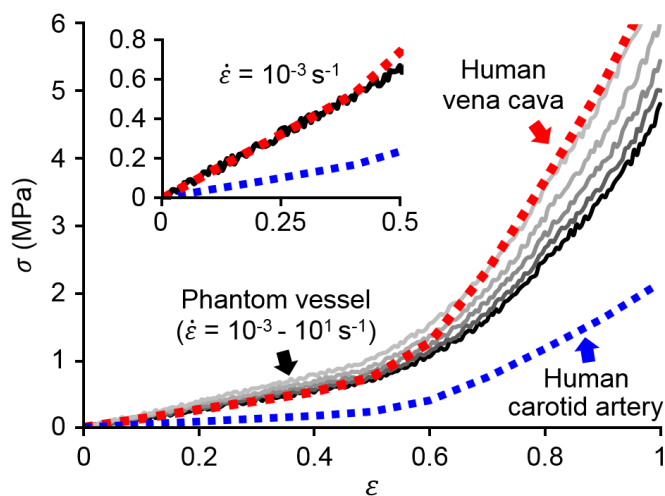
Figure 4-5. Tensile stress vs. strain curves for TMM vessels. Shown are results for model vessels (solid black and grey lines) compared to *ex vivo* human adult vena cava (red dotted line) and carotid artery (blue dotted line)[186]. The lightest-colored grey line corresponds to the slowest strain rate ($\dot{\varepsilon} = 10^{-3}$ s^{-1}) while the black line corresponds to the fastest strain rate ($\dot{\varepsilon} = 10^{1}$ s^{-1}). The diameter of the vessels was 2 mm. Inset plot shows the linear region of stretch ($\varepsilon < 0.5$) for TMM and human vessels at comparable strain rates ($\dot{\varepsilon} = 1.0 * 10^{-3}$ s^{-1} for TMM vessels, while $\dot{\varepsilon} = 1.6 * 10^{-3}$ s^{-1} for human vessels).

Table 4-4. Thickness, δ (in mm) of TMM and human skin, vessel wall, and blood.

Tissue Layer	TMM (mm)	Human (mm)	Body Location (Measurement Technique)	Ref.
Epidermis	0.117 ± 0.022	0.075 ± 0.016	forearm	[157]
		0.095 ± 0.005	forearm	[159]
		0.138 ± 0.013	forearm	[168]
Dermis	1.385 ± 0.167	0.92 ± 0.12	forearm	[162]
		1.14 ± 0.20	forearm	[167]
		1.16 ± 0.16	forearm	[164]
		1.35 ± 0.10	forearm	[166]
Hypodermis	2.093 ± 0.514	1.21 ± 0.32	forearm	[164]
		2.15 ± 0.64	forearm	[171]
Vessel Wall	1.19 to 3.18 (*diameter*) 0.28 to 0.51 (*wall thickness*)	2.1 ± 1.1 (d_{vein}) 3.0 ± 0.8 (d_{artery}) 0.31 ± 0.07 (δ_{vein}) 0.40 ± 0.08 (δ_{artery})	forearm	[181]

Table 4-5. Young's modulus, E (in kPa) of TMM and human skin, vessel wall, and blood.

Tissue Layer	TMM (kPa)	Human (kPa)	Body Location (Measurement Technique)	Ref.
Epidermis	$0.997 \pm 0.138 \cdot 10^3$ ($\varepsilon < 0.2$, $\dot{\varepsilon} = 10^{-1}\,s^{-1}$)	1 to $2 \cdot 10^3$	abdomen (indentation)	[159]
Dermis	50.71 ± 2.982 ($\varepsilon < 0.1$, $\dot{\varepsilon} = 10^{-1}\,s^{-1}$)	35	forearm (indentation)	[169]
		56	forearm (suction)	[168]
		~50 ($\varepsilon < 0.1$)	buttock, porcine (compression)	[176]
Hypodermis	1.76 ± 0.375 ($\varepsilon < 0.1$, $\dot{\varepsilon} = 10^{-1}\,s^{-1}$)	2	forearm (indentation)	[169]
		1.6 ($\varepsilon < 0.1$)	abdomen (tensile)	[171]
		1–2.5 ($\varepsilon < 0.1$)	abdomen, porcine (compression)	[164]
Vessel Wall	912.58 ± 11.32 ($\varepsilon < 0.5$, $\dot{\varepsilon} = 10^{-1}\,s^{-1}$)	$0.5 \cdot 10^3$ (vein, $\varepsilon < 0.4$) $1.0 \cdot 10^3$ (artery, $\varepsilon < 0.4$)	porcine (tensile)	[181]

Table 4-6. Shear modulus, *G* (in kPa) of TMM and human skin, vessel wall, and blood.

Tissue Layer	TMM (kPa)	Human (kPa)	Body Location (Measurement Technique)	Ref.
Epidermis	-	~10	abdomen (rheometry)	160
Dermis	14.43 ± 2.88 ($\gamma = 0.5$, $\dot{\gamma} = 1$ s^{-1})	~10	forearm (rheometry)	174
Hypodermis	3.25 ± 0.91 ($\gamma = 0.5$, $\dot{\gamma} = 1$ s^{-1})	~5	abdomen, porcine (rheometry)	174
Vessel Wall	-	~75	aorta, porcine (torsion test)	188

4.2.2.2.   Characterization of TMM optical properties

Measurements of transmittance and diffuse reflectance were obtained for the epidermis, dermis, and hypodermis mimicking TMM layers in the 400 to 1100 nm wavelength range using a commercial spectrophotometer (HR4000 UV-NIR, Ocean Optics, Inc., FL, U.S.) coupled to an integrating sphere (IS200-4 2", Thorlabs, Inc., NJ, U.S.). The inverse adding-doubling method[257] was applied to determine absorption and reduced scattering coefficients (μ_a and μ_s', respectively) (**Table 4-7**) from the transmittance and reflectance data.

Optical absorption and scattering in the TMM skin layers: **Figure 4-6 (a)** shows the absorption profiles of six different epidermis mimicking films in comparison to human epidermis measurements[76]. The absorption profiles were observed to follow a power law function, $\mu_a(\lambda) = \varphi_{mel} \ 1.2(\lambda/500)^{-0.7}$, with φ_{mel} ranging from 1% (very light-toned skin) to 45% (very dark-toned skin). The absorption profiles for the dermis and hypodermis mimicking layers are shown in **Figure 4-6 (b, c)** in comparison to results for human skin[32,74]. The baseline absorption due to India ink can be seen, as can the absorption peaks of the 552 nm dye in the dermis layer and the 935 nm dye in the hypodermis layer. **Figure 4-6 (d–f)** show scattering curves for the three skin mimicking layers in comparison to measurements on *ex vivo* human tissues[32,74].
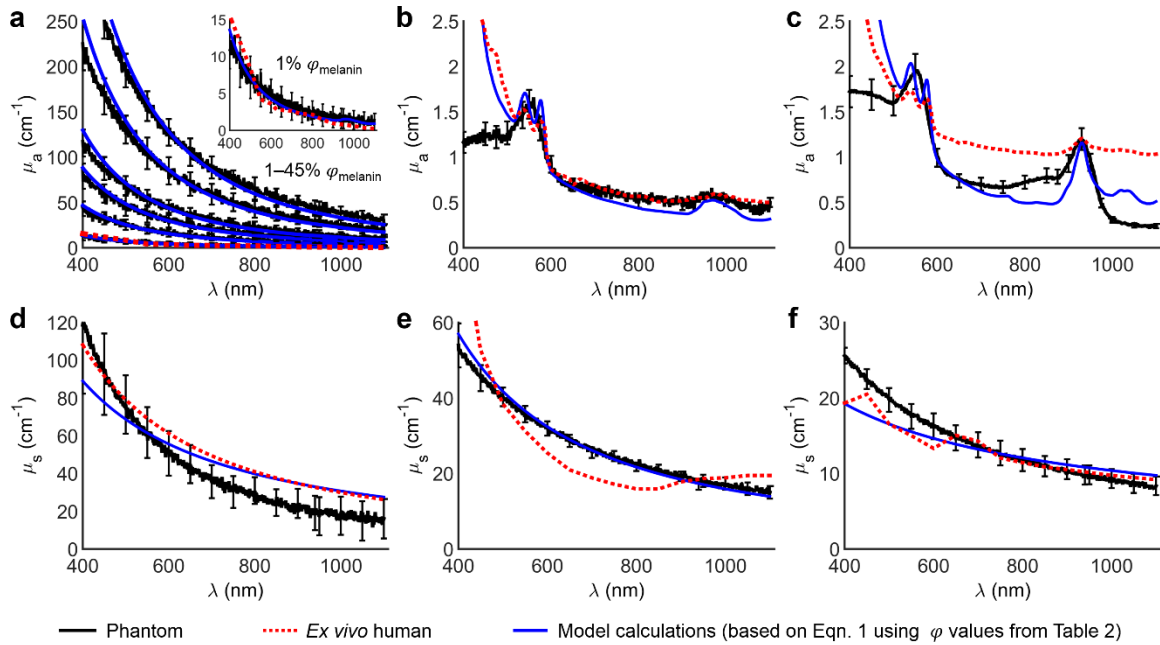
Figure 4-6. Optical absorption (μ_a, top row) and reduced scattering (μ_s', bottom row) of TMM and human skin layers. **(a)** Absorption profiles of TMM epidermis (black lines) from 400 to 1100 nm at 1, 5, 10, 15, 30, and 45% φ_{mel}. Absorption profiles were compared to desired model calculations (blue lines), derived using Eqn. 1 with φ values taken from **Table 4-3**. Also shown is the absorption curve for *ex vivo* Caucasian human epidermis[76] (red dotted lines). Inset plot shows absorption profiles for TMM and human epidermis having 1% $\varphi_{melanin}$. **(b, c)** Absorption profiles of TMM dermis and hypodermis compared to model calculations and *ex vivo* human dermis[32] and hypodermis results[74]. **(d)** Scattering profiles of TMM epidermis in comparison to model calculations and *ex vivo* human epidermis[76]. φ_{mel} for the TMM shown here was 15%. **(e, f)** Scattering profiles of TMM dermis and hypodermis compared to model calculations and *ex vivo* human measurements[32,74].

Optical properties of TMM vessels: The optical properties of the vessel wall are similar to those of dermis tissue, since the constituent materials for both tissues are similar[71]. The Sylgard 184 PDMS material in the commercial vessel tubing absorbs and scatters light minimally ($\mu_a \sim \mu_s' \sim 0 \ cm^{-1}$)[258]. The refractive index of Sylgard 184 PDMS is 1.40, which is comparable to that soft tissue (1.36 to 1.44)[250]. Thus it can be assumed that the vessels are optically transparent within the models.

Optical properties of BMF: The absorption spectra of venous and arterial BMF are shown in **Figure 4-7** in comparison to human whole blood[75]. Before the addition of the molecular dyes,

absorption was substantially lower in the BMF (< 1 cm^{-1}) than in human blood. After adding the dyes, the absorption peaks at 552 and 756 nm due to hemoglobin, as well as the absorption peak at 935 nm due to adipose tissue in the hypodermis, could be observed. Optical scattering in the BMF were not characterized here and will be a focus of future studies.
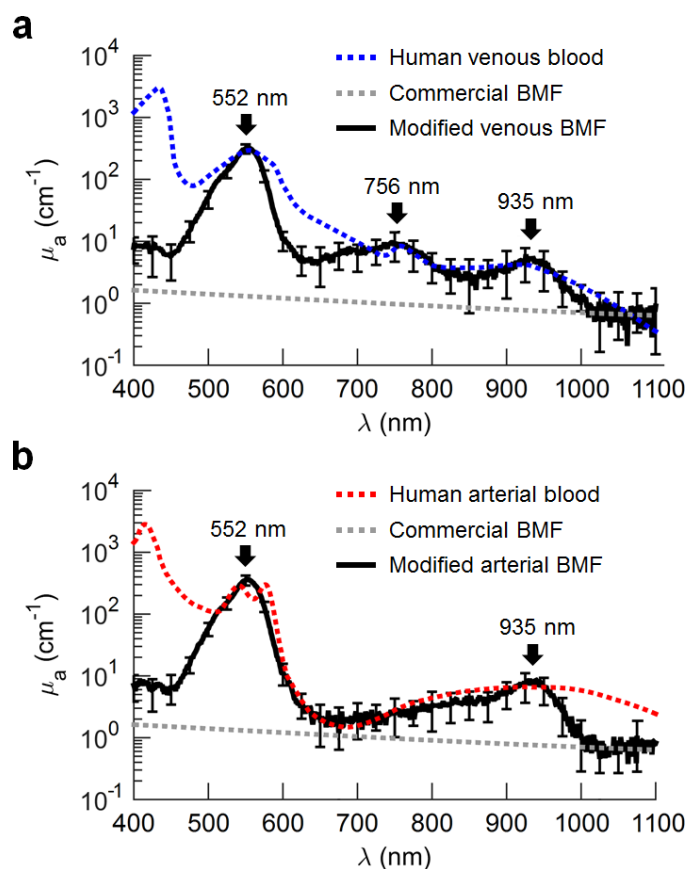
Figure 4-7. Absorption of **(a)** venous and **(b)** arterial blood mimicking fluids in comparison to human blood[75]. Hemoglobin absorption peaks were observed in the models after the addition 552 and 756 nm dyes (black arrows). Baseline absorption provided by India ink (dotted gray lines). Four samples of venous BMF and arterial BMF were tested. Absorption of the BMF, before addition of dyes, was negligible.

Table 4-7. Summary of optical properties of TMM and human skin, vessel wall, and blood.

Tissue Layer		Absorption (μ_a), cm⁻¹			Scatter (μ_s') , cm⁻¹					Ref(s)
		556 nm	758 nm	914 nm	556 nm	758 nm	914 nm	μ_{s_1}	n_s	
Epidermis (15% φ_{mel})	Human	53.64	23.41	14.25	60.73	42.38	34.10	68.70	1.16	76
	TMM	*49.73±5.14*	*25.02±2.93*	*15.06±1.62*	*51.99±12.28*	*29.86±10.45*	*17.98±6.78*	*67.01*	*2.11*	
Dermis	Human	1.56	0.58	0.48	39.55	25.46	19.52	*46.0*	*1.42*	32
	TMM	*1.43±0.19*	*0.50±0.14*	*0.38±0.16*	*38.09±3.00*	*22.12±2.33*	*18.01±2.12*	*40.32*	*1.31*	
Hypodermis	Human	1.67	0.57	0.89	17.13	13.92	12.27	*18.4*	*0.67*	74
	TMM	*1.91±0.26*	*0.66±0.18*	*1.05±0.22*	*23.44±2.14*	*13.87±1.88*	*9.46±1.05*	*20.01*	*0.87*	
Vessel Wall	Human	12.0	0.51	0.31	36.1	23.1	17.6	*42.1*	*1.45*	71
	TMM	-	-	-	-	-	-	-	-	
Blood (venous)	Human	294.52	8.43	4.20	20.5	16.7	14.8	*22.0*	*0.66*	75
	TMM	*310.37±4.98*	*9.32±1.93*	*4.47±0.76*	-	-	-	-	-	
Blood (arterial)	Human	286.17	3.10	6.58	20.5	16.7	14.8	*22.0*	*0.66*	75
	TMM	*352.99±3.45*	*2.45±0.87*	*6.28±0.51*	-	-	-	-	-	

4.2.2.3.   *Characterization of TMM acoustic properties*

Speed of sound and attenuation were measured from 2 to 9 MHz. Backscatter measurements were made at 3 MHz. The specific methods used to calculate sound speeds, attenuation coefficients, and backscatter coefficients from calibrated radiofrequency pulse-echo signals have been previously described in detail[259,260]. Two single-element transducers were used for these studies. The first had a diameter of 13 mm, a center frequency of 3.8 MHz, and bandwidth of 50% (-6 dB) from 2 to 6 MHz. The second transducer had a diameter of 10 mm, a center frequency of 7.2 MHz, and bandwidth of 50% (-6 dB) from 4.5 to 9 MHz. The transducers were mounted in a water filled tank at 20.3°C and positioned 12.75 mm (the focal distance of the transducers) above a quartz block that served as a reference reflector. For each sample, 400 pulse-echo signals were generated over a 2x2 cm area using an XYZ scanning stage. The signals were controlled by a Panametrics 5800 pulser/receiver and read by a Tektronix TDS 320 oscilloscope. The mass density of each sample was also measured. For this, a calibrated pycnometer with 0.1 mg resolution (DIN 12797, Tamson, Zoetermeer, NL) was used.
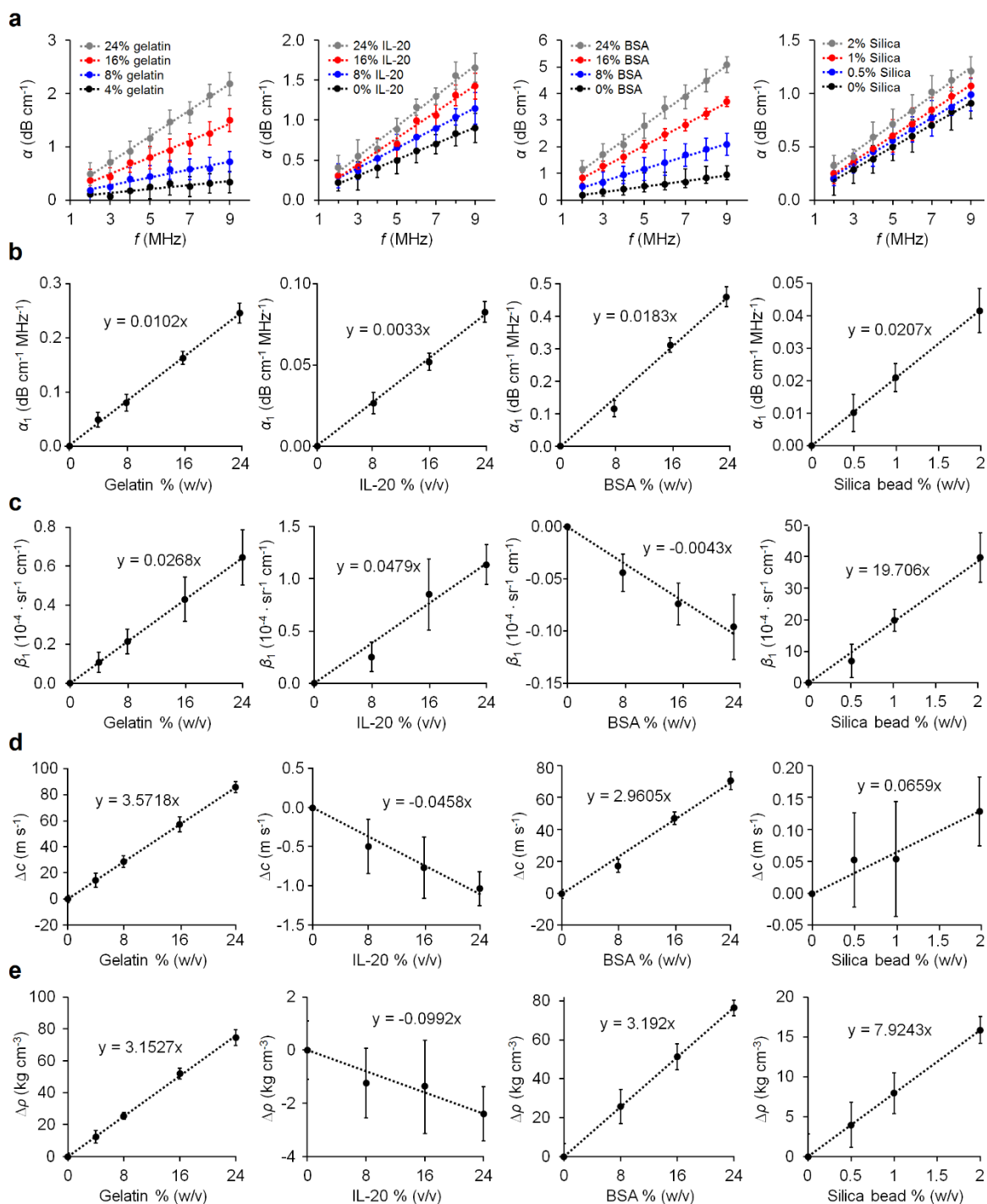
Figure 4-8. Acoustic properties of gelatin, IL-20, BSA, and silica microspheres. **(a)** Acoustic attenuation α increased linearly with increasing concentrations of attenuating materials. Dotted lines show linear fits. Error bars show standard deviations over four replicate samples. For the plots of IL-20, BSA, and silica microspheres, black dots show attenuation of 8% gelatin TMM without any additional modifiers, while the blue, red, and gray lines show 8% gelatin with the addition of increasing concentrations of each modifier. **(b)** Change in the attenuation coefficient α_1 of each material calculated from the slopes of the linear fit lines in

(a). For IL-20, BSA, and silica beads, α_1 was determined after subtracting the attenuation due to 8% gelatin (black dotted lines). **(c)** Change in backscatter coefficients β_1 of each material from the baseline backscatter of 8% gelatin. Backascatter measurements were made at 3 MHz. **(d)** Change in the speed of sound c with respect to the baseline speed of sound of 8% gelatin (1538.2 m s^{-1}). **(e)** Change in mass density ρ. For gelatin, the change in density is shown with respect to the density of water (1000 kg m^{-3}). For IL-20, BSA, and silica beads, the changes in density are shown with respect to the baseline density of 8% gelatin (1030 kg m^{-3}).

Acoustic properties of gelatin, IL-20, BSA, and silica microspheres: The acoustic properties of 4, 8, 16, and 24% gelatin were first measured without the addition of any modifiers. 8% gelatin models were then modified with the addition of IL-20, BSA, or silica at three different concentrations. Attenuation, backscatter, and speed of sound were observed to change linearly with concentration (**Figure 4-8**). The attenuation coefficient α_1 of gelatin increased by 0.010 dB cm^{-1} MHz^{-1} for each percent of gelatin added. The increase in α_1 for each percent of IL-20, BSA, and silica was 0.003, 0.018, and 0.021 dB cm^{-1} MHz^{-1}, respectively (**Figure 4-8 (a, b)**). Backscatter coefficients β_1 were low for gelatin, IL-20, and BSA (~10^{-5} to 10^{-6} sr^{-1} cm^{-1} MHz^{-1}), whereas the addition of silica beads resulted in a substantially higher β_1 of ~10^{-3} sr^{-1} cm^{-1} MHz^{-1}. The backscatter power constant n_β for all four materials was ~1 (**Figure 4-8 (c)**). The speed of sound of 8% gelatin was measured to be 1538.2 m s^{-1}. Relative to this baseline measurement, speed of sound increased by 3.57 m s^{-1} for each added percent of gelatin and 2.96 m s^{-1} for each added percent of BSA. Conversely, changes due to IL-20 and silica beads were negligible (**Figure 4-8 (d)**). Finally, mass density increased with gelatin and BSA concentration, but did not change with IL-20 or silica bead concentration (**Figure 4-8 (e)**).

Acoustic properties of the TMM skin layers and vessel wall: The acoustic properties of the TMM are summarized in **Table 4-8** and compared to the acoustic properties of human peripheral tissues. The mass densities of the TMM tissue components were comparable to the densities of the human tissues, with the largest deviation observed in the hypodermis layer. Similarly, the speed of sound in the three TMM skin layers were all within 20 m s^{-1} of the human reference data. On the other hand, the speed of sound in the PDMS material making up the vessel wall was significantly

lower than the speed of sound in human vessel wall tissue, leading to a lower acoustic impedance, as discussed earlier. Attenuation in the TMM dermis, hypodermis, and vessel wall increased linearly with frequency ($n_\alpha = 1$) (**Figure 4-9**), and the attenuation coefficients (respectively, 1.08, 0.58, and 1.14 dB cm^{-1} MHz^{-1}) closely approximated those of the human tissues. Attenuation in the epidermis layer was not measured. Backscatter coefficients of the dermis and hypodermis layers, measured at 3 MHz, ranged from 1 to 2 $\cdot$ 10^{-3} sr^{-1} cm^{-1} MHz^{-1} and were due almost entirely to the presence of silica beads. Backscatter in the epidermis was not measured, and backscatter from the PDMS of the vessel wall was lower than the sensitivity of the instrument.

Acoustic properties of BMF: The mass density and speed of sound measurements obtained on the commercial BMF (**Table 4-8**) were in agreement with the results reported in Ramnarine *et. al.*[247,248] and are comparable to measurements on human whole blood[79,261]. The addition of dyes did not cause any observable changes in the mass density or the speed of sound of the fluid. Attenuation and backscatter were below the sensitivity of the instrument.
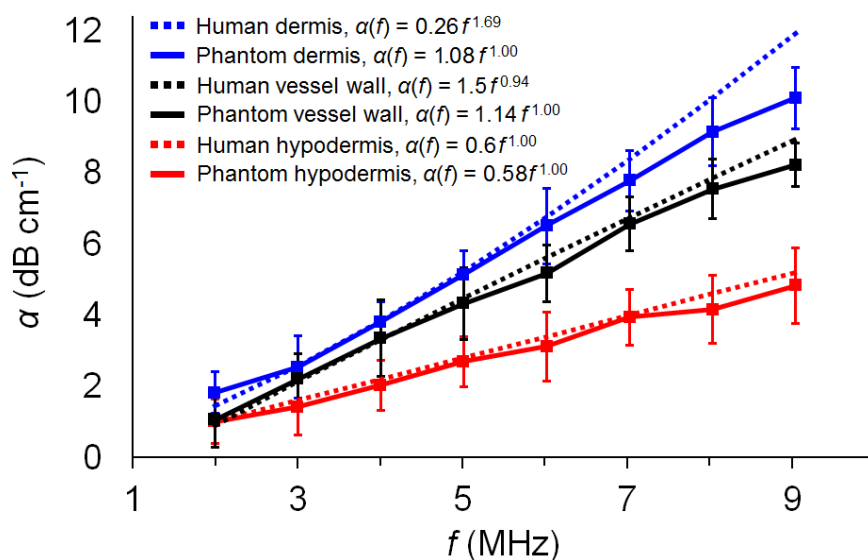
Figure 4-9. Acoustic attenuation α of TMM dermis, hypodermis, and vessel wall (solid lines). Measurements were made in the frequency range of 2 to 9 MHz and compared to human data from literature (dotted lines)[78,79,262]. The power law parameters α_1 **and** n_α are also shown for each tissue.

Table 4-8. Summary of acoustic properties of TMM and human skin, vessel wall, and blood.

Tissue Layer		ρ (kg m^{-3})	c (m s^{-1})	Z ($10^6 \cdot$ kg m^{-2} s^{-1})	α_1 (dB cm^{-1} MHz^{-1})	n_a	β_1 ($10^{-4} \cdot$ sr^{-1} cm^{-1} MHz^{-1})	n_β	Ref(s)
Epidermis	Human	1233	1645	1.99	0.44	1.6	~50	3.8	78
	TMM	*1250.8 ± 14.1*	*1625.3 ± 9.71*	*2.03 ± 0.035*	*-*	*-*	*-*	*-*	
Dermis	Human	1151	1595	1.8	0.26	1.7	~20	2.8	78
	TMM	*1064.2 ± 4.2*	*1593.1 ± 6.32*	*1.70 ± 0.013*	*1.08 ± 0.23*	*1.0*	*19.7 ± 4.2*	*1.0*	
Hypodermis	Human	928	1450	1.38	0.60	1.0	~5	1.0	79
	TMM	*1035.1 ± 6.3*	*1443.0 ± 5.55*	*1.49 ± 0.015*	*0.58 ± 0.19*	*1.0*	*8.1 ± 2.5*	*1.0*	
Vessel Wall	Human	1065	1600	1.70	1.50	0.9	~20	1.6	262,263
	TMM	*1030.1 ± 3.5*	*1089.2 ± 2.24*	*1.12 ± 0.006*	*1.14 ± 0.16*	*1.0*	*-*	*-*	
Blood	Human	1050	1584	1.66	0.15	1.2	~0.1	3.5	247,261
	TMM	*1037.4 ± 4.8*	*1578.4 ± 5.15*	*1.64 ± 0.010*	*-*	*-*	*-*	*-*	

4.2.2.4.   Quantitative comparison of TMM and human tissue material properties

The Young's modulus, optical absorption, optical scattering, and acoustic attenuation measurements obtained from the TMM were quantitatively compared to human tissue literature data using RMSE and normalized root mean squared percent error (n-RMSE %)[264], respectively defined as:

$$\text{RMSE} = \sqrt{\frac{\sum_{t=1}^{n}(\hat{m} - m)^2}{n}}$$

$$\text{nRMSE\%} = 100\% \ \times \text{RMSE}/\bar{m}$$

where $\hat{m}$ is the measured material property in the phantom, m is the desired material property from the human tissue data, $\bar{m}$ is the mean value for the human tissue data, and n is the number of data points. RMSE is expressed in the same units as the material property, while n-RMSE % is expressed as a unitless percentage. The results are provided in **Table 4-9**.

Table 4-9. RMSE and n-RMSE % errors (parentheses) for Young's modulus, optical absorption, optical scattering, and acoustic attenuation measurements in comparison to human tissue data.

	E (kPa)	μ_a (cm^{-1})	$\mu_s{'}$ (cm^{-1})	α (dB cm^{-1})
Epidermis	0.11×10^3 (7.75%)	3.73 (4.23%)	6.60 (6.16%)	N/A
Dermis	1.02 (2.21%)	0.13 (8.11%)	2.68 (6.80%)	1.94 (5.79%)
Hypodermis	0.07 (3.95%)	0.17 (9.82%)	1.73 (9.73%)	1.05 (9.04%)
Vessel wall	0.04×10^3 (1.06%)	N/A	N/A	1.54 (6.14%)
Blood	N/A	17.75 (7.88%)	N/A	N/A

4.2.3. Discussion

While a number of previous studies have described the design of peripheral tissue phantom models, there have been relatively few reports that simultaneously consider the mechanical, optical, and acoustic properties of the skin, vessels, and blood. Invariably, multimodal models containing multiple tissue types are more complicated to develop than simpler, homogenous phantoms. Challenges observed during our studies are discussed below, and future directions are outlined.

4.2.3.1. Development of customized vessel tubing

In the commercial PDMS vessel tubing, speed of sound and thus acoustic impedance were both reduced compared to human vessel tissue, leading to uncharacteristic acoustic reflections at the TMM vessel wall. An alternative to using commercial tubing is to fabricate customized vessels, which would greatly increase the material choices and allow for the addition of modifiers. Some fabrication approaches have been reported. For example, the mechanical properties of PDMS may be controlled by varying the ratio of elastomer and curing agent, or by curing at different temperatures[242]. Materials other than PDMS, including polyvinyl alcohol and hydrogels, may also be used[243,245,246]. Of particular interest are vessel substitutes fabricated from gelatin or agar, since these materials can accommodate the modifiers discussed in this paper as well as many others. Our

group is looking into developing gelatin-based vessels using 3D-printed molds that define the vessel diameter and wall thickness. Such vessels, if fabricated in a convenient manner, would greatly increase the customizability of the TMM as a whole.

4.2.3.2.   Characterizing composite TMM material properties

To allow direct comparisons to literature data on human tissues, the five phantom tissue components were assessed independently. Because the individual components were homogenous, each could be tested using conventional experimental approaches. In contrast, evaluating the behavior of the multilayered composite TMM would likely have required more complex material models and techniques[265–267]. In future studies, such approaches may be implemented to allow the composite material properties of the TMM to be characterized.

4.2.3.3.   Reliability of reference data obtained from ex vivo tissues

A combination of *in vivo* and *ex vivo* human tissue reference values were used in this study. For some properties, including the Young's modulus, optical absorption, and optical scattering, *in vivo* measurements obtained with conventional testing methods were not easily found. Here, *ex vivo* data was used because the same testing methods could be applied to characterize each model, thereby allowing direct comparisons between the TMM and human tissue results. For example, the uniaxial stress vs. strain results on the TMM skin layers and vessels could be directly compared only to *ex vivo* data, since conventional stress vs. strain tests are difficult or impossible to implement *in vivo*. The *ex vivo* measurements used here for reference were obtained under well-controlled experimental conditions, and detailed descriptions were provided of the steps taken to minimize changes in the tissue samples after excision. In most of the referenced studies, samples were maintained in saline at either physiological or room temperature for no more than a few hours before testing, and measurements were found to be in agreement with prior *in vivo* results.

4.2.3.4.   Evaluating TMM stability and longevity

In TMM that were not stored under vacuum-seal, Young's modulus increased substantially after 30 days due to water loss. For models stored under vacuum seal at room temperature, no measurable changes in mechanical properties were observed after 30 days. Differences in the dermis layer before and after were within 1.15 kPa, which was less than the variability between samples. Similarly, differences in the hypodermis layer were within 0.64 kPa, which was also less than the sample variability. No measurable changes in the optical or acoustic parameters of the TMM were observed.

Germall-Plus was used as the antimicrobial in our models, all of which were packaged and stored in vacuum-sealed bags. No measurable changes in mechanical properties were observed after 30 days at room temperature. The stability of the TMM after 30 days was not assessed. Madsen *et. al.* has previously shown that, in properly stored gelatin and agar models incorporating Germall-Plus, mechanical properties remain stable over a 7 to 10 month period[239]. In follow-up studies, the material properties of the TMM will be evaluated over similar time durations.

4.2.3.5.   Use of TMM for robotic vessel cannulation testing

Here I described the design, fabrication, and characterization of TMM that reproduce the mechanical, optical, and acoustic properties of five peripheral tissues, namely the epidermis, dermis, hypodermis, blood vessels, and blood. The mechanical properties included the tissue thickness or diameter, Young's modulus, and dynamic shear modulus at strains below 0.5. The optical properties included the optical absorption and scattering at wavelengths of 400 to 1100 nm. Finally, the acoustic properties included the acoustic attenuation and backscatter in the frequency range of 2 to 9 MHz. The models are uniquely suited to serve as test models for multimodal skin and vascular imaging techniques and image-guided interventions.

4.3. Autonomous robotic vessel cannulation in tissue phantoms

In Chapter 4.3, I investigate the potential of robotic vessel cannulation in tailorable and clinically relevant *in vitro* test models. For these studies, we used the third-generation robotic device introduced in Chapter 3.6 and the multilayered tissue-mimicking phantom models described in Chapter 4.2. A wide range of TMM are developed, each reproducing the mechanical, optical, and acoustic properties of human skin and vessel tissues over a broad demographic spectrum (**Table 4-10**). Tissue properties and needle insertion parameters hypothesized to affect cannulation performance are then evaluated in simulated intravenous blood draw and infusion experiments performed on the phantoms. Measures of accuracy and completion time are compared to results obtained by unassisted, NIR-guided, and US-guided manual cannulation. I show that the device outperforms an experienced operator with training in standard, NIR-guided, and US-guided venipuncture, and I discuss the implications of these studies on the clinical utility of image-guided robotic vessel cannulation.

4.3.1. Results

4.3.1.1. Optimization of needle insertion parameters

To first identify optimal needle insertion parameters for the device, we applied a fractional factorial experimental design based on the use of Taguchi orthogonal arrays [113]. We evaluated the effects of three parameters (insertion angle (15º and 30º), insertion speed (1 and 10 mm/s), and needle diameter (21 and 25 gauge)) on cannulation accuracy in four different tissue conditions. Specifically, we expected that the optimal insertion parameters would vary according to the diameter of the vessels and the elasticity of the surrounding hypodermis tissue. Thus, separate TMM were developed with vessel diameters ranging between 1 and 3 mm and hypodermis elastic moduli between 5 and 25 kPa. Applying an L4 (2^3) Taguchi orthogonal design to the needle insertion parameters and using a 2^2 full factorial array to represent the models, a total of 4 x 4 = 16

experimental conditions were tested **(Supplementary Table 4-1)**. 20 replicate cannulation trials were performed for each condition. The endpoint in 10 of these trials was the successful withdrawal of 2 mL of BMF from the TMM vessels. In the other 10 trials, the endpoint was the infusion of 2 mL fluid into the vessels. All trials were carried out in randomized order.

Table 4-10. TMM material property ranges used for *in vitro* device cannulation studies.

Phantom material properties	Units	Physiological range	TMM modifier(s)
Epidermis thickness, l	mm	0.1	–
Epidermis elasticity, E	kPa	1	Gelatin / agar %
Epidermis absorption, μ_a	cm^{-1}	5 – 45	Synthetic melanin
Epidermis scattering, μ_s'	cm^{-1}	12 – 24	Synthetic melanin
Epidermis attenuation, α	dB cm^{-1}	16 – 20 dB	Bovine serum albumin
Epidermis backscatter, β	10^{-3} sr^{-1} cm^{-1}	1.8 – 3.6	40 μm silica beads
Dermis thickness, l	mm	1	–
Dermis elasticity, E	kPa	50	Gelatin / agar %
Dermis absorption, μ_a	cm^{-1}	0.4 – 0.8	India ink, 552 nm dye
Dermis scattering, μ_s'	cm^{-1}	18 – 22	Intralipid-20
Dermis attenuation, α	dB cm^{-1}	16 – 20	Bovine serum albumin
Dermis backscatter, β	10^{-3} sr^{-1} cm^{-1}	1.8 – 3.6	40 μm silica beads
Hypodermis thickness, l	mm	2 – 5	–
Hypodermis absorption, μ_a	kPa	0.8 – 1.1	India ink, 935 nm dye
Hypodermis scattering, μ_s'	cm^{-1}	10 – 12	Intralipid-20
Hypodermis attenuation, α	cm^{-1}	7.5 – 10	Bovine serum albumin
Hypodermis backscatter, β	dB cm^{-1}	0.9 – 1.8	40 μm silica beads
Hypodermis elasticity, E	10^{-3} sr^{-1} cm^{-1}	5 – 25	Gelatin / agar %
Vessel depth, δ	mm	1.5 – 4.5	–
Vessel diameter, d	mm	1 – 3	Silicone tubing
Blood viscosity, η	kg m^{-1}s^{-1}	2.2 – 2.9	Glycerol, dextran

			Models (1 – 4)			
			1	2	3	4
Hypodermis elasticity, ε			−	−	+	+
Vein diameter, d			−	+	−	+
−	−	−	15% (3/20)	25% (5/20)	65% (13/20)	90% (18/20)
−	+	+	60% (12/20)	85% (17/20)	70% (14/20)	100% (20/20)
+	−	+	35% (7/20)	50% (10/20)	90% (18/20)	95% (19/20)
+	+	−	40% (8/20)	60% (12/20)	50% (10/20)	100% (20/20)
Insertion speed	Insertion angle	Needle size				

Figure 4-10. Cannulation success rates (%) vary based on needle insertion settings and tissue conditions. An L4 (2^3) Taguchi orthogonal array was used to assess three needle insertion parameters (insertion speed, insertion angle, and needle size). The insertion parameters were tested against a 2^2 full factorial array of tissue conditions (hypodermis elasticity and vessel diameter). The parameter values are provided in **Supplementary Table 4-1**. 20 replicate cannulation trials were conducted for each of the 4 x 4 = 16 experimental conditions. Black rectangular outlines show the needle insertion settings that resulted in the highest cannulation success rate for each of the four TMM. In model 4, two insertion conditions were seen to maximize the success rate. Here, the faster insertion speed (+) and larger needle size (−) were used for subsequent studies.
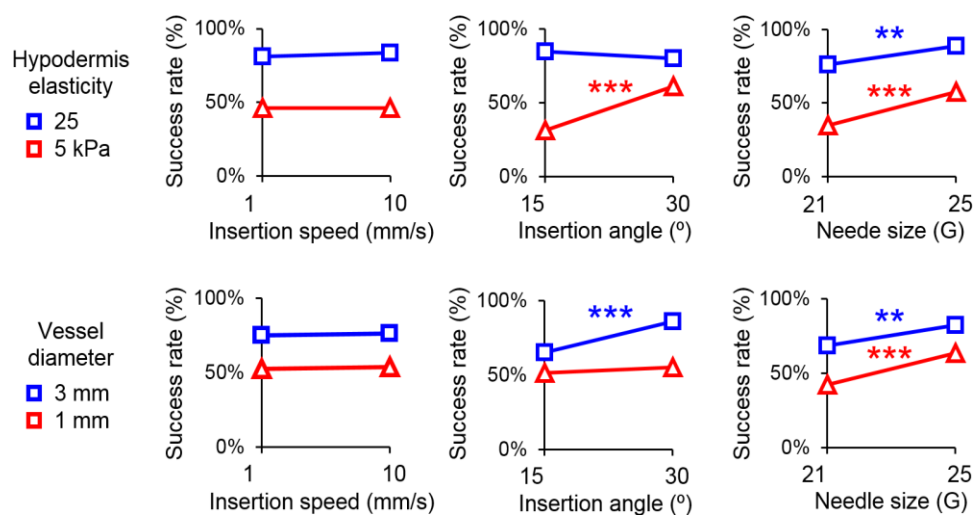
Figure 4-11. Effects of needle insertion parameters on success rates in TMM with hypodermis elastic moduli of 5 and 25 kPa and vessel diameters of 1 and 3 mm (* $p < 0.1$, ** $p < 0.05$, *** $p < 0.01$).

Shown in **Figure 4-10** are the needle insertion parameters that resulted in the highest cannulation success rate for each of the four TMM. As can be seen, the optimal insertion parameters were different between the models, indicating a dependency on the material properties of the tissue. These optimal insertion parameters are applied in later experiments to minimize performance biases that would otherwise have arisen had the insertion parameters been arbitrarily selected or held constant across all tissue conditions. **Figure 4-11** shows the effects of each insertion parameter on cannulation success. We found that the rates of success were significantly influenced by both insertion angle and needle size. Cannulations performed at a steeper insertion angle were associated with significantly increased success rates in models with low hypodermis elasticity. For cannulations on stiffer hypodermis tissue, the insertion angle did not make a difference. The steeper insertion angle was also more favored for larger vessels, whereas the opposite was true for smaller vessels. Smaller needle sizes improved success rates in low hypodermis elasticity conditions and on small vessels, but had no effect in high elasticity conditions or on large vessels. Finally, neither insertion speed nor the trial endpoint (sample withdrawal or infusion) impacted success rates in any of the tissue conditions.

4.3.1.2. *Investigation of tissue conditions affecting cannulation performance*

We next investigated a broader range of tissue parameters to evaluate their influence on device performance. For this, we performed a second fractional factorial experiment using an L16 (2^{15}) Taguchi design comprising 16 different TMM. Material property ranges for each TMM were determined based on values found in the literature and reflect the expected demographic and physiological variability of the overall patient population (**Table 4-10** and **Supplementary Table 4-2**). Phantom tissue parameters with a wider range, i.e., a greater difference between high and low values, were expected to influence device performance more strongly. 20 replicate cannulation trials (10 trials simulating sample withdrawal and 10 simulating infusion) were completed per TMM. For each model, we used the particular insertion angle and needle size that would maximize

success rate on the combination of tissue parameters simulated by that model, as determined from our previous experiments (**Figure 4-10**). In cases of ambiguity, for example in model 4, we used the insertion parameters that were closest to clinical recommendations (larger rather than smaller needle size, shallower rather than steeper angle, and faster rather than slower speed).

The overall cannulation success rate was 272 of 320 (85.0%) over all trials and ranged between 70% and 100% (**Supplementary Table 4-3**). As before, no differences in success were observed between the sample withdrawal and infusion trials. **Figure 4-12** shows the individual effects of each tissue parameter, averaged over all other parameters. Four of the 15 parameters were found to significantly affect the outcome of the experiment. Specifically, success rates were significantly lower in models with increased epidermis absorptivity or vessel depth and higher in models with increased hypodermis elasticity or vessel diameter. In the first two cases, visibility was substantially reduced. Epidermis absorption directly determines a person's skin tone, and darker skin tones are associated with reduced visual contrast between the skin and the blood vessels underneath. Meanwhile deeper vessels are more difficult to identify because the majority of the signal is lost due to optical scattering in the skin and adipose tissue layers – a common occurrence in patients with high body mass index. In the latter two cases, the mechanical aspect of the needle insertion task was affected. In weakly elastic tissues, common in elderly and chronically-ill patients, vessels are poorly held in place and tend to roll or deform away from the needle during cannulation, while in smaller vessels, a much greater level of mechanical precision is needed and slight inaccuracies when advancing the needle may lead to failed insertions.
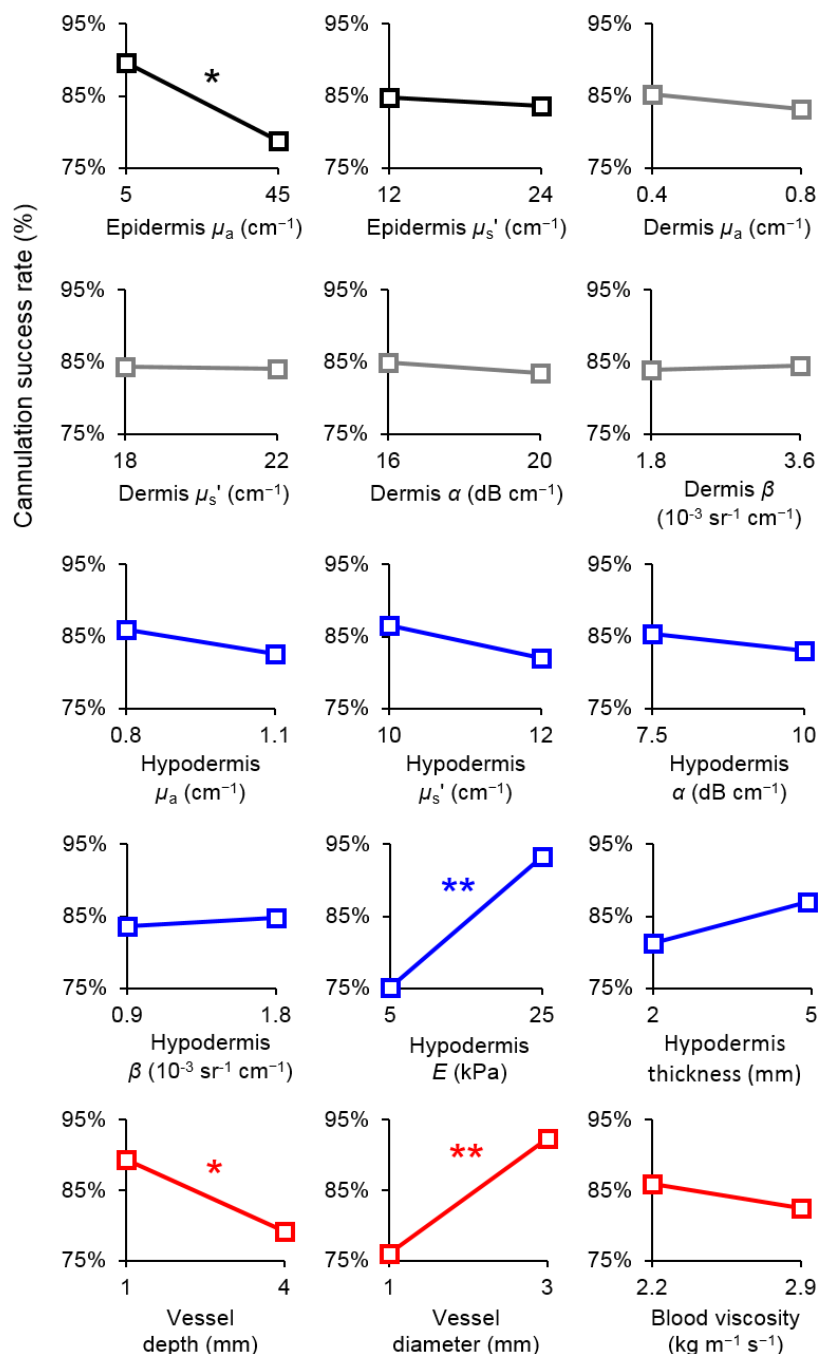
Figure 4-12. Effects of 15 TMM material properties on cannulation success rate. Success rates varied significantly in four of the 15 parameters. Specifically, success was lower in trials performed on TMM with increased epidermis absorptivity or vessel depth, and higher in trials on stiffer hypodermis tissues or larger vessel diameters. The overall success rate was 272 of 320 (85.0%) across all trials and ranged between 70% and 100%. No significant differences were observed between the withdrawal and injection trials (* $p < 0.1$, ** $p < 0.05$, *** $p < 0.01$).

4.3.1.3.   Comparative study of manual and robotic vessel cannulation

Lastly, we compared the performance of the device to un-assisted manual cannulation, NIR-guided manual cannulation, and US-guided manual cannulation with respect to the four tissue parameters observed in our previous experiments (**Figure 4-12**) to most strongly influence success rates. To allow direct comparisons between the robotic and manual trials, we used the NIR and US imaging systems of the device for all experiments. For both modalities, a video feed of the acquired images was displayed in real-time on a computer screen, and the operator was tasked with introducing the needle based on image feedback. Vessel segmentation results could be displayed on-screen or made invisible, depending on the operator's preference. The operator in these studies was *not* a clinical expert with training in human vascular procedures. However, the operator had considerable prior experience performing both unassisted and image-guided cannulations using the TMM, and before the start of each experiment, the operator was allowed become acclimated with the task by conducting practice trials as many times as was desired.

For these studies, we used a full factorial experimental design (**Supplementary Table 4-4**) consisting of 27 different TMM. The models encompassed three differing levels of hypodermis tissue elasticity (5, 15, and 25 kPa), three levels of vessel diameter (1, 2, and 3 mm), and three levels of vessel visibility (low, moderate, and high). Vessel visibility represented a lumped parameter in which the absorption coefficient of the epidermis at 940 nm and the depth of the vessel from the surface of the skin were simultaneously varied. The low, moderate, and high visibility levels corresponded to epidermis absorption coefficients of 45, 25, and 5 cm^{-1}, respectively, and vessel depths of 4.5, 3, and 1.5 mm, respectively. The overall study size was thus 4 methods of cannulation x 27 TMM = 108 experimental conditions. For each condition, we performed 10 replicate trials, all simulating sample withdrawal. Four measures of cannulation performance were quantified, namely the average number of insertion attempts needed for successful cannulation,

percent first-stick success rate, total completion time, and time per insertion attempt (**Supplementary Table 4-5 through 4-8**, respectively).

Figure 4-13 summarizes the overall performance of each method of cannulation. The average first-stick success rates for unassisted manual, NIR-guided manual, US-guided manual, and NIR+US guided robotic cannulation were 54%, 61%, 73%, and 90%, respectively. Robotic cannulation was observed to outperform manual cannulation on three out of the four outcome measures (average number of attempts, first-stick success, and total time). Unassisted manual cannulation was the most time efficient on a per-attempt basis.

Figure 4-14 shows the effects of each tissue parameter on cannulation performance. The slopes of the plots indicate the dependence of the outcomes on the varying tissue conditions. Particularly notable differences in performance between manual and robotic cannulation were observed in low visibility conditions. In TMM with decreased vessel visibility, it was substantially harder to perform the unassisted and NIR-guided manual cannulations accurately. In contrast, performance remained consistent across the visibility range in the US-guided manual trials and the NIR+US guided robotic trials. This is unsurprising, as cannulations guided by US should not be affected by epidermis optical absorption or vessel depth. The unassisted and NIR-guided trials were likewise affected by vessel diameter to a greater extent than were the US-guided and robotic cannulation trials. This may be explained by the fact that the spatial resolution of the US image is higher than the resolution of the NIR images and most likely higher than that of human vision. Thus smaller (1 mm) vessels may be visualized with greater clarity using US. Smaller vessels also represent a challenge to the mechanical precision of the insertion, and this may explain the difference in performance between the manual US trials and the robotic trials. Hypodermis tissue elasticity was seen to affect all four cannulation methods, though when results were averaged across all three elasticity levels, the robotic trials exhibited the best overall performance.

A more detailed overview of the results is provided in **Figure 4-15**, which shows the average number of insertion attempts needed in each of the 27 TMM. The results of the other three performance measures (first-stick success rate, total time, and time per attempt) are provided in **Supplementary Figure 4-1 through 4-3**). In general, the difference in performance between the cannulation methods was accentuated in more difficult tissue conditions (smaller vessel diameters, decreased vessel visibility, and low tissue elasticity) compared to easier conditions. This is further highlighted in **Figure 4-16**, which shows the performance results on the 27 TMM ranked in order of difficulty, i.e., arranged from the lowest performance for each cannulation method to the highest. In easier tissue conditions (left side of each plot), all four cannulation methods exhibited similar levels of performance. In the more difficult conditions, however, large differences in the average number of attempts, first-stick success rate, and total completion time were observed between the methods (right side of each plot). Here, the increased performance of the robotic approach could be clearly seen.

Finally, the results of the study were compared to those obtained by a clinician trained in vascular cannulation procedures. The expert trials were carried out using an L4 (2^3) Taguchi array with four different TMM, these representing a statistically unbiased subset of the full experimental space of 27 tissue conditions (**Supplementary Table 4-9**). Five replicate sample withdrawal trials were conducted for each condition using unassisted and US-guided manual cannulation. No significant increases in performance were observed in the expert trials compared to the non-expert trials (**Supplementary Figure 4-4**), therefore suggesting that the manual cannulation results in these studies are indicative of expected clinical results.
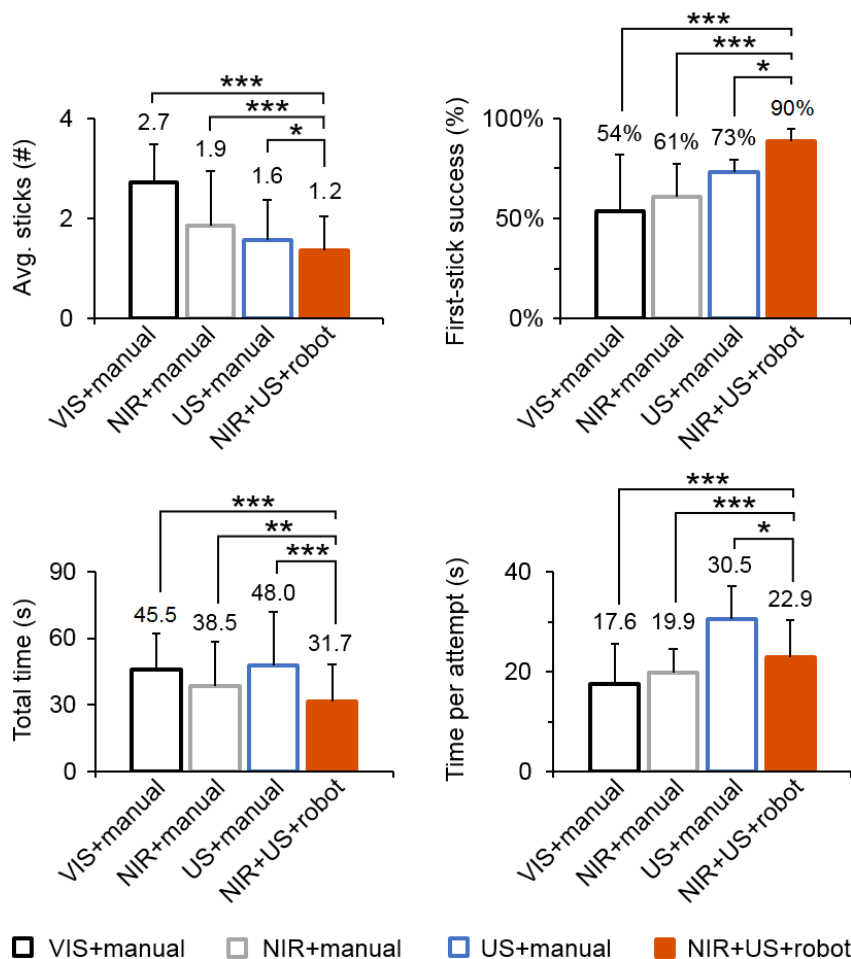
Figure 4-13. Overall performance of unassisted manual, NIR-guided manual, US-guided manual, and NIR+US guided robotic cannulation. Robotic cannulation significantly outperformed the manual cannulation approaches on three out of four outcome measures (* $p < 0.1$, ** $p < 0.05$, *** $p < 0.01$). A total of 27 TMM were used in these studies, each comprising a different combination of tissue properties. Plots show averaged scores across the 27 conditions. Error bars show the standard deviation across all 27 conditions as determined from the statistical variance within each condition.
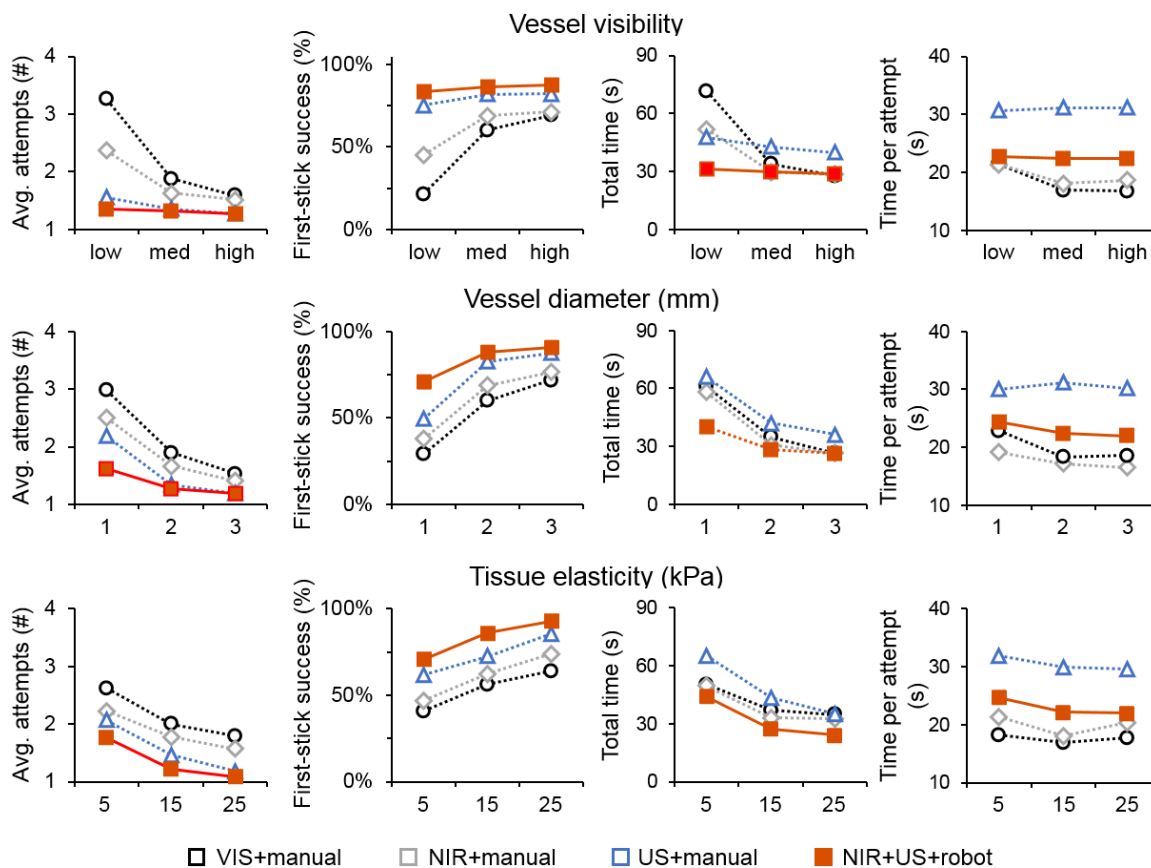
Figure 4-14. Effects of hypodermis tissue elasticity, vessel diameter, and vessel visibility on performance of unassisted manual, NIR-guided manual, US-guided manual, and NIR+US guided robotic cannulation.
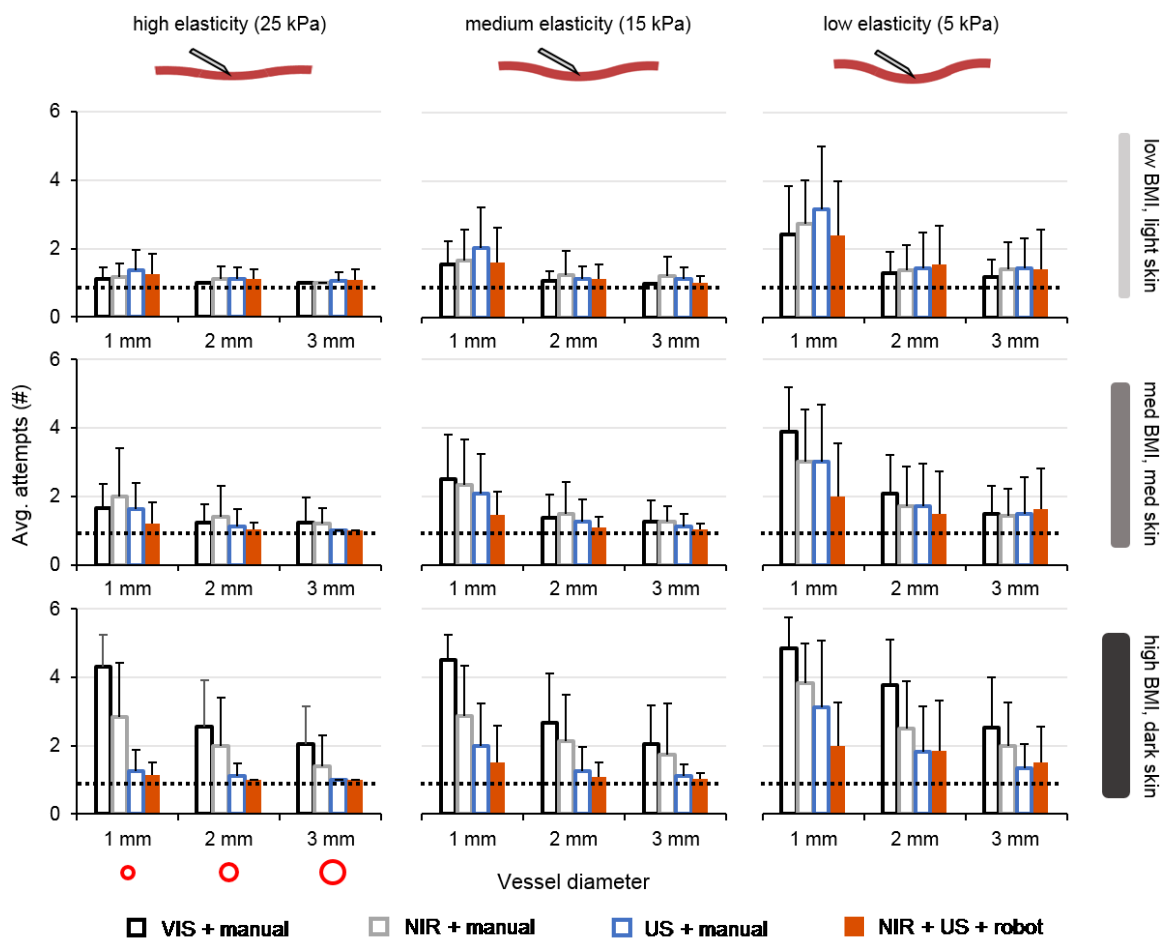
Figure 4-15. Average number of needle insertion attempts required to obtain vascular access in 27 different tissue conditions. Results of unassisted manual, NIR-guided manual, US-guided manual, and NIR+US guided robotic cannulation are compared in each plot.
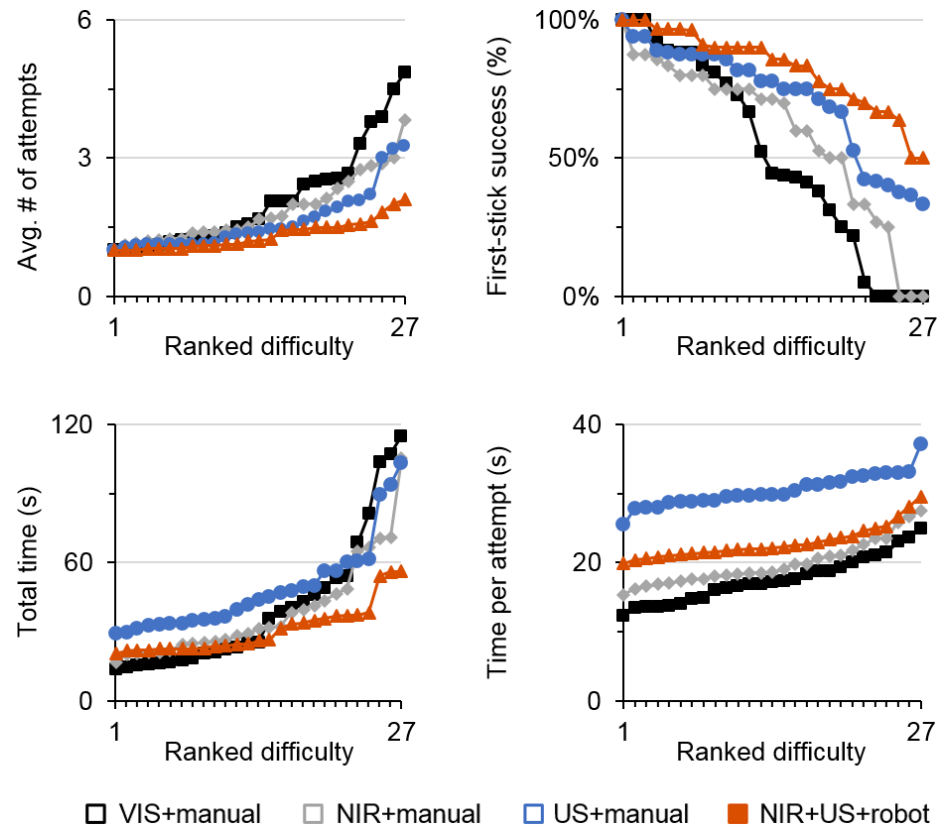
Figure 4-16. Cannulation performance in relation to the 27 TMM ranked in order of difficulty. Differences in average number of attempts, first-stick success, and total time between different cannulation methods are substantially greater in the more difficult tissue conditions (right-hand side of each plot).

4.3.2. Discussion

The results of these studies underscore some of the major advantages and current limits of the current device. In previous imaging studies on human subjects, we found that the combined use of NIR and US assistance allowed a greater percentage of veins and arteries to be identified compared to unassisted visualization by a trained clinician[58]. In the *in vitro* experiments here, we saw that the improvement in vessel detection was particularly evident when skin tones were darker or when the vessels were embedded more deeply under the skin. We also saw that the improvement in visualization translated to more accurate needle insertions, and that the combined use of NIR+US imaging and robotic needle guidance improved success rates and completion times significantly compared to unassisted and image-guided manual techniques. Finally, the studies demonstrated

that, compared to manual cannulation, the performance of the robotic system was less dependent on the particular material properties of the tissue.

4.3.2.1.   *Reducing effects of tissue elasticity on device performance*

Nevertheless, it was clear that mechanical properties, particularly hypodermis tissue elasticity, affected the accuracy of the robot more than any other tissue parameter (**Figure 4-14**). Approximately one additional insertion attempt was needed per trial in TMM with a 5 kPa hypodermis layer as opposed to a 25 kPa hypodermis layer. Similarly, the first-stick success rate was approximately 30% lower in 5 kPa phantoms, and completion time increased by about 20 seconds per trial. While the overall performance of the robot was better compared to manual cannulation when results were averaged across the three elasticity levels, the performance *slopes* for the robotic and manual approaches were largely the same. Furthermore, in a certain subset of tissue conditions involving cannulations on small and stiff vessels embedded in surrounding tissues with very low elastic moduli, the device did not outperform US-guided manual cannula insertion. The reason for this was that the use of US allowed the operator to visualize vessels that were otherwise undetectable by human eyesight or NIR alone. Meanwhile, after sufficient training, the manual dexterity of the human operator exceeded that of the robot.

To improve cannulation accuracy in weakly elastic tissues, where vessels easily deform and roll away from the needle, it may be possible to increase the maximum linear and rotational movement speeds of the robot. As discussed in Chapter 3, the maximum allowable speeds are constrained by the load and precision requirements of the kinematic chain, and these constraints limit the response of the robot to rapid vessel motions[61]. Further device miniaturization would decrease the loads, particularly on the end-effector, and allow for higher maximum speeds. Cannulation accuracy and responsiveness may also be improved with the implementation of nonlinear needle insertion trajectories and a more sophisticated control system for needle servoing.

Finally, though the device incorporates a miniaturized load sensor that detects axial reaction forces at the needle tip with a sensitivity of 0.1 N, this force information was not utilized in these studies. However, force profiles were captured from all of the robotic cannulation trials, and a future goal will be to analyze these data to identify differences in the force response with different insertion conditions. If salient force profiles can be observed for different puncture events, it may then be possible to integrate this information into the system's motion control scheme. Similarly, incorporating a multi-axis force sensor or load cell may improve the tactile sensitivity of the system.

4.3.2.2.   *Developing synthetic vessels with tunable material properties*

In the same way that hypodermis tissue properties affected cannulation rates, we expect the mechanical properties of the vessels to also be important. In these studies, we were not able to modify the mechanical characteristics of the silicone vessel tubing, and though the silicone material closely mimics the elastic behavior of the vessel wall[62], the higher-order (non-linear) properties and the insertion forces deviate from those of vessel wall tissue. The acoustic properties of silicone are also different, and this leads to uncharacteristic reflections in the US image at the interface between the tubing and surrounding phantom layers. We are currently developing a method to fabricate synthetic vessels using materials such as gelatin and agar, both of which can readily accommodate the addition of modifying agents. The synthetic vessels may then be tuned to exhibit desired tissue acoustic properties and customized to simulate a range of mechanical characteristics – for example, venous and arterial wall stiffness, compressibility, and internal pressure – known to affect cannulation, sample withdrawal, and fluid delivery success rates *in vivo*.

4.3.2.3.   *Studying additional performance measures*

Using synthetic vessels fabricated from hydrogel materials would also allow us to investigate a number of performance metrics that were omitted in this report. For instance, a common measure of accuracy in studies of US-guided needle placement is the distance between the needle tip and

the center of the vessel. Depending on the mechanical properties of the tissues, even small offsets in needle position may lead the tissue to deform away from the needle or cause the needle itself to bend. Similarly, the argument is frequently made that robotic systems can reduce the amount of random needle motion within the tissue. This is important because undesired motions, e.g., due to hand tremors, can increase the likelihood of inaccurate insertion, cause the needle to slip out from within the vessel, or result in pain or nerve damage. Currently, the acoustic imaging artifacts that arise from the silicone vessel tubing limit the visibility of the needle tip inside the lumen. By developing vessels with more representative acoustic properties, we expect to be able to reliably extract needle tip coordinates from the US images in order to compute the relative displacement and motion of the needle on a frame-by-frame basis. Such metrics could, in turn, provide more clearly defined precision requirements for the robotic system.

4.3.2.4.   *NIR and US imaging considerations*

Several aspects of the NIR and US imaging approach used in these studies should be discussed. The NIR-guided manual trials were not carried out with a commercial NIR imaging device but rather with our own customized system developed for the robot. Our NIR system uses the same illumination wavelengths and detection hardware as commercial devices but does not project the captured images back onto the skin surface (instead, the images are displayed in real-time on the computer screen). Whether this setup affected the results of the NIR-guided trials remains uncertain and should be evaluated in future studies using a commercial device. The US-guided trials, on the other hand, were performed using a standard commercial imaging transducer. The human operators preferred to use the transverse US imaging view (with the imaging plane perpendicular to the vessel axis) for the manual cannulations to avoid the challenging task of keeping the needle within the US plane during the insertion process. For the robot, this task is trivial since the end-effector is designed to align the needle with the US transducer at all times. Instead, the robot utilizes a longitudinal imaging view (with the imaging plane parallel with the vessel axis). However, both the transverse

and longitudinal approaches have their drawbacks. In the transverse view, the needle is significantly harder to see and in most cases can only be observed at its point of intersection with the transverse US plane. Meanwhile, in the longitudinal view, vessels may not be immediately visible if the transducer is not exactly positioned in the correct orientation upon initial contact with the skin. It may be possible to overcome the limitations of both methods by utilizing US technologies that can, for example, provide a top-down image[81] or reconstruct a 3D representation of the tissue volume[268].

4.3.2.5.   *Investigating vessel rolling and deformation*

Finally, it would be of interest to investigate the mechanical interactions between the needle, the vessel, and the surrounding tissue layers to determine the space of mechanical parameters that would lead to a successful or unsuccessful cannulation. In Chapter 3.5 I described a series of computational studies carried out to study vessel deformation behavior due to needle insertion using FE modeling. In those studies, we demonstrated how the robot can compensate for vessel motion by steering the needle in real-time under image guidance. However, both the *in vitro* and computational models were simplified. For one, we assumed all materials to exhibit simple elastic properties, whereas human tissues are highly complex heterogeneous materials exhibiting viscoelastic and other higher-order material behaviors. Furthermore, in the FE models, we did not simulate the actual penetration of the tissue by the needle. Future work will focus on refining the computational and *in vitro* models to incorporate these parameters. The improved models may be used to study other factors that affect venipuncture accuracy, such as the effects of vessel motion speeds due to deflection and deformation. The outcomes may then help to determine whether any changes to the mechanical design of the system are required. We will also use the models to compare experimentally observed force profiles with theoretical solutions, and to further validate the force sensing component of the robot. Together, this information could ultimately be incorporated into the robot's control algorithms and allow the device to make predictive inferences

and subtle needle pose adjustments. Such models are analogous to the tactile inferences made by trained human operators when performing complex interventional tasks.

4.3.3. Supplementary results

	–	+
Insertion speed (mm/s)	1	10
Insertion angle (º)	15	30
Needle size (G)	21	25
Hypodermis E (kPa)	5	25
Vessel diameter (mm)	1	3

Supplementary Table 4-1. Needle insertion parameters evaluated to optimize cannulation accuracy. An L4 (2^3) Taguchi orthogonal array was used to assess insertion speed, insertion angle, and needle size. The parameters were tested against a 2^2 full factorial array of tissue conditions (hypodermis elasticity and vessel diameter). The range of values (– / +) represent the low and high extremes expected in the clinical setting.

	–	+
Epidermis μ_a (cm^{-1})	5	45
Epidermis μ_s' (cm^{-1})	12	24
Dermis μ_a (cm^{-1})	0.4	0.8
Dermis μ_s' (cm^{-1})	18	22
Dermis α (dB cm^{-1})	16	20
Dermis β (10^{-3} sr^{-1} cm^{-1})	1.8	3.6
Hypodermis μ_a (cm^{-1})	0.8	1.1
Hypodermis μ_s' (cm^{-1})	10	12
Hypodermis α (dB cm^{-1})	7.5	10
Hypodermis β (10^{-3} sr^{-1} cm^{-1})	0.9	1.8
Hypodermis E (kPa)	5	25
Hypodermis thickness (mm)	2	5
Vessel depth (mm)	1.5	4.5
Vessel diameter (mm)	1	3
Blood viscosity (kg m^{-1} s^{-1})	2.2	2.9

Supplementary Table 4-2. Fifteen tissue parameters evaluated using customizable TMM. The material property ranges (– / +) were determined based on range values found in the literature and reflect the expected demographic and physiological variability of the overall patient population.

	Phantoms (1 – 16)															
	1	2	3	4	5	6	7	8	9	10	11	12	13	14	15	16
Epidermis μ_a (cm⁻¹)	–	–	–	–	–	–	–	–	+	+	+	+	+	+	+	+
Epidermis μ_s' (cm⁻¹)	–	–	–	–	+	+	+	+	–	–	–	–	+	+	+	+
Dermis μ_a (cm⁻¹)	–	–	–	–	+	+	+	+	+	+	+	+	–	–	–	–
Dermis μ_s' (cm⁻¹)	–	–	+	+	–	–	+	+	–	–	+	+	–	–	+	+
Dermis α (dB cm⁻¹)	–	–	+	+	–	–	+	+	+	+	–	–	+	+	–	–
Dermis β (10⁻³ sr⁻¹ cm⁻¹)	–	–	+	+	+	+	–	–	–	–	+	+	+	+	–	–
Hypodermis μ_a (cm⁻¹)	–	–	+	+	+	+	–	–	+	+	–	–	–	–	+	+
Hypodermis μ_s' (cm⁻¹)	–	+	–	+	–	+	–	+	–	+	–	+	–	+	–	+
Hypodermis α (dB cm⁻¹)	–	+	–	+	–	+	–	+	+	–	+	–	+	–	+	–
Hypodermis β (10⁻³ sr⁻¹ cm⁻¹)	–	+	–	+	+	–	+	–	–	+	–	+	+	–	+	–
Hypodermis E (kPa)	–	+	–	+	+	–	+	–	+	–	+	–	–	+	–	+
Hypodermis thickness (mm)	–	+	+	–	–	+	+	–	–	+	+	–	–	+	+	–
Vessel depth (mm)	–	+	+	–	–	+	+	–	+	–	–	+	+	–	–	+
Vessel diameter (mm)	–	+	+	–	+	–	–	+	–	+	+	–	+	–	–	+
Blood viscosity (kg m⁻¹ s⁻¹)	–	+	+	–	+	–	–	+	+	–	–	+	–	+	+	–
Success (%), withdrawal	80%	100%	90%	90%	100%	70%	90%	70%	70%	80%	100%	70%	80%	90%	80%	80%
Success (%), injection	90%	90%	80%	90%	100%	80%	90%	100%	80%	90%	100%	70%	80%	80%	70%	90%
Success rate (%), overall	85%	95%	85%	90%	100%	75%	90%	85%	75%	85%	100%	70%	80%	85%	75%	85%

Supplementary Table 4-3. Experimental design used to evaluate effects of 15 tissue material properties on the cannulation success rate of the device. An L16 (2^{15}) Taguchi orthogonal array was used to reduce the experimental size. Red boxes correspond to higher overall success rates.

	–	o	+
Hypodermis E (kPa)	5 kPa	15 kPa	25 kPa
Vessel diameter (mm)	1 mm	2 mm	3 mm
Vessel visibility [epidermis μ_a (cm⁻¹), vessel depth (mm)]	5 cm⁻¹ 1.5 mm	25 cm⁻¹ 3 mm	45 cm⁻¹ 4.5 mm

Supplementary Table 4-4. Tissue conditions tested to assess manual and robotic cannulation. A full factorial experimental design with 27 different TMM was used. The tissue models encompassed three differing levels of hypodermis tissue elasticity (5, 15, and 25 kPa), three levels of vessel diameter (1, 2, and 3 mm), and three levels of vessel visibility (low, moderate, and high). The vessel visibility condition was a lumped parameter in which the absorption coefficient of the epidermis at 940 nm, as well as the depth of the vessel from the surface of the phantom, were varied. The low, moderate, and high visibility levels corresponded to epidermis absorption coefficients of 45, 25, and 5 cm⁻¹, respectively, and vessel depths of 4.5, 3, and 1.5 mm, respectively. The material property ranges (– / o / +) reflect the expected demographic and physiological variability of the overall patient population.

Supplementary Table 4-5 — Average insertion attempts

Phantoms (1 – 27)

	1	2	3	4	5	6	7	8	9	10	11	12	13	14	15	16	17	18	19	20	21	22	23	24	25	26	27	
Elasticity	−	−	−	−	−	−	−	−	−	o	o	o	o	o	o	o	o	o	+	+	+	+	+	+	+	+	+	
Visibility	−	−	−	o	o	o	+	+	+	−	−	−	o	o	o	+	+	+	−	−	−	o	o	o	+	+	+	
Diameter	−	o	+	−	o	+	−	o	+	−	o	+	−	o	+	−	o	+	−	o	+	−	o	+	−	o	+	
Manual+VIS	4.9	3.8	2.5	3.9	2.1	1.5	2.4	1.3	1.2	4.5	2.7	2.1	2.5	1.4	1.3	1.6	1.1	1.0	4.3	2.6	2.1	1.7	1.2	1.2	1.1	1.0	1.0	2.14 ± 1.18
Manual+NIR	3.8	2.5	2.0	3.0	1.7	1.4	2.8	1.4	1.4	2.9	2.1	1.8	2.3	1.5	1.3	1.7	1.3	1.2	2.8	2.0	1.4	2.0	1.4	1.2	1.2	1.1	1.0	1.86 ± 0.72
Manual+US	3.1	1.8	1.3	3.0	1.7	1.5	3.2	1.5	1.4	2.0	1.3	1.1	2.1	1.3	1.1	2.1	1.1	1.1	1.7	1.1	1.0	1.6	1.1	1.0	1.4	1.1	1.1	1.59 ± 0.63
Device	2.3	1.9	1.5	2.5	1.5	1.6	2.8	1.6	1.4	1.8	1.1	1.0	1.7	1.1	1.0	1.8	1.1	1.0	1.3	1.0	1.0	1.2	1.0	1.0	1.4	1.1	1.1	1.44 ± 0.49
																												$\mu \pm \sigma$

Supplementary Table 4-5. Average insertion attempts for manual and robotic cannulation. Results are shown for unassisted manual, NIR-guided manual, US-guided manual, and NIR+US guided robotic cannulation. A full factorial experiment was conducted with 27 different TMM and $n = 10$ replicate cannulation trials per phantom. Shown also is the mean (μ) and standard deviation (σ) for each cannulation method. Red boxes correspond to better performance, and blue boxes to worse performance.

Supplementary Table 4-6 — First-stick success rates

Phantoms (1 – 27)

	1	2	3	4	5	6	7	8	9	10	11	12	13	14	15	16	17	18	19	20	21	22	23	24	25	26	27	
Elasticity	−	−	−	−	−	−	−	−	−	o	o	o	o	o	o	o	o	o	+	+	+	+	+	+	+	+	+	
Visibility	−	−	−	o	o	o	+	+	+	−	−	−	o	o	o	+	+	+	−	−	−	o	o	o	+	+	+	
Diameter	−	o	+	−	o	+	−	o	+	−	o	+	−	o	+	−	o	+	−	o	+	−	o	+	−	o	+	
Manual+VIS	0.0	0.1	0.3	0.1	0.4	0.7	0.4	0.8	0.9	0.0	0.3	0.4	0.3	0.7	0.8	0.5	0.9	1.0	0.0	0.3	0.4	0.4	0.8	0.9	0.9	1.0	1.0	0.54 ± 0.34
Manual+NIR	0.0	0.3	0.5	0.3	0.7	0.7	0.3	0.8	0.7	0.3	0.5	0.8	0.3	0.8	0.8	0.5	0.9	0.9	0.3	0.6	0.8	0.6	0.8	0.8	0.8	0.9	1.0	0.61 ± 0.25
Manual+US	0.4	0.7	0.8	0.3	0.7	0.8	0.4	0.8	0.8	0.5	0.9	0.9	0.4	0.8	0.9	0.4	0.9	0.9	0.6	0.9	1.0	0.5	0.9	1.0	0.7	0.9	0.9	0.72 ± 0.21
Device	0.3	0.7	0.8	0.5	0.8	0.8	0.4	0.8	0.9	0.7	0.9	1.0	0.6	0.9	1.0	0.6	0.9	1.0	0.8	1.0	1.0	0.8	1.0	1.0	0.8	0.9	0.9	0.80 ± 0.18
																												$\mu \pm \sigma$

Supplementary Table 4-6. First-stick success rates for manual and robotic cannulation.

Supplementary Table 4-7 — Total completion times

Phantoms (1 – 27)

	1	2	3	4	5	6	7	8	9	10	11	12	13	14	15	16	17	18	19	20	21	22	23	24	25	26	27	
Elasticity	−	−	−	−	−	−	−	−	−	o	o	o	o	o	o	o	o	o	+	+	+	+	+	+	+	+	+	
Visibility	−	−	−	o	o	o	+	+	+	−	−	−	o	o	o	+	+	+	−	−	−	o	o	o	+	+	+	
Diameter	−	o	+	−	o	+	−	o	+	−	o	+	−	o	+	−	o	+	−	o	+	−	o	+	−	o	+	
Manual+VIS	115	81	49	69	36	25	41	18	17	104	60	39	46	23	15	22	15	14	107	54	43	25	18	17	21	16	16	40.9 ± 30.3
Manual+NIR	105	46	41	76	32	28	71	25	24	65	38	32	49	25	22	26	20	21	67	44	29	40	25	21	31	21	17	38.6 ± 21.4
Manual+US	94	60	42	89	56	50	103	48	45	56	41	33	62	36	33	61	35	37	42	34	28	47	33	29	39	35	30	48.0 ± 19.9
Device	54	44	34	56	33	37	63	38	36	39	23	22	34	24	23	39	25	22	25	23	20	26	25	22	30	23	23	31.9 ± 11.6
																												$\mu \pm \sigma$

Supplementary Table 4-7. Total completion times for manual and robotic cannulation.

Supplementary Table 4-8 — Mean time-per-attempt

Phantoms (1 – 27)

	1	2	3	4	5	6	7	8	9	10	11	12	13	14	15	16	17	18	19	20	21	22	23	24	25	26	27	
Elasticity	−	−	−	−	−	−	−	−	−	o	o	o	o	o	o	o	o	o	+	+	+	+	+	+	+	+	+	
Visibility	−	−	−	o	o	o	+	+	+	−	−	−	o	o	o	+	+	+	−	−	−	o	o	o	+	+	+	
Diameter	−	o	+	−	o	+	−	o	+	−	o	+	−	o	+	−	o	+	−	o	+	−	o	+	−	o	+	
Manual+VIS	24	21	19	18	17	17	17	14	14	23	22	19	18	17	12	14	13	14	25	21	21	15	15	14	19	16	16	17.6 ± 3.5
Manual+NIR	28	19	21	25	19	20	26	18	17	23	18	18	21	17	17	15	16	17	24	22	21	20	18	18	27	19	17	19.9 ± 3.4
Manual+US	30	33	31	30	33	33	33	33	31	28	33	30	30	28	29	30	30	33	25	30	28	29	30	29	29	32	28	30.2 ± 2.0
Device	23	24	23	23	22	23	23	25	25	22	21	21	20	22	22	22	21	20	23	20	22	24	22	22	21	21		22.0 ± 1.3
																												$\mu \pm \sigma$

Supplementary Table 4-8. Mean time-per-attempt for manual and robotic cannulation.

		Phantoms		
	1	9	21	25
Hypodermis *E* (kPa)	–	–	+	+
Vessel diameter (mm)	–	+	–	+
Vessel visibility	–	+	+	–

Supplementary Table 4-9. Fractional factorial subset of four TMM used to compare expert and non-expert cannulation performance. These models represent an L4 (2^3) Taguchi orthogonal array over the full experimental space of the 27 tissue conditions evaluated in the non-expert studies (see experimental design shown in **Supplementary Table 4-5**, for example).
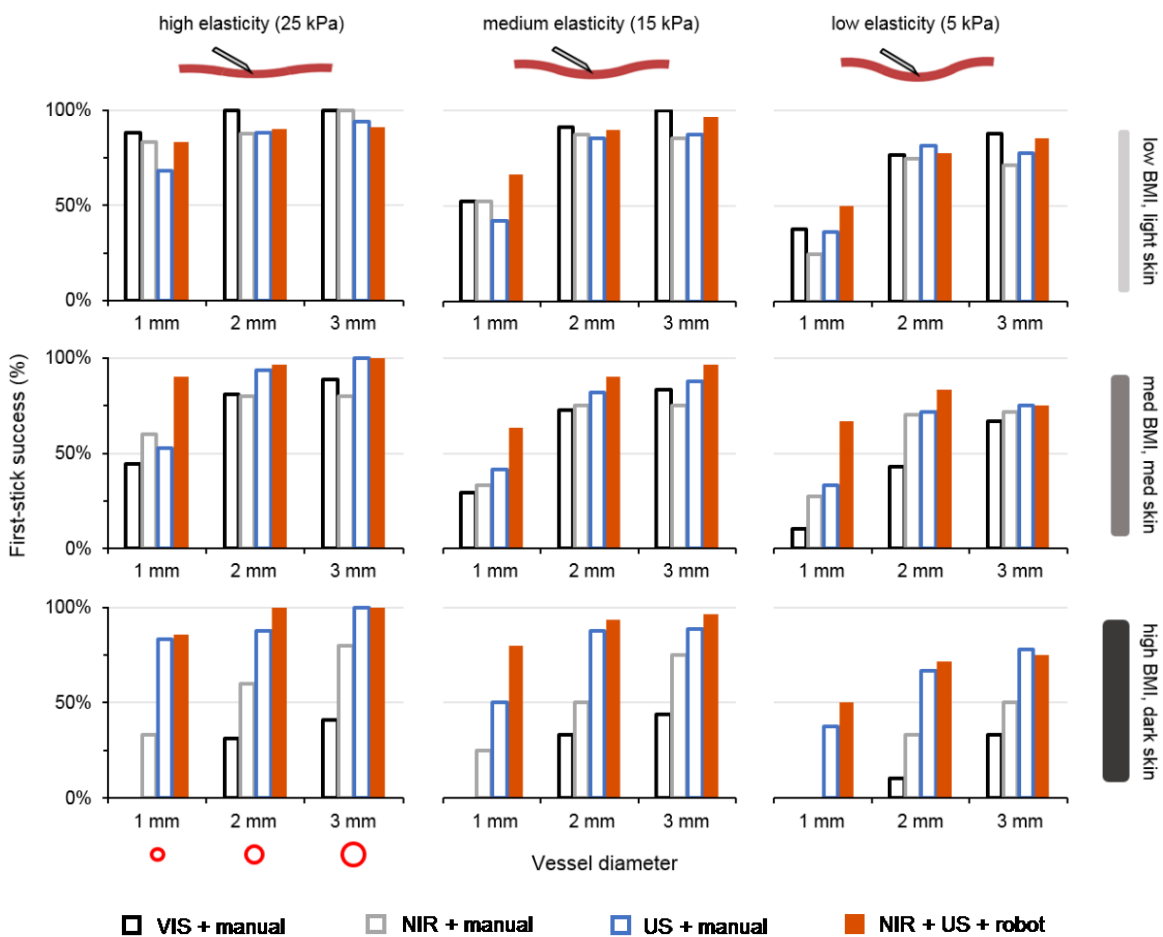
Supplementary Figure 4-1. First-stick success rates, shown with respect to three tissue properties and four cannulation methods.
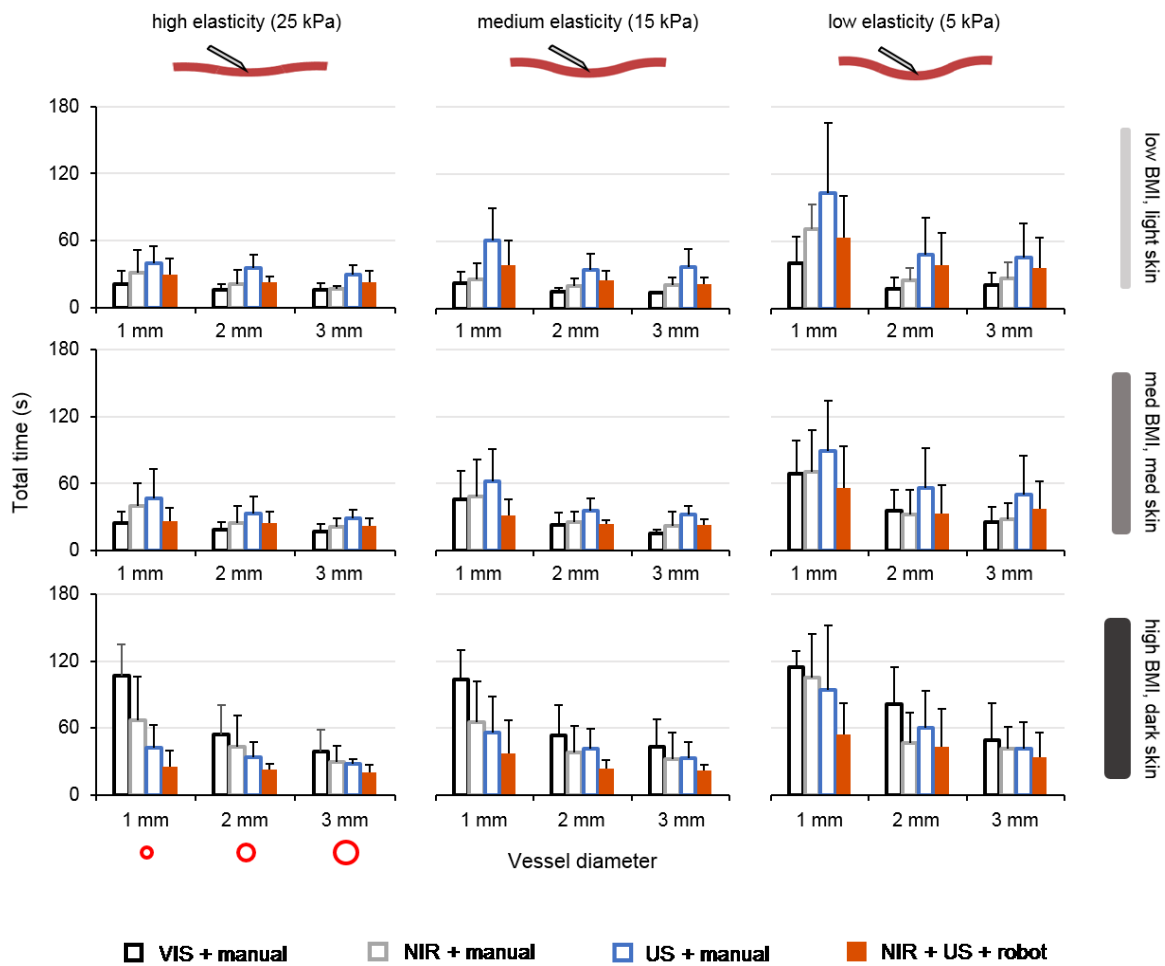
Supplementary Figure 4-2. Total procedure completion times, shown with respect to three tissue properties and four cannulation methods.
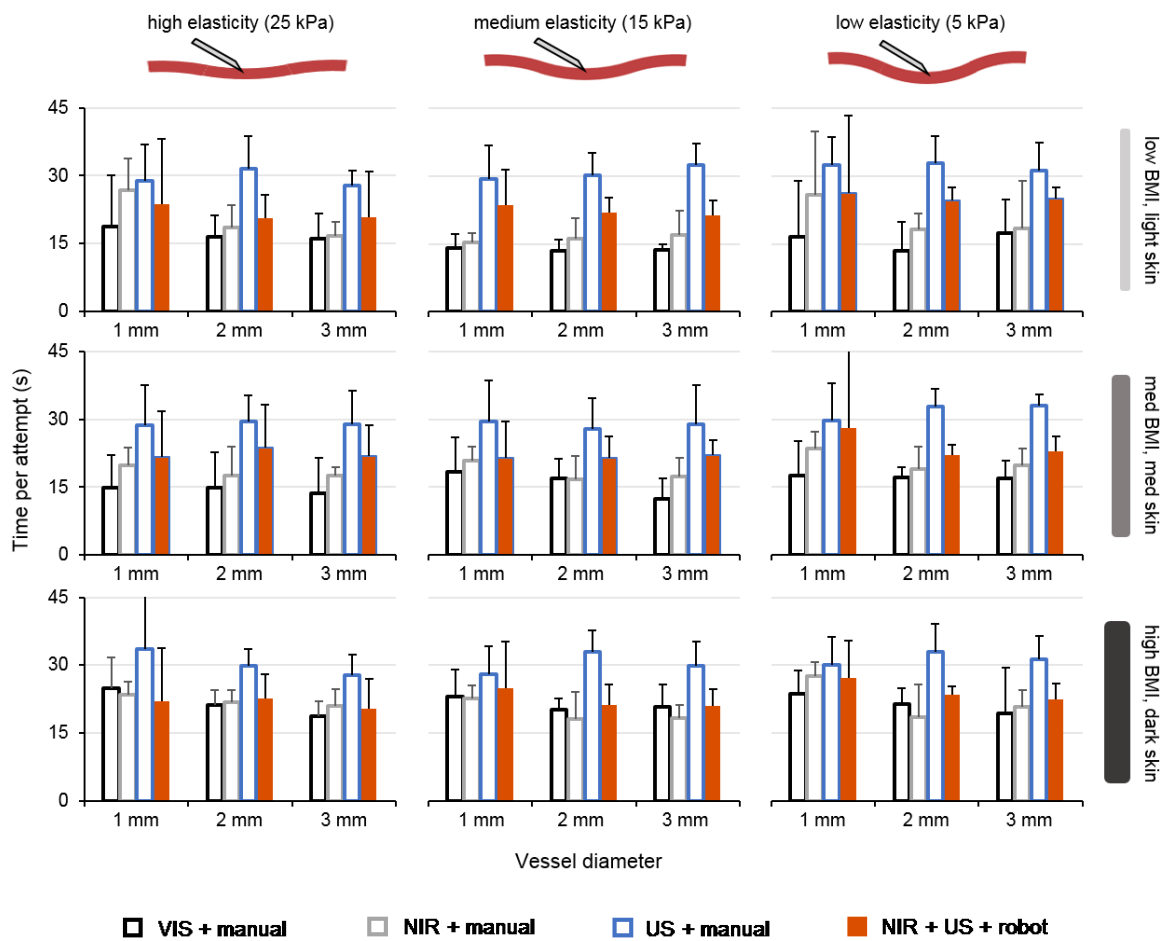
Supplementary Figure 4-3. Total procedure completion times normalized by the average number of cannulation attempts, shown with respect to three tissue properties and four cannulation methods.
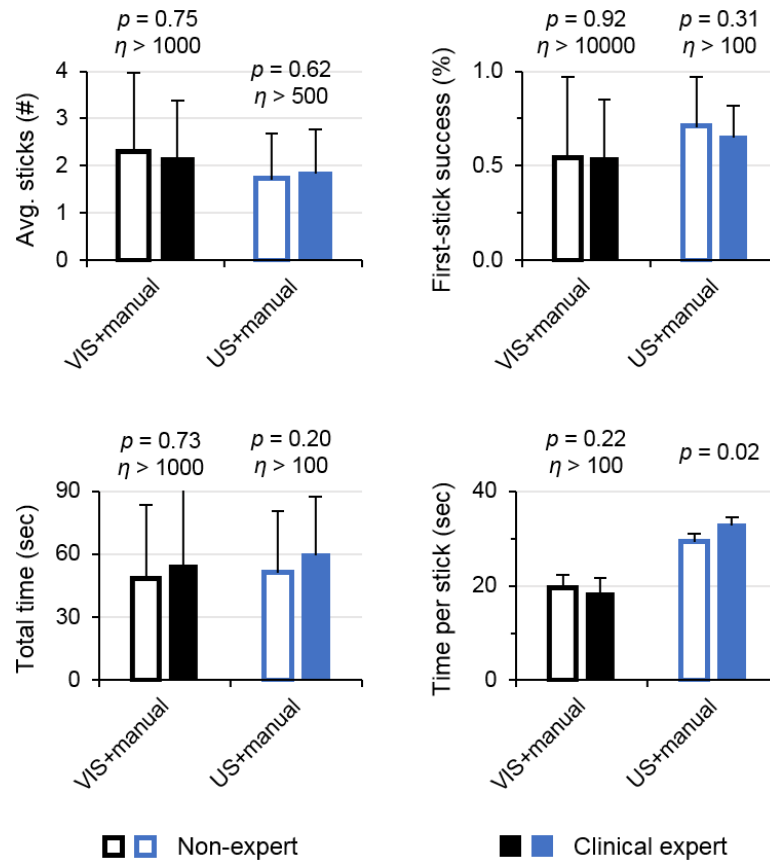
Supplementary Figure 4-4. Comparison of manual cannulation performance by clinical expert and non-expert. No significant increases in performance ($p < 0.05$ in favor of the expert) were observed in the expert trials compared to the non-expert trials. Statistical analysis was carried out using one-tailed t-tests examining for better expert performance relative to the non-expert baseline. Power analyses were then performed to determine whether the lack of significance was a result of small sample sizes. Results of the power analysis showed that significantly large trial sizes (η) would be required to observe significance, thus indicating that the expert and non-expert results were statistically comparable.

4.4. Autonomous robotic tail vein cannulation in rats

In Chapter 4.4, I describe studies evaluating *in vivo* device efficacy in rats. The diameter of the lateral and dorsal tail veins in adult rats range between 0.5 and 1 mm, which is comparable to the diameter of neonatal peripheral forearm and hand veins (1 to 1.2 mm)[269]. The ventral artery ranges between 0.4 and 0.7 mm. Reflectance and transillumination modes of NIR imaging were assessed in 13 white Sprague-Dawley rats and 7 black Sentinel rats. Vessel imaging at two US frequencies (12 MHz and 40 MHz) were also compared. Finally, lateral tail vein cannulations were performed and blood samples were collected using manual and automated cannulation techniques. We compared five methods of venipuncture: (1) unassisted manual cannulation; (2) manual cannulation under NIR image guidance; (3) manual cannulation under US image guidance; (4) robotic cannulation under NIR guidance; and (5) robotic cannulation under bimodal NIR+US guidance.

The use of NIR and US imaging improved the percentage of vessels detected as well as the visual contrast of the vessels. Meanwhile, robotic cannulations, guided by either or both modes of imaging, resulted in an increase in first-stick accuracy and a decrease in the average number of needle stick attempts per trial. In these studies, the robotic system performs cannulations using a linear insertion motion; I suggest methods to implement nonlinear trajectories into the robotic insertions to further improve cannulation and blood collection success rates. These studies also highlighted a number of anatomical and physiological differences between the rat tail and the human forearm. These differences required significant modifications to the design of both the imaging and robotic components of the device, as is discussed. The anatomical differences also suggest that it may be possible to develop a substantially simplified device to perform automated rodent tail vessel cannulations, for example to assist in preclinical research studies; an initial prototype of a low-cost, handheld device is introduced at the end of the chapter.

4.4.1. Results:

All animal studies were conducted under an approved animal study protocol. The average weight of the rats was 260.9 g, with the smallest at 151 g and the largest at 318 g. The mean diameter of the tail across the 11 animals was 11.5 mm, with measurements taken 2 cm distal to the base of the tai, i.e., the proximal end. Each animal was anesthetized by 5% isoflurane induction, followed by maintenance under 2.5% isoflurane. A tourniquet was then applied at the proximal end of the tail, and the animal was positioned on a raised platform mounted to the device that secures the tail. A heating pad was placed underneath the animal to prevent blood flow reduction resulting from potential hypothermia. Prior to each imaging and cannulation trial, the animal's tail was soaked in 43°C water for 1 min to induce vasodilation and then disinfected with 70% ethanol.

4.4.1.1.   *Comparison of NIR tail vein imaging under reflectance and transillumination*

Two methods of NIR imaging were evaluated. In the first method, the NIR light source was arranged on the same side as the cameras to provide reflectance-based NIR illumination (this is the same approach as used for the human imaging studies described in previous chapters). In the second method, the light source is positioned on the opposite side of the tail, and only light transmitted through the tail was collected by the cameras. Since the average diameter of a rat tail is substantially less than the diameter of a human arm, it is possible to collect a sufficient amount of transmitted to produce a coherent image. In both cases, we used 830 nm LED arrays as the light source. Blood vessels within the FOV were segmented in real-time with the same algorithms used to segment human forearm vessels (see Chapter 2.4.3). **Figure 4-17** shows representative images of the lateral tail vein in a 262 g rat acquired with the reflectance and transillumination configurations. The results of imaging under broadband VIS light and 830 nm NIR light are also shown, as are the results of the vessel segmentation routines applied to the NIR images.

The NIR imaging experiments were carried out on 20 animals (13 white male Sprague-Dawley rats and 7 black male Sentinel rats), and the results are summarized in **Figure 4-18**. In all 13 of 13

white rats (100%), at least one of the two lateral tail veins were identified by the NIR imaging system, and both veins were identified in 11 of the 13 rats (85%) **Figure 4-18 (a)**. Under manual visualization without NIR guidance, at least one tail vein was identified in 10 of 13 rats (77%) (-33% compared to the NIR group) and both veins were identified in 7 of 13 rats (54%) (-31% compared to the NIR group). Meanwhile, using NIR imaging, at least one vein was identified in 6 of the 7 black rats (86%), and both veins were identified in 5 rats (71%). In comparison, under manual visualization, at least one vein was identified in 4 of the 7 rats (57%) (-29% compared to the NIR group), and both were identified in 2 of 7 rats (29%) (-42% compared to the NIR group). In 15 of the 20 rats (75%), the ventral artery was identified under NIR imaging, whereas the ventral artery was observed in only 6 of the 20 rats (30%) under manual visualization. In both white and black rats, use of transillumination imaging improved vessel detection rates compared to reflectance imaging (+15% and +14%, respectively). The ability to locate a larger number of blood vessels may be particularly important in preclinical animal studies where repeated cannulations must be performed within rapid succession, for example to collection samples at multiple time points within a 24 hr period. In these situations, reuse of the same vessel may lead to difficulties in sampling or delivery. Access to the left and right lateral tail veins, the dorsal vein, and the ventral artery would minimize the need for vessel reuse and allow more time for the tissue to heal.

The image contrast of the lateral tail veins was also compared (**Figure 4-18 (b)**). In both white- and black-skinned rats, vessel contrast was significantly increased with the use of NIR imaging (+27% compared to VIS imaging). Contrast was higher with transillumination (+31% compared to VIS imaging) than with reflectance-based illumination (+23% compared to VIS imaging).
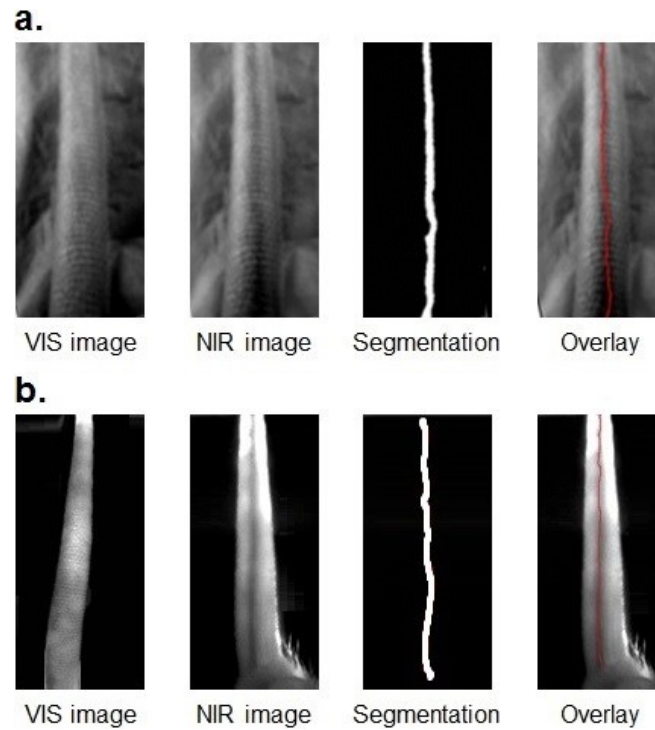
Figure 4-17. Representative VIS and NIR images of rat lateral tail veins under (a) reflectance imaging and (b) transillumination imaging. Segmentation of the tail was performed using the NIR images.
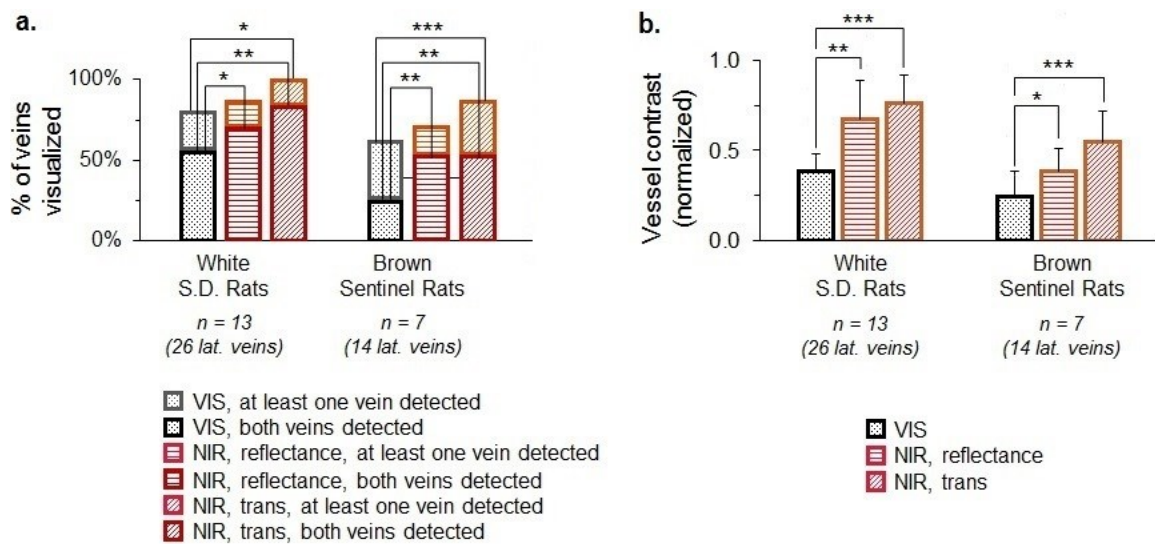
Figure 4-18. Comparison of VIS and NIR tail vein imaging in white- and black-skinned rats. **(a)** Percentage of tail veins visualized under VIS imaging, NIR reflectance imaging, and NIR transillumination imaging. **(b)** Vessel image contrast (normalized) under the three modes of imaging. (* $p < 0.1$, ** $p < 0.05$, *** $p < 0.01$).

4.4.1.2.   Comparison of 12 MHz and 40 MHz US tail vein imaging

Figure 4-19 shows representative transverse (left column) and longitudinal (center column) US images at 12 MHz of the lateral veins and ventral artery in a 262 g rat. The 25 G cannula can also be seen entering the blood vessel in the longitudinal view (right column). The US probe was oriented and aligned robotically. B-mode images were analyzed and segmented in real-time while being displayed on the GUI. Overall, at least one lateral tail vein was identified in only 5 of 11 animals using the 12 MHZ transducer. The ventral artery could be visualized in B-mode in 3 of 11 animals. The dorsal vein was not detected in any of the animals. The mean diameter of vessels that were detected with US was 0.72 mm, which is significantly smaller than the median antecubital vein diameter of a neonatal or pediatric patient (1.1 to 1.9 mm). The smallest detectable tail vessel was 0.60 mm, and the largest observed vessel was 1.05 mm. Variation in vessel diameter between different animals was small, and correlation with weight was insignificant ($R^2 = 0.47$). Vessels below 0.60 mm were difficult to visualize in the B-mode image. In ideal conditions where attenuation and acoustic scatter do not occur, a 0.60 mm object in the US image would appear 6 pixels in size. However, when the high acoustic attenuation and scatter of the rat tail skin and muscle tissue are considered, such small vessels are no longer visible in the US image.

We also compared rat tail imaging using an US system with a higher acoustic frequency. Specifically, a 40 MHz linear array transducer with 50 μm image resolution and 10 mm penetration (Vevo VisualSonics) was used for this second set of studies. **Figure 4-20** shows representative B-mode (**Figure 4-20 (a)**) and Color Dopper (**Figure 4-20 (b)**) images of a 0.51 mm lateral tail vein in a 154g rat acquired using the 40 MHz probe. Also shown is a Doppler image of a 0.39 mm ventral artery in the same animal (**Figure 4-20 (c)**) after rotating the tail. Using the 12 MHz transducer, neither the lateral veins nor the ventral artery could be visualized in this animal. **Figure 4-20 (d–f)** show images of the needle entering into the vessel under robotic guidance. Unlike with the 12 MHz probe, the needle tip could be seen inside the vessel lumen in both the longitudinal and

transverse views using the 40 MHz probe. The segmentation steps were not performed here because the 40 MHz transducer was interfaced with a third-party commercial US beamformer, and thus the images could not be processed in real-time. In future studies, we will implement an interface between the high-frequency beamformer and our system to allow for real-time image analysis.
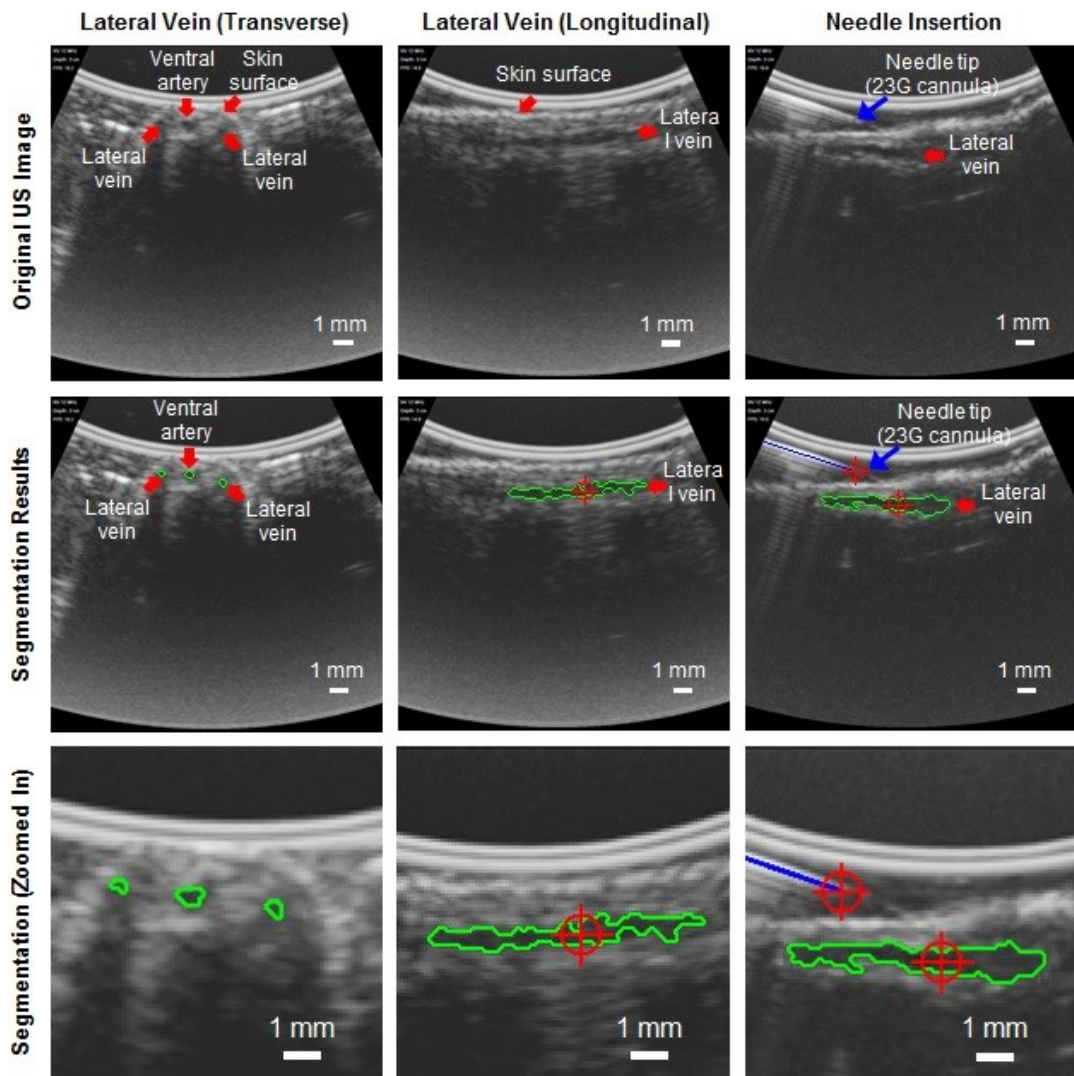
Figure 4-19. Transverse and longitudinal US images of the left lateral tail vein of a 262 g female Sprague Dawley rat acquired using a 12 MHz transducer. Vessel segmentation was performed using the adaptive region grow algorithm, needle segmentation was achieved with a log-Gabor wavelet filter and a probabilistic Hough transform line detector, and needle tip extraction was performed via a Shi-Tomasi corner detector.
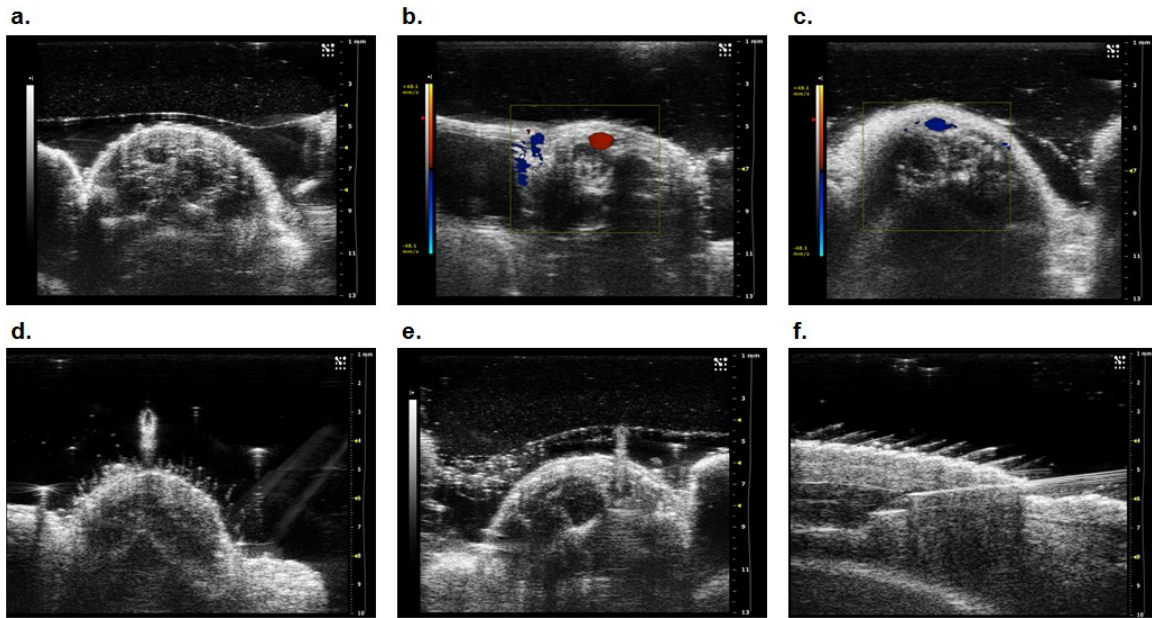
Figure 4-20. Transverse and longitudinal US images of the left lateral tail vein and ventral artery of a 154 g male Sprague Dawley rat acquired using a 40 MHz transducer. **(a)** Transverse B-mode image of lateral tail vein (diameter 0.51 mm). **(b)** Color Doppler image of lateral tail vein. **(c)** Color Doppler image of ventral artery (diameter 0.39 mm). **(d)** Transverse B-mode image of 25 G needle just prior to skin puncture. **(e)** Transverse B-mode image of 25 G needle inside vessel lumen. **(f)** Longitudinal B-mode image of 25 G needle inside vessel lumen.

4.4.1.3.   *Comparison of manual and robotic tail vein cannulation*

In a final set of experiments, lateral tail vein cannulations were performed manually and with the device under different imaging conditions. In total, five methods of cannulation were compared: (1) unassisted (standard) manual cannulation, (2) manual cannulation under NIR image guidance, (3) manual cannulation under US image guidance, (4) robotic cannulation under NIR guidance, and (5) robotic cannulation under bimodal NIR+US guidance. In these studies, successful cannulation was defined by two metrics. The first was the visualization of the needle tip within the vessel lumen following insertion, and second was the collection of 0.2 mL of blood. The manual cannulation trials were performed following two-months of training carried out twice per week.
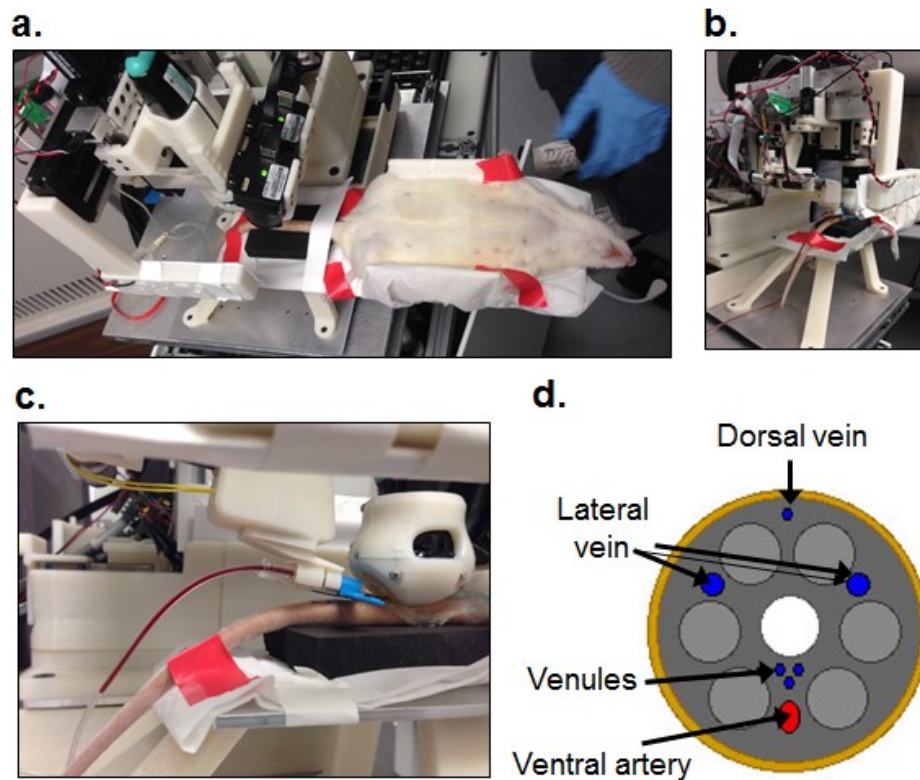
Figure 4-21. *In vivo* assessment of device cannulation in rats. **(a)** Immobilization of anesthetized rat on raised platform with tail secured at distal and proximal ends. **(b)** Robotic needle insertion. **(c)** Cannulation and withdrawal of 0.2 mL of blood into the catheter tube. **(d)** Vessel anatomy in the rat tail.

The results of the study are summarized in **Table 4-11** and depicted in **Figure 4-22**. As in the previous imaging studies, a significantly higher percentage of lateral tail veins could be identified using the device compared to manual visualization. In particular, the combined use of NIR and US imaging resulted in the visualization of 90% of the tail veins (**Figure 4-22 (a)**), which was higher than using either imaging modality alone. Likewise, the device (either using only NIR imaging or combined NIR+US imaging) provided a significant improvement in first-stick success rate (**Figure 4-22 (b)**) and a decrease in the average number of needle stick attempts needed to achieve successful cannulation (**Figure 4-22 (c)**) compared to unassisted, NIR-guided, and US-guided manual cannulations. **Figure 4-22 (d)** shows the percentage of trials in which at least 0.2 mL of blood was successfully collected on the first stick attempt. Similarly, **Figure 4-22 (e)** shows the

average number of stick attempts needed in order to achieve successful blood collection. Again, significant improvements were observed compared to unassisted manual cannulations and US-guided manual cannulations. However, the blood collection performance using the device was not significantly improved compared to NIR-guided manual cannulations by the trained operator.
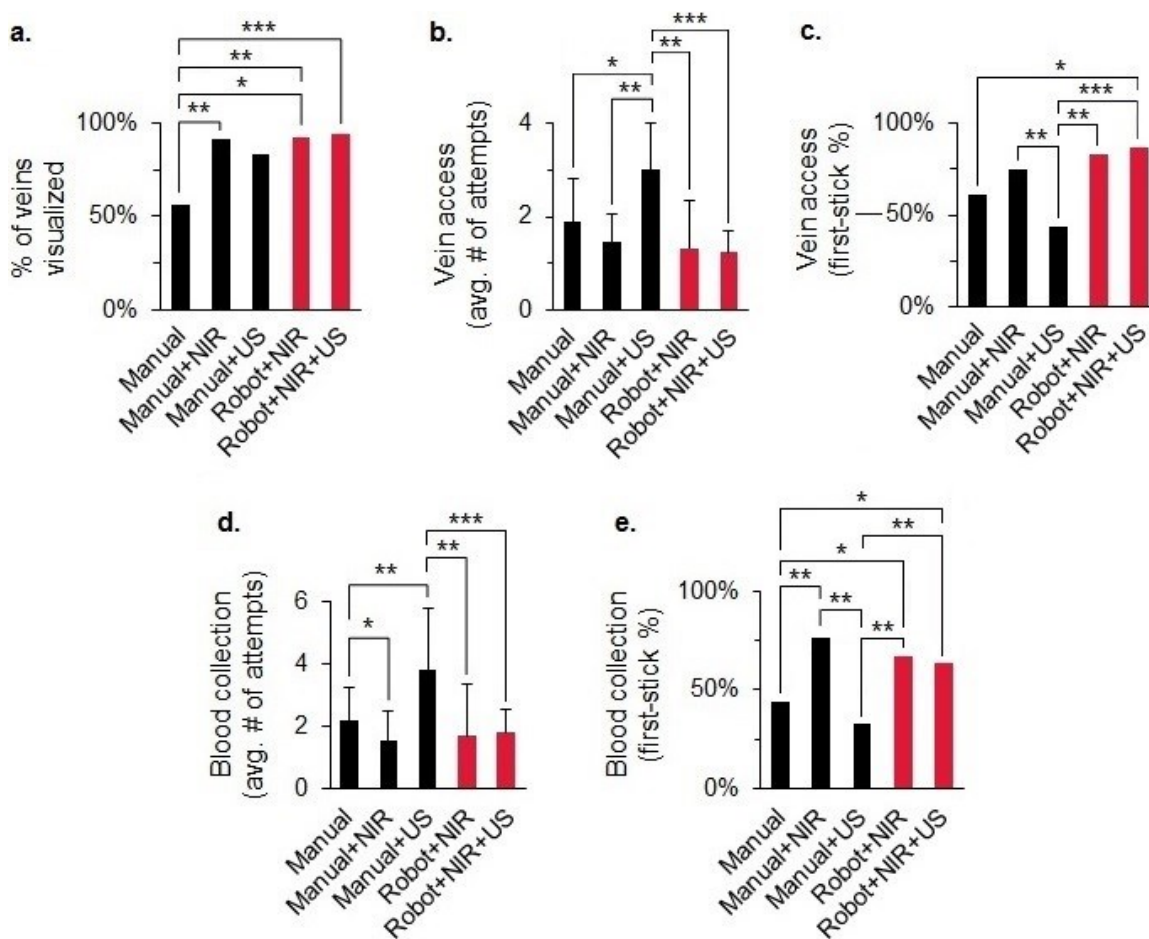
Figure 4-22. Comparison of unassisted manual, NIR-guided manual, US-guided manual, NIR-guided robotic, and NIR+US-guided robotic vessel cannulations in 88 rat tail blood draw trials. The manual cannulation trials were performed following a two-month formal training period. Successful vein access was defined as the visualization of the needle tip inside the lumen of the target vessel upon examination by high-frequency US. Successful blood collection was defined as the collection of at least 0.2 mL of venous blood. Animals were under isoflurane anesthesia throughout the experiments. Statistical analyses were performed using two-way ANOVA followed by post-hoc assessment using F-LSD (* $p < 0.1$, ** $p < 0.05$, *** $p < 0.01$).

**Table 4-11.** Comparison of unassisted manual, NIR-guided manual, US-guided manual, NIR-guided robotic, and NIR+US-guided robotic vessel cannulations in 88 rat tail blood draw trials.

	No. of trials	% of veins visualized (2 per trial)	Avg. # of attempts for successful vein access (first-stick %)	Avg. # of attempts for successful blood collection (first-stick %)
Manual	23	67.4%	1.89 ± 0.94 (60.9%)	2.18 ± 1.05 (45.7%)
Manual+NIR	16	90.6%	1.55 ± 0.82 (71.9%)	1.63 ± 0.84 (75.0%)
Manual+US	9	77.8%	3.02 ± 1.01 (44.4%)	3.90 ± 1.88 (33.3%)
Robot+NIR	20	90.0%	1.28 ± 0.74 (82.5%)	1.75 ± 1.06 (70.0%)
Robot+NIR+US	20	92.5%	1.30 ± 0.70 (85.0%)	1.80 ± 0.98 (67.5%)

4.4.2. Discussion

The *in vivo* studies demonstrated that robotic cannulations guided by NIR or NIR+US imaging resulted in increased success rates and decreased needle insertion attempts compared to cannulations performed manually following extensive training. Blood collection success rates were significantly improved using the device compared to unassisted manual sampling, though the addition of NIR transillumination imaging dramatically improved the manual success rate. On the other hand, manual cannulations performed under US guidance exhibited the lowest success rates among the five techniques evaluated. While the incorporation of US imaging, particularly at a high acoustic frequency, allowed the vessels and the needle to be seen with greater clarity compared to unassisted or NIR imaging alone, this improvement in visualization did not translate into a significant increase in cannulation accuracy.

These observations were in contrast with the results of our previous phantom studies, where US-guided manual and robotic cannulations both outperformed the unassisted and NIR-guided methods. The discrepancies between the phantom and animal results reflect several important physiological and anatomical differences between the rat tail and the human forearm. In humans, US imaging allows a greater percentage of blood vessels to be detected compared to NIR imaging,

largely because US imaging is more effective in high-BMI patient populations. Vessel visibility under NIR illumination decreases with increasing BMI in humans (see **Figure 2-19**), whereas BMI has little effect on vessel visibility in the rat tail. Unlike the human forearm, rat tails have little to no subcutaneous adipose tissue, and the tail vessels are generally located between 1 and 3 mm below the tail surface. Even in obese rat models, the vessels do not exceed 3 mm in depth. As such, we were able to identify one or more vessels in each animal using NIR imaging alone in 19 of 20 (95%) animals tested in the imaging studies and 33 of 36 (92%) animals in the cannulation studies.

On the other hand, rat tail veins are significantly smaller than human veins and therefore have comparatively decreased blood flow. Thus, the absorption of hemoglobin affects the visibility of the tail vessels to a greater extent than the scatter caused by adipose tissue. In these studies, 830 nm LEDs were used for NIR imaging. However, a lower wavelength such as 757 nm may improve vessel visibility and cannulation accuracy, as 757 nm represents a local peak in the absorption of deoxyhemoglobin. A camera with higher pixel resolution than the current 752 x 480 camera could also potentially improve visualization and accuracy. Whereas the effects of increased camera resolution would likely be insignificant in humans, the effects may be significant in rats because of their smaller vessels. Normally, the disadvantage of using a higher resolution camera is the decreased pixel sensitivity of the CMOS sensor to higher wavelengths (higher resolution cameras have CMOS sensors with smaller individual elements). However, at wavelengths such as 757 nm, the pixel sensitivity of modern cameras is more than sufficient. Moreover, because the rat tail is smaller than the human forearm, a significantly reduced proportion of the incident light is lost to random scatter within the tissue; thus the camera sensor's quantum efficiency at any given wavelength is not as important in determining the final image quality as is its pixel resolution.

Meanwhile, to visualize tail vessels using US, a standard 12 MHz clinical transducer exhibited insufficient spatial resolution. Instead, a high frequency 40 MHz transducer was needed. The cost of the high-frequency US imaging beamformer exceeds the cost of the device itself, and would

most likely be impractical to incorporate into devices designed for either human or animal venipuncture. Furthermore, the acoustic reflections at the skin surface of the rat tail was noticeably higher than typical acoustic reflections in human skin tissue. The strong reflections were likely due to the increased thickness of the keratinized layers in the rat tail, which exhibit nearly twice the backscatter coefficient of human epidermis and a higher sound speed (and thus, a higher acoustic impedance)[270]. Particularly at higher frequencies, the strong reflections created artifacts in the US image that reduced the visibility of the underlying vessels. Thus while the 40 MHz transducer provided a higher spatial resolution (0.05 mm) than the 12 MHz clinical probe (0.5 mm), the higher frequency images also exhibited much stronger echogenicity.

The other major limitation of using the high-frequency 40 MHz US system for these studies was that real-time vessel and needle segmentation could not be performed by the device. The high-frequency transducer that we used was part of a third-party commercial imaging system that, at present, cannot be easily interfaced with the device's control software. Because real-time image analysis could not be performed during the US-guided cannulation trials, the vessel center positions were assumed to remain static as the needle was inserted. As such, small movements of the vessel or the tail were not accounted for, and this could have affected the accuracy of the device. It is also possible that, despite our visualizing the needle inside the vessel lumen, the tip of the needle was inserted past the posterior vessel wall in multiple trials. This would have been difficult to visualize in US images, and would have compromised the pressure inside the vessel, thereby causing the vessel to collapse and reducing the blood flow into the needle's flashback chamber.

Finally, it is possible that device performance was affected because, in these studies, the needle was inserted in a linear manner and without the use of force feedback. Trained operators are taught to insert the needle along a nonlinear trajectory – that is, to lower the angle of insertion immediately following the initial puncture so that the needle was nearly parallel with the vessel. We found that the nonlinear motions allowed the needle to be advanced further into the vessel without puncturing

the posterior wall, reducing the likelihood that the needle would move or slip during collection. With linear insertion, the device could not have reproduced these motions. Meanwhile, to determine when to stop the needle, the operator relies almost solely on the tactile response produced when the needle punctures the vessel wall. Due to differences in the mechanical properties of the rat tail compared to those of human skin and vessels, the tactile response when performing tail vein punctures is much subtler. The insertion force needed to puncture the outermost skin layers of the rat tail typically exceeds 1 N, whereas the puncture force in human epidermis is closer to 0.2 N. In our studies, the high skin penetration forces made it difficult to resolve salient force responses during vessel puncture. Since we could rely on neither the force response nor implement real-time US image analysis, the cannulations were performed entirely in an open-loop manner.

The current robot design allows for nonlinear insertions, but the trajectory planning algorithms require the vessel position to be updated in real-time based on segmentation. In future studies, we will modify the trajectory planning routines to operate under static conditions. Aside from the insertion kinematics, we also observed that not all 9 of the DOF in the third-generation device were not utilized in performing tail vein cannulations. In particular, since the tail veins run parallel with the direction of insertion once the tail is fixed to the device, the two lateral rotations were unnecessary. Furthermore, the travel lengths of the Cartesian positioning system far exceeded the necessary workspace, and overall kinematic design was not optimal for animal venipuncture.

These observations suggest that a simplified system may be designed to perform dedicated venipuncture procedures in rodents. In particular, since NIR imaging was shown to provide comparable cannulation results to US imaging, and since the dexterity of the current robotic system is unnecessary for rodent cannulations, it may be possible to develop a device with a dramatically reduced form factor, complexity, and cost. **Figure 4-23** shows the design of a low-cost, handheld device for rodent cannulations that works by attaching directly to the animal's tail. The system is able to rotate about the full 360° circumference of the tail to target all four vessels, and the insertion

mechanism is highly simplified compared to the device currently designed for clinical use. The device may be clipped to the tail with one hand, allowing the operator to hold the animal with the other. In this way, it may be possible to perform the automated cannulations without the use of anesthesia, which would significantly reduce the procedure time and labor, improve animal welfare, and eliminate the potential effects of anesthesia on blood specimen quality. The miniaturized device is currently being evaluated on phantoms and will subsequently be tested *in vivo*.
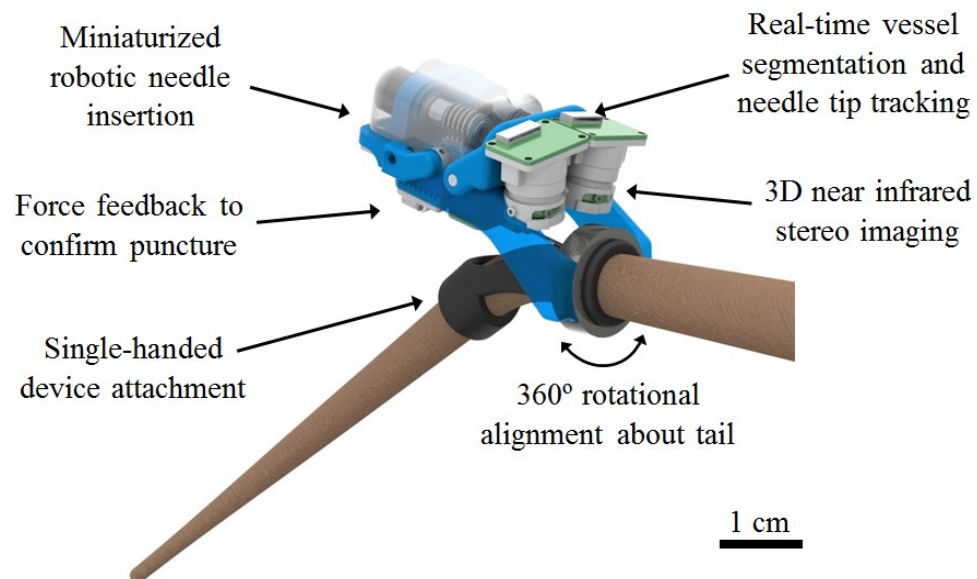
Figure 4-23. Low-cost, handheld device for automated, image-guided tail vessel cannulations in rodents. The device is able to rotate about the full 360° circumference of the tail to target all four vessels, and is designed to be attached to the tail with one hand, allowing the operator to hold the animal with the other.

Chapter 5 – Conclusions and future directions

5.1. Summary

This dissertation described the development of a portable, image-guided, robotic device for automated peripheral venous access, blood collection, and intravenous delivery. The device is designed with the purpose of minimizing adverse events during venipuncture, particularly in challenging populations for whom the rate of success depends significantly on practitioner skill. The device operates by mapping the position of a selected vessel target and guiding the cannula into the center based on real-time image feedback. Our rationale was that, by automating the cannulation procedure, the device would be able to reduce the number of needle placement attempts in normal and difficult patient populations compared to manual cannulation techniques. Once translated, such a system would have the potential to provide healthcare professionals the ability to draw blood and start intravenous lines with unparalleled accuracy and speed. The device may also serve as an equalizer among patients (by minimizing the influence of demographic parameters) and among practitioners (by reducing variability due to training and experience). Finally, the device can entirely remove the practitioner from contact with exposed sharps, thus eliminating the risk of accidental needle stick injuries and blood-borne transfections.

5.2. Conclusions, challenges, and outlook

5.2.1. Vessel imaging and robust computer vision

In order to perform these tasks in an autonomous manner, image analysis and robotic control software had to be developed that could extract 3D position and pose information from the acquired images and relay this information to the robotic controller. To account for patient movement, tissue motion, vessel deformation, and other sources of uncertainty, it was important that the image information was updated in real-time to allow the robot to make subtle and rapid adjustments during

the needle insertion. Furthermore, the algorithmic approaches needed to be robust in the presence of multiple sources of variability and noise, including differences patient physiology and demographic makeup, changes in the imaging conditions, and unexpected events that may occur in the real world. These influences represent a major challenge of the current work.

In Chapter 2, I presented a method for peripheral vessel localization combining 3D NIR and US imaging. The imaging approach is suited for use both as a standalone imaging tool and as a means for image-guided, robotic cannulation. I also described image analysis techniques and algorithms to extract structure and position information about the vessels. The algorithms comprise a combination of "off-the-shelf" solutions, made available through open-source computer vision libraries, and newly developed approaches. The majority of the open-source software that we used was already optimized for efficient performance on a CUDA-based GPU system. On the other hand, CUDA-optimized solutions are much more difficult to modify. For this reason, the image analysis steps, e.g., segmentation, disparity estimation, structure labeling, and motion tracking, have mostly been implemented as a series of standalone functions along a processing pipeline.

Unfortunately, information is lost when each step is carried out in an independent fashion. Thus, in Chapter 2.7.6, I proposed a probabilistic framework for integrating the outputs of the individual processing steps. In this approach, the labels generated in the segmentation and motion estimation steps are incorporated into the messages passed around the Markov network in the stereo disparity computation. Similarly, motion may be incorporated as a prior in the energy formulation used to drive the evolution of active contours during vessel segmentation. At present, we have developed early software prototypes implementing some of these concepts, but work is needed to optimize the code for real-time performance. An early prototype of a hardware-based solution incorporating structured illumination has also been developed, but the system requires further testing.

5.2.2. *Robotic vessel cannulation*

The development of the actual robotic system also represented a challenge, and the main design considerations were discussed in Chapter 3. The robotic manipulators that we've developed primarily consist of a base positioning system and a needle insertion end-effector. In the more recent systems, added rotational DOF were implemented to allow for alignment with the 6 pose of the target vessel. In total, it is estimated that at least eight DOF are needed to achieve fully autonomous needle servoing. Meanwhile, the required workspace is governed by the expected length of an adult human forearm and the range of vessels that must be reached. Additionally, high translational and rotational speeds are needed to adjust the needle to rapid tissue deformations or patient arm movements during puncture. Thus the challenge was to design a portable robot with the necessary dexterity, workspace, accuracy, and speed while ensuring that a reasonable cost was maintained.

A focus of future research will be to investigate alternative robotic designs, e.g., hexapod, delta, and other parallel mechanisms, that can accommodate the dexterity requirements of the task while minimizing size and complexity. Meanwhile, cannulation accuracy and responsiveness may be improved with the implementation of nonlinear needle insertion trajectories based on dynamic rather than kinematic control. This would allow the system to adjust more fluidly to higher-order motions[206–209]. It is also possible that probabilistic state estimation and control systems may be implemented to reduce errors by predicting future positions from current trajectories[202–204,210].

5.2.3. *In vitro validation in tissue-mimicking phantoms*

To validate the imaging and robotic systems, we developed an *in vitro* model of human skin and vessel tissues in which the mechanical, optical, and acoustic properties of each model may be tuned to simulate a broad spectrum of patient demographic characteristics. These models allowed us to study the effects of patient variability on system performance without requiring large human

trials. In this way, the phantoms fill a gap in the current field arising from the lack of suitable preclinical models for peripheral vascular interventions. As discussed in Chapter 4, we characterized each tissue-mimicking component and compared the results to human tissue values found in the literature. We compared the performance of the device to manual cannulations with and without the use of assistive imaging devices, and we evaluated a number of clinically-relevant metrics, including vessel visibility, first-stick cannulation success rate, average number of needle stick attempts, and total and per-attempt completion time. The results of these studies highlighted some of the major advantages and current limitations of the technology. In particular, we observed that the use of bimodal NIR+US imaging allowed a greater percentage of vessels to be identified compared to unassisted visualization. We also saw that the improvement in visualization translated to more accurate needle insertions by the device, and that this increase in accuracy was particularly evident in difficult conditions, for example, darker skin tones and higher BMI.

5.2.4. *In vivo validation in rats*

Chapter 4 also described studies to evaluate the imaging and cannulation performance of the device in a rat model. Similar to the *in vitro* experiments, the *in vivo* studies compared the first-stick accuracy of the device to unassisted, NIR-guided, and US-guided cannulations by a manual operator. From a qualitative perspective, the device was found to simplify the overall workflow of the animal cannulation trials and reduce the manual labor by performing the task in an automated fashion. More quantitatively, the device significantly increased the rate of first-stick cannulation success and decreased the average number of needle stick attempts compared to unassisted manual and US-guided manual cannulations. However, robotic cannulation accuracy was not better than accuracies achieved by manual cannulation under NIR transillumination imaging. Our observations suggested that an NIR-based device may be useful as a solution for performing animal tail vein cannulations, and the design of one such device was introduced. The studies also highlighted some of the limitations of the rat tail as a suitable preclinical *in vivo* model of human venipuncture. Many

of the mechanical, optical, and acoustic properties of the rat tail are substantially different from those of the human forearm and hand. These differences further underscore the importance of realistic *in vitro* models such as the customizable tissue-mimicking phantoms described earlier.

5.2.5. *Preparing for first-in-human validation*

The *in vitro* and *in vivo* studies have served as groundwork for human feasibility studies that will be initiated in the near future. As currently planned, the studies will be carried out in a sample population of 20 to 40 healthy adult volunteers with no prior history of difficult venous access and will include one treatment arm and no control, i.e., venipuncture will be performed only with the device. The goals of these studies will be to assess device safety, evaluate first-stick accuracy, and obtain data to guide further technical development. The outcomes will also allow proper endpoints and statistical power to be determined for subsequent clinical investigations, for example, to measure device efficacy in difficult patient populations.

5.2.6. *Addressing safety and usability*

Beyond these initial clinical studies, further translation of the technology will entail addressing concerns related to safety and usability. While these considerations are largely beyond the scope of the dissertation, they were nevertheless integral to the design of the device. Currently, a number of safety features have been incorporated into our most recent prototypes. These features include software for monitoring the electrical and mechanical components in the device. Safety measures have also been implemented to varying degrees in the GUI, disposables design, automated needle handling system, and device sterilization protocol. We have also performed preliminary failure mode and effects analyses, conducted an assessment of potential device-related hazards, and completed early studies evaluating risk factors associated with the operation and maintenance of the device in hospital and diagnostic laboratory settings.

The next generation prototype will incorporate at least three major functional changes. First, the software architecture will be moved from the general operating system to a dedicated (embedded) operating system, which will consist of an FPGA-based platform (for example, the Xilinx architecture), a dedicated GPU platform (for example, the NVIDIA architecture), or a combination of the two. Currently, the device utilizes a laptop workstation as the host processor. The control software is compiled to the laptop's CPU, and the majority of the computer vision algorithms are processed on a GPU. With this architecture, the computer can perform the imaging and robotics computations at real-time frame rates using of 800 MB of CPU memory and 500 MB of GPU memory. Approximately 100 MB/s of data is communicated between the laptop and the robot via a single USB 3.0 connection. Inside the robot, a USB 3.0 receiver hub splits the input into five independent outputs that interface, respectively, with the cameras, LED circuitry, US transducer, base positioning robot, and manipulator robot. This architecture will most likely be maintained during the transition to the embedded design.

The second major change will be to fully integrate the user-facing elements of the device. As described in earlier chapters, early prototypes for several components with which the patient and practitioner directly interact (namely, the GUI, patient arm rest, disposables) have been developed (see Chapter 3.5). The GUI assists the clinician through the major steps of the procedure and displays processed NIR and US images for real-time visualization. The arm rest serves to minimize motions at the wrist and elbow and serves as a tourniquet at the upper forearm. The disposables include an attachable clip that contains a solid US coupling material and a second clip that allows the needle to be easily attached to the end-effector. Both the arm rest and the disposables may come into contact with patient fluids and therefore need to be manufactured from medical-grade materials and packaged in a sterile environment. The sterilization protocol for the device as a whole will also need to be refined; the particular method of sterilization must be compatible with the electronic, mechanical, and optical components within the system.

The third critical component of transitioning from an engineering prototype to clinical device is centered on the design control process. As development moves farther out of the research lab, it will be critical to define detailed specifications for each component of the clinical device, to comply with FDA good manufacturing practices (GMP), and to establish a means for system verification and validation. Evidence of these controls would then be submitted as part of the regulatory review.

5.2.7. *Addressing cost and clinical acceptance*

Lastly, to relate the results of this work to more direct measures of clinical value, the true medical costs associated with difficult venipuncture must be considered[271]. For the hospital, these costs are reimbursed by payers, and the amount of reimbursement differs greatly depending on the specific procedure and payer. The amount reimbursed by a private payer for peripheral intravenous catheterization, for example, greatly exceeds the amount reimbursed by a government program for a standard blood draw[272]. In difficult cases, the actual costs may far exceed the reimbursement rate, and these losses may represent a significant burden on the healthcare institution when aggregated across all patients and over time. Costs due to difficult venipuncture include the wasted consumable supplies and the resources devoted to additional personnel time. Substantial costs are also invested in training practitioners on alternative techniques, including NIR and US guidance, and in hiring specialized intravenous teams. Further costs may be associated with the compromised specimen quality that commonly results from difficulties and delays during sample collection. Finally, costs are incurred as a result of complications and adverse events, unintended needle stick injuries to practitioners, and decreased patient satisfaction ratings (which affects reimbursement).

The various costs in specialized care facilities, for example the pediatric hospital, oncology care center or elderly nursing home, are typically scaled in proportion to the costs incurred in the general hospital. In the diagnostic lab, the costs are also similar, though in these settings only blood draws will be performed. To date, some preliminary data has been collected to quantify the

influence of difficult venipuncture on time, material, and labor costs in hospitals and diagnostic facilities (see Appendix for a summary of the findings). Ultimately, the clinical adoption of automated venipuncture, either to address difficult clinical scenarios or to replace standard techniques as a *de facto* method of care, will be determined by the extent to which the technology can minimize these varied costs.

5.3.   Future research directions

5.3.1.   *Automated point-of-care blood testing*

Elements of the work described in this dissertation may be extended to clinical and research problems outside of venipuncture. **Figure 5-1** summarizes some of the ongoing and future research directions. As one example, our group has recently begun to investigate the possibility of developing the device as a platform for comprehensive point-of-care blood testing. While blood-based assays account for the vast majority of diagnostic testing administered in ambulatory and emergency care settings, the results are generated almost exclusively in centralized laboratories from large-volume blood samples acquired by manual venipuncture techniques[273]. A major focus of ongoing and future research will be to merge automated blood drawing with microfluidics-based analytic techniques to obtain quantitative chemistry, protein, and cellular measurements at the patient bedside, ideally within minutes of the blood draw[65,66]. Such a system would represent an end-to-end solution to point-of-care testing that does not exist today. The integrative approach may be particularly suited for infant and neonatal applications, where difficult venipuncture and low blood volume requirements challenge the safety and quality of care[274].
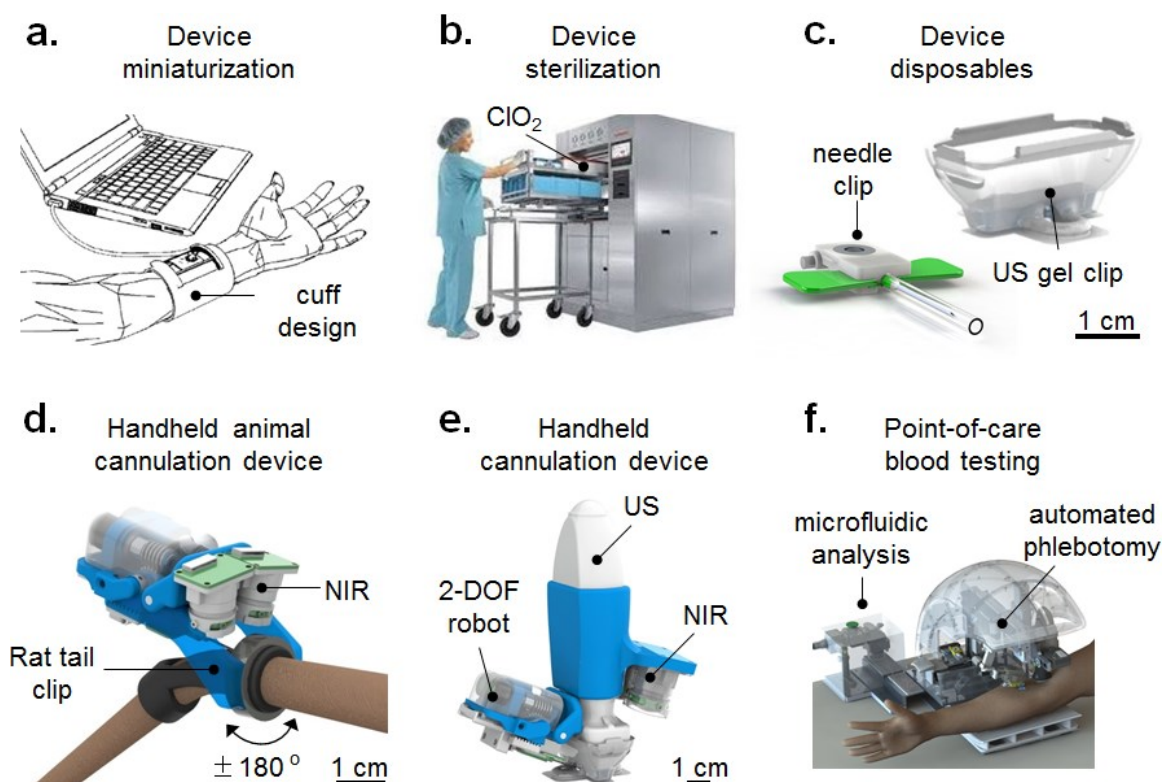
Figure 5-1. Summary of ongoing and future project directions. **(a)** Investigating miniaturized robotic mechanisms that can reduce device form factor, cost, and complexity. **(b)** Implementing sterilization protocols compatible with sensitive electronic, mechanical, and optical components within the device. **(c)** Incorporating disposable products to improve device usability and minimize the need for manual setup and operation. **(d)** Developing a low-cost, handheld device to perform tail vessel cannulations in rodents (rats and mice), e.g., as an assistive tool for preclinical research. **(e)** Developing a handheld image-guided venipuncture device, e.g., for primary care, at-home, mobile, and low-resource settings. **(f)** Developing a platform for rapid point-of-care blood testing combining automated venipuncture and microfluidic analysis.

5.3.2. *Peripheral vascular procedures*

The device may also be adapted for other interventional procedures, including PICC placement, peripheral endovascular procedures, and other surgical procedures on peripheral tissues. In these procedures, the margin for error may arguably be higher than it is for routine venipuncture, particularly since the difficulty level for practitioners and the risk for patients are both substantially increased. Moreover, whereas the evidence regarding the clinical utility of US-guided venipuncture remains inconclusive (see Chapter 2.2.4), there is strong literature support for effectiveness of US imaging to aid clinicians in guiding catheters that are inserted peripherally and then advanced into

the central vessels[275,276]. Image-guided robotic systems developed to perform central vascular catheterization procedures, e.g., for diagnosing venous thrombosis[277], examining arterial occlusion[223,278–281], or performing percutaneous biopsies[54–56], have also shown promise, though no system has reached the marketplace yet. Surgical operations on peripheral tissues, for example, to remove varicose veins[282] in the leg or to treat vessel occlusions in the retina[283–285], represent additional areas in which NIR or US-guided robotic systems may provide clinical value. Such operations require extreme mechanical precision, and robotic devices may be effective in correcting hand tremors by the surgeon[286] or performing aspects of the operation autonomously.

The venipuncture device may furthermore be adapted to place hemodialysis catheters without requiring fundamental changes to the imaging, image analysis, or control systems in the current prototype design. Hundreds of thousands of people in the U.S. are on hemodialysis, and while new dialysis machines have made it possible for patients to receive regular treatment in their own homes, a major limitation to the adoption of at-home dialysis regimens is the difficulty of performing self-administered cannulation[287,288]. Most commonly, a nurse practitioner must travel to the patient's home to provide dialysis care. It may be possible to integrate the venipuncture device with modern home dialysis machines to improve the quality-of-life of patients with chronic kidney diseases.

5.3.3. Looking outside the clinic

Finally, image-guided robots have also seen adoption in industrial environments[289–291], for military applications[292,293], for consumer use[294–298], and on the road[299,300]. The common thread among the robotic systems developed for these varied applications is the ability to extrapolate 3D positional information from a dynamic environment and provide this information to an actuation system (surgical robot, car, etc.) that directs movement commands. Thus, the methods described in the preceding chapters for robust computer vision, image recognition, and adaptive motion control may be applied toward unmet needs both in and outside of healthcare.

Appendix

Supplementary Table 6-1. Total addressable U.S. market for automated venous access.

Key Market Segments	Time-line (years)	Total procedures per year (M)	Total facilities	Avg. devices per facility	Procedures per device per day	Total market (no. of devices)
Diagnostic Facilities	**1**	**239**	**3,900**	**6**	**25.7**	**23,400**
Gen. Hospitals >200 beds	**2**	**113**	**1,422**	**9**	**22.0**	**12,798**
Gen. Hospitals <200 beds	3	132	2,911	5	23.0	14,555
Large Group Practices	3	88	8,517	1	22.0	8,517
Pediatric Hospitals	4	24	481	2	24.8	962
Pediatric Group Practices	4	21	2,005	1	24.0	2,005
Skilled Nursing Facilities	5+	147	16,003	1	23.5	16,003
Veterans Hospitals	5+	29	1,642	2	21.8	3,284
Oncology Hospitals	5+	20	855	2	24.3	1,710
IVF/Infusion Clinics	5+	20	2,830	2	16.7	2,666
Ambulatory Care / EMT	5+	70	8,583	1	27.5	8,583
Veterinary clinics	5+	97	9,600	2	17.0	13,200
Animal facilities	5+	92	11,800	2	19.0	11,800
Totals		**1.1 B**	**70,549**	**2.0**	**22.3**	**119,483**

Supplementary Table 6-2. Primary observations of venipuncture accuracy and time over 24 hr period in one major U.S. hospital.

Venipuncture Accuracy and Time	Value
Number of venipuncture procedures / hr	10.1
Number of trained personnel per ward	3.4
Percent with DVA (3+ sticks)	24 %
Percent requiring additional personnel	16 %
Percent utilizing vein imaging assist device	7 %
Pediatric failure rate	47 %
Adult failure rate	10 %
Geriatric failure rate	25 %
Avg. number of sticks per patient (overall)	1.8 sticks
Avg. number of sticks per patient (DVA)	2.8 sticks
Avg. per-procedure time (overall)	12 minutes
Avg. per-procedure time w/ DVA (DVA)	20 minutes

Supplementary Table 6-3. Primary observations of venipuncture-related costs over 24 hr period in one major U.S. hospital.

Venipuncture Costs	Value
Nursing staff / phlebotomist average salary ($ / hr)	$13.5 to 15.5
Per-procedure full time equivalents	1.4
Venipuncture material costs ($ / unit)	$2.05
Needle set	*$0.90*
Blood collection vial set	*$0.80*
Alcohol swab, gauze, bandage, gloves	*$0.35*
Avg. per-procedure labor cost (overall)	$3.72
Avg. per-procedure material cost (overall)	$3.69
Avg. per-procedure cost, labor + material (overall)	**$7.41**
Avg. per-procedure labor cost (DVA)	$3.72
Avg. per-procedure material cost (DVA)	$3.69
Avg. per-procedure cost, labor + material, (DVA)	**$12.50**

Supplementary Table 6-4. Primary observation studies of venipuncture time, accuracy, and costs at a multi-personnel diagnostic laboratory testing facility in the U.S.

	Current hospital phlebotomy standards
Administrative and preparatory	*4 min*
Needle stick and sample collection, initial attempt	*3 min*
Needle stick and sample collection, additional	*5 min*
Total minutes per procedure	**12 min**
Avg. needle sticks / procedure, pediatrics	*2.7*
Avg. needle sticks / procedure, adults	*1.4*
Avg. needle sticks / procedure, geriatrics	*1.9*
Avg. needle sticks / procedure, overall	**1.81**
Avg. labor cost / procedure	*$3.72*
Avg. material cost / procedure	*$3.69*
Avg. labor + material cost / procedure	**$7.41**
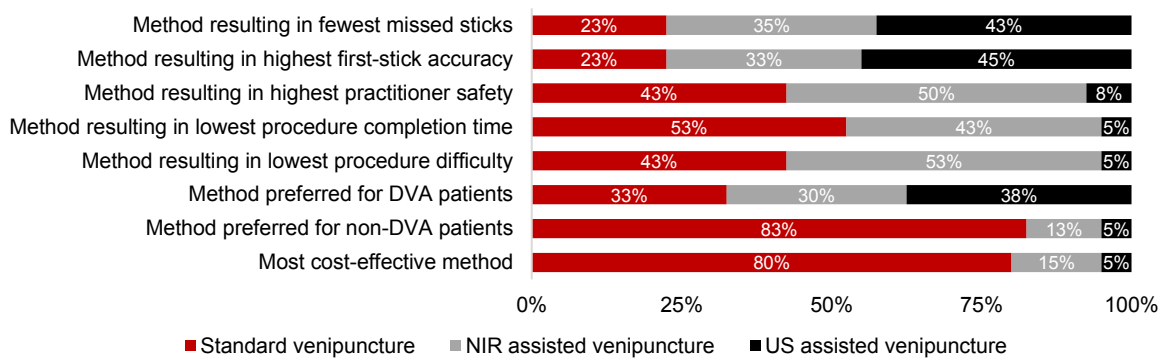
Supplementary Figure 6-1. Practitioner opinions on current methods of NIR and US imaging for peripheral venous access. Data was obtained through surveys to phlebotomists in four major metropolitan hospitals. In a second market study, nurses, phlebotomists, and clinicians from 4 hospitals and 1 diagnostic testing facility were surveyed about their preferred methods of performing venipuncture. For this study, participants were asked to vote on the eight questions shown here, indicating whether standard, NIR-assisted, or US-assisted methods of venipuncture were preferred for the different clinical scenarios presented.

References

1. Niska, R., Bhuiya, F. & Xu, J. National Hospital Ambulatory Medical Care Survey: 2007 emergency department summary. *Natl. Health Stat. Report.* 1–31 (2010).

2. Hing, E., Hall, M. J., Ashman, J. J. & Xu, J. National Hospital Ambulatory Medical Care Survey: 2007 outpatient department summary. *Natl. Health Stat. Report.* 1–32 (2010).

3. McCann, M., Einarsdottir, H., Van Waeleghem, J.-P., Murphy, F. & Sedgewick, J. Vascular access management 1: an overview. *Journal of renal care* **34,** 77–84 (2008).

4. Carr, P. J. *et al.* Development of a clinical prediction rule to improve peripheral intravenous cannulae first attempt success in the emergency department and reduce post insertion failure rates: the Vascular Access Decisions in the Emergency Room (VADER) study protocol. *BMJ Open* **6,** e009196 (2016).

5. Jacobson, A. F. & Winslow, E. H. Variables influencing intravenous catheter insertion difficulty and failure: an analysis of 339 intravenous catheter insertions. *Hear. lung J. Crit. care* **34,** 345–359 (2005).

6. Campbell, J. Intravenous cannulation: potential complications. *Prof. Nurse London Engl.* **12,** S10–S13 (1997).

7. Kuensting, L. L. *et al.* Difficult venous access in children: taking control. *J. Emerg. Nurs.* **35,** 419–24 (2009).

8. Rauch, D. *et al.* Peripheral difficult venous access in children. *Clin. Pediatr. (Phila).* **48,** 895–901 (2009).

9. Mbamalu, D. & Banerjee, A. Methods of obtaining peripheral venous access in difficult situations. *Postgrad. Med. J.* **75,** 459–462 (1999).

10. Walsh, G. Difficult peripheral venous access: recognizing and managing the patient at risk. *J. Assoc. Vasc. Access* **13,** 198–203 (2008).

11. Galena, H. J. Complications occurring from diagnostic venipuncture. *J. Fam. Pract.* **34,** 582–584 (1992).

12. Hagley, M. T., Martin, B., Gast, P. & Traeger, S. M. Infectious and mechanical complications of central venous catheters placed by percutaneous venipuncture and over guidewires. *Crit. Care Med.* **20,** 1426–1430 (1992).

13. CDC. Updated U.S. Public Health Service Guidelines for the Management of Occupational Exposures to HBV,HCV and HIV and Recommendations for Postexposure Prophylaxis. *MMWR* **50,** (2001).

14. Zaidi, M. A., Beshyah, S. A. & Griffith, R. Needle stick injuries : an overview of the size of the problem , pre- vention & management. **2,** 53–61 (2010).

15. Kuhar, D. T. *et al.* Updated US Public Health Service guidelines for the management of occupational exposures to human immunodeficiency virus and recommendations for postexposure prophylaxis. *Infect. Control Hosp. Epidemiol.* **34,** 875–92 (2013).

16. The Freedonia Group. *In Vitro Diagnostics: United States. Rinsho byori. The Japanese journal*

of clinical pathology **59,** (2011).

17. de Negri, D. C., Avelar, A. F. M., Andreoni, S., Pedreira Mda, L. & Pedreira, M. D. L. G. Predisposing factors for peripheral intravenous puncture failure in children. *Rev. Lat. Am. Enfermagem* **20,** 1072–80 (2012).

18. Pettross, B. Blood collection adverse reactions and patient blood volumes. *Fremont Heal. Gr. Lab. Serv.* **4,** 1–6 (2011).

19. Chen, A., L. Yarmush, M. & Maguire, T. Physiologically based pharmacokinetic models: integration of in silico approaches with micro cell culture analogues. *Current Drug Metabolism* **13,** 863–880 (2012).

20. Walco, G. a. Needle pain in children: contextual factors. *Pediatrics* **122 Suppl ,** S125–9 (2008).

21. Kennedy, R. M., Luhmann, J. & Zempsky, W. T. Clinical implications of unmanaged needle-insertion pain and distress in children. *Pediatrics* **122,** S130–3 (2008).

22. Uman, L. S., Chambers, C. T., McGrath, P. J. & Kisely, S. A systematic review of randomized controlled trials examining psychological interventions for needle-related procedural pain and distress in children and adolescents: An abbreviated cochrane review. *Journal of Pediatric Psychology* **33,** 842–854 (2008).

23. Stitik, T. P., Foye, P. M., Nadler, S. F. & Brachman, G. O. Phlebotomy-related lateral antebrachial cutaneous nerve injury. *Am. J. Phys. Med. Rehabil.* **80,** 230–4 (2001).

24. Boeson, M. B., Hranchook, A. & Stoller, J. Peripheral nerve injury from intravenous cannulation: a case report. *J. Am. Assoc. Nurse Anesth.* **68,** 53–57 (2000).

25. Rayegani, S. M. & Azadi, A. Lateral antebrachial cutaneous nerve injury induced by phlebotomy. *J. Brachial Plex. Peripher. Nerve Inj.* **2,** 6 (2007).

26. Malach, T. *et al.* Prospective surveillance of phlebitis associated with peripheral intravenous catheters. *Am. J. Infect. Control* **34,** 308–312 (2006).

27. Thigpen, J. L. Peripheral intravenous extravasation: nursing procedure for initial treatment. *Neonatal Netw.* **26,** 379–84 (2007).

28. Au, A. K., Rotte, M. J., Grzybowski, R. J., Ku, B. S. & Fields, J. M. Decrease in central venous catheter placement due to use of ultrasound guidance for peripheral intravenous catheters. *Am. J. Emerg. Med.* **30,** 1950–1954 (2012).

29. Porta, C., Handelman, E. & McGovern, P. Needlestick injuries among health care workers. A literature review. *AAOHN J. Off. J. Am. Assoc. Occup. Heal. Nurses* **47,** 237–244 (1999).

30. *Quest Diagnostics 2015 annual report.* (2015).

31. *Laboratory Corporation 2015 annual report.* (2015).

32. Bashkatov, A. N., Genina, E. A., Kochubey, V. I. & Tuchin, V. V. Optical properties of human skin, subcutaneous and mucous tissues in the wavelength range from 400 to 2000 nm. *J. Phys. D. Appl. Phys.* **38,** 2543–2555 (2005).

33. Curtis, J. *et al.* Ultrasound or near-infrared vascular imaging to guide peripheral intravenous catheterization in children: a pragmatic randomized control trial. *CMAJ* **187,** (2015).

34. Heinrichs J, Fritze Z, Klassen T & Curtis S. A systematic review and meta-analysis of new

interventions for peripheral intravenous cannulation of children. *Pediatr. Emerg. Care* **29,** 858–866 (2013).

35. Troianos, C. A. *et al.* Guidelines for performing ultrasound guided vascular cannulation: recommendations of the American Society of Echocardiography and the Society of Cardiovascular Anesthesiologists. *J. Am. Soc. Echocardiogr.* **24,** 1291–1318 (2011).

36. Heinrichs, J., Fritze, Z., Vandermeer, B., Klassen, T. & Curtis, S. Ultrasonographically guided peripheral intravenous cannulation of children and adults: A systematic review and meta-analysis. *Annals of Emergency Medicine* **61,** (2013).

37. Liu, Y. T., Alsaawi, A. & Bjornsson, H. M. Ultrasound-guided peripheral venous access: a systematic review of randomized-controlled trials. *Eur. J. Emerg. Med.* **21,** 18–23 (2014).

38. Stolz, L. A., Stolz, U., Howe, C., Farrell, I. J. & Adhikari, S. Ultrasound-guided peripheral venous access: a meta-analysis and systematic review. *J. Vasc. Access* **16,** 321–326 (2015).

39. Moustris, G. P., Hiridis, S. C., Deliparaschos, K. M. & Konstantinidis, K. M. Evolution of autonomous and semi-autonomous robotic surgical systems: A review of the literature. *International Journal of Medical Robotics and Computer Assisted Surgery* **7,** 375–392 (2011).

40. Taylor, R. H. & Stoianovici, D. Medical robotics in computer-integrated surgery. *IEEE Transactions on Robotics and Automation* **19,** 765–781 (2003).

41. Hutchinson, S., Hager, G. D. & Corke, P. I. A tutorial on visual servo control. *IEEE Trans. Robot. Autom.* **12,** 651–670 (1996).

42. Silveira, G. & Malis, E. Direct visual servoing: Vision-based estimation and control using only nonmetric information. *IEEE Trans. Robot.* **28,** 974–980 (2012).

43. Cleary, K., Melzer, A., Watson, V., Kronreif, G. & Stoianovici, D. Interventional robotic systems: applications and technology state-of-the-art. *Minim. invasive Ther. allied Technol. MITAT Off. J. Soc. Minim. Invasive Ther.* **15,** 101–113 (2006).

44. Camarillo, D. B., Krummel, T. M. & Salisbury, J. K. Robotic technology in surgery: Past, present, and future. *American Journal of Surgery* **188,** (2004).

45. Sridhar, A. N. *et al.* Image-guided robotic interventions for prostate cancer. *Nat Rev Urol* 1–11 (2013). doi:10.1038/nrurol.2013.129

46. Fütterer, J. J. & Barentsz, J. O. MRI-guided and robotic-assisted prostate biopsy. *Curr. Opin. Urol.* **22,** 316–319 (2012).

47. Joskowicz, L. *et al.* Image-guided system with miniature robot for precise positioning and targeting in keyhole neurosurgery. *Comput. aided Surg. Off. J. Int. Soc. Comput. Aided Surg.* **11,** 181–193 (2006).

48. McGee, M. F. *et al.* A primer on natural orifice transluminal endoscopic surgery: building a new paradigm. *Surg. Innov.* **13,** 86–93 (2006).

49. Tanaka, H. *et al.* Implementation of bilateral control system based on acceleration control using FPGA for multi-DOF haptic endoscopic surgery robot. in *IEEE Transactions on Industrial Electronics* **56,** 618–627 (2009).

50. Podder, T. K. *et al.* Reliability of EUCLIDIAN: an autonomous robotic system for image-guided prostate brachytherapy. *Med. Phys.* **38,** 96–106 (2011).

51. Shademan, A. *et al.* Supervised autonomous robotic soft tissue surgery. *Sci. Transl. Med.* **8,** 337ra64 (2016).

52. Antoniou, G. A., Riga, C. V., Mayer, E. K., Cheshire, N. J. W. & Bicknell, C. D. Clinical applications of robotic technology in vascular and endovascular surgery. *Journal of Vascular Surgery* **53,** 493–499 (2011).

53. Lin, J. C. The role of robotic surgical system in the management of vascular disease. *Annals of Vascular Surgery* **27,** 976–983 (2013).

54. Kobayashi, Y. *et al.* Development of an integrated needle insertion system with image guidance and deformation simulation. *Comput. Med. Imaging Graph.* **34,** 9–18 (2010).

55. Kobayashi, Y. *et al.* Development of a needle insertion manipulator for central venous catheterization. *Int. J. Med. Robot. Comput. Assist. Surg.* **8,** 34–44 (2012).

56. Kobayashi, Y. *et al.* Preliminary in vivo evaluation of a needle insertion manipulator for central venous catheterization. *Robomech. J.* **1,** (2014).

57. Chen, A. I., Balter, M. L., Maguire, T. J. & Yarmush, M. L. 3D near infrared and ultrasound imaging of peripheral blood vessels for real-time localization and needle guidance. *Med. Image Comput. Comput. Interv.* **9902,** 130–137 (2016).

58. Chen, A. I., Nikitczuk, K., Nikitczuk, J., Maguire, T. J. & Yarmush, M. L. Portable robot for autonomous venipuncture using 3D near infrared image guidance. *Technology* **1,** 72–87 (2013).

59. Balter, M., Chen, A., Maguire, T. & Yarmush, M. The system design and evaluation of a 7-DOF image-guided venipuncture robot. *IEEE Trans. Robot.* **31,** 1044 – 1053 (2015).

60. Chen, A. I., Balter, M. L., Maguire, T. J. & Yarmush, M. L. Real-time needle steering in response to rolling vein deformation in a 9-DOF image-guided venipuncture robot. in *IEEE International Conference on Intelligent Robots and Systems* (2015).

61. Balter, M. L., Chen, A. I., Maguire, T. J. & Yarmush, M. L. Adaptive kinematic control of a robotic venipuncture device based on stereo vision, ultrasound, and force guidance. *IEEE Trans. Ind. Electron.* **PP,** 1 (2016).

62. Chen, A. I. *et al.* Multilayered tissue mimicking skin and vessel phantoms with tunable mechanical, optical, and acoustic properties. *Med. Phys.* **43,** 3117–3131 (2016).

63. Chen, A. I., Balter, M. L., Maguire, T. J. & Yarmush, M. L. Performance of an automated, image-guided cannulation robot on multilayered tissue phantoms in comparison to manual cannula insertion. *IEEE Trans. med* (2016).

64. Chen, A. I., Balter, M. L., Maguire, T. J. & Yarmush, M. L. Automated lateral tail vein blood collection and fluid delivery in rats using a portable, image-guided, robotic vessel cannulation device. *Phys. Med. Biol.* (2016).

65. Balter, M. L. *et al.* System design and development of a robotic device for automated venipuncture and diagnostic blood cell analysis. *IEEE Int. Conf. Intell. Robot. Syst.* (2016).

66. Balter, M. L. *et al.* Differential leukocyte counting via fluorescent detection and image processing on a centrifugal microfluidic platform. *Anal. Methods* 1–9 (2016). doi:10.1039/2016

67. Cheong, W. F., Prahl, S. A. & Welch, A. J. A review of the optical properties of biological tissues. *Quantum Electron. IEEE J.* **26,** 2166–2185 (1990).

68. Jacques, S. L. Optical properties of biological tissues: a review. *Phys. Med. Biol.* **58,** R37–61 (2013).

69. Jacques, S. L. Skin optics. *Oregon Medical Laser Center Monthly news and articles on Biomedical Optics and Medical Lasers* (1998). at <http://omlc.ogi.edu/news/jan98/skinoptics.html>

70. Jacques, S. L. Optical properties spectra. *OMLC* (2015). at <http://omlc.org/spectra/index.html>

71. van Gemert, M. J. *et al.* Optical properties of human blood vessel wall and plaque. *Lasers Surg. Med.* **5,** 235–237 (1985).

72. Keijzer, M., Richards-Kortum, R. R., Jacques, S. L. & Feld, M. S. Fluorescence spectroscopy of turbid media: Autofluorescence of the human aorta. *Appl. Opt.* **28,** 4286–4292 (1989).

73. Oraevsky, A. A., Jacques, S. L. & Tittel, F. K. Measurement of tissue optical properties by time-resolved detection of laser-induced transient stress. *Appl. Opt.* **36,** 402–415 (1997).

74. Bashkatov, A. N. Optical properties of the subcutaneous adipose tissue in the spectral range 400–2500 nm. *Optics and Spectroscopy* **99,** 836–842 (2005).

75. Roggan, A., Friebel, M., Dörschel, K., Hahn, A. & Müller, G. Optical properties of circulating human blood in the wavelength range 400–2500 nm. *Journal of Biomedical Optics* **4,** 36 (1999).

76. Salomatina, E., Jiang, B., Novak, J. & Yaroslavsky, A. N. Optical properties of normal and cancerous human skin in the visible and near-infrared spectral range. *Journal of Biomedical Optics* **11,** 064026 (2006).

77. Shung, K. K. Ultrasonic scattering in biological tissues. *The Journal of the Acoustical Society of America* **94,** 3033 (1993).

78. Moran, C. M., Bush, N. L. & Bamber, J. C. Ultrasonic propagation properties of excised human skin. *Ultrasound Med. Biol.* **21,** 1177–1190 (1995).

79. Azhari, H. in *Basics of Biomedical Ultrasound for Engineers* 313–314 (2010).

80. Baran, J. M. & Webster, J. G. Design of low-cost portable ultrasound systems: Review. in *Proceedings of the 31st Annual International Conference of the IEEE Engineering in Medicine and Biology Society: Engineering the Future of Biomedicine, EMBC 2009* 792–795 (2009). doi:10.1109/IEMBS.2009.5332754

81. Fuller, M. I., Owen, K., Blalock, T. N., Hossack, J. A. & Walker, W. F. Real time imaging with the sonic window: A pocket-sized, C-scan, medical ultrasound device. in *Proceedings - IEEE Ultrasonics Symposium* (2009). doi:10.1109/ULTSYM.2009.5441943

82. Fuller, M. I., Blalock, T. N., Hossack, J. a. & Walker, W. F. A portable, low-cost, highly integrated, 3D medical ultrasound system. *IEEE Symp. Ultrason. 2003* **1,** 38–41 (2003).

83. Sánchez-Morago, G.-V. S. *et al.* Viewing veins with AccuVein AV300. *Rev. Enferm. Barcelona Spain* **33,** 33–38 (2010).

84. Highton, L. & Ekwobi, C. Use of the AccuVein device to map the superficial venous system. *Eur. J. Plast. Surg.* **34,** 305–306 (2011).

85. Paquit, V. *et al.* Near-infrared imaging and structured light ranging for automatic catheter insertion. *Proc. SPIE - Int. Soc. Opt. Eng.* **6141,** (2006).

86. Paquit, V. & Price, J. Combining near-infrared illuminants to optimize venous imaging. *Proc. SPIE 6509, Med. imaging* 65090H (2007). doi:10.1117/12.712576

87. Strehle, E.-M. Making the invisible visible: near-infrared spectroscopy and phlebotomy in children. *Telemed. J. E. Health.* **16,** 889–93 (2010).

88. Evena Eyes-On Glasses, 2014. at <http://evenamed.com/products/glasses>

89. Parker, S., Benzies, K., Hayden, A. & Lang, E. Effectiveness of interventions for adult peripheral intravenous catheterization: A systematic review and meta-analysis of randomized controlled trials. *Int. Emerg. Nurs.* (2016).

90. De Graaff, J. C. *et al.* Near-infrared light to aid peripheral intravenous cannulation in children: A cluster randomised clinical trial of three devices. *Anaesthesia* **68,** 835–845 (2013).

91. Aulagnier, J. *et al.* Efficacy of Accuvein to facilitate peripheral intravenous placement in adults presenting to an emergency department: A randomized clinical trial. *Acad. Emerg. Med.* **21,** 858–863 (2014).

92. Cuper, N. J., de Graaff, J. C., Verdaasdonk, R. M. & Kalkman, C. J. Near-infrared imaging in intravenous cannulation in children: a cluster randomized clinical trial. *Pediatrics* **131,** e191–7 (2013).

93. Stolka, P. J. *et al.* Needle guidance using handheld stereo vision and projection for ultrasound-based interventions. in *Lecture Notes in Computer Science (including subseries Lecture Notes in Artificial Intelligence and Lecture Notes in Bioinformatics)* **8674 LNCS,** 684–691 (2014).

94. Zharov, V. P. *et al.* Infrared Imaging of Subcutaneous Veins. *Lasers Surg. Med.* **34,** 56–61 (2004).

95. Gui, C. & Tu, L. A stereo camera calibration based on robotic vision. *IEEE 10th Int. Conf. Cogn. Informatics Cogn. Comput. ICCICC11* 318–323 (2011). doi:10.1109/COGINF.2011.6016159

96. Heikkilä, J. Geometric camera calibration using circular control points. *Pattern Anal. Mach. Intell. IEEE Trans.* **22,** 1066–1077 (2000).

97. Berkhoff, A., Huisman, H., Thijssen, J., Jacobs, E. & Homan, R. Fast scan conversion algorithms for displaying ultrasound sector images. *Ultrason. Imaging* **16,** 97–108 (1994).

98. Lasso, A. *et al.* PLUS: Open-source toolkit for ultrasound-guided intervention systems. *IEEE Trans. Biomed. Eng.* **61,** 2527–2537 (2014).

99. Chenyang, X. & Prince, J. L. Gradient vector flow: a new external force for snakes. *Proc. IEEE Comput. Soc. Conf. Comput. Vis. Pattern Recognit.* **2,** 66–71 (1997).

100. Xu, C. & Prince, J. L. Snakes, shapes, and gradient vector flow. *IEEE Trans. Image Process.* **7,** 359–369 (1998).

101. Smistad, E., Elster, A. C. & Lindseth, F. Real-time gradient vector flow on GPUs using OpenCL. *J. Real-Time Image Process.* **10,** 67–74 (2015).

102. Frangi, A. F., Niessen, W. J., Vincken, K. L. & Viergever, M. A. Multiscale vessel enhancement filtering. *Med. Image Comput.* **1496,** 130–137 (1998).

103. Myronenko, A. & Song, X. Point set registration: Coherent point drifts. *IEEE Trans. Pattern Anal. Mach. Intell.* **32,** 2262–2275 (2010).

104. Yang, Q. Y. Q., Wang, L. W. L. & Ahuja, N. A constant-space belief propagation algorithm for stereo matching. *Comput. Vis. Pattern Recognit. (CVPR), 2010 IEEE Conf.* 1458–1465 (2010). doi:10.1109/CVPR.2010.5539797

105. Bouguet, J.-Y. Pyramidal implementation of the affine lucas kanade feature tracker—description of the algorithm. *Pages.Slc.Edu* **2,** 3 (2001).

106. Matas, J., Galambos, C. & Kittler, J. Robust detection of lines Using the progressive probabilistic Hough transform. *Comput. Vis. Image Underst.* **78,** 119–137 (2000).

107. Horn, B. K. P. & Schunck, B. G. Determining optical flow. *Artif. Intell.* **17,** 185–203 (1981).

108. Brox, T., Papenberg, N. & Weickert, J. High accuracy optical flow estimation based on a theory for warping. *Comput. Vis. - ECCV 2004* **4,** 25–36 (2004).

109. Bai, X. B. X. & Latecki, L. J. Path similarity skeleton graph matching. *IEEE Trans. Pattern Anal. Mach. Intell.* **30,** 1282–1292 (2008).

110. Kuhn, H. W. in *50 Years of Integer Programming 1958-2008: From the Early Years to the State-of-the-Art* 29–47 (2010). doi:10.1007/978-3-540-68279-0_2

111. Mori, G., Belongie, S. & Malik, J. Efficient shape matching using shape contexts. *IEEE Trans. Pattern Anal. Mach. Intell.* **27,** 1832–1837 (2005).

112. Zhu, S. C. Region competition: Unifying snakes, region growing, and Bayes/MDL for multiband image segmentation. *IEEE Trans. Pattern Anal. Mach. Intell.* **18,** 884–900 (1996).

113. Antony, J. & Kaye, M. Methodology for Taguchi Design of experiments for continuous quality improvement. *Qual. World* 98–102 (1995).

114. Bass, I. *Six Sigma Statistics with Excel and Minitab. Information & Management* **41,** (2007).

115. Ott, L. & Longnecker, M. *An Introduction to Statistical Methods and Data Analysis, 6th Edition*. (2010).

116. Brox, T. & Malik, J. Large displacement optical flow: Descriptor matching in variational motion estimation. *IEEE Trans. Pattern Anal. Mach. Intell.* **33,** 500–513 (2011).

117. Amiaz, T. & Kiryati, N. Piecewise-smooth dense optical flow via level sets. *Int. J. Comput. Vis.* **68,** 111–124 (2006).

118. Anandan, P. The robust estimation of multiple motions: parametric and piecewise smooth flow fields. *Comput. Vis. Image Underst.* **63,** 75–104 (1996).

119. Farneback, G. Very high accuracy velocity estimation using orientation tensors, parametric motion, and simultaneous segmentation of the motion field. in *Proceedings Eighth IEEE International Conference on Computer Vision. ICCV 2001* **1,** 171–177 (2001).

120. Chan, C., Lam, F. & Rohling, R. A needle tracking device for ultrasound guided percutaneous procedures. *Ultrasound Med. Biol.* **31,** 1469–1483 (2005).

121. Najafi, M. & Rohling, R. Single camera closed-form real-time needle trajectory tracking for ultrasound. *Med. Imaging - Vis. Image Guid. Proced. Model.* **7964,** 1–7 (2011).

122. Zhang, H. Freehand 3D ultrasound calibration using an electromagnetically tracked needle. *Proc. SPIE* **6141,** 61412M–61412M–9 (2006).

123. Hakime, A. *et al.* Electromagnetic-tracked biopsy under ultrasound guidance: preliminary results. *Cardiovasc. Intervent. Radiol.* **35,** 898–905 (2012).

124. Choquet, O., Abbal, B. & Capdevila, X. The new technological trends in ultrasound-guided regional anesthesia. *Curr Opin Anaesthesiol* (2013). doi:10.1097/01.aco.0000432512.15694.dd

125. Sun, S. Y., Gilbertson, M. & Anthony, B. W. Computer-guided ultrasound probe realignment by optical tracking. in *Proceedings - International Symposium on Biomedical Imaging* 21–24 (2013). doi:10.1109/ISBI.2013.6556402

126. Bengio, Y. Learning Deep Architectures for AI. *Found. Trends® Mach. Learn.* **2,** 1–127 (2009).

127. Kannala, J., Heikkilä, J. & Brandt, S. S. Geometric camera calibration. *Wiley Encycl. Comput. Sci. Eng.* 1–11 (2007). doi:10.1002/9780470050118.ecse589

128. Kannala, J. & Brandt, S. S. A generic camera model and calibration method for conventional, wide-angle, and fish-eye lenses. *IEEE Trans. Pattern Anal. Mach. Intell.* **28,** 1335–1340 (2006).

129. Hartley, R. & Zisserman, A. *Multiple View Geometry in Computer Vision. Cambridge University Press* **2,** (2004).

130. Bouguet, J.-Y. Complete camera calibration toolbox for Matlab. *Jean-Yves Bouguet's Homepage* (1999). at <http://www.vision.caltech.edu/bouguetj/>

131. Kass, M., Witkin, A. & Terzopoulos, D. Snakes: Active contour models. *Int. J. Comput. Vis.* **1,** 321–331 (1988).

132. Scharstein, D., Szeliski, R. & Zabih, R. A taxonomy and evaluation of dense two-frame stereo correspondence algorithms. in *Proceedings - IEEE Workshop on Stereo and Multi-Baseline Vision, SMBV 2001* 131–140 (2001). doi:10.1109/SMBV.2001.988771

133. Jian Sun, Nan-Ning Zheng & Heung-Yeung Shum. Stereo matching using belief propagation. *IEEE Trans. Pattern Anal. Mach. Intell.* **25,** 787–800 (2003).

134. Tappen, M. F. & Freeman, W. T. Comparison of graph cuts with belief propagation for stereo, using identical MRF parameters. *Proc. Ninth IEEE Int. Conf. Comput. Vis.* 900–906 (2003). doi:10.1109/ICCV.2003.1238444

135. Felzenszwalb, P. F. & Huttenlocher, D. P. Efficient belief propagation for early vision. *Int. J. Comput. Vis.* **70,** 41–54 (2006).

136. Yang, Q. Y. Q., Wang, L. W. L. & Ahuja, N. A constant-space belief propagation algorithm for stereo matching. *Comput. Vis. Pattern Recognit. CVPR 2010 IEEE Conf.* 1458–1465 (2010). doi:10.1109/CVPR.2010.5539797

137. Zhang, T. Y. & C.Y., S. A fast parallel algorithm for thinning digital patterns. *Image Process. Comput. Vis.* **27,** (1984).

138. Lucas, B. D. & Kanade, T. An iterative image registration technique with an application to stereo vision. *Proc. 7th Int. Jt. Conf. Artif. Intell.* 674–679 (1981). doi:Doi 10.1145/358669.358692

139. Yang, Q., Wang, L., Yang, R., Stewénius, H. & Nistér, D. Stereo matching with color-weighted correlation, hierarchical belief propagation, and occlusion handling. *IEEE Trans. Pattern Anal. Mach. Intell.* **31,** 492–504 (2009).

140. Zhang, L. & Seitz, S. M. Estimating optimal parameters for MRF stereo from a single image pair. *IEEE Trans. Pattern Anal. Mach. Intell.* **29,** 331–342 (2007).

141. Comaniciu, D. & Meer, P. Mean shift: A robust approach toward feature space analysis. *IEEE Trans. Pattern Anal. Mach. Intell.* **24,** 603–619 (2002).

142. Adams, R. & Bischof, L. Seeded region growing. *IEEE Trans. Pattern Anal. Mach. Intell.* **16,** 641–647 (1994).

143. Mehnert, A. & Jackway, P. An improved seeded region growing algorithm. *Pattern Recognit. Lett.* **18,** 1065–1071 (1997).

144. Fan, J., Zeng, G., Body, M. & Hacid, M. S. Seeded region growing: An extensive and comparative study. *Pattern Recognit. Lett.* **26,** 1139–1156 (2005).

145. Mitchell, D. G. Color Doppler imaging: principles, limitations, and artifacts. *Radiology* **177,** 1–10 (1990).

146. Pozniak, M., Zagzebski, J. & Scanlan, K. Spectral and color Doppler artifacts. *Radiographics* **12,** 35–44 (1992).

147. Rubens, D. J., Bhatt, S., Nedelka, S. & Cullinan, J. Doppler artifacts and pitfalls. *Radiologic Clinics of North America* **44,** 805–835 (2006).

148. Ramamurthy, B. S. & Trahey, G. E. Potential and limitations of angle-independent flow detection algorithms using radio-frequency and detected echo signals. *Ultrason. Imaging* **13,** 252–268 (1991).

149. Hein, I. A. & O Brien, W. D. Current time-domain methods for assessing tissue motion by analysis from reflected ultrasound echoes—a review. *IEEE Trans. Ultrason. Ferroelectr. Freq. Control* **40,** 84–102 (1993).

150. Golemati, S. *et al.* Comparison of block matching and differential methods for motion analysis of the carotid artery wall from ultrasound images. *IEEE Trans. Inf. Technol. Biomed.* **16,** 852–858 (2012).

151. Becker, F., Wieneke, B., Petra, S., Schröder, A. & Schnörr, C. Variational adaptive correlation method for flow estimation. *IEEE Trans. Image Process.* **21,** 3053–65 (2012).

152. Cohen, B. & Dinstein, I. New maximum likelihood motion estimation schemes for noisy ultrasound images. *Pattern Recognit.* **35,** 455–463 (2002).

153. Yeung, F., Levinson, S. F., Fu, D. & Parker, K. J. Feature-adaptive motion tracking of ultrasound image sequences using a deformable mesh. *IEEE Trans. Med. Imaging* **17,** 945–956 (1998).

154. Yeung, F., Levinson, S. F. & Parker, K. J. Multilevel and motion model-based ultrasonic speckle tracking algorithms. *Ultrasound Med. Biol.* **24,** 427–441 (1998).

155. Nam, K. H., Yeom, E., Ha, H. & Lee, S. J. Velocity field measurements of valvular blood flow in a human superficial vein using high-frequency ultrasound speckle image velocimetry. *Int. J. Cardiovasc. Imaging* **28,** 69–77 (2012).

156. Klarhöfer, M., Csapo, B., Balassy, C., Szeles, J. C. & Moser, E. High-resolution blood flow velocity measurements in the human finger. *Magn. Reson. Med.* **45,** 716–9 (2001).

157. Sandby-Møller, J., Poulsen, T. & Wulf, H. C. Epidermal thickness at different body sites: relationship to age, gender, pigmentation, blood content, skin type and smoking habits. *Acta Derm. Venereol.* **83,** 410–413 (2003).

158. Agache, P. G., Monneur, C., Leveque, J. L. & Rigal, J. Mechanical properties and Young's

modulus of human skin in vivo. *Archives of Dermatological Research* **269,** 221–232 (1980).

159. Geerligs, M. *et al.* In vitro indentation to determine the mechanical properties of epidermis. *J. Biomech.* **44,** 1176–1181 (2011).

160. Geerligs, M., Oomens, C., Ackermans, P., Baaijens, F. & Peters, G. Linear shear response of the upper skin layers. *Biorheology* **48,** 229–245 (2011).

161. Hendriks, F. M. Mechanical behavior of human epidermal and dermal layers in vivo. (2005).

162. Diridollou, S. *et al.* In vivo model of the mechanical properties of the human skin under suction. *Ski. Res. Technol.* **6,** 214–221 (2000).

163. Diridollou, S. *et al.* Sex- and site-dependent variations in the thickness and mechanical properties of human skin in vivo. *Int. J. Cosmet. Sci.* **22,** 421–435 (2000).

164. Diridollou, S. *et al.* An in vivo method for measuring the mechanical properties of the skin using ultrasound. *Ultrasound Med. Biol.* **24,** 215–224 (1998).

165. Zahouani, H. *et al.* Characterization of the mechanical properties of a dermal equivalent compared with human skin in vivo by indentation and static friction tests. *Ski. Res. Technol.* **15,** 68–76 (2009).

166. Hendriks, F. M. *et al.* A numerical-experimental method to characterize the non-linear mechanical behaviour of human skin. *Ski. Res. Technol.* **9,** 274–83 (2003).

167. Gennisson, J.-L. *et al.* Assessment of elastic parameters of human skin using dynamic elastography. *IEEE Trans. Ultrason. Ferroelectr. Freq. Control* **51,** 980–989 (2004).

168. Hendriks, F. M., Brokken, D., Oomens, C. W. J., Bader, D. L. & Baaijens, F. P. T. The relative contributions of different skin layers to the mechanical behavior of human skin in vivo using suction experiments. *Med. Eng. Phys.* **28,** 259–266 (2006).

169. Pailler-Mattei, C., Bec, S. & Zahouani, H. In vivo measurements of the elastic mechanical properties of human skin by indentation tests. *Med. Eng. Phys.* **30,** 599–606 (2008).

170. Holt, B., Tripathi, A. & Morgan, J. Viscoelastic response of human skin to low magnitude physiologically relevant shear. *J. Biomech.* **41,** 2689–2695 (2008).

171. Tan, C. Y., Statham, B., Marks, R. & Payne, P. A. Skin thickness measurement by pulsed ultrasound: its reproducibility, validation and variability. *Br. J. Dermatol.* **106,** 657–667 (1982).

172. Jain, S., Pandey, K., Lahoti, A. & Rao, K. P. Evaluation of skin and subcutaneous tissue thickness at insulin injection sites in Indian, insulin naïve, type-2 diabetic adult population. *Indian J Endocrinol Metab* **17,** 864–870 (2013).

173. Comley, K. & Fleck, N. The compressive response of porcine adipose tissue from low to high strain rate. *Int. J. Impact Eng.* **46,** 1–10 (2012).

174. Geerligs, M., Peters, G. W., Ackermans, P. A., Oomens, C. W. & Baaijens, F. P. Linear viscoelastic behavior of subcutaneous adipose tissue. *Biorheology* **45,** 677–688 (2008).

175. Alkouli, N. *et al.* Alkhouli 2013 The mechanical properties of human adipose tissues and their relationships to the structure and composition of the extracellular matrix. *Am J Phsiol Endocrinol Metab* **305,** 1427–1435 (2013).

176. Shergold, O. A., Fleck, N. A. & Radford, D. The uniaxial stress versus strain response of pig

skin and silicone rubber at low and high strain rates. *Int. J. Impact Eng.* **32,** 1384–1402 (2006).

177. Comley, K. & Fleck, N. A. A micromechanical model for the Young's modulus of adipose tissue. *Int. J. Solids Struct.* **47,** 2982–2990 (2010).

178. Comley, K. & Fleck, N. The mechanical response of porcine adipose tissue. *ASME J. Biomech. Eng.* 1–30 (2009).

179. Planken, R. N. *et al.* Diameter measurements of the forearm cephalic vein prior to vascular access creation in end-stage renal disease patients: Graduated pressure cuff versus tourniquet vessel dilatation. *Nephrol. Dial. Transplant.* **21,** 802–806 (2006).

180. Kiray, A., Ergur, I., Tayefi, H., Bagriyanik, H. & Bacakoglu, A. Anatomical evaluation of the superficial veins of the upper extremity as graft donor soruce in microvascular reconstructions: a cadaveric study. *Acta Orthop Traumatol Turc* **47,** 405–410 (2013).

181. Jacot, J. G. *et al.* Early adaptation of human lower extremity vein grafts: Wall stiffness changes accompany geometric remodeling. *J. Vasc. Surg.* **39,** 547–555 (2004).

182. Bergel, D. H. The static elastic properties of the arterial wall. *J. Physiol.* **156,** 445–457 (1961).

183. Shadwick, R. E. Mechanical design in arteries. *J. Exp. Biol.* **202,** 3305–3313 (1999).

184. Huang, W. & Yen, R. T. Zero-stress states of human pulmonary arteries and veins. *J. Appl. Physiol.* **85,** 867–873 (1998).

185. Silver, F. H., Horvath, I. & Foran, D. J. Viscoelasticity of the vessel wall: the role of collagen and elastic fibers. *Crit. Rev. Biomed. Eng.* **29,** 279–301 (2001).

186. Silver, F. H., Snowhill, P. B. & Foran, D. J. Mechanical behavior of vessel wall: A comparative study of aorta, vena cava, and carotid artery. *Ann. Biomed. Eng.* **31,** 793–803 (2003).

187. Li, T. *et al.* Simultaneous measurement of deep tissue blood flow and oxygenation using noncontact diffuse correlation spectroscopy flow-oximeter. *Sci. Rep.* **3,** 1358 (2013).

188. Vossoughi, J. & Tozeren, A. Determination of an effective shear modulus of aorta. *Rus J Biomech* **1,** 20–36 (1998).

189. Tortora, G., Dimitracopoulos, A., Valdastri, P., Menciassi, A. & Dario, P. Design of miniature modular in vivo robots for dedicated tasks in minimally invasive surgery. in *IEEE/ASME International Conference on Advanced Intelligent Mechatronics, AIM* 327–332 (2011). doi:10.1109/AIM.2011.6027004

190. Shah, B. C., Buettner, S. L., Lehman, A. C., Farritor, S. M. & Oleynikov, D. Miniature In Vivo Robotics and Novel Robotic Surgical Platforms. *Urologic Clinics of North America* **36,** 251–263 (2009).

191. Arai, F. Micro-nano robotic manipulation and biomedical applications. *Proceeding SPIE* **8548,** 854844–1 (2012).

192. Zivanovic, A. & Davies, B. L. A robotic system for blood sampling. *IEEE Trans. Inf. Technol. Biomed.* **4,** 8–14 (2000).

193. Sorenson, A. Tactile sensing methods for automated blood samples on humans. in *Proceedings of the 11th International Conference on Climbing and Walking Robots. Special Session on Manipulation and Grasping* 875–889 (2008).

194. de Boer, T., Steinbuch, M., Neerken, S. & Kharin, A. Laboratory study on needle-tissue interaction: toward the development of an instrument for automated venipuncture. *Journal of Mechanics in Medicine and Biology* **07,** 325–335 (2007).

195. Carvalho, P., Kesari, A., Weaver, S., Flaherty, P. & Fischer, G. Robotic assistive device for phlebotomy. *Proc. ASME 2015 Int. Des. Eng. Tech. Conf. Comput. Inf. Eng. Conf.* **3,** 1–6 (2015).

196. Brewer, R. Improving peripheral IV catheterization through robotics - from simple assistive devies to a fully autonomous system. (Stanford University, 2015).

197. Brewer, R. D. & Salisbury, J. K. Visual vein-finding for robotic IV insertion. in *Proceedings - IEEE International Conference on Robotics and Automation* 4597–4602 (2010). doi:10.1109/ROBOT.2010.5509575

198. Harris, R., Mygatt, J. & Harris, S. System and methods for autonomous intravenous needle insertion. (2012). doi:10.1016/j.micromeso.2003.09.025

199. Hartenberg, R. S. & Denavit, J. A kinematic notation for lower-pair mechanisms based on metrics. *Trans. ASME. J. Appl. Mech.* **22,** 215–221 (1955).

200. Kobayashi, Y. *et al.* Use of puncture force measurement to investigate the conditions of blood vessel needle insertion. *Med. Eng. Phys.* **35,** 684–689 (2013).

201. Garcia-Aracil, N., Perez-Vidal, C., Sabater, J. M., Morales, R. & Badesa, F. J. Robust and cooperative image-based visual servoing system using a redundant architecture. *Sensors* **11,** 11885–11900 (2011).

202. Wan, E. a & Van Der Merwe, R. The unscented Kalman filter for nonlinear estimation. *Adapt. Syst. Signal Process. Commun. Control Symp. 2000. AS-SPCC. IEEE 2000* 153–158 (2002). doi:10.1109/ASSPCC.2000.882463

203. Simon, D. Kalman filtering with state constraints: a survey of linear and nonlinear algorithms. *IET Control Theory Appl.* **4,** 1303 (2010).

204. Liu, J. S. & Chen, R. Sequential Monte Carlo methods for dynamic systems. *J. Am. Stat. Assoc.* **93,** 1032–1044 (1998).

205. Yilmaz, A., Javed, O. & Shah, M. Object tracking: A survey. *ACM Comput. Surv.* **38,** 13 (2006).

206. Wen, S. & Alterovitz, R. Motion planning under uncertainty for medical needle steering using optimization in belief space. in *IEEE International Conference on Intelligent Robots and Systems* 1775–1781 (2014). doi:10.1109/IROS.2014.6942795

207. Reed, K. B. *et al.* Integrated planning and image-guided control for planar needle steering. in *Proceedings of the 2nd Biennial IEEE/RAS-EMBS International Conference on Biomedical Robotics and Biomechatronics, BioRob 2008* 819–824 (2008). doi:10.1109/BIOROB.2008.4762833

208. Webster, R. J., Memisevic, J. & Okamura, A. M. Design considerations for robotic needle steering. in *Proceedings - IEEE International Conference on Robotics and Automation* **2005,** 3588–3594 (2005).

209. Du Toit, N. E. & Burdick, J. W. Robotic motion planning in dynamic, cluttered, uncertain environments. in *Proceedings - IEEE International Conference on Robotics and Automation* 966–973 (2010). doi:10.1109/ROBOT.2010.5509278

210. Patil, S., Van Den Berg, J. & Alterovitz, R. Estimating probability of collision for safe motion planning under Gaussian motion and sensing uncertainty. in *Proceedings - IEEE International Conference on Robotics and Automation* 3238–3244 (2012). doi:10.1109/ICRA.2012.6224727

211. Konishi, S. *et al.* Pneumatic micro hand and miniaturized parallel link robot for micro manipulation robot system. in *Proceedings - IEEE International Conference on Robotics and Automation* **2006,** 1036–1041 (2006).

212. Tsai, T.-C. T. T.-C. & Hsu, Y.-L. H. Y.-L. Development of a parallel surgical robot with automatic bone drilling carriage for stereotactic neurosurgery. *2004 IEEE Int. Conf. Syst. Man Cybern. (IEEE Cat. No.04CH37583)* **3,** 2156–2161 (2004).

213. Hwang, M. J., Bebek, O., Liang, F., Fei, B. & Cavusoglu, M. C. Kinematic calibration of a parallel robot for small animal biopsies. in *2009 IEEE/RSJ International Conference on Intelligent Robots and Systems, IROS 2009* 4104–4109 (2009). doi:10.1109/IROS.2009.5353969

214. Scharstein, D. & Szeliski, R. High-accuracy stereo depth maps using structured light. *Comput. Vis. Pattern Recognition, 2003. Proceedings. 2003 IEEE Comput. Soc. Conf.* **1,** I–195 – I–202 (2003).

215. Salvi, J., Pagès, J. & Batlle, J. Pattern codification strategies in structured light systems. *Pattern Recognit.* **37,** 827–849 (2004).

216. Jang, W., Je, C., Seo, Y. & Lee, S. W. Structured-light stereo: Comparative analysis and integration of structured-light and active stereo for measuring dynamic shape. *Opt. Lasers Eng.* **51,** 1255–1264 (2013).

217. Curless, B. & Seitz, S. M. Spacetime stereo: shape recovery for dynamic scenes. *2003 IEEE Comput. Soc. Conf. Comput. Vis. Pattern Recognition, 2003. Proceedings.* **2,** II–367–74 (2003).

218. Zhang, L., Curless, B. & Seitz, S. M. Rapid shape acquisition using color structured light and multi-pass dynamic programming. in *Proceedings - 1st International Symposium on 3D Data Processing Visualization and Transmission, 3DPVT 2002* 24–36 (2002). doi:10.1109/TDPVT.2002.1024035

219. Davis, J., Nehab, D., Ramamoorthi, R. & Rusinkiewicz, S. Spacetime stereo: A unifying framework for depth from triangulation. *IEEE Trans. Pattern Anal. Mach. Intell.* **27,** 296–302 (2005).

220. Zhang, S. & Huang, P. High-resolution, real-time 3D shape acquisition. in *IEEE Computer Society Conference on Computer Vision and Pattern Recognition Workshops* **2004-Janua,** (2004).

221. Schaffer, M., Grosse, M. & Kowarschik, R. High-speed pattern projection for three-dimensional shape measurement using laser speckles. *Appl. Opt.* **49,** 3622–3629 (2010).

222. Tahri, O., Mezouar, Y., Chaumette, F. & Corke, P. Decoupled image-based visual servoing for cameras obeying the unified projection model. *IEEE Trans. Robot.* **26,** 684–697 (2010).

223. Abolmaesumi, P., Salcudean, S. E., Zhu, W.-H. Z. W.-H., Sirouspour, M. R. & DiMaio, S. P. Image-guided control of a robot for medical ultrasound. *IEEE Trans. Robot. Autom.* **18,** 11–23 (2002).

224. Nadeau, C. & Krupa, A. Intensity-based direct visual servoing of an ultrasound probe. in *Proceedings - IEEE International Conference on Robotics and Automation* 5677–5682 (2011). doi:10.1109/ICRA.2011.5979673

225. Krupa, A. & Chaumette, F. Control of an ultrasound probe by adaptive visual servoing. in *2005 IEEE/RSJ International Conference on Intelligent Robots and Systems, IROS* 2007–2012 (2005). doi:10.1109/IROS.2005.1545272

226. Bachta, W. & Krupa, A. Towards ultrasound image-based visual servoing. in *Proceedings - IEEE International Conference on Robotics and Automation* **2006,** 4112–4117 (2006).

227. Krupa, A. & Chaumette, F. Guidance of an ultrasound probe by visual servoing. *Adv. Robot.* **20,** 1203–1218 (2006).

228. Mahvash, M. & Dupont, P. E. Mechanics of dynamic needle insertion into a biological material. *IEEE Trans. Biomed. Eng.* **57,** 934–943 (2010).

229. Abolhassani, N., Patel, R. & Moallem, M. Needle insertion into soft tissue: A survey. *Med. Eng. Phys.* **29,** 413–431 (2007).

230. Okamura, A. M., Simone, C. & O'Leary, M. D. Force modeling for needle insertion into soft tissue. *IEEE Trans. Biomed. Eng.* **51,** 1707–1716 (2004).

231. Xu, M. & Wang, L. V. Photoacoustic imaging in biomedicine. *Review of Scientific Instruments* **77,** (2006).

232. Sarvazyan, A. *et al.* An overview of elastography-an emerging branch of medical imaging. *Curr. Med. Imaging Rev.* **7,** 28 (2011).

233. Cleary, K. & Peters, T. Image-guided interventions: technology review and clinical applications. *Annu Rev Biomed Eng* **12,** 119–142 (2010).

234. Pogue, B. W. & Patterson, M. S. Review of tissue simulating phantoms for optical imaging. *J. Biomed. Opt.* **11,** 041102 (2006).

235. Culjat, M. O., Goldenberg, D., Tewari, P. & Singh, R. S. A review of tissue substitutes for ultrasound imaging. *Ultrasound in Medicine and Biology* **36,** 861–873 (2010).

236. Hall, T. J., Bilgen, M., Insana, M. F. & Krouskop, T. A. Phantom materials for elastography. *IEEE Trans. Ultrason. Ferroelectr. Freq. Control* **44,** 1355–1365 (1997).

237. Lamouche, G. *et al.* Review of tissue simulating phantoms with controllable optical, mechanical and structural properties for use in optical coherence tomography. *Biomed. Opt. Express* **3,** 1381–1398 (2012).

238. Madsen, E. L., Zagzebski, J. a, Banjavie, R. a & Jutila, R. E. Tissue mimicking materials for ultrasound phantoms. *Medical physics* **5,** 391–394 (2008).

239. Madsen, E. L., Hobson, M. A., Shi, H., Varghese, T. & Frank, G. R. Tissue-mimicking agar/gelatin materials for use in heterogeneous elastography phantoms. *Phys. Med. Biol.* **50,** 5597–5618 (2005).

240. Cook, J. R., Bouchard, R. R. & Emelianov, S. Y. Tissue-mimicking phantoms for photoacoustic and ultrasonic imaging. *Biomedical Optics Express* **2,** 3193 (2011).

241. Hungr, N., Long, J.-A., Beix, V. & Troccaz, J. A realistic deformable prostate phantom for multimodal imaging and needle-insertion procedures. *Medical Physics* **39,** 2031 (2012).

242. Poepping, T. L., Nikolov, H. N., Thorne, M. L. & Holdsworth, D. W. A thin-walled carotid vessel phantom for Doppler ultrasound flow studies. *Ultrasound Med. Biol.* **30,** 1067–1078 (2004).

243. Surry, K. J., Austin, H. J., Fenster, A. & Peters, T. M. Poly (vinyl alcohol) cryogel phantoms for use in ultrasound and MR imaging. *Phys. Med. Biol.* **49,** 5529 (2004).

244. King, D. M., Moran, C. M., McNamara, J. D., Fagan, A. J. & Browne, J. E. Development of a vessel-mimicking material for use in anatomically realistic Doppler flow phantoms. *Ultrasound Med. Biol.* **37,** 813–826 (2011).

245. de Korte, C. L., Céspedes, E. I., van der Steen, A. F., Norder, B. & te Nijenhuis, K. Elastic and acoustic properties of vessel mimicking material for elasticity imaging. *Ultrason. Imaging* **19,** 112–26 (1997).

246. Ryan, L. K. & Foster, F. S. Tissue equivalent vessel phantoms for intravascular ultrasound. *Ultrasound Med. Biol.* **23,** 261–273 (1997).

247. Ramnarine, K. V., Nassiri, D. K., Hoskins, P. R. & Lubbers, J. Validation of a new blood-mimicking fluid for use in Doppler flow test objects. *Ultrasound Med. Biol.* **24,** 451–459 (1998).

248. Ramnarine, K. V., Hoskins, P. R., Routh, H. F. & Davidson, F. Doppler backscatter properties of a blood-mimicking fluid for Doppler performance assessment. *Ultrasound Med. Biol.* **25,** 105–110 (1999).

249. Bashkatov, A. N. *et al.* Optical properties of melanin in the skin and skin-like phantoms. *Control. Tissue Opt. Prop. Appl. Clin. Study* **1,** 219–226\r270 (2000).

250. Ding, H., Lu, J. Q., Wooden, W. A., Kragel, P. J. & Hu, X.-H. Refractive indices of human skin tissues at eight wavelengths and estimated dispersion relations between 300 and 1600 nm. *Phys. Med. Biol.* **51,** 1479–1489 (2006).

251. Di Ninni, P., Martelli, F. & Zaccanti, G. The use of India ink in tissue-simulating phantoms. *Opt Express* **18,** 854–865 (2010).

252. Di Ninni, P., Martelli, F. & Zaccanti, G. Intralipid: towards a diffusive reference standard for optical tissue phantoms. *Phys. Med. Biol.* **56,** N21–N28 (2011).

253. Spinelli, L. *et al.* Determination of reference values for optical properties of liquid phantoms based on Intralipid and India ink. *Biomed. Opt. Express* **5,** 2037–53 (2014).

254. Zell, K., Sperl, J. I., Vogel, M. W., Niessner, R. & Haisch, C. Acoustical properties of selected tissue phantom materials for ultrasound imaging. *Phys. Med. Biol.* **52,** N475–N484 (2007).

255. Lafon, C. *et al.* Gel phantom for use in high-intensity focused ultrasound dosimetry. *Ultrasound Med. Biol.* **31,** 1383–1389 (2005).

256. Ejofodomi, O. a, Zderic, V. & Zara, J. M. Tissue-mimicking bladder wall phantoms for evaluating acoustic radiation force-optical coherence elastography systems. *Med. Phys.* **37,** 1440–1448 (2010).

257. Prahl, S. A., van Gemert, M. J. & Welch, A. J. Determining the optical properties of turbid mediaby using the adding-doubling method. *Appl. Opt.* **32,** 559–568 (1993).

258. Deguchi, S., Hotta, J., Yokoyama, S. & Matsui, T. Viscoelastic and optical properties of four different PDMS polymers. *J. micromechanics microengineering* **25,** (2015).

259. Chen, J. F., Zagzebski, J. A. & Madsen, E. L. Tests of backscatter coefficient measurement using broadband pulses. *IEEE Trans. Ultrason. Ferroelectr. Freq. Control* **40,** 603–607 (1993).

260. Madsen, E. L. *et al.* Interlaboratory comparison of ultrasonic backscatter, attenuation, and speed

measurements. *J. Ultrasound Med.* **18,** 615–631 (1999).

261. Yuan, Y. W. Ultrasonic backscatter from flowing whole blood, I: Dependence on shear rate and hematocrit. *J. Acoust. Soc. Am.* **84,** 52 (1988).

262. Fraser, K. H., Poepping, T. L., McNeilly, A., Megson, I. L. & Hoskins, P. R. Acoustic speed and attenuation coefficient in sheep aorta measured at 5-9 MHz. *Ultrasound Med. Biol.* **32,** 971–980 (2006).

263. Lockwood, G. R., Ryan, L. K., Hunt, J. W. & Foster, F. S. Measurement of the ultrasonic properties of vascular tissues and blood from 35-65 MHz. *Ultrasound Med. Biol.* **17,** 653–666 (1991).

264. Daintith, J. & Oxford Reference Online (Online Service). *A Dictionary of Physics. Oxford paperback reference.* (2009). doi:10.1093/acref/9780199233991.001.0001

265. Freutel, M., Schmidt, H., Dürselen, L., Ignatius, A. & Galbusera, F. Finite element modeling of soft tissues: material models, tissue interaction and challenges. *Clinical Biomechanics* **29,** 363–372 (2014).

266. Treeby, B. E., Jaros, J., Rendell, A. P. & Cox, B. T. Modeling nonlinear ultrasound propagation in heterogeneous media with power law absorption using a k-space pseudospectral method. *J. Acoust. Soc. Am.* **131,** 4324–36 (2012).

267. Prahl, S. A., Keijzer, M., Jacques, S. L. & Welch, A. J. Monte-Carlo model of light propagation in tissue. *SPIE Proc. Dosim. Laser Radiat. Med. Biol.* **IS,** 102–111 (1989).

268. Prager, R. W., Ijaz, U. Z., Gee,   a H. & Treece, G. M. Three-dimensional ultrasound imaging. *Proc. Inst. Mech. Eng. H.* **224,** 193–223 (2010).

269. Staszyk, C., Bohnet, W., Gasse, H. & Hackbarth, H. Blood vessels of the rat tail: a histological re-examination with respect to blood vessel puncture methods. *Lab. Anim.* **37,** 121–125 (2003).

270. Coatney, R. W. Ultrasound imaging: principles and applications in rodent research. *ILAR J.* **42,** 233–247 (2001).

271. Frey, A. M. Success rates for peripheral i.v. insertion in a children's hospital. Financial implications. *J. Intraven. Nurs.* **21,** 160–165 (1998).

272. Casto, A. B. & Layman, E. Principles of Healthcare Reimbursement. *Am. Heal. Inf. Manag. Assoc.* (2006). at <http://www.bilozix.com/hcreimburesement.pdf>

273. Lee-Lewandrowski, E. & Lewandrowski, K. Point-of-care testing. An overview and a look to the future. *Clin. Lab. Med.* **21,** 217–239, vii (2001).

274. Howie, S. R. C. Blood sample volumes in child health research: review of safe limits. *Bull. World Health Organ.* **89,** 46–53 (2011).

275. Shokoohi, H. *et al.* Ultrasound-guided peripheral intravenous access program is associated with a marked reduction in central venous catheter use in noncritically ill emergency department patients. *Ann. Emerg. Med.* **61,** 198–203 (2013).

276. Stokowski, G., Steele, D. & Wilson, D. The use of ultrasound to improve practice and reduce complication rates in peripherally inserted central catheter insertions: final report of investigation. *J. Infus. Nurs.* **32,** 145–155 (2009).

277. Vilchis-González, A., Avila-Vilchis, J. C. & García-Torres, A. TERMI robot. in *Electronics,*

Robotics and Automotive Mechanics Conference, CERMA 2007 - Proceedings 464–469 (2007). doi:10.1109/CERMA.2007.4367730

278. Abolmaesumi, P., Sirouspour, M. R. & Salcudean, S. E. Real-time extraction of carotid artery contours from ultrasound\nimages. *Proc. 13th IEEE Symp. Comput. Med. Syst. CBMS 2000* 2–7 (2000). doi:10.1109/CBMS.2000.856897

279. Nakadate, R. *et al.* Implementation of an automatic scanning and detection algorithm for the carotid artery by an assisted-robotic measurement system. in *IEEE/RSJ 2010 International Conference on Intelligent Robots and Systems, IROS 2010 - Conference Proceedings* 313–318 (2010). doi:10.1109/IROS.2010.5651667

280. Nakadate, R. *et al.* Out-of-plane visual servoing method for tracking the carotid artery with a robot-assisted ultrasound diagnostic system. in *Proceedings - IEEE International Conference on Robotics and Automation* 5267–5272 (2011). doi:10.1109/ICRA.2011.5979594

281. Nakadate, R. *et al.* Development of a robot assisted carotid blood flow measurement system. *Mech. Mach. Theory* **46,** 1066–1083 (2011).

282. Gudeloglu, A., Brahmbhatt, J. V. & Parekattil, S. J. Robotic-assisted microsurgery for an elective microsurgical practice. *Semin. Plast. Surg.* **28,** 11–19 (2014).

283. Fleming, I. *et al.* Cooperative robot assistant for retinal microsurgery. in *Lecture Notes in Computer Science (including subseries Lecture Notes in Artificial Intelligence and Lecture Notes in Bioinformatics)* **5242 LNCS,** 543–550 (2008).

284. Sznitman, R. *et al.* Data-driven visual tracking in retinal microsurgery. *Med. Image Comput. Comput. Assist. Interv.* **15,** 568–75 (2012).

285. Sznitman, R., Richa, R., Taylor, R. H., Jedynak, B. & Hager, G. D. Unified detection and tracking of instruments during retinal microsurgery. *IEEE Trans. Pattern Anal. Mach. Intell.* **35,** 1263–1273 (2013).

286. Ang, W. T., Pradeep, P. K. & Riviere, C. N. Active tremor compensation in microsurgery. *Conf. Proc. IEEE Eng. Med. Biol. Soc.* **4,** 2738–2741 (2004).

287. Faratro, R., Jeffries, J., Nesrallah, G. E. & Macrae, J. M. The care and keeping of vascular access for home hemodialysis patients. *Hemodial. Int.* **19,** S80–S92 (2015).

288. McFarlane, P. A., Bayoumi, A. M., Pierratos, A. & Redelmeier, D. A. The quality of life and cost utility of home nocturnal and conventional in-center hemodialysis. *Kidney Int.* **64,** 1004–1011 (2003).

289. Hajduk, M., Jenčík, P., Jezný, J. & Vargovčík, L. Trends in industrial robotics development. *11th International Conference Industrial, Service and Humanoid Robotics, ROBTEP 2012* **282,** 1–6 (2013).

290. Stenmark, M. & Malec, J. Knowledge-based instruction of manipulation tasks for industrial robotics. *Robot. Comput. Integr. Manuf.* **33,** 56–67 (2015).

291. Heyer, C. Human-robot interaction and future industrial robotics applications. in *IEEE/RSJ 2010 International Conference on Intelligent Robots and Systems, IROS 2010 - Conference Proceedings* 4749–4754 (2010). doi:10.1109/IROS.2010.5651294

292. Singer, P. W. Military robotics and ethics: A world of killer apps. *Nature* **477,** 399–401 (2011).

293. Mies, G. Military robots of the present and the future. *Aarms* **9,** 125–137 (2010).

294. Pirjanian, P., Karlsson, N., Goncalves, L. & Di Bernardo, E. Low-cost visual localization and mapping for consumer robotics. *Ind. Robot. Int. J.* **30,** 139–144 (2003).

295. Pirjanian, P. Challenges for standards for consumer robotics. in *2005 IEEE Workshop on Advanced Robotics and its Social Impacts* **2005,** 260–264 (2005).

296. Nickerson, R. Pioneering the personal robotics industry. in *2009 IEEE International Conference on Technologies for Practical Robot Applications, TePRA 2009* 179–185 (2009). doi:10.1109/TEPRA.2009.5339625

297. Xu, Y. *et al. Household Service Robotics*. *Household Service Robotics* (2015). doi:10.1016/B978-0-12-800881-2.00023-2

298. Alimisis, D. Educational robotics: Open questions and new challenges. *Themes Sci. Technol. Educ.* **6,** 63–71 (2013).

299. Veres, S. M., Molnar, L., Lincoln, N. K. & Morice, C. P. Autonomous vehicle control systems -- a review of decision making. *Proc. Inst. Mech. Eng. Part I J. Syst. Control Eng.* **225,** 155–195 (2011).

300. Özgüner, Ü., Stiller, C. & Redmill, K. Systems for safety and autonomous behavior in cars: The DARPA grand challenge experience. *Proc. IEEE* **95,** 397–412 (2007).